

Design of Adaptive Robust Controllers for Renewable Energy Sources Integrated Smart Grid System

Thesis

Submitted in partial fulfillment of the requirements for the degree of
DOCTOR OF PHILOSOPHY

by

Hemachandra.G

Reg.No.EE14F03

Under the Guidance of

Dr. K. Manjunatha Sharma

Associate Professor

Dept. of EEE



DEPARTMENT OF ELECTRICAL AND ELECTRONICS ENGINEERING,
NATIONAL INSTITUTE OF TECHNOLOGY KARNATAKA,
SURATHKAL, MANGALORE -575025

JUNE, 2020

DECLARATION

I hereby *declare* that the research Thesis entitled **Design of Adaptive Robust Controllers for Renewable Energy Sources Integrated Smart Grid System** which is being submitted to the *National Institute of Technology Karnataka, Surathkal* in partial fulfillment of the requirement for the award of the Degree of *Doctor of Philosophy* in Department of Electrical and Electronics Engineering is a *bonafide report of the research work carried out by me*. The material contained in this Research Thesis has not been submitted to any University or Institution for the award of any degree.



.....
Hemachandra Gudimindla, Reg. No.145079EE14F03.
Department of Electrical and Electronics Engineering.

Place: NITK-Surathkal.

Date:

CERTIFICATE

This is to certify that the Research Thesis entitled **Design of Adaptive Robust Controllers for Renewable Energy Sources Integrated Smart Grid System** submitted by **Hemachandra Gudimindla** (Reg. No. 145079EE14F03) as the record of the research work carried out by him, is accepted as the *Research Thesis submission* in partial fulfillment of the requirements for the award of degree of **Doctor of Philosophy**.

Dr. K.Manjunatha Sharma
(Research Guide) Associate Professor
Department of Electrical and Electronics Engineering
NITK Surathkal 575025

Dr. Shubhanga K N
(Chairman - DRPC)
Professor and Head of the Department
Department of Electrical and Electronics Engineering
NITK Surathkal 575025

Acknowledgements

It gives me immense pleasure and a great sense of satisfaction to express my heartfelt gratitude to those who made this dissertation possible.

I would like to express my sincere gratitude to my supervisor **Dr. K. Manjunatha Sharma**, Associate Professor, Department of Electrical and Electronics Engineering, NITK Surathkal, for his guidance, encouragement. He has been a constant source of inspiration throughout this journey. I feel proud to have worked under his guidance.

I wish to thank my research progress assessment committee (RPAC) members **Prof. Sitaram Nayak**, Professor, Department of Civil Engineering, NITK Surathkal **Dr. H Nagendrappa** Assistant Professor, Department of Electrical and Electronics Engineering, NITK Surathkal for their insightful comments and encouragement, but also for the hard questions which incited me to widen my research from various perspectives.

I wish to express my sincere thanks to **Prof. Uma Maheswara Rao**, Director, NIT surathkal for his support and encouragement.

I thank National Institute of Technology Karnataka (NITK), Surathkal for giving me an opportunity for doing research and Ministry of Human Resource Development (MHRD), Government of India for awarding research scholarship.

My special and sincere acknowledge, heartfelt gratitude and indebtedness are due to my parents Sri G.Mogilaiah and Smt. G. Eswari for their sincere prayers, blessings, constant encouragement. I would like to express my deepest gratitude towards my wife S Sandhya for shouldering the responsibilities and moral support rendered to me through my life, without which my research work would not have been possible. My heart gratitude to my father in law and mother in law Sri. S. Sundaresan babu and

Smt. M. Padma kumari for their blessings, support and encouragement. I heartly acknowledge all my family members for their love and patience which kept me going in this journey. Their faith and unconditional love towards me are the reason for whatever I have achieved in my life.

Above all, I express my deepest regards and gratitude to "ALMIGHTY" whose divine light and warmth showered upon me the perseverance, inspiration, faith and enough strength to keep the momentum of work high even at tough moments of research work.

Abstract

Energy supply and consumption from conventional fossil fuel is seen as a factor to global warming and deterioration of the environment. It is essential to use clean, non-polluting and alternative energy sources. Wind energy conversion technologies have proved attractive and competitive in terms of conventional fossil energy technologies with increased demand for electricity. It may reduce the negative impacts of traditional energy sources on the environment and reducing dependency on fossil fuels. Because of its high efficiency, the wind energy system can be an alternative source of energy for the future. The most frequently used variable-speed wind turbine is to enhance energy capture at distinct wind speeds. Self-excitation, elevated efficiency, power density, a wide variety of velocity, certainty and full isolation of the PMSG from the power grid have rendered it preferable for various wind systems.

In addition to the wind power system, photovoltaic (PV) system developments are heightened the need for injecting the PV power in to the grid. PV array is composed of series and parallel PV cell combinations to maintain the required current and voltage levels operate in centralized grid connected inverter. However, substantial power losses have been reported due to the imbalanced generation between PV panels, which is mainly due to partial shading.

Fuel cell (FC) act as continuous power source to mitigate the intermittent nature of PV and wind system. FC's are clean and high efficient independent power generating source with zero emissions.

Investigation of the performance of robust and non-linear controllers under varying wind speed scenarios is explored as a preliminary study. It is discovered that automated robust controller design is essential for the renewable power systems applications. Proposed research work intends to address the maximum power tracking issue for the autonomous wind power system and grid connected PMSG based wind energy conversion system, sub-module level PV system, and fuel cell. Genetic algorithm is used to design a new robust Quantitative Feedback Theory (QFT) controller based on automatic loop shaping methodology. The outcome of research work

is to extract the maximum power from hybrid renewable energy sources with automated robust QFT control strategy.

Keywords:

Automatic Loop-Shaping, Genetic Algorithm, Hybrid Renewable Energy System, Maximum Power Point Tracking, Quantitative Feedback Theory, Robust Controller, Smart Grid, Uncertainty.

Contents

Acknowledgements	i
Abstract	iii
List of figures	xi
List of tables	xviii
Nomenclature	xx
Abbreviations	xx
Nomenclature	xxi
1 Introduction	1
1.1 Background	1
1.2 Wind Turbine Classification	3
1.2.1 Small, Medium and Large scale wind turbines	3
1.2.2 Passive, Active Stall-, and Pitch-controlled Wind Turbines	3
1.2.3 Wind turbines-Horizontal and Vertical Axis	4
1.2.4 Variable and Fixed Speed wind Turbines	4
1.3 Literature Review	5
1.3.1 Maximum power point techniques in PMSG based WECS	5
1.3.1.1 Research Gap	8
1.4 Introduction to Quantitative Feedback Theory	8
1.5 Uncertainty	9
1.5.1 Sources of Uncertainty and Classification	9
1.6 QFT Design Procedure	10
1.7 Performance Specifications	11
1.7.1 Robust Stability	11
1.7.2 Output Disturbance Rejection	11
1.7.3 Reference Tracking	12

1.8	Step-by-Step QFT based Controller Design	12
1.8.1	High Frequency Gain	14
1.8.2	Automatic Loop-shaping methodology based Quantitative feed- back theory (QFT) Controller	14
1.8.2.1	Research Gap	15
1.8.3	Photovoltaic (PV) circuit model Identification	16
1.8.3.1	Research Gap	17
1.8.4	Grid connected Photovoltaic System	18
1.8.4.1	Research Gap	18
1.8.5	Grid connected Fuel Cell	18
1.8.5.1	Research Gap	19
1.8.6	DC-coupled Hybrid microgrid	19
1.8.6.1	Research Gap	20
1.9	Research Objectives	20
1.10	Thesis outline	21
1.10.1	Thesis Organization	21
2	QFT controller design for PMSG based wind energy conversion sys- tems	24
2.1	Grid Connected Wind Power System Configurations	24
2.1.1	SCIG based FSWT system	25
2.1.2	WRIG based semi-variable speed wind system	26
2.1.3	DFIG based semi-variable speed wind system	26
2.1.4	Wide speed range of full-variable speed wind system	27
2.2	PMSG based Variable speed wind energy conversion system	28
2.3	Feedback Linearization controller for PMSG based WECS	33
2.4	Existing manual Loop-shaping methods	35
2.5	Proposed automated QFT Design	38
2.5.1	Problem Statement	38
2.5.2	Fitness Function Formulation	38
2.5.3	Genetic Algorithm	40
2.6	Application And Results	41
2.6.1	Selection of plant with parameter uncertainty	41
2.6.2	Template generation	42

2.6.3	Bounds computation	42
2.6.4	Loop shaping	43
2.6.5	Pre-filter Design	45
2.6.6	Validation	46
2.7	Simulation Results	49
2.7.1	Constant wind speed	50
2.7.2	Step change in wind speed	52
2.8	Stochastic wind speed	58
2.9	Grid connected PMSG based WECS with full-scale Power converters .	60
2.10	Step change in wind profile	61
2.11	Stochastic wind profile	65
2.12	Summary	66
3	QFT controller for Grid connected Photovoltaic system	67
3.1	Introduction	67
3.2	Photovoltaic-system classification	68
3.3	Centralized MPPT Systems	69
3.4	Distributed MPPT Systems	71
3.4.1	String Level	71
3.4.2	Module Level	72
3.4.2.1	Module-integrated parallel inverters	72
3.4.2.2	Module-integrated Parallel Converters	73
3.4.2.3	Module-integrated Series Converters	73
3.4.2.4	Module-integrated Series Inverters	73
3.4.3	Sub-module Level	74
3.4.3.1	Submodule-integrated Converters	74
3.4.4	Cell Level	74
3.4.5	Ideal and Complete single Diode PV Models	75
3.4.6	ISPV Parameterization	75
3.4.7	ISPV-1 Parameterization	78
3.4.8	ISPV-2 Parameterization	79
3.4.9	CSPV Parameterization	82
3.5	System Performance Evaluation and Necessary Steps	85
3.5.1	Performance Indices	85

3.5.2	Circuit Model Identification	88
3.5.3	PV Converter	89
3.6	QFT controller design application to PV	92
3.6.1	Selection of plant with parameter uncertainty	92
3.6.2	Template generation	92
3.6.3	Bounds computation	93
3.6.4	Loop shaping	93
3.6.5	Pre-filter Design	95
3.6.6	Validation	96
3.7	Simulation Results	97
3.7.1	Comparison of existing and proposed MPPT controllers simulation	97
3.7.2	Comparison of switching and average model simulation with Proposed MPPT controller	100
3.7.3	Real time environmental data (24-Hrs.)	104
3.7.4	Real time environmental data (24-Hrs.) with partial shading condition	107
3.7.5	Real time environmental data (24-Hrs.) with wide range of tem- perature	113
3.8	Summary	118
4	QFT controller design for grid connected PEM fuel cell	119
4.1	Introduction	119
4.2	Dynamic Electric circuit Model of PEMFC	120
4.2.1	PEMFC Voltage Drops	121
4.2.2	Ohmic Voltage Drop	121
4.2.3	Concentration Voltage drop	122
4.2.4	Double-Layer Charge effect	122
4.3	Thermal Model of PEMFC	124
4.4	DC-DC Converter Modelling	125
4.5	PEMFC Boost Converter Circuit Design	127
4.6	Controller Design for Boost converter	129
4.7	LCL Filter Design	131
4.8	Voltage and current loop controllers design	133
4.9	Simulation Results	135

4.9.1	Case 1: Unity power factor operation	136
4.9.2	Case 2: Desired Active power P=7.2 kW and Q= 1 kVar injected to grid	138
4.9.3	Case 3: Desired Active power P=7.2 kW injected to grid and Q= - 1 kW Consumed from grid	140
4.9.4	Case 4: DC-link Voltage uncertainty	143
4.9.5	Case 5: Grid Voltage uncertainty	145
4.10	Summary	146
5	QFT controller for Hybrid green renewable energy power system	147
5.1	Unit Sizing	147
5.2	80 kW PMSG based WECS Performance	150
5.3	57.7 kW Grid connected PV	153
5.4	80 kW PMSG based WECS and 57.7 kW Grid connected PV	160
5.5	32 kW PEMFC Grid connected operation	162
5.5.1	Boost Converter Circuit Design	162
5.6	80 kW WT, 57.7 kW PV and 32 kW PEMFC Grid connected operation	166
5.7	Summery	167
6	Conclusion	168
6.1	Scope for Future Work	169
	Bibliography	170

List of Figures

1.1	Wind energy conversion system configuration.	2
1.2	Wind turbine power regulation methods.	4
1.3	Block diagram of optimal TSR control.	6
1.4	Block diagram of power curve based control.	6
1.5	Block diagram of optimal torque control.	7
1.6	Uncertainty in physical systems.	9
1.7	Two degree of freedom (2DOF) control system structure.	11
1.8	QFT Controller Design steps.	13
2.1	Schematic diagram of fixed-speed SCIG based wind system.	25
2.2	WRIG based semi-variable-speed (10%) WECS.	26
2.3	DFIG based semi-variable-speed ($\pm 30\%$) WECS.	27
2.4	Wide range of speed (0 - 100%) wind generators for WECS.	27
2.5	PMSG based autonomous wind turbine power system.	29
2.6	Boost chopper circuit.	31
2.7	Block Diagram of Feedback Linearization control Structure.	33
2.8	Block Diagram of QFT control Structure.	36
2.9	Block Diagram of Multi-Model QFT control Structure.	37
2.10	Template Generation for different frequencies.	42
2.11	Intersection of Performance Bounds.	44
2.12	Closed loop frequency response with proposed controller $G_1(s)$	45
2.13	Closed loop frequency response with proposed controller $G_2(s)$	46
2.14	Robust stability margin ananalysis for $G_1(s)$	48
2.15	Robust stability margin ananalysis for $G_2(s)$	48
2.16	Frequency domain analysis of reference tracking with $G_1(s)$	48
2.17	Frequency domain analysis of reference tracking with $G_2(s)$	48
2.18	Time domain analysis of reference tracking with $G_1(s)$	48

2.19	Time domain analysis of reference tracking with $G_2(s)$	48
2.20	Constant wind speed (a) Wind Profile (b) Load Resistance (c) output Power (d) Wind Turbine Torque	51
2.21	Step change in wind speed (a) Wind Profile (b) Speed tracking (c) Load Resistance (d) Error Square	53
2.22	Step change in wind speed (e) output Power (f) Wind Turbine Torque (g) Generator Torque (h) Torque difference	54
2.23	Load Resistance.	55
2.24	Power.	55
2.25	Wind turbine torque.	55
2.26	Torque difference.	55
2.27	Load Resistance	57
2.28	Power.	57
2.29	Wind Turbine torque.	57
2.30	Torque difference.	57
2.31	Stochastic wind speed (a) Wind Profile (b) Load Resistance (c) output Power (d) Wind Turbine Torque	59
2.32	Block Diagram of PMSG based WECS with full-scale power converter.	60
2.33	wind profile	61
2.34	Reference tracking	62
2.35	Speed error	62
2.36	DC-link voltage	63
2.37	Current Injection	63
2.38	Grid Voltage	64
2.39	Power injection	64
2.40	Power injection	64
2.41	wind profile	65
2.42	Power injection	65
3.1	Centralised MPPT with galvanic isolation (a) three-stage (b) two-stage (c) single-stage	70
3.2	Centralised MPPT without galvanic isolation (a) two-stage (b) single- stage	71
3.3	Distributed MPPT at PV string level (a) parallel inverter (b) parallel converter operation	71

3.4	Configurations of (a) MIPI (b) MIPC for grid interconnections	72
3.5	Configurations of (a) MISC (b) MISI for grid interconnections	73
3.6	Series configurations of (a) submodule-integrated (b) cell- integrated series converters to form a DC link	75
3.7	Equivalent circuit of PV models (a) ISPV (b) ISPV-1 (c) ISPV-2 (d) CSPV	76
3.8	(a) $I - V$ curve (b) $P - V$ curve of PV cell under constant irradiation (1000 W/m ²) and standard test conditions (STC) for ISPV	78
3.9	(a) $I - V$ curve (b) $P - V$ curve of PV cell under constant irradiation (1000 W/m ²) and STC for ISPV-1	80
3.10	(a) $I - V$ curve (b) $P - V$ curve of PV cell under constant irradiation (1000 W/m ²) and STC for ISPV-2	82
3.11	(a) $I - V$ curve (b) $P - V$ curve of PV cell under constant irradiation (1000 W/m ²) and STC for CSPV	84
3.12	Flowchart of PV circuit model identification	86
3.13	Flowchart of $I - V$ and $P - V$ curves plotting under varying environmental condition	87
3.14	(a) $I - V$ curve (b) $P - V$ curve of PV cell under varying irradiance	88
3.15	(a) $I - V$ curve (b) $P - V$ curve of PV cell under varying temperature	88
3.16	Synchronous buck converter (SBC)	89
3.17	Bode diagram of uncertain plant	92
3.18	Uncertain plant templates	94
3.19	Robust stability bound	94
3.20	performance bound of disturbance rejection at plant output	94
3.21	Reference tracking bounds	94
3.22	Superposition of bounds	94
3.23	Intersection of bounds	94
3.24	Automated loop-shaping	95
3.25	Reference tracking in frequency domain	95
3.26	Stability margins	96
3.27	Disturbance rejection	96
3.28	Block diagram of Submodule integrated grid connected PV system	97
3.29	Simulated partial shading pattern	98
3.30	PV output voltage	98

3.31	PV output current	99
3.32	Output voltage of subMICs	99
3.33	Total output power	99
3.34	grid voltage V_g , grid current i_g , dc-link voltage V_{dc} , and output current of the string i_o	100
3.35	PV output voltage	101
3.36	PV output current	101
3.37	Output voltage of subMICs	101
3.38	Duty cycle of subMIC	102
3.39	SubMICs output power	102
3.40	Total output power	102
3.41	grid voltage V_g , grid current i_g , dc-link voltage V_{dc} , and output current of the string i_o	103
3.42	Irradiation	105
3.43	Temperature	105
3.44	PV voltage	105
3.45	PV current	105
3.46	SMICs power	105
3.47	Total power	105
3.48	Grid voltage	106
3.49	Grid current	106
3.50	Grid current	106
3.51	Irradiation	107
3.52	Temperature	107
3.53	PVSV ₁₋₃₉	107
3.54	PVSC ₁₋₃₉	107
3.55	PVSV ₄₀₋₄₅	108
3.56	PVSC ₄₀₋₄₅	108
3.57	PVSP ₁₋₃₉	108
3.58	PVSP ₄₀₋₄₅	108
3.59	PV output power	108
3.60	Grid voltage	108
3.61	Grid current	109
3.62	Irradiation	110

3.63	Temperature	110
3.64	PVSV ₁₋₃₉	110
3.65	PVSC ₁₋₃₉	110
3.66	PVSV ₄₀₋₄₅	110
3.67	PVSC ₄₀₋₄₅	110
3.68	PVSP ₁₋₃₉	111
3.69	PVSP ₄₀₋₄₅	111
3.70	PV output power	111
3.71	Grid current	111
3.72	Irradiation	113
3.73	Temperature	113
3.74	PV voltage	113
3.75	PV current	113
3.76	SMICs power	114
3.77	Total power	114
3.78	DC-link voltage	114
3.79	Grid voltage	114
3.80	Grid current	114
3.81	Irradiation	115
3.82	Temperature	115
3.83	PV voltage	116
3.84	PV current	116
3.85	SMICs power	116
3.86	Total power	116
3.87	DC-link voltage	116
3.88	Grid voltage	116
3.89	Grid current	117
4.1	Electrical circuit model of PEMFC	123
4.2	Dynamic model of PEMFCwith thermal effect	123
4.3	Block diagram of boost converter with voltage feedback control	125
4.4	fuel cell output voltage	128
4.5	fuel cell output current	128
4.6	fuel cell output Power	128
4.7	fuel cell stack output Voltage	128

4.8	fuel cell stack output Current.	128
4.9	fuel cell stack output Power	128
4.10	Bode response of uncertain DC-DC converter	130
4.11	Block diagram of QFT controller for the PEM fuel cell	131
4.12	LCL-Filter response	133
4.13	Bode response of uncertain LCL filter	134
4.14	Current and Voltage control loops for PEMFC	135
4.15	Block Diagram of Single-phased grid connected Fuel cell	136
4.16	fuel cell output (a) voltage (b) current (c) Power	137
4.17	DC-link Voltage	138
4.18	Grid voltage and current	138
4.19	Active and Reactive power injection into grid	138
4.20	(a) Phase difference between grid voltage and current (b) Power factor	138
4.21	fuel cell output (a) voltage (b) current (c) Power	139
4.22	DC-link Voltage	139
4.23	Grid voltage and current	139
4.24	Active and Reactive power injection into grid	140
4.25	(a) Phase difference between grid voltage and current (b) Power factor	140
4.26	fuel cell output (a) voltage (b) current (c) Power	141
4.27	Active and Reactive power injection into grid	142
4.28	(a) Phase difference between grid voltage and current (b) Power factor	142
4.29	DC-link Voltage	142
4.30	Grid voltage and current	142
4.31	fuel cell output (a) voltage (b) current (c) Power	143
4.32	Grid voltage and current	143
4.33	DC-link Voltage	143
4.34	Active and Reactive power injection into grid	144
4.35	(a) Phase difference between grid voltage and current (b) Power factor	144
4.36	fuel cell output (a) voltage (b) current (c) Power	145
4.37	Grid voltage and current	145
4.38	DC-link Voltage	145
4.39	Active and Reactive power injection into grid	146
4.40	(a) Phase difference between grid voltage and current (b) Power factor	146
5.1	24-Hrs Load data (Mammen et al., 2018).	149

5.2	Grid Connected Hybrid Renewable energy system	149
5.3	Schematic diagram of grid connected wind power system	150
5.4	wind profile	151
5.5	Power injection	151
5.6	Current Injection	152
5.7	Grid Voltage	152
5.8	Schematic diagram three-phase grid tied PV system	153
5.9	Irradiation	154
5.10	PV voltage current and power	154
5.11	SMIC voltage current and power	155
5.12	Total output voltage current and power	156
5.13	DC-link voltage	157
5.14	Grid Voltage	158
5.15	Inverter grid and load power	158
5.16	Inverter grid and load current	158
5.17	Current Injection	159
5.18	Current Injection	159
5.19	Grid Voltage	159
5.20	Grid Voltage	159
5.21	Schematic diagram of grid connected PV and wind power system . . .	160
5.22	Inverter grid and load power	161
5.23	Inverter grid and load current	161
5.24	Schematic diagram three-phase grid tied FC power plant	162
5.25	FC stack current	163
5.26	FC stack Voltage	163
5.27	FC stack power	163
5.28	Inverter, grid and load power	165
5.29	Schematic diagram of grid connected hybrid renewable power system .	166
5.30	Power	167

List of Tables

2.1	Templates points.	43
2.2	Comparison of controllers.	45
2.3	System Parameters.	50
2.4	Proposed controller performance at constant wind speed	52
2.5	Proposed controller performance under step variation 7-9 m/s	56
2.6	Proposed controller performance under step variation 9-11 m/s	58
2.7	PMSG and Wind Turbine parameters	61
3.1	Comparison of Circuit Model Accuracy	87
3.2	MPP under varying Environmental Conditions	89
3.3	Comparison of existing and proposed controller based Power extraction	106
3.4	Comparison of existing and proposed controller under partial shading (09:30 Hrs.-11:30 Hrs.)	109
3.5	Comparison of existing and proposed controller under partial shading (14:30 Hrs.-16:30 Hrs.)	112
3.6	Comparison of existing and proposed controller under wide range of temperature	115
3.7	Comparison of existing and proposed controller under wide range of temperature with partial shading pattern	117
4.1	Single phase LCL filter parameters	133
4.2	Real Power Injection to Grid (UPF operation)	139
4.3	Real and reactive power Injection	140
4.4	Real power Injection and reactive power consumption	142
5.1	PV voltage and current under step variation of irradiation	155
5.2	PV-SMIC voltage, current and power under step variation of irradiation	156

5.3	Total SMIC voltage, current and power under step variation of irradiation	157
5.4	Boost converter parameters	165

Nomenclature

ρ	Air density (kg/m ³)
v_ω	Wind speed (m/s)
$G(s)$	Transfer function of controller
$F(s)$	Transfer function of pre-filter
R_T	Wind turbine blade radius (m)
$P(s)$	Transfer function of uncertain plant
$p(s)$	Set of uncertain plants
P_m	Mechanical power (W)
P_k	Wind kinetic power (W)
P_s^*	Reference generator power (W)
P_s	Generator power (W)
T_e^*	Reference electromagnetic torque (N-m)
T_e	Electromagnetic torque (N-m)
C_P	Power coefficient
C_P^{op}	Optimal power coefficient
C_T	Torque coefficient
ω_l	Blade rotational speed (rad/s)
ω_T	Wind turbine angular speed (rad/s)
ω_h^*	Generator reference speed

ω_h	Generator speed
λ	Tip-speed ratio
λ_T^{op}	Optimal tip-speed ratio
β	Blade pitch angle (Deg)
r_{gb}	Gear-box ratio
E	Irradiation (W/m ²)
T	Temperature (°C)
q	Electron Charge ($1.6 \times 10^{-19}C$)
K	Boltzmann constant ($1.38 \times 10^{-23}J/K$)
A	Diode ideality factor
i_{ph}	Temperature dependent photon current (A)
$i_s(E, T)$	Temperature dependent diode saturation current (A)
R_s	Series resistance (Ω)
R_{sh}	Shunt resistance (Ω)
$R_{s,ch}$	chopper equivalent variable resistance (Ω)
η	Efficiency
V_{rms}	Grid voltage
V_{dc}	DC-link voltage
L	Buck-converter inductance (H)
R_L	Load resistance
α	Duty-ratio
r_{pv}	Ratio of PV voltage to current (Ω)
V_t	Thermal Voltage
n_s	Number of series connected cells
$V_{fc,cell}$	Fuel cell voltage per each cell

V_{fc}	Fuel cell voltage
C_{pv}	Buck converter input capacitance (F)
C_o	Buck converter output capacitance (F)
R	Stator resistance (Ω)
L_d, L_q	Stator d-axis and q-axis inductance (H) respectively.
p	Pole pairs
ϕ_m	Flux linkage (Wb)
τ_{em}	Electromagnetic torque (N-m)
τ_{wt}	Wind turbine torque (N-m)
L_s	Load inductance (H)
\mathcal{L}	Lie-derivative
i_d, i_q	d-axis and q-axis current (A) respectively.
K_G	Controller gain
z_i	Controller zeros
p_k	Controller poles
$\psi(x)$	Penalty function
$A(\omega_1, \omega_2)$	Area constraint function
i_{pv}	PV output current (A)
v_{pv}	PV output voltage (V)
V_{oc}	PV output voltage (V)
I_{sc}	PV cell short-circuit current (A)
α_T	Current temperature coefficient (%/K)
β_T	Voltage temperature coefficient (%/K)
γ_T	Voltage irradiance coefficient (m^2/kW)
$P(s)$	Transfer function of uncertain plant

$G(s)$	Transfer function of controller
$F(s)$	Transfer function of pre-filter
$R(s)$	Reference tracking
$D_o(s), D_1(s)$	Plant input disturbance signals
$D_x(s), D_2(s)$	Plant output disturbance signals
$N(s)$	Noise signal
$U(s)$	Control Signal
$T_1(j\omega)$	Robust stability transfer function
γ_1	Upper boundary for robust stability
$T_2(j\omega)$	Output disturbance rejection transfer function
γ_1	Upper boundary for output disturbance rejection
$T_7(j\omega)$	Reference tracking transfer function
γ_{7L}	Lower boundary for reference tracking
γ_{7U}	Upper boundary for reference tracking
$L_g(j\omega)$	Loop-gain transfer function
ω_i	Frequency array
ΔP_{dcs}	Sub-module output power difference
ΔP_{dc}	Total output power difference
$PVSV_{1-39}$	PV sub-module voltage for SMIC1-SMIC39
$PVSV_{40-45}$	PV sub-module voltage for SMIC40-SMIC45
$PVSC_{1-39}$	PV sub-module current for SMIC1-SMIC39
$PVSC_{40-45}$	PV sub-module current for SMIC40-SMIC45
$PVSP_{1-39}$	PV sub-module power for SMIC1-SMIC39
$PVSP_{40-45}$	PV sub-module power for SMIC40-SMIC45
E_{fc}	Fuel cell stack internal voltage (V)

V_{out}	Fuel cell stack output voltage (V)
n_s	Number of cells in the stack (V).
$V_{act}, V_{act,cell}$	Activation voltage drop at stack and cell level respectively.
$V_{ohm}, V_{ohm,cell}$	Ohmic voltage drop at stack and cell level respectively.
$V_{conc}, V_{conc,cell}$	Concentration of voltage drop at stack and cell level respectively.
\dot{q}_{net}	Heat energy (J)
\dot{q}_{chem}	Chemical energy (J)
\dot{q}_{elec}	electrical energy (J)
\dot{q}_{loss}	Heat energy loss
$\dot{q}_{sens+latent}$	sensible and latent heat (J)
C_{FC}	Total specific heat capacity
M_{FC}	Mass of fuel cell stack

Abbreviations

AC	Alternating current
ALP	Automatic loop-shaping
AQFT	Automated Quantitative Feedback Theory
AWPS	Autonomous wind power system
CAD	Computer aided design
CSD	Control system design
CSPV	Complete single diode model
DC	Direct current
DFIG	Doubly fed induction generator
DG	Distributed generation
DMPPT	Distributed maximum power point tracking
DPV	Double diode PV model
EC	Existing controller
FC	Fuel cell
FSWT	Fixed speed wind turbine
GA	Genetic Algorithm
GPV	Grid connected PV
GSC	Grid side converter
HFG	High frequency gain

ISPV	Ideal single diode PV model
LFAC	Low frequency AC
LTI	Linear time Invariant
MATLAB	Matrix Laboratory
MIMO	Multi input multi output
MIPI	Module integrated parallel inverter
MISC	Module integrated series converter
MISI	Module integrated series inverter
MPPT	Maximum power point tracking
MSC	Machine side converter
NC	Nichols Chart
NRMSD	Normalised root mean square error
PCC	Point of common coupling
PEMFC	Proton exchange membrane fuel cell
PLL	Phase locked loop
PMSG	Permanent magnet synchronous generator
PV	Photovoltaic
PVSC	PV current at sub-module
PVSP	PV power at sub-module
PVSV	PV voltage at sub-module
PWM	Pulse width modulation
QFT	Quantitative Feedback Theory
RMSD	Root mean square error
SBC	Synchronous buck converter
SCIG	Squirrel cage induction generator

SISO	Single input single output
SPV	Single diode PV model
Sub-MIC	Sub-module Integrated Converter
TSR	Tip-speed ratio
VSWT	Variable Speed Wind Turbine
WECS	Wind Energy Conversion System
WRIG	Wound rotor induction generator
WRSG	Wound rotor synchronous generator
WT	Wind Turbine
2-DOF	Two degree of freedom

Chapter 1

Introduction

1.1 Background

Renewable energy sources have received great attention due to global warming, higher tariff rates and limited resources of fossil fuels in conventional generation system. Non-conventional energy sources play a prominent role in the electric power generation due to their inexhaustible and unpolluted nature. In comparison to coal and oil, renewable energies are clean, plentiful, regenerated naturally, accessible across the world and have no environmental impacts. Wind energy is one of the most rapidly increasing sources of renewable energy due to the stochastic behaviour. Wind energy based power generation became central for both exploration and commercial advances. Currently wind plants contributing significant amount of power in the world's electrical power generation (Mathur, 2009, William and Li, 2017).

Wind power utilisation for electricity generation has been started late eighteenth century as 12 kW wind mill generator. However, technology advancements are started to generate reliable and efficient electricity power from wind around 1980's. The latest developments in wind power plants focus on the efficient conversion capability with cost-effective. The advancement in physical structure of wind turbines enabled on-shore and off-shore application with higher ratings to extract more energy with high energy density. The wind energy market has experienced significant technological developments in aerodynamic design, converters and their control together with integration issues (Yaramasu et al., 2015).

Due to economic and physical considerations electrical power grids are unavailable in some remote areas. For these areas standalone hybrid wind power plants which

are connected to local loads are the promising solution to overcome the shortage of power supply. Due to the stochastic behavior of the wind, wind energy becomes the primary energy source and solar, Fuel cell, battery, etc. are secondary energy sources for standalone hybrid wind power systems (Kaldellis, 2010). To meet the local loads power demand, coordination is required between primary and secondary source of energy. The wind subsystem plays prominent role in generation and regulation of the extracted power, among energy subsystems in a wind energy conversion system (WECS). When the load power demand is greater than the wind power generation, the wind energy conversion subsystem is regulated such that the power from the wind energy is extracted as much as possible according to the changes in wind speed. On the other hand, when the load power demand is less than the wind power generation, the output power from the wind energy subsystem is delimited. The wind power generation system is mainly consisting of the wind turbine and AC generators. Mechanical and electrical components are employed in wind turbines to generate electricity from kinetic energy as shown in Figure. 1.1. Wind turbine blades converts kinetic energy into mechanical energy. The power generated by rotor blades with radius of r_T (m) and air density ρ (kg/m^3) at wind speed v_w (m/s) is,

$$P_k = \frac{1}{2} \rho \pi R_T^2 v_w^3 \quad (1.1)$$

Mechanical power P_m extraction from kinetic power is limited with a factor of power coefficient C_p , given by

$$P_m = P_k \times C_p \quad (1.2)$$

The maximum value of C_p ranges between 0.32 to 0.593 for various commercial WT's can be found in (Carrillo et al., 2013).

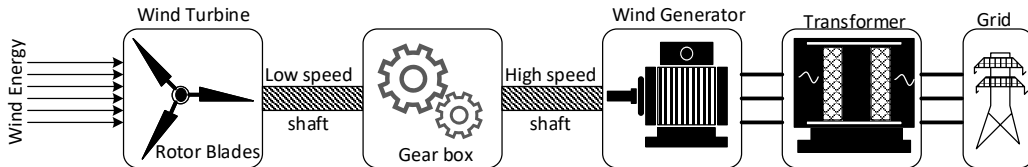


Figure 1.1: Wind energy conversion system configuration.

1.2 Wind Turbine Classification

Wind turbines are classified based on the rating, orientation, rotational speed, grid availability and location.

1.2.1 Small, Medium and Large scale wind turbines

Wind turbines are classified based on the output electric power rating,

1. **Small scale wind turbines** ($< 30kW$): These turbines are used to power homes and batteries in remote areas.
2. **Medium scale wind turbines** ($30 - 300kW$): These turbines are employed along with other alternative energy sources and battery, at distribution level to supply load demand for small communities.
3. **Large scale wind turbines** ($> 300kW$): These turbines are employed to generate bulk power at wind farms.

1.2.2 Passive, Active Stall-, and Pitch-controlled Wind Turbines

According to theory, wind turbine may generate higher than the nominal power, at above rated wind speed v_w . Wind turbine output power should be restricted to its nominal value during large wind to perform reliable and secure operation. Aerodynamic power control operation is performed to avoid the above mentioned issues and the control action is classified as passive stall ,active stall and pitch control shown in Figure. 1.2.

In case of stall control mechanisms, turbine are attached to the center of the rotor. Passive stall method can be applied to low to medium power wind turbines and active stall method applied to medium to high power wind turbine applications. Pitch control method, the rotor blades are turned to minimize the air incidence to the blades so that effectively protects the wind turbine above the rated wind speeds.

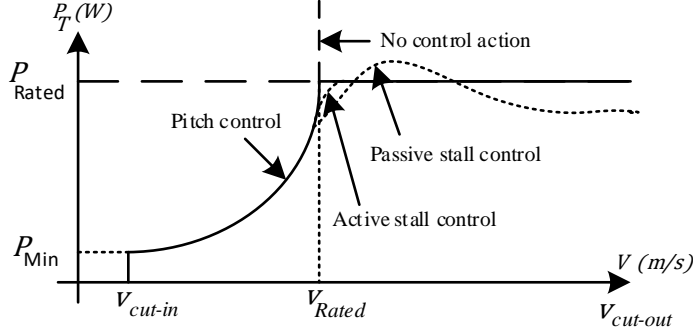


Figure 1.2: Wind turbine power regulation methods.

1.2.3 Wind turbines-Horizontal and Vertical Axis

Wind turbines are classified based on the orientation of the gear box and wind generator shaft with reference to ground. In case of horizontal axis wind turbines (HAWT), gear and generator shaft is horizontally fixed to the ground and placed at top of the tower. In vertical axis wind turbines (VAWT), the shaft is placed perpendicular to ground so that the gear box and wind generator are placed near to the ground, hence easy for the installation and maintenance. Therefore, HAWT wind power conversion efficiency is higher than the VAWT and suitable for medium and high power applications.

1.2.4 Variable and Fixed Speed wind Turbines

Wind turbines are categorised as fixed speed WT's (FSWT) and variable speed WT's (VSWT) depends on the orientation of the rotor blade. The power coefficient C_p is depends on the blade tip speed ratio (TSR) and pitch angle. The ratio of tangential blade tip speed to wind speed is defined as TSR (Chen et al., 2009).

$$\begin{aligned}
 \lambda_T &= \frac{\omega_T R_T}{v_w} \\
 C_p(\lambda_T, \beta) &= 0.5 \left(116 \frac{1}{\lambda_i} - 0.4\beta - 5 \right) e^{-\left(\frac{21}{\lambda_i}\right)} + 0.0068\lambda_i \\
 \frac{1}{\lambda_i} &= \frac{1}{(\lambda + 0.08\beta)} - \frac{0.035}{(1 + \beta^3)}
 \end{aligned} \tag{1.3}$$

where ω_T is the wind turbine angular speed (rad/s).

The FSWT technology is introduced in first generation during 1980's and directly

connected to grid without any power electronic converter, resulting in lesser cost and easier to operate. The speed of the FSWT generator is independent of wind speed and depends on the grid frequency, pole pairs and gear ratio. At constant turbine speed, optimal value of (λ_T) is inversely proportional to the wind speed and optimal power coefficient given in equation 1.3. Further, mechanical stress on gearbox increases causes reduction in turbine output power and conversion capacity.

In VSWTs, the wind speed directly proportional to the rotor speed, so that the turbine operates at maximum power coefficient and an optimal TSR. So that, turbine power and optimal power coefficient holds a relationship with v_w^3 . Therefore, in comparison with FSWT, VSWT has higher conversion efficiency. High power losses and increase in cost due to additional power converter.

1.3 Literature Review

A survey on the relevant papers has been done to understand the background, concept and performance comparison among the different control methods are discussed in following sections.

1.3.1 Maximum power point techniques in PMSG based WECS

Non-conventional energy sources play a prominent role in the electric power generation due to their inexhaustible and unpolluted nature. Currently wind plants are contributing significant amount of power in the world's electrical power generation (William and Li, 2017). Different techniques for extracting maximum power from PMSG based WECS have been suggested by various authors.

Conventional methods discussed in (Koutroulis and Kalaitzakis, 2006, Yaramasu and Wu, 2016) are basically optimal tip-speed ratio control, wind turbine power curve based control and optimal torque control. Optimal tip speed ratio control block diagram is shown in Figure 1.3. Generator reference speed ω_h^* is calculated based on the wind speed v_w and wind turbine parameters. To attain MPP operation ω_h^* should alter in proportion to v_w , so the wind turbine always operates at the λ_T^{op} . Wind turbine power curve based MPP method is shown in Figure 1.4. This method is based on the manufacturers data (P_T versus wind speed v_w curve). This method requires memory space to store the P_T versus wind speed v_w curve data. The instantaneous

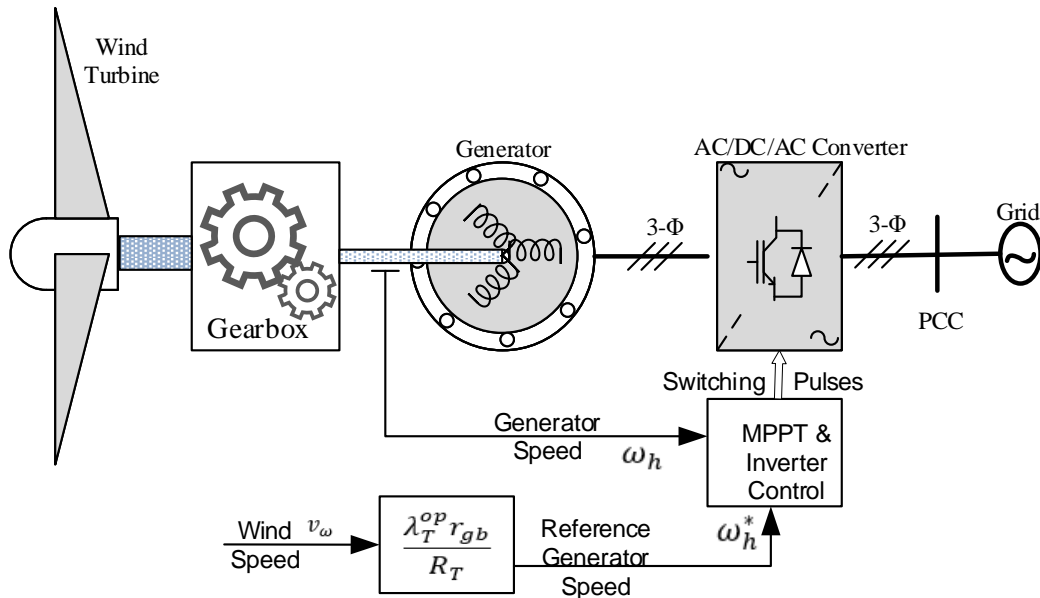


Figure 1.3: Block diagram of optimal TSR control.

power is calculated using generator output currents and voltages. Optimal torque control method uses the generator speed sensor is shown in Figure 1.5. Memory is required to store the speed data. In addition to above methods, intelligent methods are introduced to achieve MPPT operation from wind energy conversion systems.

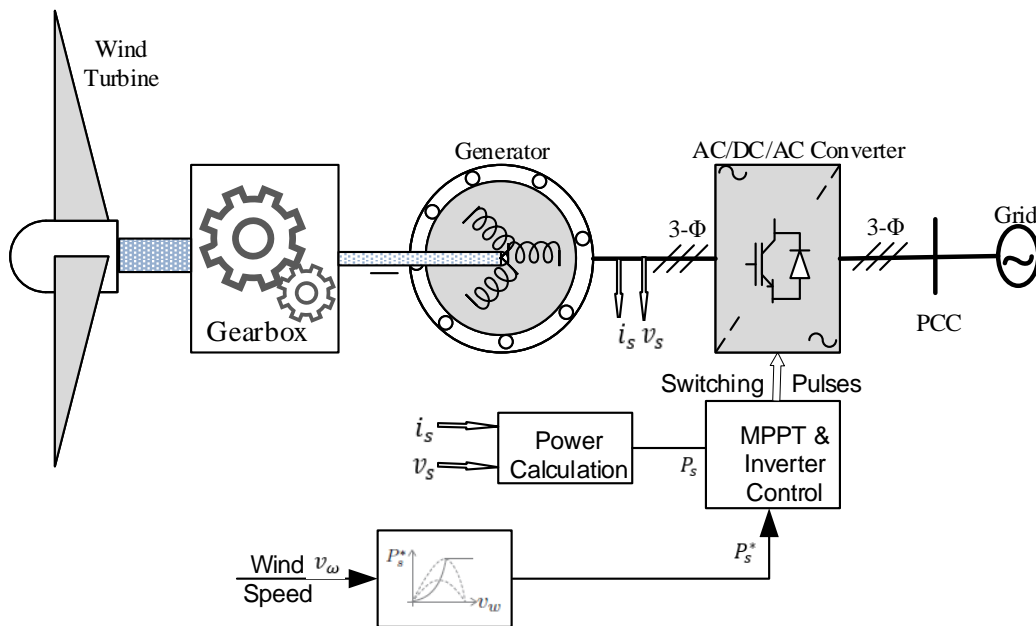


Figure 1.4: Block diagram of power curve based control.

In the phase-shift controller (Wang et al., 2010b), PWM inverter shifts the phase angle of the output voltage with respect to that of the grid voltage. At higher wind speed range, the controller tracks the maximum power very well but some sharp deviations are not tracked well due to delay in the phase-shift controller. In the H_∞ gain scheduling controller (Wang et al., 2010a), linearization is done at different operating points for the non-linear model and H_∞ gain scheduling controller is designed for every operating point range.

A new method based on speed sensorless Jordan type recurrent neural network based control algorithm and back-propagation method used for online training (Thongam et al., 2010). The main drawback in this method for a constant wind speed, rotor speed is decreasing and also speed error is oscillatory and noisy due to the speed sensorless MPPT controller. A new estimator based on back-EMF observer (Yang et al., 2010) and a PLL has been designed to get the rotor speed and position. The performance of the estimator diminishes with the parameter deviations. A control strategy (Errami et al., 2013) combines the technique of direct torque control and sliding mode control theory. In this method optimal power coefficient is not maintained.

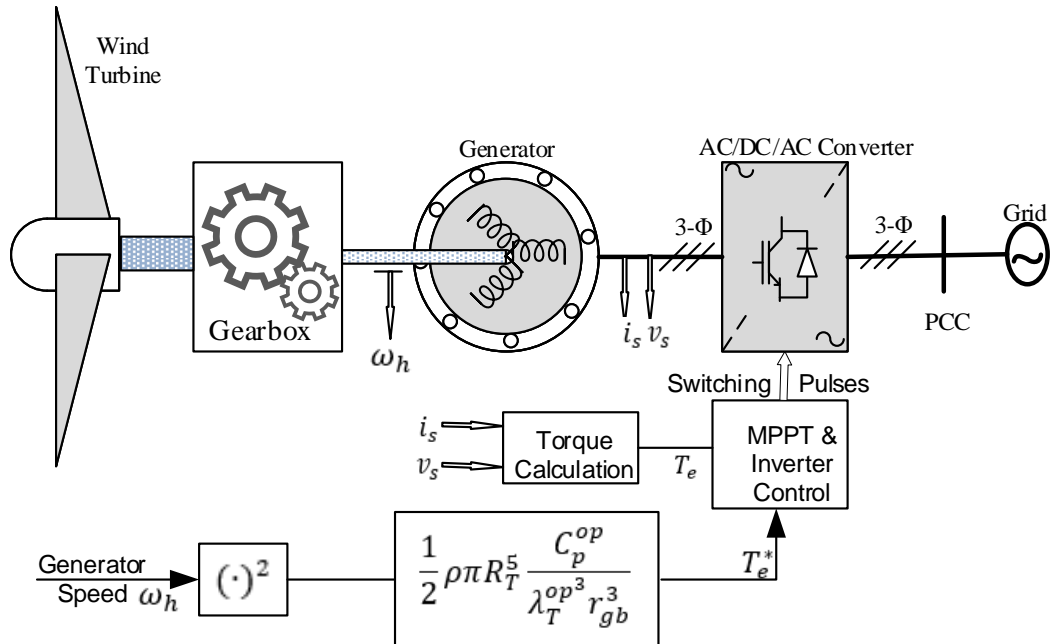


Figure 1.5: Block diagram of optimal torque control.

A review is presented on the maximum power point tracking controllers (Heydari and Smedley, 2015) namely tip speed ratio control, power signal feedback control,

optimal torque control, and perturb and observe method. Artificial neural network based Q-learning algorithm (Wei et al., 2016) is used to search for the maximum power points to learn the optimal relationship between rotor speed and electrical power. Online learning algorithm is executed every time due to environmental change or system aging to obtain a new optimal power curve. The robust control (Cutululis et al., 2006a) and nonlinear control (Yuehua et al., 2014) strategies were used to extract the maximum power from the WECS directly driven by PMSG under stochastic wind speed.

1.3.1.1 Research Gap

The oscillations are present in mechanical torque and control input. In order to overcome the above-mentioned drawbacks design of appropriate automated robust controller is extremely important.

1.4 Introduction to Quantitative Feedback Theory

Closed loop system stability margins and performance criteria maintenance is difficult due to high uncertainties present in practical non-linear systems. If there is a change in plant parameters we cannot guarantee about the system behavior hence it is required to design robust controllers for these uncertain plants.

Quantitative Feedback Theory (QFT), is first introduced by Isaac Horowitz in 1963. It is engineering design approach in frequency domain for tackling robust control problems and robust performance objectives with feedback structure. The system dynamics described by a series of transfer functions within uncertainty. QFT was first introduced to design robust controllers for linear time invariant (LTI), single-input single-output (SISO) systems and highly uncertain plants. Extension of this method to handle multi input-multi output (MIMO), time varying and nonlinear plants.

One feature that differentiates QFT from other frequency-domain techniques is it can able to deal directly with highly uncertain plants to achieve performance objectives. The QFT method collects quantitative information on uncertainty range for plants, robust performance specifications and expected disturbance at plant input or output level with their attenuation requirements. Explicitly, it has a 2-DOF control structure which is having a controller, a pre-filter, and output feedback to reduce plant output variations due to uncertainties and disturbances present in the

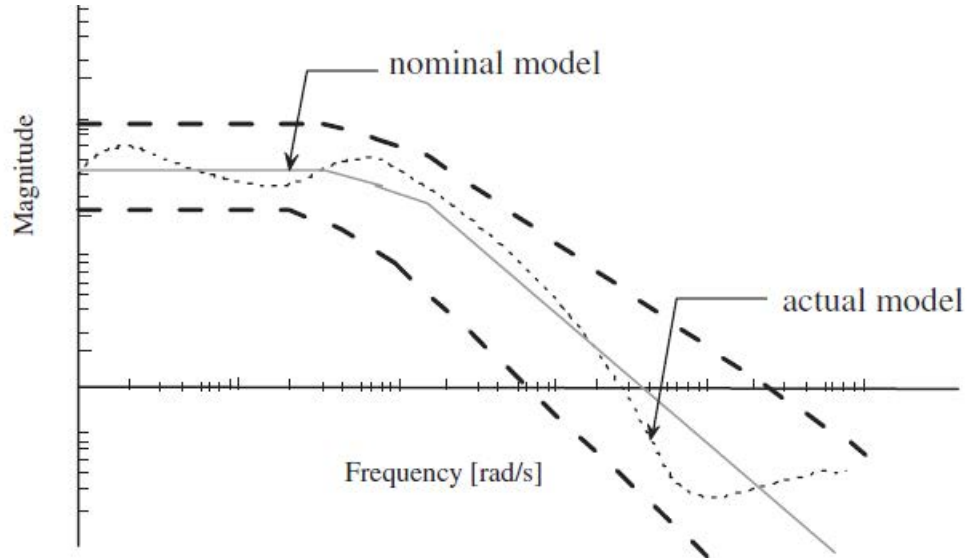


Figure 1.6: Uncertainty in physical systems.

plant. QFT uses Nichols chart (NC) to represent the performance specifications in frequency domain. QFT based controllers design steps are discussed below (Houpis and Garcia-Sanz, 2012).

1.5 Uncertainty

It is difficult to perform modelling of an exact mathematical model of a physical system which is valid for every operating condition. The uncertainties are unavoidable in a real time environment. Uncertainties present in the system model often lead to some undesirable phenomenon in the control system. The Figure 1.6 represents the uncertain model physical system.

1.5.1 Sources of Uncertainty and Classification

Unmodeled system dynamics or model order reduction, Unknown or unpredictable inputs (input /output disturbances, sensor noise), change of operating point etc. Based on their origination, sources of uncertainties are given by,

1. Disturbance signals: Wind gust, actuator noise and sensor noise
2. Dynamic perturbations: The deviation of the physical system from the ideal system when they are operating in real time.

3. Mathematical equation based modelling replicates the approximation of real system dynamic behaviour.
4. The uncertainty is present in the system due to high-frequency or fast dynamics. ignorance of no-linearities and reduced order models.
5. Plant parameter depends on the climatic conditions.
6. Industrial control systems are the sources of perturbations in the system dynamics, these perturbations alters the system parameters, and affects the performance under low-frequency range, called parametric uncertainty.
7. Parametric uncertainties are classified as,
 - i. **Structured Uncertainty** Specific knowledge about the variations in plant parameters are known. That is uncertainties caused by the variation of parameter of standard mathematical model can be termed as structural uncertainty.
 - ii. **Unstructured Uncertainty** Unmodeled high- frequency dynamics occurring in different parts of system. It also arises from change of operating point.

1.6 QFT Design Procedure

In real environment, the conventional control system fails to meet the necessary design specifications owing to its incapability to handle the uncertainties and disturbances that are inevitable in any practical operating conditions. In order to attribute to these requirements, a highly robust CSD is essential. A two degree of freedom (2DOF) control structure shown in Figure 1.7 is used to design the robust controller and pre-filter in QFT framework (Molins and Garcia-Sanz, 2009). Where $P(s)$ represents transfer function of the uncertain plant with $P \in \{p\}$, p representing the family of possible uncertain plants. The rationale behind the design of controller $G(s)$ and pre-filter $F(s)$ is to achieve robust stability and to meet the following performance specifications

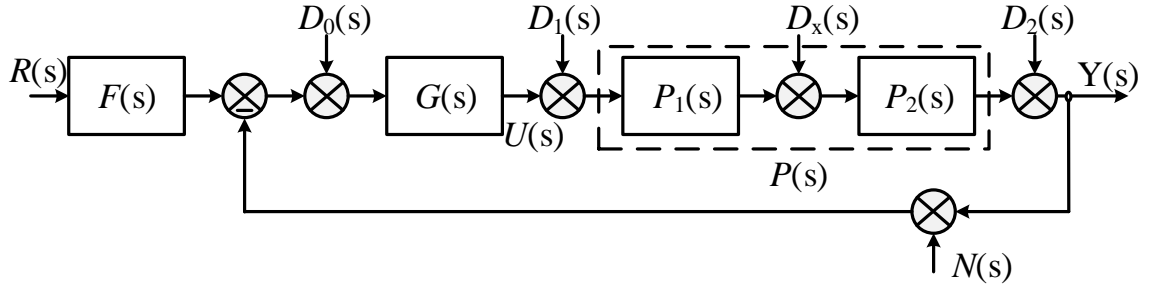


Figure 1.7: Two degree of freedom (2DOF) control system structure.

1.7 Performance Specifications

Generally closed loop performance specifications are converted into frequency domain functions $\gamma_k(\omega)$ that are represented as transfer functions of robust stability and performance specifications, $|T_k(j\omega)|$ so that: $|T_k(j\omega)| \leq \gamma_k(\omega), k = 1 \dots 7$

1.7.1 Robust Stability

When all possible loops of an uncertain plant family P with a single controller G are internally stable, then the controller G provides Robust Stability for the plant family P . The robust controller has to fulfil the following conditions

- The envelope of Nichols plot does not encircle or intersect at the critical point $(-180^\circ, 0 \text{ dB})$
- Placing complementary sensitivity function magnitude constraint is given by,

$$|T_1(j\omega)| = \left| \frac{U}{D_1} \right| = \left| \frac{Y}{D_0} \right| = \left| \frac{Y}{N} \right| = \left| \frac{L_g(j\omega)}{1 + L_g(j\omega)} \right| = \left| \frac{Y(j\omega)}{F(j\omega)R(j\omega)} \right| \leq \gamma_1(\omega) \quad (1.4)$$

1.7.2 Output Disturbance Rejection

In feedback control systems, robust controller has to be minimize the error generated from the difference of input and plant output. If any noise is added to plant output, it is very difficult to minimize the error, so it is compulsory to reject the disturbances present in the system. This specification qualitatively extract the controller perfor-

mance under disturbances.

$$|T_2(j\omega)| = \left| \frac{Y}{D_2} \right| = \left| \frac{1}{1 + L_g(j\omega)} \right| \leq \gamma_2(\omega) \quad (1.5)$$

1.7.3 Reference Tracking

The basic criteria for any control system, is that output should track or follow the system input. If there is any disturbances in the system the controller has to make system to follow the input. Pre-filter and robust controller are important to accomplish this specification.

$$\gamma_{7L}(\omega) \leq |T_7(j\omega)| = \left| \frac{Y}{R} \right| = \left| F(j\omega) \frac{L_g(j\omega)}{1 + L_g(j\omega)} \right| \leq \gamma_{7U}(\omega) \quad (1.6)$$

1.8 Step-by-Step QFT based Controller Design

The necessary procedure to be followed in the process of designing a QFT controller is comprehensively described below :

Step 1: Select the uncertain plant and define it's uncertainty range

Step 2: Establish the performance specifications

Step 3: Generate the template for an uncertain plant $P(s) \in p$, and select the frequency array $\omega_i, i = 1, \dots, l$. At each frequency obtain the variations of the plant parameters using the Nichols chart.

Step 4: Compute the QFT bounds by selecting the nominal plant such that the template points fulfils the performance specifications and are stable at every frequency for $\omega_i, i = 1, \dots, l$. Further compute the worst case bounds from the intersection of all the performance bounds at every frequency for $\omega_i, i = 1, \dots, l$.

Step 5: Perform the loop shaping $G(s)$ using the Nichols chart until the worst case bounds for every frequency are satisfied and a stable point for the closed loop nominal system is reached.

Step 6: Design the Pre-filters $F(s)$ using same principle of loop-shaping in order to enable the output to track the reference input.

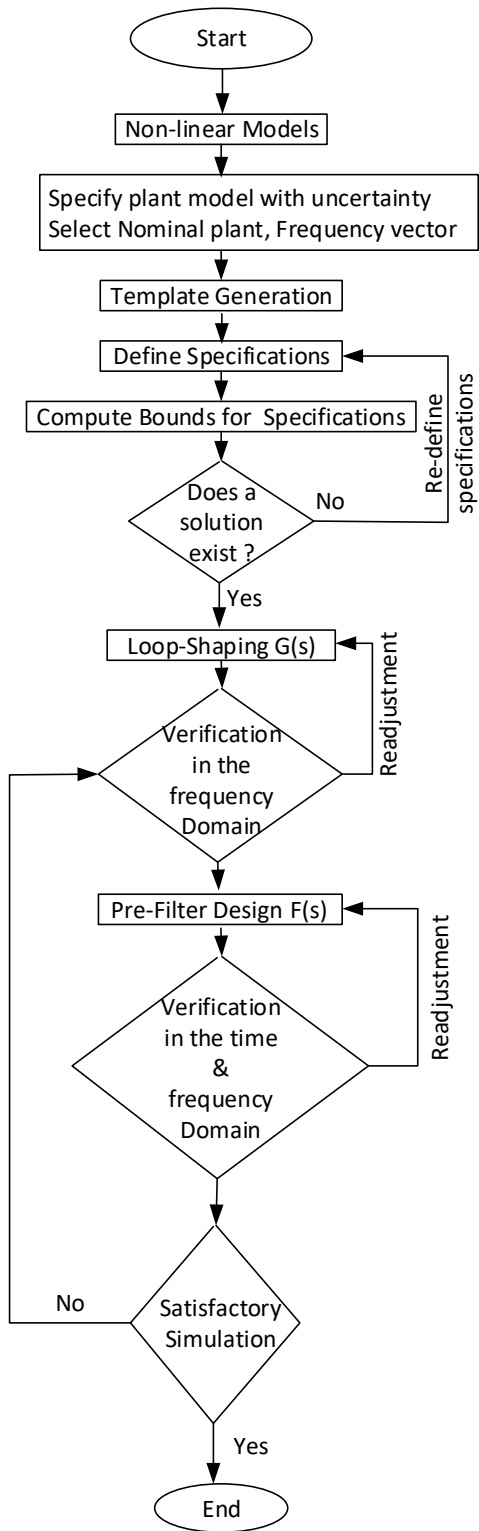


Figure 1.8: QFT Controller Design steps.

1.8.1 High Frequency Gain

Reduction of high frequency noises at the sensor output and plant disturbances is desired to utilise the feedback benefits and is achieved by reducing high frequency gain (HFG) expressed as follows

$$HFG = \lim_{s \rightarrow \infty} s^r G(s) \quad (1.7)$$

where r represents the excess poles in $G(s)$

1.8.2 Automatic Loop-shaping methodology based Quantitative feedback theory (QFT) Controller

Quantitative feedback theory (QFT) Horowitz (1963), Garcia-Sanz (2017), is a robust control system design (CSD) approach which employs system output as an feedback variable to achieve the desired dynamic performance in presence of plant uncertainties and disturbances. In general, QFT is well applicable for handling uncertainty in frequency domain. Ever since its inception, QFT is applied to solve various real time CSD problems (Houpis et al., 2005, Garcia-Sanz and Houpis, 2012, Garcia-Sanz et al., 2008). Although QFT was initially applied to different to various single input - single output (linear time variant, time invariant and non-linear) systems, its extension to multiple input - multiple output (linear and nonlinear) systems is presented in (Borghesani et al., 2003, Ali et al., 2012). It is well known that for adequate implementation of QFT, system gain-phase loop-shaping is imperative and can be performed either manually or automatically. On this line many computer aided design (CAD) tools are developed to perform manual loop shaping like the pioneer Air Force Institute of Technology CAD tool (Houpis et al., 2005, Chait and Yaniv, 1993, Houpis and Sating, 1997), QFT control toolbox by European space agency author's group (Garcia-Sanz and Molins, 2008, Gutman, 1996), QFT MATLAB toolbox (Garcia-Sanz et al., 2009, Borghesani et al., 2003) and Qsyn (Sating et al., 1993). Despite its simplicity in design, the method primarily depends on the trial and error approach which indeed results in the system performance highly dependent on the designer. It is well known that for adequate implementation of QFT, system gain-phase loop-shaping is imperative and can be performed either manually or automatically. Despite its simplicity in design, the method primarily depends on the trial and error approach which indeed results in

the system performance highly dependent on the designer. Further, the complexity increases profoundly for unstable and non-minimum phase uncertain systems in order to fulfil all the necessary performance specifications resulting in the need for automatic loop shaping (ALS) methods.

Concerning the attempts in developing the ALS methods, Gera and Horowitz proposed design of QFT robust controller based on iterative procedure to derive the shape of a nominal loop transfer function ($L(j\omega) = G(j\omega)P(j\omega)$) using Bode's gain phase integral (Horowitz, 2001). However, the method requires a rational function approximation and straight line approximations leading to an under-performing CSD. Although Ballance and Gawthrop simplified the Bode's gain-phase integral iteration process, the possibility to address satisfactorily the specifications pertaining to noise rejection and stability is not well appreciable (Gera and Horowitz, 1980). A method to approximate uncertain plant frequency responses using the nonlinear programming method is demonstrated in (Ballance and Gawthrop, 1991). Approximation of templates based on the aforementioned method results in over bounding rectangles. To confront the issue of overbounding, linear programming based ALS using a series of linear approximations reported in (Thompson and Nwokah, 1989) fails to define the QFT nonlinear bounds with linear inequalities. This drawback has been overcome by transforming the nonconvex closed loop bounds into linear inequalities by considering zeros alone as the optimization variables (Bryant and Halikias, 1995).

In addition, the authors, Garcia-sanz and Guillen (Chen and Hollot, 1999), Garcia-sanz and Oses (Garcia-Sanz and Guillen, 2000), and Garcia-sanz and Molins (Garcia-Sanz and Oses, 2004), have proposed the evolutionary and Genetic algorithm (GA) based ALS. Unlike the aforesaid methods, a phase independent controller is developed using the least square type algorithm (Molins and Garcia-Sanz, 2009). Similarly, the application of particle swarm optimization, hybrid optimization (interval consistency and hull consistency), teaching learning-based optimization algorithm, flower pollination algorithm and convex concave optimization methods are presented in (Garcia-Sanz and Molins, 2010, Ali et al., 2012, Jeyasenthil et al., 2014, Katal and Narayan, 2016b,a) respectively.

1.8.2.1 Research Gap

A simple design methodology to devise a controller with an overall satisfactory performance has to be developed . With this motivation, a controller structure exhibiting

the characteristics of descending modular trace within the close vicinity of the universal bound has been formulated in this proposed research work. A modified fitness function is formulated by considering the suitable cost function terms in order to accurately capture the desired descending modular trace close-packed to the universal bound. The minimization of the fitness function is accomplished by the application of Genetic Algorithm.

1.8.3 Photovoltaic (PV) circuit model Identification

Recent developments in photovoltaics (PV) and adverse effect on environment due to fossile fuel burning have heightened the need for injecting the green power in to the grid (Khan and Xiao, 2016). In general, it is imperative to carryout the modeling and simulation of such systems a priori its practical implementation. Further, mathematical modeling of PV employed for simulation studies should be precise and reliable in order to extract maximum available power under varying environmental conditions (Huang et al., 2016, Chatterjee et al., 2011). In practice, it is strenuous to obtain an accurate PV model from datasheet parameters (DP), since it deliberate only the electrical characteristics, which include open circuit voltage, maximum power point, and short circuit current of the realistic PV panel. However, the DP being the fundamental reference for matching the actual and modelled PV characteristics, considerable effort has been made towards this challenge in various directions. Among which, the parameter extraction based modelling (single diode PV (SPV) and double diode PV (DPV) model) is widespread.

The majority of the research till date has focused on adopting the simplified PV models rather than its accurate counterpart at the cost of reduced accuracy. On contrary, the DPV exhibits a greater degree of accuracy and requires a higher computational efforts (Villalva et al., 2009, Adamo et al., 2011, Romero-Cadaval et al., 2013a). The application of SPV for various power electronics based simulation studies is well-known as it provides a fair trade-off between the model simplicity and accuracy (Yang et al., 2010, Kadri et al., 2011). The attractive feature of SPV lies in the fact that, it can be parameterized solely based on DP (Chatterjee et al., 2011, Yazdani et al., 2011). The use of SPV in studies concerning the partial shading conditions is demonstrated in (Villa et al., 2013). The influence of doping concentration on PV model with equations based on $I - V$ charecteristics is studied in (Hyvarinen and Karila, 2003). Besides, a simplified look-up table model describing the approximate

PV cell characteristics as presented in (Ropp and Gonzalez, 2009) fails in tracking the true maximum power point (MPP).

The suitability of analytical/numerical techniques in computing the $I - V$ curve based PV parameter is detailed in (Lingyun et al., 2011, Chatterjee et al., 2011, Adamo et al., 2011, Yang et al., 2010). However, these methods require the actual measured data points of the $I - V$ curve. Furthermore, a five parameter model of SPV is investigated in (Villalva et al., 2009, Soon and Low, 2012) while their extraction is practically constraint. Lambert W function is a non-iterative method proposed to reduce the computation efforts (Cannizzaro et al., 2014b,a). Where as several methods to compute the unknown parameters of the five parameter model by assuming one variable as a priori is also observed (Huang et al., 2016). The accuracy and convergence of such iterative methods depend on the chosen initial values. In order to combat this, differential evolution, particle swarm optimization methods (Soon and Low, 2012, Qin and Kimball, 2011, Ishaque and Salam, 2011) and linear least square approach (Lim et al., 2015) is proposed.

In light of these recent developments in PV parameterization, a considerable concern about the simplified single diode models is witnessed. One of the way is to eliminate either series, shunt resistance or both (Veerachary and Khas, 2006, Celik and Acikgoz, 2007, Benavides and Chapman, 2008). However, this approach fails to in operating at true MPP. Unlike equation based models, parameters of no physical meaning (shunt or series resistance might be negative) is often difficult to use in circuit based models (Xiao et al., 2004, 2007). Recapitulating the afore-mentioned remarks, an attempt is made to develop a simple and fast convergent parametrizing method while achieving the desired accuracy of PV modeling for simulation studies. On contrary, the double diode PV (DPV) exhibits a greater degree of accuracy and requires a higher computational efforts (Romero-Cadaval et al., 2013a).

1.8.3.1 Research Gap

Recapitulating the afore-mentioned remarks, an attempt is made to develop a simple and fast convergent parametrizing method while achieving the desired accuracy of PV modeling for simulation studies.

1.8.4 Grid connected Photovoltaic System

Over the last decades, different simulation strategies have been proposed in the literature (Ortiz-Conde et al., 2012), with critically concentrated on PV simulation modelling. PV system consists the series-parallel configuration of solar cells to achieve the required voltage and current to inject power into the grid. The power mismatch problem is significant when the centralized power inverter is used under partial shading conditions. The DC-DC converter along with maximum power point tracking (MPPT) controller is incorporated at each PV panel in order to extradict the losses due to partial shading at interpanel level (Yong and Huiqing, 2019). Further, submodule-integrated converters (SMIC) are developed to mitigate the intra-panel power losses in order to inject maximum avail-able power to the grid (Wang et al., 2013).

1.8.4.1 Research Gap

In this research work, a robust MPPT controller for the SMIC converter has been developed for addressing the requirement of improved controller for Grid Connected PV System.

1.8.5 Grid connected Fuel Cell

Increase in energy utilization, CO₂ emanations and natural resources depletion is heading to investigate green (fuel cell and renewable based) power generation systems. Photovoltaic (PV) and wind generation (renewable) is relying upon the climatic conditions. In order to compensate for interruption of PV output and wind in hybrid power system, the fuel cell (FC) can act as a permanent source (Erdinc and Uzunoglu, 2012). Grid integration of the green power technology is major concern, specifically fuel cell (FC), due to less maintenance, light weight, zero emissions, compact in size (Larminie et al., 2003) (Corrêa et al., 2004). A basic method to model the FC based distributed generation (DG) modelling is presented in (Corrêa et al., 2004). In comparison with PV and wind based DG technologies, efficient performance can achieve with FC, because it is independent of geographical location and its modular nature. The steady state performance is more reliable compared to transient state due to internal factors (Jang et al., 2012, Nehrir and Wang, 2009, Khanh et al., 2010, Blunier and Miraoui, 2007, Cheng et al., 2017, Cownden et al., 2001). The comprehensive equations are formulated based on electrochemical reaction, are used to model steady state and also

dynamic state PEM fuel cell (PEMFC) (Maggio et al., 2001, Hamelin et al., 2001, Wang and Nehrir, 2001, Blaabjerg et al., 2004, Liserre et al., 2010, Dwari and Parsa, 2010, Siwakoti and Blaabjerg, 2016). Further, dynamic modelling of fuel cells related to fuel-cell terminal characteristics are reported (Maggio et al., 2001, Hamelin et al., 2001, Wang and Nehrir, 2001, Blaabjerg et al., 2004, Liserre et al., 2010, Dwari and Parsa, 2010, Siwakoti and Blaabjerg, 2016). In addition, charging effect of catalyst layers in the fuel cell, are used to replicate the accurate modelling. The reaction period is short, the problem of cold start and its voltage changes with the variability in load and heat. In addition, many inner and external parameters, such as water distribution scheme, fuel supply system or temperature control scheme, affect the lifespan of FC (Corrêa et al., 2004, Jang et al., 2012).

The fuel cell's lifespan can be improved by using appropriate FC regulator and power converters. DC-DC power converters contribute to stack resistance by preventing load transients that affect FC output. These energy converters control not only voltages and currents but also help to stabilize the energy transfer between primary and auxiliary power sources. The controllers should be prepared to provide the system with a predefined quantity of real and reactive power or to follow a time-change load profile.

1.8.5.1 Research Gap

Therefore, proper controllers must be designed to make their performance characteristics as desired for a fuel cell system.

1.8.6 DC-coupled Hybrid microgrid

The integration of various alternative energy sources into the form of a hybrid system in the microgrid is usually divided into two categories: DC and AC microgrid (Nejabatkhah and Li, 2014). Due to the advantages of AC microgrid such as, transformation of voltage levels as per the requirement, power transfer over long distance, standards in frequency, voltage and protection. However, the construction and transmission involves in increases AC microgrid cost. The power electronic technology development led to increase the DC loads and DC converters are utilised to set the voltages as per the required level. Restructuring of power system is mandatory to meet the future load demand with more flexible operation. Most of the renewable

energy sources produces DC, so DC microgrid will help the power system to meet the load demand.

In this work, DC Microgrid consists wind turbine, PV, and PEMFC along with the proposed methodology based automated robust controllers to operate the system to meet the load demand. The main advantage of DC microgrid is to avoid synchronization issue with renewable energy sources (Stark et al., 2015a). Further, the sizing of the renewables are done with conventional methods and intelligent methods are discussed in literature (?). Effective and simple unit size algorithm is mandatory for DC microgrid modeling. Robust controller design is important to control the power electronic converters to integrate the renewable energy sources with utility grid to meet the load demand (?).

1.8.6.1 Research Gap

In order to obtain a required load distribution among the distinct inverters, a proper power-sharing management system is proposed.

1.9 Research Objectives

Based on the literature review and research gaps discussed in the previous section, the objectives for the research work are presented below:

1. To develop improvised automatic loop-shaping methodology for robust QFT controller design
2. To design, modeling and performance analysis of proposed QFT robust controller for the PMSG based wind energy system
3. To design, modeling and performance analysis of proposed QFT robust controller for the grid connected photovoltaic (GPV) system
 - i. To parametrize and to identify pertinent PV circuit model for GPV system simulation.
 - ii. To perform Real time long-term GPV simulation under various environmental conditions.

4. To design, modeling and performance analysis of proposed QFT robust controller for grid connected fuel cell.
5. To design, modeling and performance analysis of proposed QFT robust controller for hybrid renewable energy power system.

1.10 Thesis outline

There are six chapters in this thesis, that has been organized as follows.

1.10.1 Thesis Organization

Chapter 1: Introduction

The background of the thesis along with literature review are briefly presented. Further, research gaps, research objectives, contributions and thesis outline are provided.

Chapter 2: Design and modelling of Robust Controller for PMSG Based Wind Energy Conversion System (WECS)

The High initial overshoot in control input and wind torque along with oscillatory behaviour in autonomous permanent magnet synchronous generator (PMSG) based wind energy conversion system (WECS) is observed. To overcome the above-mentioned issues, modified fitness function is formulated in order to accurately capture the desired controller characteristics and also to enhance the power extraction capability. The minimization of the objective function is accomplished by the application of Genetic algorithm using automatic loop-shaping methodology in QFT framework. The performance evaluation is carried out for step change and stochastically varying wind speed conditions. Finally, benchmarking of the proposed controller against those available in the literature is accomplished through extensive MATLAB simulations.

It is observed that the proposed controller requires the minimum control input while operating as desired. Also, it noteworthy that the proposed controller facilitates in extracting the maximum power corresponding to a given wind velocity in comparison to other well established techniques.

It is highly desired to have a smooth torque variation. In addition, comparison of proposed and existing literature controllers is performed for three phase grid connected PMSG based WECS under step change and stochastic wind speed conditions. The application of the proposed controller improves maximum power extraction and reduces the overshoot in mechanical torque.

Chapter 3: Design and modelling of Robust controller for Grid connected Photovoltaic (PV) system

An accurate model of photovoltaic (PV) panel is indispensable for simulations studies. The majority of the research till date has focused on adopting the simplified PV models rather than its accurate counterpart at the cost of reduced accuracy. In this chapter, a methodology is proposed for selection of pertinent single diode photovoltaic model for simulation studies. Adomian decomposition based cubic convergence method is used to accurate parametrization with improved simulation accuracy.

Once the pertinent circuit model is identified, the proposed methodology based robust controller is designed for the proposed sub-module integrated PV converter grid connected applications to enhance the maximum power extraction. The effectiveness of the proposed controller is studied and simulated for single phase grid connected PV system under step change in temperature and irradiation conditions to realize the real-world system behaviour. Further, average model of single phase grid connected is designed and validated with the switching model to perform long term simulations. The performance of the proposed QFT robust controller and Q-parametrization controller is investigated under real time irradiation and temperature data with normal operating and partial shading conditions at a practical site of our Institute National Institute of Technology Karnataka (NITK). The application of proposed controller increases the power extraction over Q-parametrization method.

Chapter 4: Design and modelling of Robust controller for Grid connected Fuel cell

Fuel cells are placed at distribution level, for grid reinforcement and improving system integrity, reliability, and efficiency. Fuel cells are able to deliver a pre-set amount of real and reactive power to the grid, or be able to follow a time-varying load profile. Therefore, proper controllers need to be designed for a fuel cells to make its performance characteristics as desired.

In this chapter, Dynamical electrical circuit modelling of fuel cell, design of DC-DC boost converter and selection criteria of LCL filter are discussed. Automatic loopshaping methodology based robust controller is designed for boost converter to maintain the DC-link voltage and for the inverter to control the active and reactive power between inverter and grid. Performance comparison of proposed QFT robust controller with the PI controller is analysed at unity power factor operation. Further, the controller performance is evaluated under pre-set value of active and reactive power requirement, DC-link voltage and grid voltage uncertainties.

Chapter 5: Modelling and power management strategy for Smart Grid.

In this chapter, unit sizing procedure for DC-coupled hybrid system is deliberated as per the load profile. The configuration of DC-coupled hybrid microgrid comprising of PV, wind, and PEM fuel cell. Firstly, three phase grid connected PMSG based WECS , PV and Fuel cell individual performance is analysed and the necessity of the hybrid system briefly explained. The analysis of power management strategy in three phase grid connected hybrid DC couple system is performed.

Chapter 6: Conclusions and Future Scope

Summarizes the research work carried out and research extensions for future work is suggested.

Chapter 2

QFT controller design for PMSG based wind energy conversion systems

2.1 Grid Connected Wind Power System Configurations

In this section, the evolution of grid tied wind system is elaborated to bring out the technological advancements. The grid connected wind system consists wind turbine to convert wind energy to mechanical energy, gear box or drive train used to multiply the turbine speed. The generator interfaced between gearbox and power electronic converter, converts mechanical power to electrical energy. Further, transformer is utilised to perform step-up operation for grid integration. The above mentioned electrical and mechanical components are connected to make wind power system more reliable with efficient energy harnessing configurations. Commercially available wind turbine configurations are given below, such as

- **Type 1:** Squirrel cage induction generator (SCIG) based FSWT system
- **Type 2:** Wound rotor induction generator (WRIG) based semi-variable-speed wind system
- **Type 3:** Doubly fed induction generator (DFIG) based semi-variable-speed wind system

- **Type 4:** SCIG, wound rotor synchronous generator (WRSG), permanent magnet synchronous generator (PMSG) based Full-variable-speed wind system.

2.1.1 SCIG based FSWT system

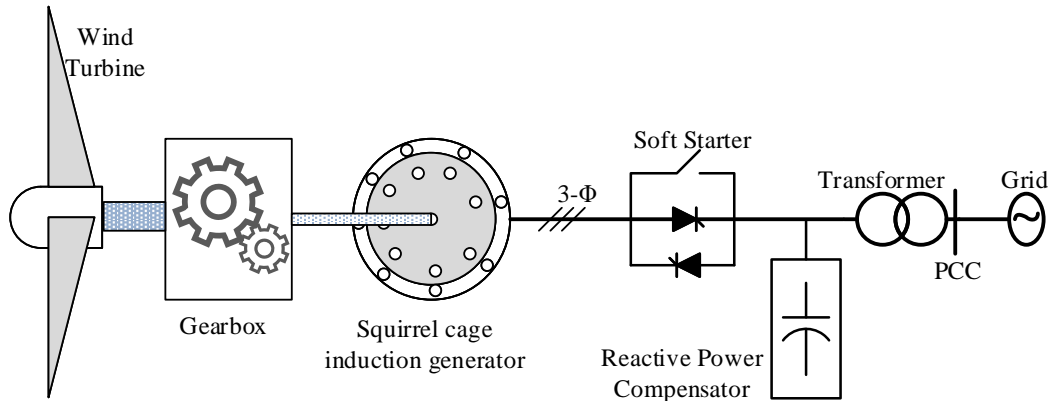


Figure 2.1: Schematic diagram of fixed-speed SCIG based wind system.

Squirrel cage induction generator (SCIG) based fixed-speed grid connected wind system also called Type-1 configuration which is shown in Figure 2.1. This configuration was developed during 1980s wherein soft starter is used to inject power from wind turbine to the grid. Type-1 wind turbines have less initial cost and more reliable (Li and Chen, 2008). In this type of generators, usually fixed number of four or six poles are employed which implies the fixed rotational speed (1% tolerance) with 50-60 Hz frequency. In this configuration, two-speed rotation is also implemented under stochastic wind speed conditions by changing the number of poles. Premature wind farms used passive stall control for aerodynamic power control, while new turbines employed pitch or active stall control. A 3-stage gear box is typically used to match the velocity gap between the turbine rotor and the wind generator.

At initial starting process, high current flows in the circuit due to voltage difference between grid and wind turbine generator. To limit high initial currents, anti-parallel thyristors and a bypass switch known as soft starter are used shown in Figure 2.1. The process of limiting inrush currents is done by adjusting thyristor firing angle. Following the start-up operation, the thyristors are removed from the circuit with the help of bypass switch to limit thermal power losses. Further no power electronic component employed in the circuit (Wu et al., 2011). The reactive power requirement for the wind generator draws from the compensation block or capacitor bank. Due

to fixed speed operation poor performance in energy conversion efficiency and grid frequency variations are observed.

2.1.2 WRIG based semi-variable speed wind system

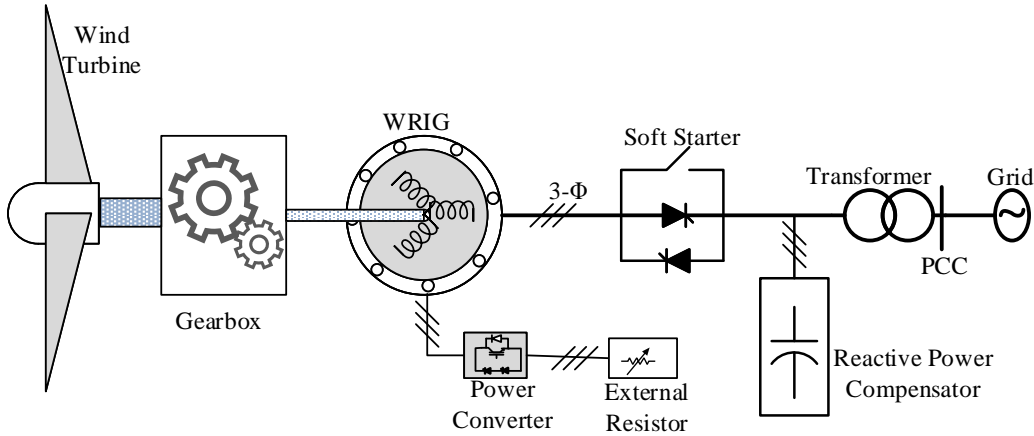


Figure 2.2: WRIG based semi-variable-speed (10%) WECS.

The wind energy sector has developed semi-variable speed WTs (Type-2) to overcome the disadvantages in Type-1 WTs. In this configuration 10% of speed variation is allowed with wound rotor induction generator. The Type-2 WECS configuration is shown in Figure 2.2. The physical constructional development is observed from type-2 WT's is external resistor is connected through the converter. This rotor resistance circuit enables variable speed operation, also known as Optislip WT (Li and Chen, 2008). With the help of this configuration, higher power extraction and with lower mechanical stress is achieved. The addition of power electronic component with rotor circuit increases complexity, high initial cost, maintenance and power losses

2.1.3 DFIG based semi-variable speed wind system

The technological developments in power electronics have utilised the power electronic components effectively to improve power conversion efficiency. This configuration also known as Type-3, here soft starter and grid side reactive power components are replaced with back to back converter configuration is shown in Figure 2.3 (Pena et al., 1996). In this configuration, DFIG is utilised effectively to inject power to the grid from rotor and stator windings. The wind generator speed variation of 30% of

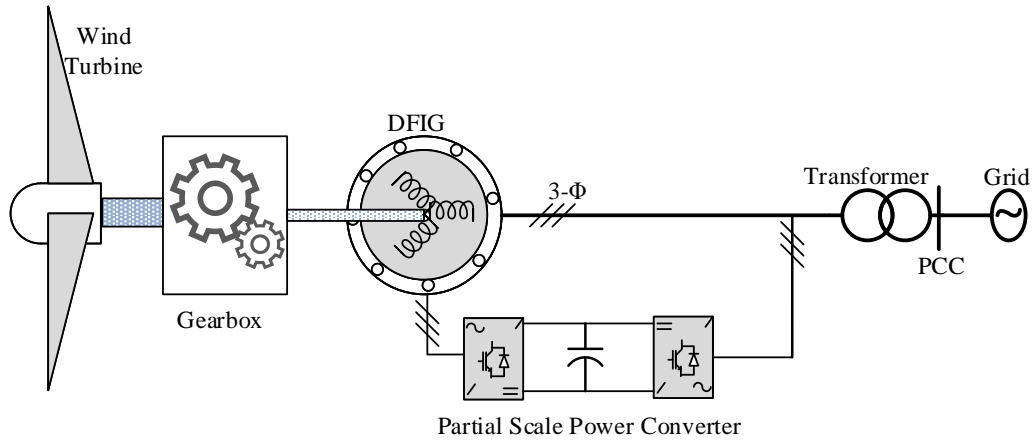


Figure 2.3: DFIG based semi-variable-speed ($\pm 30\%$) WECS.

synchronous speed leads to high efficiency with reduction in cost (Muller et al., 2002). The converter compensates the reactive power required by the generator, therefore capacitor bank and soft starters are eliminated (Ekanayake and Jenkins, 2004). Type 3 wind systems have a market share of about 50% and are among the most prominent technology in today's wind power sector. (Cárdenas et al., 2013).

2.1.4 Wide speed range of full-variable speed wind system

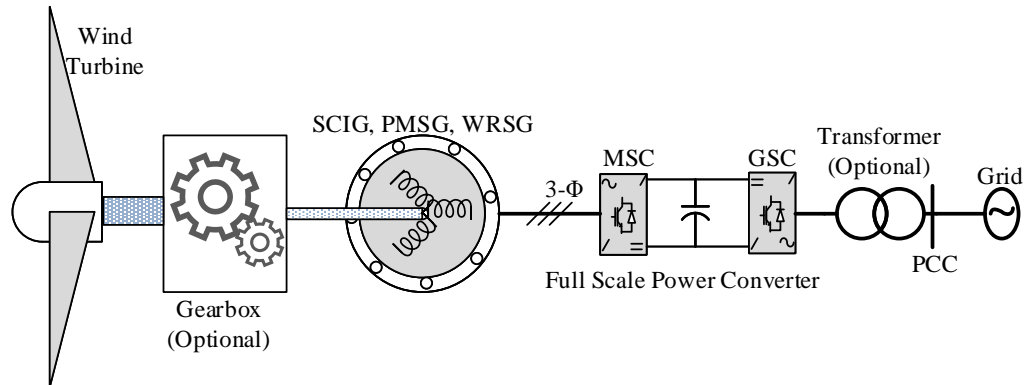


Figure 2.4: Wide range of speed (0 - 100%) wind generators for WECS.

After the development of these many configurations, a full scale variable speed variation configurations are indispensable, that are developed in 1990's. The configuration consists of the machine side and grid side converter with intermediate DC-link capacitor is placed as shown in Figure 2.4 (Yaramasu et al., 2015, Blaabjerg et al.,

2011). Power conversion capacity is increased from 30% to 100%, and the maximum power extraction is achievable over a wide speed range with low mechanical stress on the components. In this configuration, gearbox completely eliminated so that installation and maintenance costs are ignored (Conroy and Watson, 2008).

2.2 PMSG based Variable speed wind energy conversion system

A permanent magnet synchronous generator (PMSG) - based AWPS shown in Figure 2.5 is considered as the test system to demonstrate the applicability and suitability of the proposed QFT based robust controller under stochastic wind speeds. Assuming that the other system components excluding those within the local control loop as highlighted in Figure 2.5 works as intended, with suitable assumptions, the chopper equivalent circuit is obtained (Cutululis et al., 2006a). Neglecting the dynamics of power electronic converters, dynamics pertaining to the aerodynamic model of wind turbine, PMSG and gear system are accounted. The aerodynamic torque is given as,

$$T_{wt} = \frac{P_w}{\omega_l} = \frac{1}{2} \rho \pi R_T^3 v_\omega^2 C_T(\lambda) \quad (2.1)$$

where ρ is the air density, R_T is the blade radius and the torque coefficient, denoted by $C_T(\lambda)$,

$$C_T(\lambda) = a_0 + a_1 \lambda + a_2 \lambda^2 + a_3 \lambda^3 + a_4 \lambda^4 + a_5 \lambda^5 + a_6 \lambda^6 \quad (2.2)$$

The mechanical power at the turbine shaft, P_w , is

$$P_w = \frac{1}{2} \rho \pi R_T^2 v_\omega^3 C_P(\lambda) \quad (2.3)$$

C_P is the power coefficient defining the aerodynamic efficiency of the wind turbine rotor. This is usually a function of the tip speed ratio λ and the blade pitch angle θ , but here θ is assumed to be constant.

$$C_P(\lambda) = \lambda C_T(\lambda) \quad (2.4)$$

The tip speed is defined as the ratio between the peripheral speed of the blades

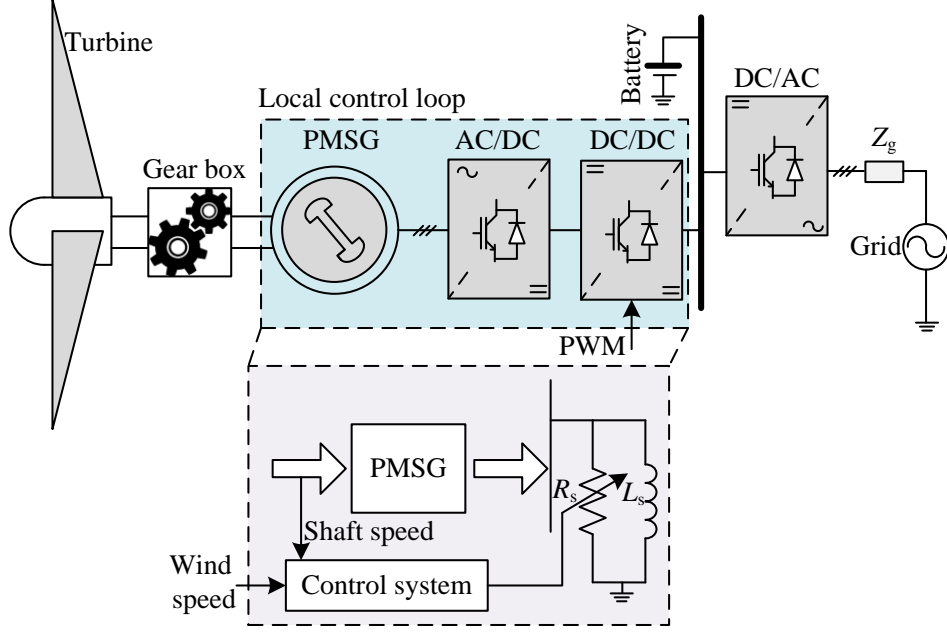


Figure 2.5: PMSG based autonomous wind turbine power system.

and the wind speed

$$\lambda = \frac{R_T \omega_l}{v_\omega} \quad (2.5)$$

Where ω_l is the rotational speed of the blades. In order to maximize the power extracted from the wind, the tip speed ratio should be kept around its optimal value λ_T^{opt} . Thus the wind power system is controlled in closed loop in such a way that the shaft speed tracks the speed reference calculated according to the measured wind speed v :

$$\omega_{ref} = \frac{\lambda_T^{opt}}{R_T} v_\omega \quad (2.6)$$

The torque coefficient, denoted by $C_T(\lambda)$,

$$C_T(\lambda) = a_0 + a_1 \lambda + a_2 \lambda^2 + a_3 \lambda^3 + a_4 \lambda^4 + a_5 \lambda^5 + a_6 \lambda^6 \quad (2.7)$$

The mechanical power at the turbine shaft, P_w , is

$$P_w = \frac{1}{2} \rho \pi R_T^2 v_\omega^3 C_P(\lambda) \quad (2.8)$$

The dynamic model of PMSG with chopper equivalent variable resistance $R_{s,ch}$ in

synchronous reference frame is given as,

$$\begin{aligned}
\frac{di_d}{dt} &= -\frac{(R + R_{s,ch})}{(L_d + L_s)}i_d + p\frac{(L_q - L_s)}{(L_d + L_s)}i_q\omega_h \\
\frac{di_q}{dt} &= -\frac{(R + R_{s,ch})}{(L_q + L_s)}i_q - p\frac{(L_d + L_s)}{(L_q + L_s)}i_d\omega_h + p\phi_m \\
\frac{d\omega_h}{dt} &= -\frac{\eta}{iJ_h}\tau_{wt} - \frac{\tau_{em}}{J_h} \\
\tau_{em} &= p[(L_d - L_q)i_d i_q - \phi_m i_q]
\end{aligned} \tag{2.9}$$

In order to ensure proper functioning of the VSWT-PMSG power system, there are several control loops are present. The local control loops are the control loop regarding grid connection through power electronics and the control loop that ensures optimum wind energy extraction. The latter controls the shaft speed according to the wind speed in order to ensure optimum wind energy extraction, by means of an inner current control loop acting on the DC link. This will result in modifying the equivalent resistance at the generator terminal. The global control acts on the load/unload regimes of the battery in such a manner that the active power produced by the wind turbine meets the active power required by the load. The local control loop that ensures optimum wind energy extraction and assumes that the other control loops are present and working. The power electronics dynamic is significantly more rapid than the VSWT-PMSG dynamic and is therefore neglected. Generator and rectifier circuits which supplied the boost chopper circuit with electric power were replaced in a DC voltage source in order to facilitate the analysis. The equivalent circuit of the inverter which is connected to an AC grid can be represented as a battery charger E_L with series a resistor R_L , where the three phase AC current come from inverter is controlled to keep its phase exactly in phase with that phase of three-phase AC voltage of the grid.

The E_L can be considered to be fixed value during transient response, so the battery charger E_L can be ignored here.

When it is assumed that the inductance and the capacitance of the equivalent circuit are sufficiently large, the current of the switching device is smoothed by the inductance, and DC output voltage is smoothed by the capacitance. The energy is stored in L_s , when SW was turned on in the period of t_{on} . And, the energy is transferred to C when SW was turned off in the period of t_{off} . Following equation is

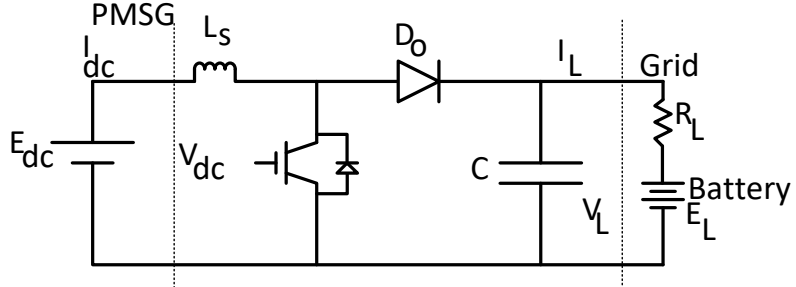


Figure 2.6: Boost chopper circuit.

obtained

$$V_{dc}t_{on} = V_L t_{off} \quad (2.10)$$

$$V_L = \frac{t_{on}}{t_{off}} V_{dc} = \frac{1}{1 - \alpha} V_{dc}$$

where $\alpha = \frac{t_{on}}{t_{on} + t_{off}}$

It is possible that boost chopper circuit and load resistance R_L , are considered a kind of variable resistance changed by duty ratio from the viewpoint of the DC voltage source. This variable resistance R_s is defined as:

$$I_{dc} = \frac{V_{dc}}{R_s, ch} \quad (2.11)$$

The output current I_L is expressed by output voltage V_L and load resistance R_L ,

$$I_L = \frac{V_L}{R_L} \quad (2.12)$$

Input power and output power of the Boost chopper is equal then we can write the following equation

$$V_{dc}I_{dc} = V_L I_L \quad (2.13)$$

By substituting Equation ?? in Equation 2.13, V_{dc} and V_L are eliminated.

$$I_L = (1 - \alpha)I_{dc} \quad (2.14)$$

By substituting Equation ?? in Equation 2.12,

$$\begin{aligned}\frac{V_L}{I_L} &= \left(\frac{1}{1-\alpha}\right)^2 \frac{V_{dc}}{I_{dc}} \\ R_L &= \left(\frac{1}{1-\alpha}\right)^2 R_s\end{aligned}\quad (2.15)$$

Then chopper equivalent resistance,

$$R_s = (1-\alpha)^2 R_L \quad (2.16)$$

From Equation 2.16, it was confirmed that the boost chopper equivalent resistance from the viewpoint of the DC voltage source could be expressed in the function of the duty ratio. The output power from the WECS fluctuating according to wind changes, other energy sources such as battery or solar systems or diesel generators must be added to ensure a constant power supply to the local grid. Maximum power conversion of the WECS is obtained by adjusting the generator speed $\omega(g)$ as wind speed V changes. This is achieved by modifying the equivalent load at the generator terminal via power electronics converters. The equivalent standalone WECS is depicted in Figure 2.5, where $R_{s,ch}$ and L_S are the equivalent load resistance and inductance, respectively. The equivalent load resistance is considered the control input for the control system.

one-mass model of the gear-box is given by,

$$\frac{d\omega_h}{dt} = \frac{\eta}{iJ_h} T_{wt} - \frac{T_{em}}{J_h} \quad (2.17)$$

where J_h , i and η are the generator side equivalent inertia, gear ratio and efficiency of gear box respectively. wind and electromagnetic torque is represented as T_{wt} and T_{em} . The generator side inertia is calculated as,

$$J_h = (J_{wt} + J_l) \frac{\eta}{i^2} \quad (2.18)$$

where J_{wt} and J_l are inertia of wind turbine and the low-speed shaft..

2.3 Feedback Linearization controller for PMSG based WECS

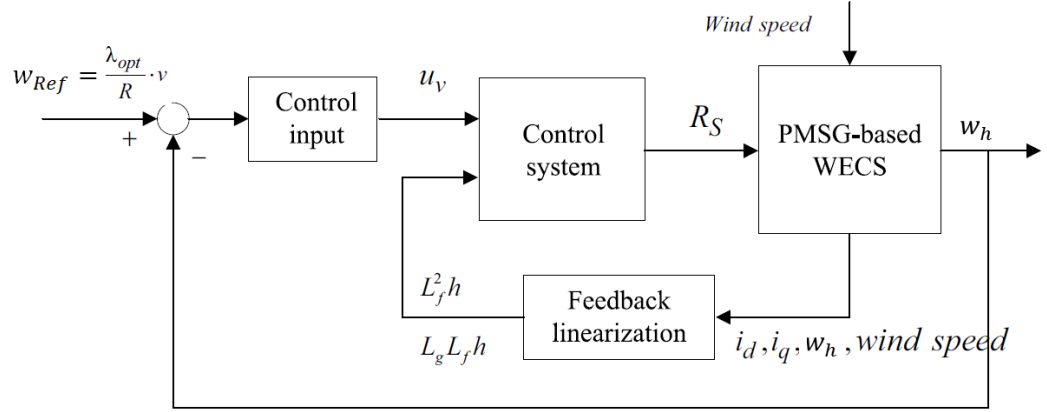


Figure 2.7: Block Diagram of Feedback Linearization control Structure.

In this section, the design of partial feedback linearization controller for PMSG based WECS is performed and the block diagram is shown in Figure 2.7. The mathematical model of PMSG based WECS can be written in the following form,

$$\begin{aligned}\dot{X} &= f(X) + g(X)u \\ y &= h(X)\end{aligned}\quad (2.19)$$

state space representation of the equation 2.9 is given by,

$$\begin{aligned}X &= [I_d \ I_q \ \omega_h]^T \\ f(X) &= \begin{bmatrix} f_1 \\ f_2 \\ f_3 \end{bmatrix} = \begin{bmatrix} \frac{1}{L_d+L_s}(-Rx_1 + p(L_q - L_s)x_2x_3) \\ \frac{1}{L_q+L_s}(-Rx_2 - p(L_d + L_s)x_1x_3 + p\phi_m x_3) \\ \frac{1}{J_h}(d_1v^2 + d_2vx_3 + d_3x_3^2 - p\phi_m x_2) \end{bmatrix} \\ g(x) &= \begin{bmatrix} g_1 \\ g_2 \\ g_3 \end{bmatrix} = \begin{bmatrix} \frac{1}{L_d+L_s}x_1 \\ \frac{-1}{L_q+L_s}x_2 \\ 0 \end{bmatrix}\end{aligned}\quad (2.20)$$

where $u = R_s$ and $y = x_3 = \omega_h$

1. Step 1: Relative degree Calculation

Relative degree corresponding to the output function $h(x) = x_3$ can be calculated as

$$\begin{aligned}\mathcal{L}_g \mathcal{L}_f^{1-1} h(X) &= \mathcal{L}_g h(X) = \frac{\partial h(X)}{\partial X} g(X) = \frac{\partial h(X)}{\partial x_1} g(x_1) + \frac{\partial h(X)}{\partial x_2} g(x_2) + \frac{\partial h(X)}{\partial x_3} g(x_3) \\ \frac{\partial h(X)}{\partial X} g(X) &= [0 \ 0 \ 1] \begin{bmatrix} \frac{1}{L_d+L_s} x_1 \\ \frac{-1}{L_q+L_s} x_2 \\ 0 \end{bmatrix} = 0 \\ \mathcal{L}_g \mathcal{L}_f^{2-1} h(X) &= \mathcal{L}_g \mathcal{L}_f h(X) = \frac{\partial[\mathcal{L}_f h(X)]}{\partial X} g(X) \\ \mathcal{L}_f h(X) &= \frac{\partial h(X)}{\partial X} f(X) = f_3 = \frac{1}{J} (d_1 v^2 + d_2 v x_3 + d_3 x_3^2 - p \phi_m x_2) \\ \frac{\partial[\mathcal{L}_f h(X)]}{\partial X} &= [0 \ -p \phi_m \ d_2 v + 2d_3 x_3] \begin{bmatrix} \frac{1}{L_d+L_s} x_1 \\ \frac{-1}{L_q+L_s} x_2 \\ 0 \end{bmatrix} = p \phi_m \frac{1}{L_q + L_s} x_2\end{aligned}\quad (2.21)$$

2. $\mathcal{L}_g \mathcal{L}_f^{2-1} h_1(X) \neq 0$ then the relative degree corresponding to $h(x)$ is $r=2$. This means that only a partial linearization is possible.
3. Using diffeomorphism condition, the system is represented as normal form, given by,

$$\begin{aligned}\frac{\partial z_3}{\partial x_1} g_1 + \frac{\partial z_3}{\partial x_2} g_2 + \frac{\partial z_3}{\partial x_3} g_3 &= 0 \\ \frac{\partial z_3}{\partial x_1} \left(\frac{-1}{L_d + L_s} x_1 \right) + \frac{\partial z_3}{\partial x_2} \left(\frac{-1}{L_q + L_s} x_2 \right) &= 0 \quad (L_d = L_q) \\ \frac{\partial z_3}{\partial x_1} x_1 + \frac{\partial z_3}{\partial x_2} x_2 &= 0 \quad (a_3 = -\frac{1}{L_d + L_s} = -\frac{1}{L_q + L_s})\end{aligned}\quad (2.22)$$

The condition is fulfilled for $z_3 = a_3 \frac{x_1}{x_2}$

4. The coordinate transform that leads to a partial linearization of the system is

$$z = \Phi(x_1, x_2, x_3) = \begin{bmatrix} \Phi_1(x_1, x_2, x_3) \\ \Phi_2(x_1, x_2, x_3) \\ \Phi_3(x_1, x_2, x_3) \end{bmatrix} = \begin{bmatrix} x_3 \\ d_1 v^2 + d_2 v x_3 + d_3 x_3^2 - p \phi_m x_2 \\ a_3 \frac{x_1}{x_2} \end{bmatrix}\quad (2.23)$$

In order to be able to perform the inverse transform $\Phi(x_1, x_2, x_3)$ should not be singular. The direct coordinates transform is

$$\begin{aligned} Z_1 &= h(X) = x_3 \\ Z_2 &= \mathcal{L}_f h(X) = d_1 v^2 + d_2 v x_3 + d_3 x_3^2 - d_4 x_2 \\ Z_3 &= a_3 \frac{x_1}{x_2} \end{aligned} \quad (2.24)$$

and the inverse coordinate transform is,

$$\begin{aligned} x_1 &= \frac{z_3}{a_3} \frac{d_1 v^2 + d_2 v z_1 + d_3 z_1^2 - z_2}{d_4} \\ x_2 &= \frac{d_1 v^2 + d_2 v z_1 + d_3 z_1^2 - z_2}{d_4} \\ x_3 &= z_1 \end{aligned} \quad (2.25)$$

5. Derivation of the robust control law

$$\begin{aligned} u &= \frac{1}{\mathcal{L}_g} \mathcal{L}_f h(X) (-\mathcal{L}_f^2 h(X) + u_v) \\ \mathcal{L}_f h(X) &= d_1 v^2 + d_2 v x_3 + d_3 x_3^2 - d_4 x_2 \\ \mathcal{L}_f^2 h(X) &= \frac{\partial \mathcal{L}_f h(X)}{\partial x} f(x) = [0 \quad -d_4 \quad d_2 v + 2d_3 x_3] [f_1 \quad f_2 \quad f_3]^T \\ &= -d_4 f_2 + (d_2 v + 2d_3 x_3) f_3 \end{aligned} \quad (2.26)$$

$$\begin{aligned} \mathcal{L}_g \mathcal{L}_f h(X) &= \frac{\partial \mathcal{L}_f h(X)}{\partial X} g(X) = [0 \quad -p\phi_m \quad d_2 v + 2d_3 x_3] \left[\frac{-1}{L_d + L_s} x_1 \quad \frac{-1}{L_q + L_s} x_2 \quad 0 \right]^T \\ &= p\phi_m \frac{1}{L_q + L_s} x_2 = -d_4 a_3 x_2 \\ u_v &= -k_1 Z_1 - k_2 Z_2 + k_I \epsilon \end{aligned} \quad (2.27)$$

2.4 Existing manual Loop-shaping methods

The procedure to obtain manual loop-shaping based controller is elaborated and shown in Figure 2.7 and Figure 2.9. At a fixed frequency, the plant's frequency response set

is called a template. Template is a powerful tool in robust control engineering, widely used for representing the span of the frequency response of an uncertain plant family. The design is performed mainly on the Nichols chart, which is an integration of Bode's magnitude and phase plots. This plant template is used throughout the design process, ensuring the design robustness. Suppose we know the plant transfer function and its variations a priori, the plant templates can be generated on the Nichols chart. There are still three main tasks in QFT. First, we must obtain closed-loop specifications in frequency domain. Second, with the aid of the plant templates, frequency-domain specifications are used to calculate various bounds. A bound, belonging to a specific frequency, gives a valid region that the open-loop transfer function must lay. Third is the loop shaping process, where the controller is designed to shape the open-loop transfer function to be in the valid region.

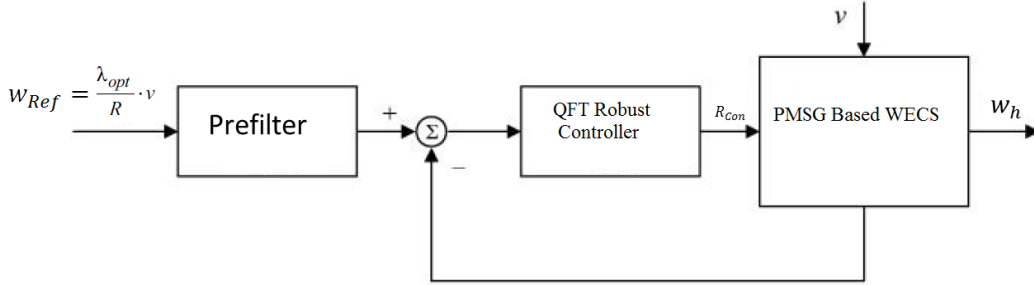


Figure 2.8: Block Diagram of QFT control Structure.

Manual loop-shaping based QFT controller and pre-filter is represented as transfer function is given by,

$$G_{QFT}(s) = \frac{6.84 (s + 62.5) (s + 10.06) (s + 9.93)}{s (s + 1265) (s + 5.24)}$$

$$F_{QFT}(s) = \frac{5478.55}{(s + 343.7) (s + 15.94)} \quad (2.28)$$

Addition of pole and zero to the above controller made the second controller, transfer function model is given by,

$$G_{MMQFT}(s) = \frac{8332 (s + 61.32) (s + 10.6) (s + 10.04) (s + 9.92)}{s (s + 1265) (s + 163.1) (s + 73.6) (s + 5.24)}$$

$$F_{QFT}(s) = \frac{5478.55}{(s + 343.7) (s + 46.16) (s + 15.94)} \quad (2.29)$$

Two different QFT controllers and pre-filter are designed and applied based on the total control input applied to the WECS is,

$$u = \frac{w_1 u_1 + w_2 u_2}{w_1 + w_2} \quad (2.30)$$

With the shaping parameters,

$$w_1 = \begin{cases} 1, & \text{if } v < 0 \\ 1 - 0.25(v - 5), & \text{if } 5 < v \leq 9 \\ 0, & \text{if } v > 9 \end{cases}$$

$$w_2 = \begin{cases} 1, & \text{if } v > 9 \\ 1 - 0.25(v - 5), & \text{if } 5 \leq v \leq 9 \\ 0, & \text{if } v < 5 \end{cases}$$

The total control applied to the considered power system is computed by shaping the individual control structure command

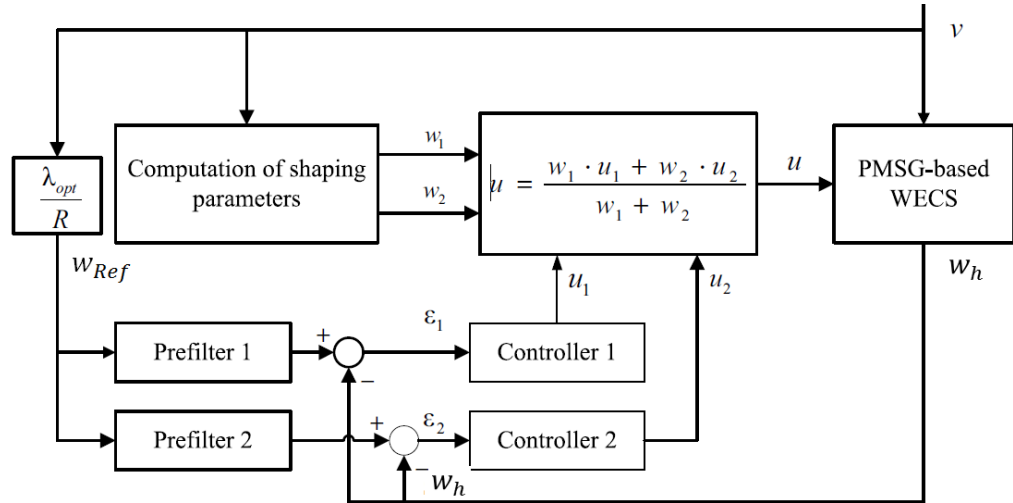


Figure 2.9: Block Diagram of Multi-Model QFT control Structure.

controller 1 and pre-filter-1 is selected G_{QFT} and F_{QFT} . controller-2 and pre-filter-2 is chosen as G_{MMQFT} and F_{MMQFT} . The above mentioned feedback linearization, QFT and multi-QFT based controller is designed for the PMSG based WECS for

preliminary simulation.

2.5 Proposed automated QFT Design

2.5.1 Problem Statement

The critical design specifications such as reducing HFG there by maximizing the feedback benefits along with the minimization of cost of feedback are translated into a mathematical formulation given as,

$$G(x, j\omega) = K_G \frac{\prod_{i=1}^{n_z} (j\omega + z_i)}{\prod_{k=1}^{n_p} (j\omega + p_k)} \quad (2.31)$$

where $x = [K_G, p_1 \dots p_{n_p}, z_1 \dots z_{n_z}]$, K_G, p_k ($(k = 1 \dots n_p)$) and z_i ($(i = 1 \dots n_z)$) represents the real space parameters, gain, real poles and zeros respectively.

2.5.2 Fitness Function Formulation

In general, fitness function defined as combining an expression of constraints and objectives ideally defines quality of controller and its estimated behaviour. Hence it is very vital to formulate an effective fitness function and its coefficients which translates all the requisite CSD specifications into a mathematical expression. As a first step the controller excess gain-band width area on ω expressed as an integral form is given as,

$$A(\omega_1, \omega_2) = \int_{\omega_1}^{\omega_2} \ln |G(j\omega)| d\omega \quad (2.32)$$

The foregoing assumptions permit the computation of the definite integral of (2.32) in terms of z_i, p_i, K_G, ω_1 and ω_2 as follows (a proper controller, ($n_z = n_p$)):

$$A(\omega_1, \omega_2) = [\ln(K_G^2)(\omega_2 - \omega_1) + \sum_{i=1}^{n_z} \left(\omega_2 \ln \left[\frac{\omega_2^2 + z_i^2}{\omega_2^2 + p_i^2} \right] - \omega_1 \ln \left[\frac{\omega_1^2 + z_i^2}{\omega_1^2 + p_i^2} \right] + 2z_i \tan^{-1} \left(\frac{\omega_2}{z_i} \right) - 2p_i \tan^{-1} \left(\frac{\omega_2}{p_i} \right) + 2z_i \tan^{-1} \left(\frac{\omega_1}{z_i} \right) - 2p_i \tan^{-1} \left(\frac{\omega_1}{p_i} \right) \right) \quad (2.33)$$

Finally, the controller gain-bandwidth area measure is used to form an augmented cost function. As an outcome, the formulated fitness function is given as,

$$J(x) = a_0 k_G^2 + a_1 \sum_{i=1}^{n_z} \frac{(p_i - z_i)^4 + 1}{p_i z_i} + a_2 A(\omega_1, \omega_2) + a_3 \psi(x) + a_4 \sum_{i=1}^{n_z} \tan^{-1} \left(\frac{p_i - z_i}{p_i z_i} \right) \quad (2.34)$$

In the above cost function, the first two terms corresponds to high frequency gain and lead ratios respectively while the third and fourth terms refers to constraint pertaining to the area and the penalty respectively. The third term in (2.34) facilitates the tight control of gain at any frequency of interest. Thus, helps in diminishing the over-design at low frequencies. Similarly, additional terms can be included in order to cater other frequency ranges as well.

In general the nominal loop transmission should satisfy the bounds of intersection and are described as a function q with lower and upper parts, q_l and q_u respectively, such that,

$$\begin{aligned} L_m q_u(\angle L_0(x, j\omega_i), \omega_i) &\leq L_m L_0(x, j\omega_i) & i \in I \\ L_m L_0(x, j\omega_i) &\leq L_m q_l(\angle L_0(x, j\omega_i), \omega_i) \end{aligned} \quad (2.35)$$

where $L_0 = GP_0$, I represents the frequency array points of interest, L_m indicates \log_{10} magnitude, and P_0 is the nominal plant. Further, the lower and upper bound violation limits are given by,

$$\begin{aligned} \theta_{x,i} &= \angle L_0(x, \omega_i) \\ \psi_u(x, \omega_i) &= \max \{ \log q_u(\theta_{x,i}, \omega_i) - \log L_0(x, \omega_i), 0 \} \\ \psi_l(x, \omega_i) &= \max \{ \log L_0(x, \omega_i) - \log q_l(\theta_{x,i}, \omega_i), 0 \} \end{aligned} \quad (2.36)$$

$$\psi_\omega(x, \omega_i) = \begin{cases} \min \{ \psi_u(x, \omega_i), \psi_l(x, \omega_i) \}, \\ \text{if } q_u(\theta_{x,i}, \omega_i) \geq q_l(\theta_{x,i}, \omega_i) \\ \max \{ \psi_u(x, \omega_i), \psi_l(x, \omega_i) \}, \\ \text{otherwise} \end{cases} \quad (2.37)$$

Thus, the penalty function $\psi(x)$ to penalise the unfeasible solutions that do not fulfil the performance specifications and assist in comprehending the degree of disparity of

each bound at frequency ω_i is given by,

$$\psi(x) = \sum_{i \in I} \psi_{\omega}^2(x, \omega_i) \quad (2.38)$$

It is worth noting that despite the addition of the prominent and wide spread terms into the fitness function, the inclusion of the proposed fifth term greatly aids in obtaining the desired descending modular plot of the controller. The inherent characteristics of the proposed term results in impelling the locus of the closed loop transmission $L_0(s)$ as much as nearer to the Universal bound while exhibiting descending phase response. The so formulated fitness function helps in realising a well-nigh controller that performs well against real time system uncertainties and disturbances.

2.5.3 Genetic Algorithm

Genetic Algorithm (Goldberg and Holland, 1988) based automatic loop-shaping developed to design the robust controller in QFT framework. Genetic algorithm (GA) are generally designed to maximize the objective function. The inverse of the cost function (2.34) is used for GA to identify the controller parameters in order to minimize the objective function. GA based AQFT controller using ALS is developed to minimize the cost of feedback Stark et al. (2015b). The programming steps are as follows:

Step 1: Initialization: Population can be generated at random.

Step 2: Evaluation: Fitness value should be compute for each individual by using objective function. Fitness value of an individual gives the information about how potential solution for optimization. Parents can be selected based on their fitness value. Higher fitness level individuals are selected for reproduction operator as parent chromosomes.

Step 3: Reproduction: Stochastic remainder selection without replacement method used for reproduction operation.

Step 4: Mutation: A small change in genetic information for every offspring's to generate best potential solution. Flip bit operator is used

Step 5: At last, selection of mutation probability, crossover probability, population size and the fitness parameters $\omega_1, \omega_2, a_0, a_1, a_2, a_3$ and a_4 required to run the program.

Use of a robust controller for handling the operational uncertainties has become imperative in real time. This thesis presents a modified fitness function based automated robust controller with the aid of quantitative feedback theory (QFT) using Genetic algorithm (GA). A controller exhibiting the desired decreasing modular plot and descending phase response is devised. The addition of arctangent function as one of the fitness function term is the proposed modification that facilitates in capturing the ideal controller characteristics.

2.6 Application And Results

In this section, The proposed controller design and application to extract maximum power from a permanent magnet synchronous generator based autonomous wind power system is presented. The step by step design guidelines for the automated QFT robust controller is deliberated in detail. The performance evaluation is carried out for step change and stochastically varying wind speed. Finally, benchmarking of the proposed controller against those available in the literature is accomplished through extensive simulations and it will be shown that the maximum power extraction along with least electromagnetic torque oscillations are achieved with the proposed fitness function based automated QFT controller. QFT based robust controller and pre-filter design steps are discussed below.

2.6.1 Selection of plant with parameter uncertainty

The transfer function model of PMSG based AWPS can be represented as uncertain system, variation of parameters are depends on the operating points.

$$P(s) = \frac{k}{(1 + 2T\xi s + s^2T^2)} \quad (2.39)$$

Where the uncertainty of plant parameter is given by

$$6 \leq k \leq 20, \quad 0.01 \leq T \leq 0.09, \quad \xi = 0.8$$

Nominal plant parameters $k = 20, T = 0.09$.

2.6.2 Template generation

Templates are the pictorial representation of the uncertain plant's magnitude and phase frequency response at fixed frequency. The sketch of the templates for the frequency vector $\omega = [1 \ 5 \ 10 \ 20 \ 40 \ 100] \text{ rad/s}$ shown in the Nichols chart in Figure 2.10.

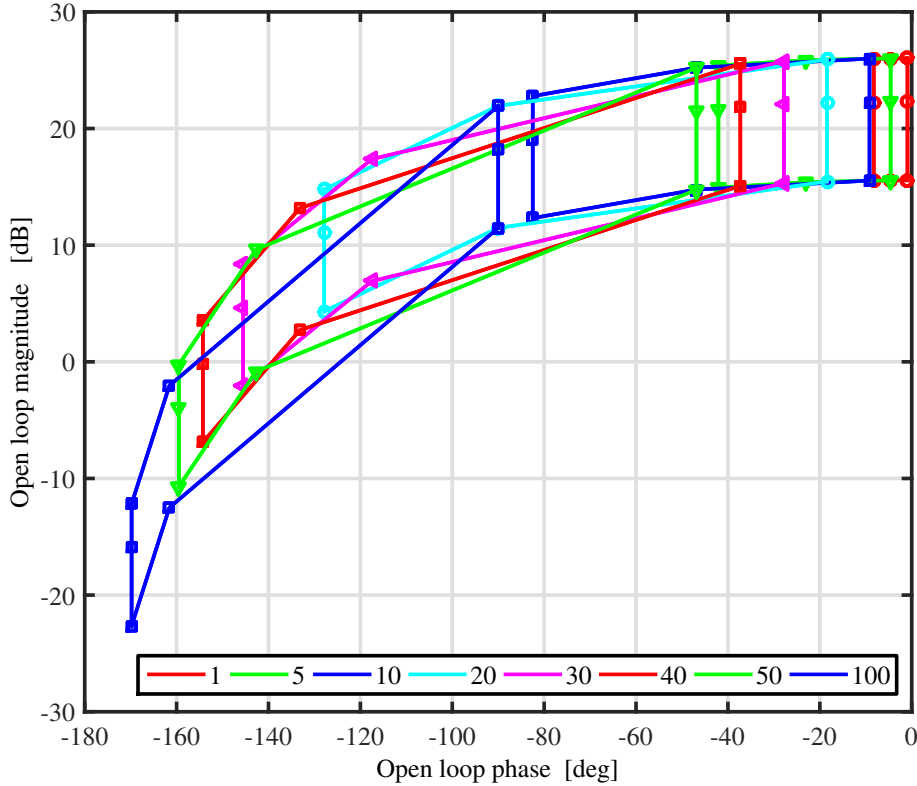


Figure 2.10: Template Generation for different frequencies.

2.6.3 Bounds computation

Edge point templates are used here to obtain QFT bounds. Stability margins and performance specifications are transformed to frequency domain to represent the QFT bounds. These QFT bounds are represented in Nichols chart. The computation of QFT bounds is done with quadratic inequalities. Closed loop robust stability margins are expressed as follows

$$\left| \frac{L_g}{1 + L_g} \right| \leq \gamma_1 \quad \forall P \in \{p\} \quad (2.40)$$

Table 2.1: Templates points.

Point	ω_i	1	5	10	20	40	100	
K=6	T=0.01	P	15.5628	15.5569	15.5383	15.4600	15.0895	11.4806
		$\angle P$	-0.9167	-4.5853	-9.1805	-18.4349	-37.3039	-90
	T=0.05	P	15.5569	15.3973	14.7622	11.4806	2.7210	-12.4988
		$\angle P$	-4.5853	-23.1063	-46.8476	-90	-133.1524	-161.5651
	T=0.09	P	15.5431	14.9394	12.3208	4.3206	-6.8975	-22.6373
		$\angle P$	-8.2603	-42.0764	-82.4836	-127.8750	-154.2843	-169.7960
K=13	T=0.01	P	22.2786	22.2728	22.2542	22.1759	21.8053	18.1965
		$\angle P$	-0.9167	-4.5853	-9.1805	-18.4349	-37.3039	-90
	T=0.09	P	22.2589	21.6553	19.0367	11.0364	-0.1817	-15.9214
		$\angle P$	-8.2603	-42.0764	-82.4836	-127.8750	-154.2843	-169.7960
	T=0.01	P	26.0204	26.0145	25.9959	25.9176	25.5471	21.9382
		$\angle P$	-0.9167	-4.5853	-9.1805	-18.4349	-37.3039	-90
K=20	T=0.05	P	26.0145	25.8548	25.2197	21.9382	13.1785	-2.0412
		$\angle P$	-4.5853	-23.1063	-46.8476	-90	-133.1524	-161.5651
	T=0.09	P	26.0007	25.3970	22.7784	14.7782	3.5601	-12.1797
		$\angle P$	-8.2603	-42.0764	-82.4836	-127.8750	-154.2843	-169.7960

Usually $\gamma_1 = 1.2 = 1.6dB < 2dB$ then

gain margin = 5.26483 and phase margin= 49.2486. The gain margin indicates the amount of gain can be increased and the phase margin indicates the requirement of phase lag to reach the stability limit.

The upper and lower reference tracking bounds for the considered wind energy conversion system are defined by

$$\begin{aligned} \gamma_{7U}(s) &= \frac{16.67s + 400}{s^2 + 36s + 400} \\ \gamma_{7L}(s) &= \frac{12000}{s^3 + 80s^2 + 1900s + 12000} \end{aligned} \quad (2.41)$$

by grouping all the stability and tracking bounds to calculate the worst case possibilities shown in Figure 2.11.

2.6.4 Loop shaping

Loop shaping is nothing but adding gain, zeros, and poles to the open loop system manually or automatically to satisfy the worst case specifications. Accordingly, we

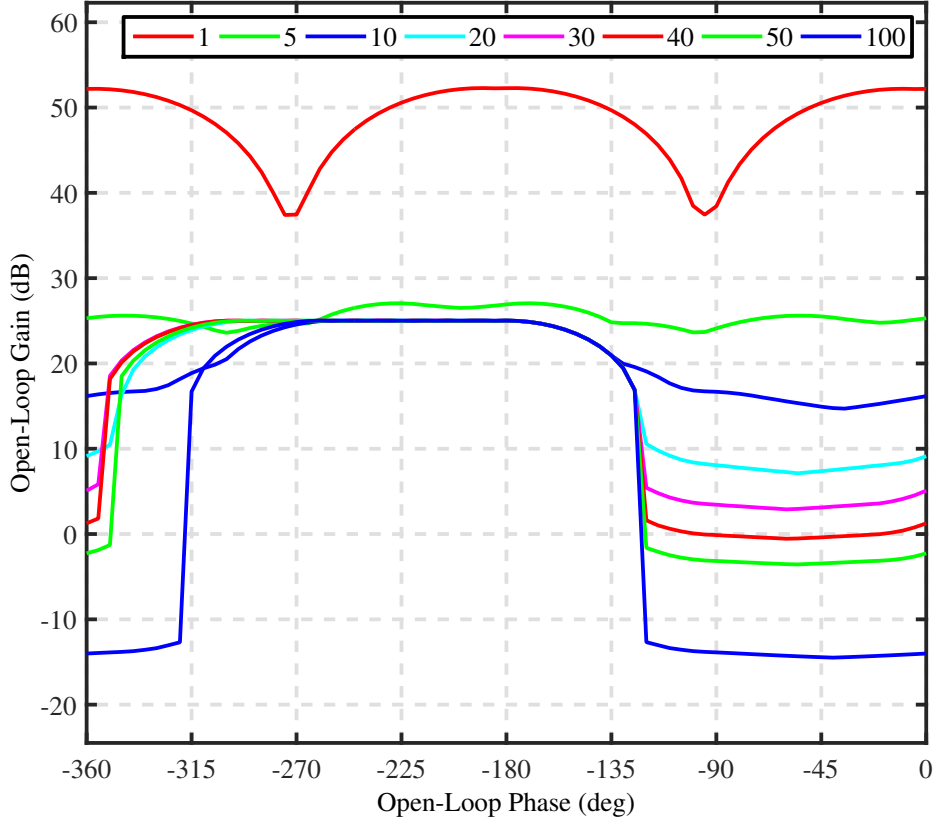


Figure 2.11: Intersection of Performance Bounds.

can design a controller in the frequency domain. Manual loop shaping is difficult for the beginners. So automatic controller design algorithms are interesting in real world problems. The intersection of bounds or worst case bounds is significant for the design QFT robust controller. ALS methodology used to design GA based QFT robust controllers with the existing and proposed cost function shown in (2.42) and (2.43) respectively.

$$G_1(s) = \frac{15.701(s + 42.29)(s + 38.43)(s + 10.42)}{(s + 354)(s + 134)(s + 0.01765)} \quad (2.42)$$

$$G_2(s) = \frac{5.7074(s + 53.06)(s + 23.58)(s + 13.63)}{(s + 125.1)(s + 109.6)(s + 0.07097)} \quad (2.43)$$

It is evident from Figure 2.12 and Figure 2.13 that the open loop phase of $L_0(s)$ is closer to the universal bound for the proposed controller between the frequency 10 to 100 rad/s. In addition, performance comparison of existing and proposed controllers

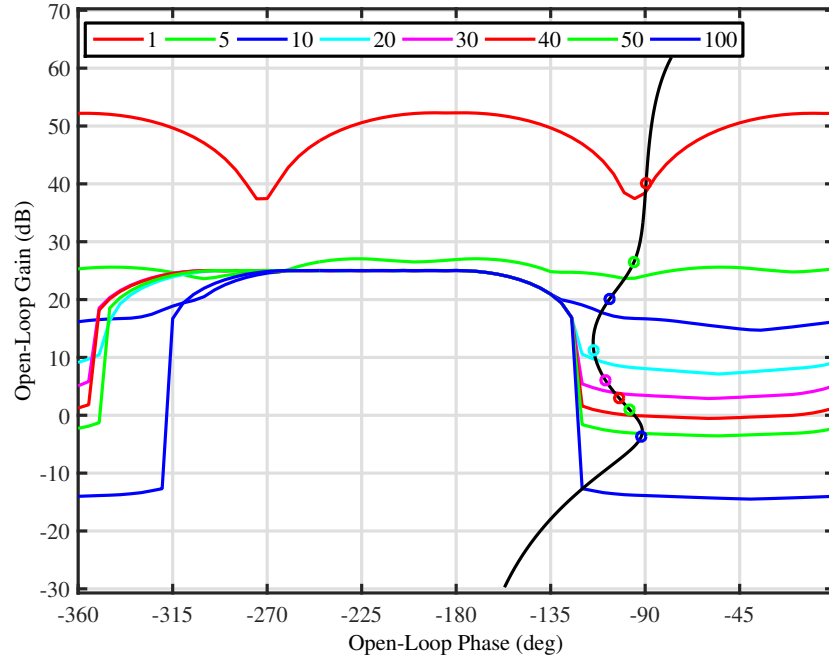


Figure 2.12: Closed loop frequency response with proposed controller $G_1(s)$.

in terms of HFG and cost value is tabulated in Table 2.2. With the application of proposed controller, the HFG is reduced to a value of 63.65% as compared to the application of existing method described in the literature. Thus, the sensitivity of proposed controller to high frequency noise is minimum and requires reduced control effort. The reduced cost function value attests the lesser feedback cost requirement of the proposed controller.

Table 2.2: Comparison of controllers.

Performance Index	Automated QFT Controller	Modified Automated QFT Controller
HFG	15.701	5.7074
$J(x)$	1.2286×10^5	1.0622×10^4

2.6.5 Pre-filter Design

Once the controller is designed the final task is to design pre-filter in two degrees of freedom control structure. Pre-filter designing or pre-filter shaping is same as loop shaping. The importance of pre-filter design is to track the desired output from the

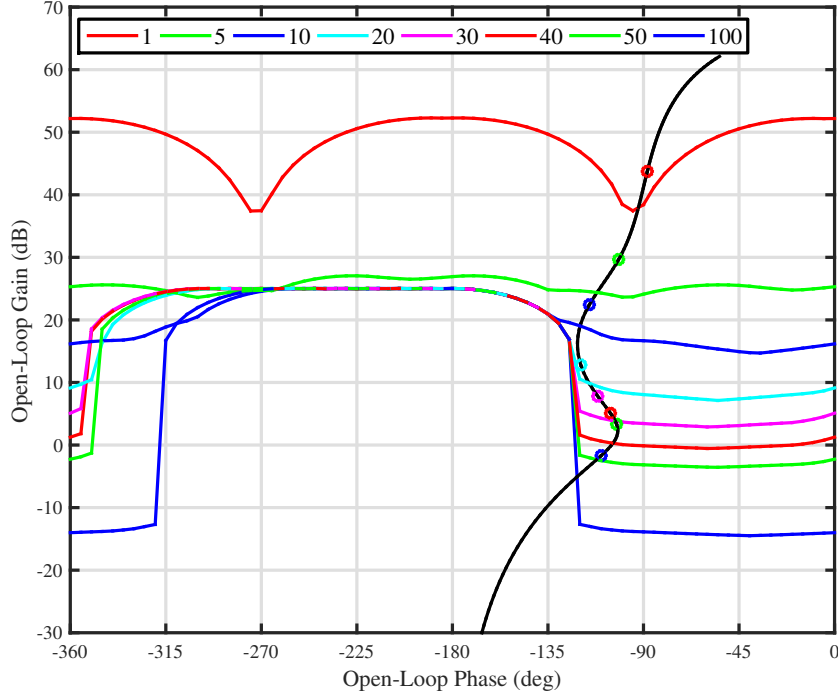


Figure 2.13: Closed loop frequency response with proposed controller $G_2(s)$.

input. The plant with the designed pre-filter response may satisfy all the performance specifications and need not lie between the extreme limits of the frequency domain responses. Pre-filter designed for the above controllers is shown in (2.44).

$$F(s) = \frac{1}{7.614 \times 10^{-6}s^3 + 0.001556s^2 + 0.08707s + 1} \quad (2.44)$$

2.6.6 Validation

After completion of the controller and pre-filter design in QFT background, we need to validate the designed one. In order to validate the proposed controller and pre-filter design, we need to do the time domain and frequency domain analysis for the given performance specifications.

Figure 2.14 and Figure 2.15 shows that both controllers $G_1(s)$ and $G_2(s)$ are satisfying the worst case stability margin i.e., $\gamma_1 = 1.6$ dB for the given frequency array and uncertainty range for the plant. Figure 2.16 and Figure 2.17 are shows the frequency response for the reference tracking specification. All the given set of plants with uncertainty are lie with in the upper and lower bounds. Figure 2.18 and Figure

2.19 shows the step response for the reference tracking specification. Step input is applied at the reference the steady state error should become zero then we can say that the system is tracking the reference. Now it is clear that $T_s = 0.7s$ for existing controller $G_1(s)$ and $T_s = 0.65s$ for existing controller $G_2(s)$. The designed controller and pre-filter along with the plant uncertainty with frequency array is satisfying the upper and lower limits of reference tracking.

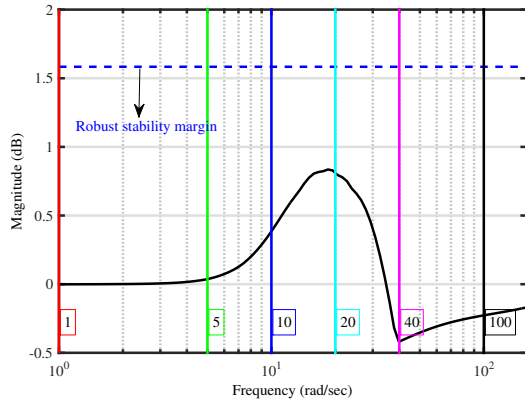


Figure 2.14: Robust stability margin analysis for $G_1(s)$.

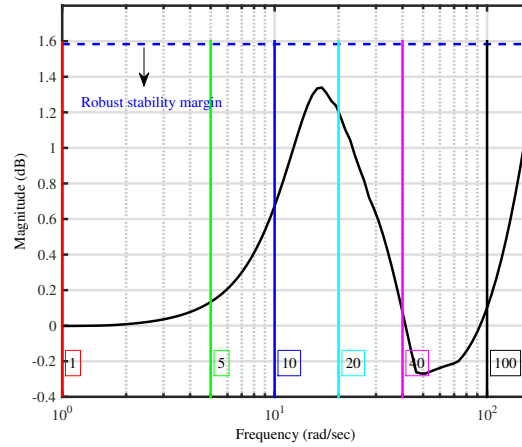


Figure 2.15: Robust stability margin analysis for $G_2(s)$.

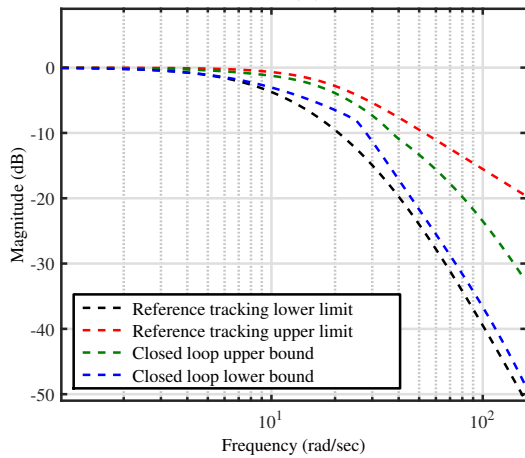


Figure 2.16: Frequency domain analysis of reference tracking with $G_1(s)$.

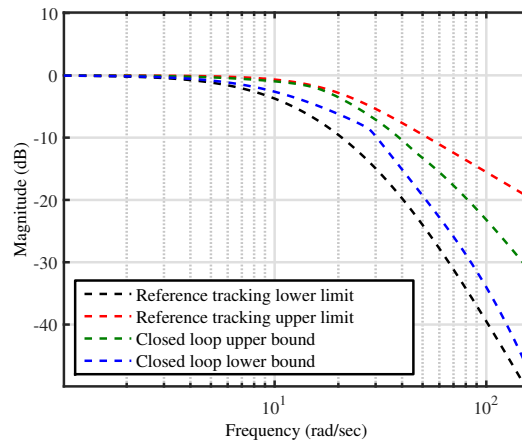


Figure 2.17: Frequency domain analysis of reference tracking with $G_2(s)$.

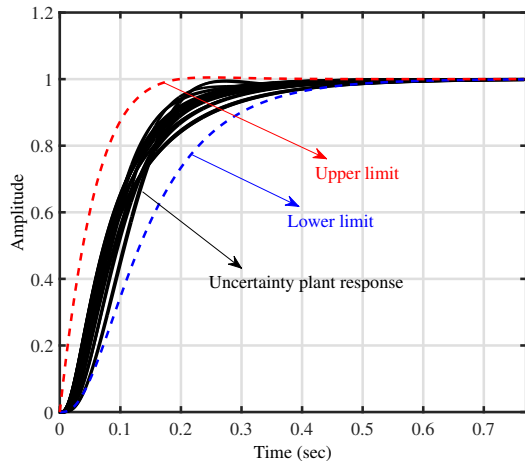


Figure 2.18: Time domain analysis of reference tracking with $G_1(s)$.

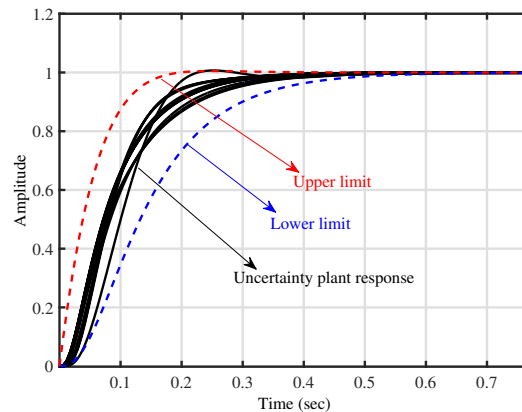


Figure 2.19: Time domain analysis of reference tracking with $G_2(s)$.

2.7 Simulation Results

In this section, the performance of the partial feedback linearization, QFT, multi-model QFT, existing and proposed fitness function based controllers for PMSG based autonomous WECS at below rated wind speed were evaluated at different wind scenarios through MATLAB simulations. PMSG and wind turbine parameters are given in Table 2.3. The description of the controllers is deliberated as follows,

1. A Non-linear control method preferably partial feedback linearization method (Yuehua et al., 2014) is chosen from the literature. The control law is derived for the proposed test system is given in equation 2.27. Pole-placement technique is used to find the control-law parameters, $k_1 = 4000$, $k_2 = 136$ $k_I = 40000$. the block diagram of feedback linearization controller structure is shown in Figure 2.7.
2. Manual loop-shaping based QFT and multi-model QFT controller design methodology (Cutululis et al., 2006b) is selected to show the effectiveness of the robust controller performance against non-linear method. The controller structure of the QFT and multi-model QFT is shown in Figure 2.8 and Figure 2.9 respectively. The designed controller transfer function are given in equation 2.28. Multi-model QFT controller structure will use the both the controller equation 2.28 and 2.29 as per the control input given in equation 2.30.
3. In the previous section, the comparison of the existing fitness function and the formulated fitness function based controllers are performed to achieve the ideal controller characteristics.
4. In this work, Genetic algorithm based automatic loop-shaping methodology is developed to design the robust controller based on existing (Molins and Garcia-Sanz, 2009, Garcia-Sanz and Molins, 2010), given in equation 2.42 and modified formulated fitness function given in equation 2.43 and the pre-filter given in equation 2.44 in QFT framework to extract maximum power from the autonomous PMSG based WECS.

Table 2.3: System Parameters.

Wind Turbine Parameters	
Blade radius R_T	2.5 m
Air Density ρ	1.25 kg m s ⁻³
Moment of inertia J	0.005 kg m s ⁻²
c_0	0.1253
c_1	-0.0047
c_2	-0.0005
Optimal Tip-speed Ratio	7
Power coefficient c_p	0.48
moment of inertia of the gear low-speed shaft	2.5 kg m s ⁻²
PMSG Parameters	
Stator Resistance R	3.3 Ω
Stator Inductances $L_d = L_q$	0.04156 H
p	3
ϕ_m	0.4382 Wb
L_s	0.08 H

2.7.1 Constant wind speed

In this case, PMSG based autonomous wind system working under constant wind speed. If suddenly 7 m/s wind speed applied, the wind turbines takes 1-2 seconds to reach its nominal reference speed. The load resistance represents the control input shown in Figure 2.20 (b), it is observed that less time to settle and less control effort for the proposed controller. Maximum power extraction is achieved with the proposed controller in comparison with the existing controller shown in Figure 2.20 (c). Application of proposed controller to the test system, achieved reduced oscillations shown in Figure 2.20 (d). The maximum power extraction, control effort (Load resistance) and wind turbine torque values are tabulated in Table 2.4.

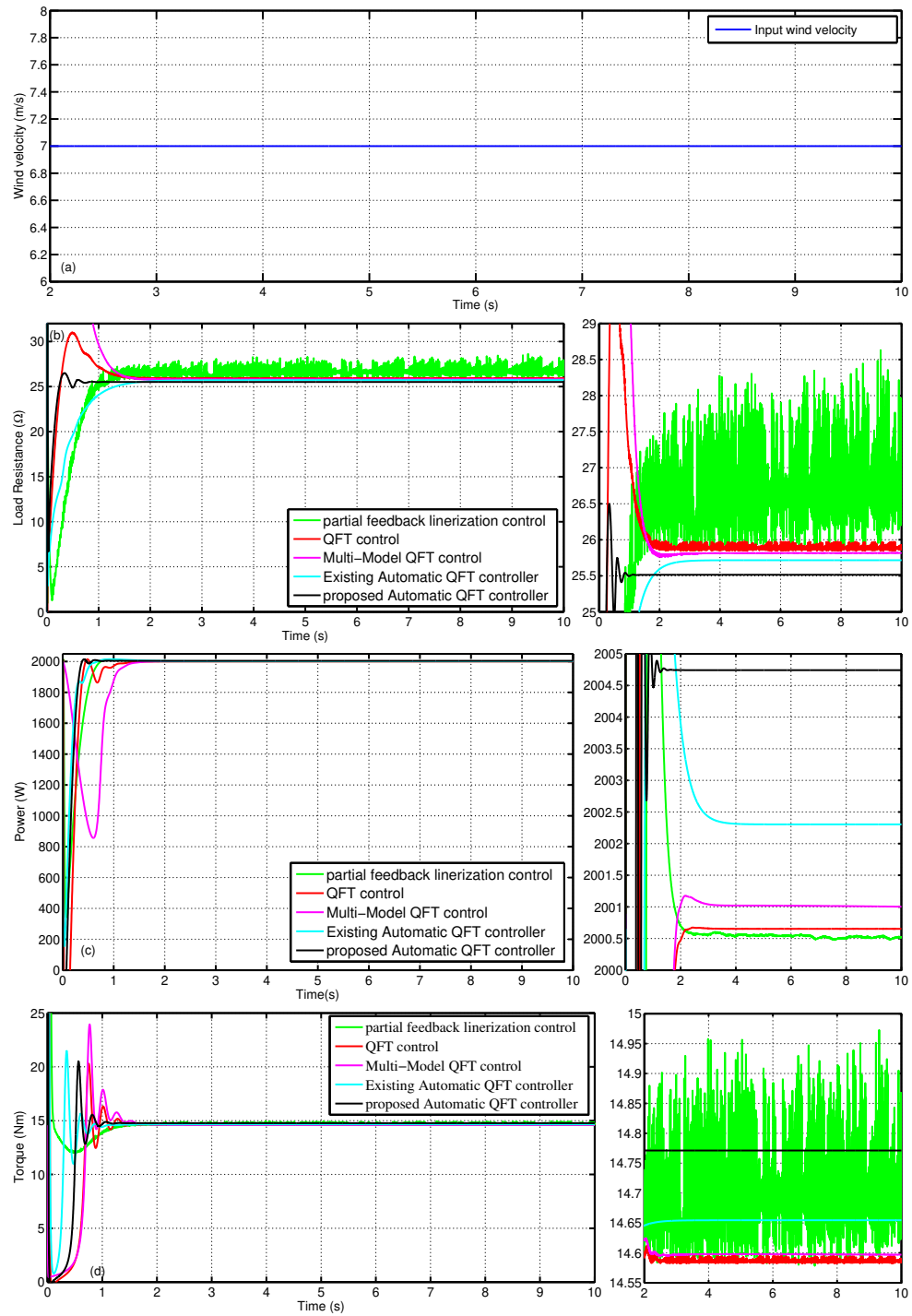


Figure 2.20: Constant wind speed (a) Wind Profile (b) Load Resistance (c) output Power (d) Wind Turbine Torque

Table 2.4: Proposed controller performance at constant wind speed

Parameter	Existing Method	Existing Value	Proposed Method	Proposed Value
Control effort (Load Resistance) Ω Wind Speed 7 m/s	Partial Feedback	Oscillatory	Modified Automated QFT Controller	25.52 Ω
	Linearization Control	$27 \pm 0.3\% \Omega$		
	QFT control	25.9 Ω		
	Multi-Model QFT Controller	25.82 Ω		
Maximum Power Extraction (W) $P = 0.5\rho\pi R_T^2 v_w^3 C_p(\lambda)$ $P_{max} = 2020.4W$ Wind Speed 7 m/s	Partial Feedback	2000.54 W	Modified Automated QFT Controller	2004.75 W $\eta = 99.23\%$
	Linearization Control	$\eta = 99.02\%$		
	QFT control	2000.65 W $\eta = 99.02\%$		
	Multi-Model QFT Controller	2001.02 W $\eta = 99.04\%$		
Wind Torque (N-m) Wind Speed 7 m/s	Partial Feedback	Oscillatory	Modified Automated QFT Controller	14.755 N-m
	Linearization Control	$14.7 + 0.15\% \text{ N-m}$		
	QFT control	14.59 N-m		
	Multi-Model QFT Controller	14.598 N-m		
	Automated QFT	14.65 N-m		

2.7.2 Step change in wind speed

In this case, the step variation is highlighted at 7-9 m/s shown in Figure 2.23 - Figure 2.26 and 9-11 m/s Figure 2.27- Figure 2.30. The proposed controller has more reference tracking capability shown in Figure 2.21 (b). Less control effort shown in Figure 2.21 (c). Maximum power extraction with least wind torque oscillations are observed with the proposed controller shown in Figure 2.22 (e) and (h) respectively. Further the key observations proving the proposed controllers competency is enlisted for 7-9 m/s and 9-11 m/s in Table 2.5 and Table 2.6 respectively.

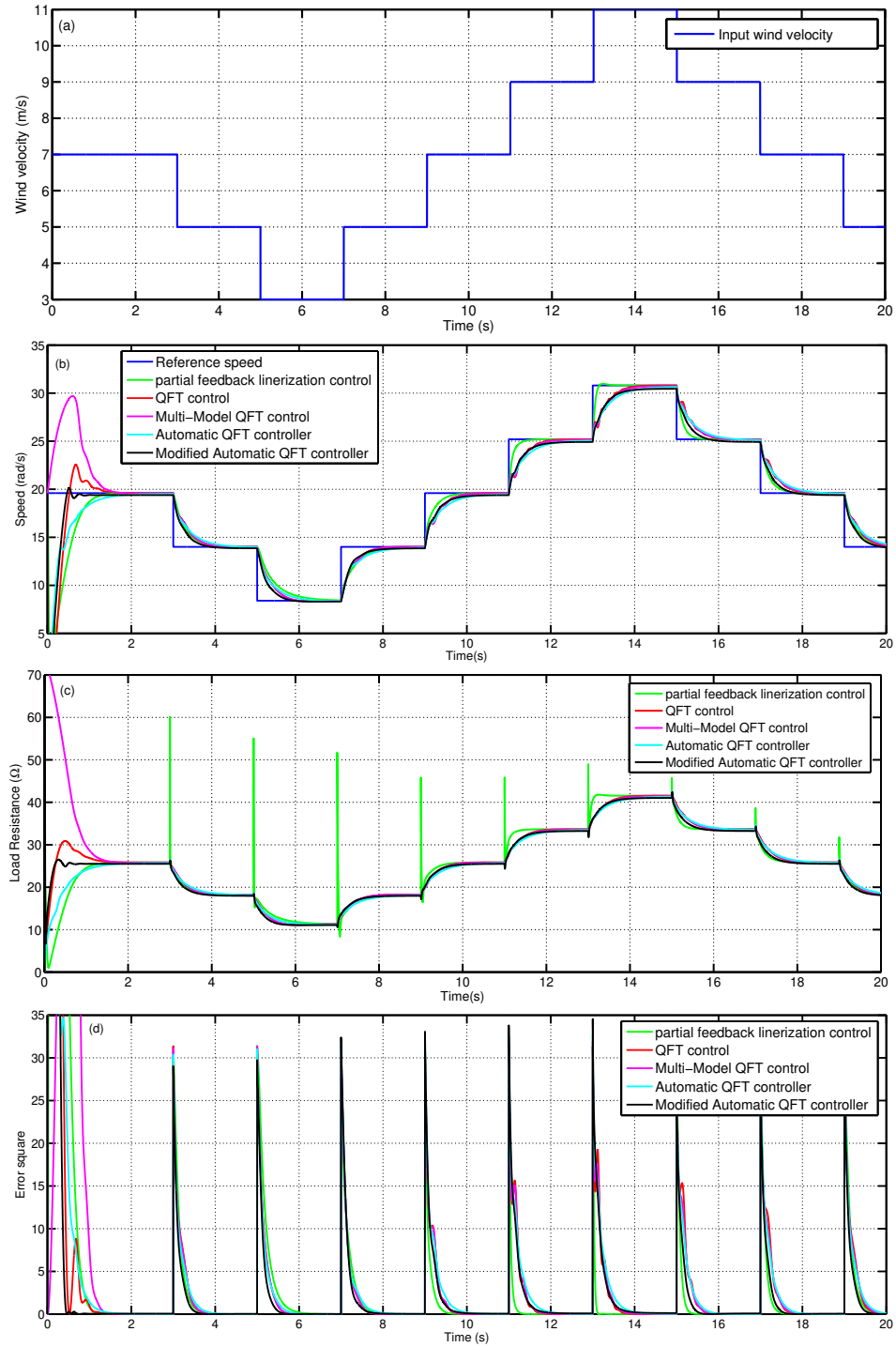


Figure 2.21: Step change in wind speed (a) Wind Profile (b) Speed tracking (c) Load Resistance (d) Error Square

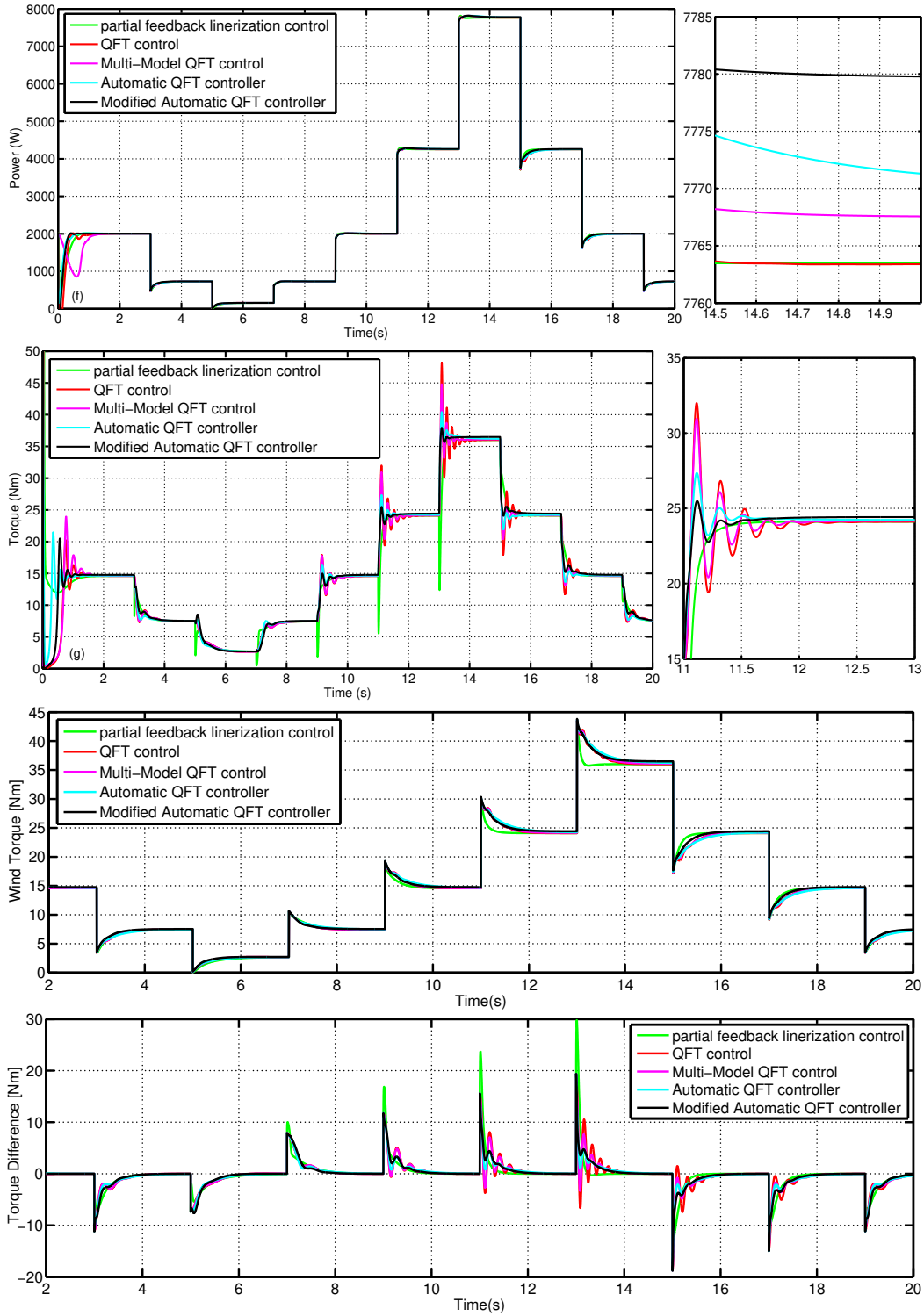


Figure 2.22: Step change in wind speed (e) output Power (f) Wind Turbine Torque (g) Generator Torque (h) Torque difference

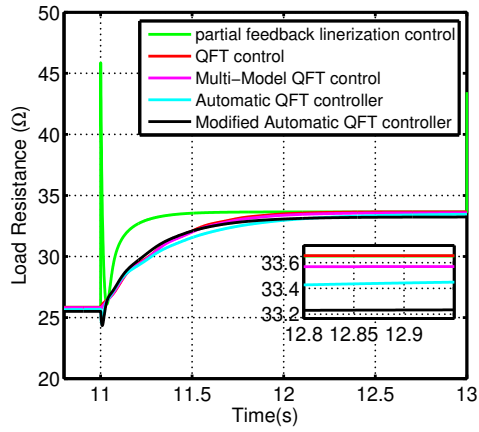


Figure 2.23: Load Resistance.

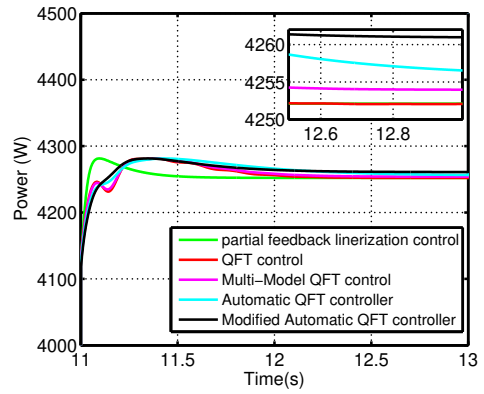


Figure 2.24: Power.

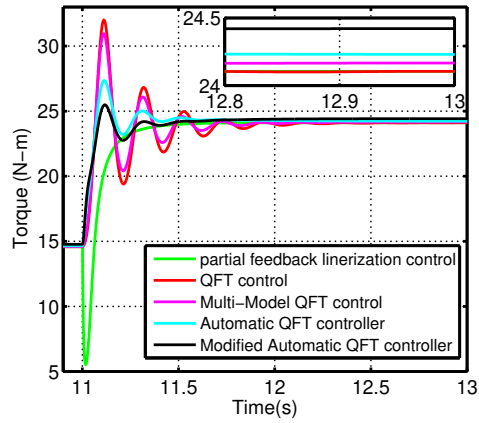


Figure 2.25: Wind turbine torque.

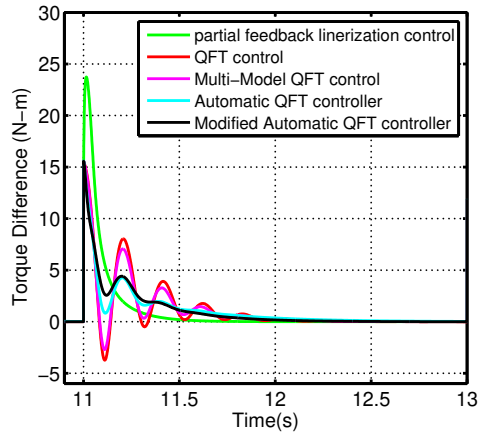


Figure 2.26: Torque difference.

Table 2.5: Proposed controller performance under step variation 7-9 m/s

Parameter	Existing Method	Existing Value	Proposed Method	Proposed Value
Control effort (Load Resistance) Ω Step change in Wind Speed 7- 9 m/s	Partial Feedback Linearization Control	33.65+36.33 % Ω Ts=0.8 s	Modified Automated QFT Controller	33.24 Ω Ts=1.5 s
	QFT control	33.65 Ω Ts=1.3 s		
	Multi-Model QFT Controller	33.55 Ω Ts=1.5 s		
	Automated QFT	33.45 Ω Ts=1.5 s		
Maximum Power Extraction (W) Wind Speed 7-9 m/s $P_{max} = 4294.2W$	Partial Feedback Linearization Control	4252 W $\eta = 99.02\%$	Modified Automated QFT Controller	4261 W $\eta = 99.23\%$
	QFT control	4252 W $\eta = 99.02\%$		
	Multi-Model QFT Controller	4254 W $\eta = 99.06\%$		
	Automated QFT	4256.6 $\eta = 99.12\%$		
Wind Torque (N-m) Wind Speed 7-9 m/s	Partial Feedback Linearization Control	24 - 75.00% N-m Ts= 0.5 s	Modified Automated QFT Controller	24.42+4.42 % N-m Ts=0.6 s
	QFT control	24.1+32.78% N-m Ts=1.2 s		
	Multi-Model QFT Controller	24.16+28.31% N-m Ts=1 s		
	Automated QFT	24.23+13 % N-m Ts=0.6 s		

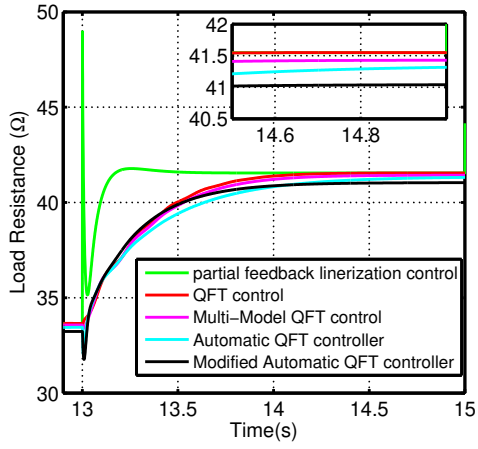


Figure 2.27: Load Resistance .

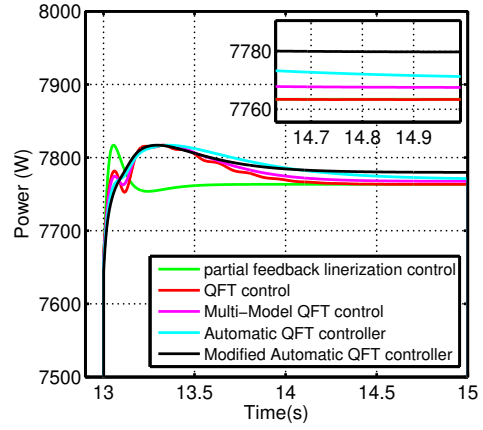


Figure 2.28: Power.

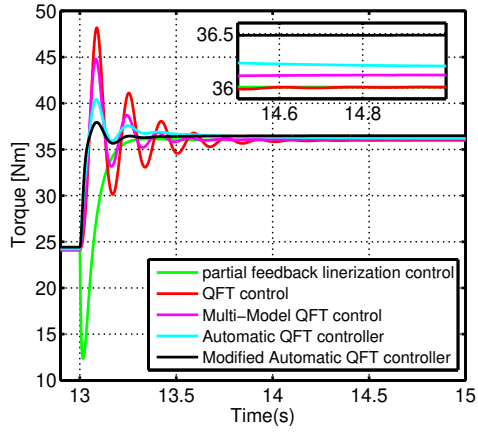


Figure 2.29: Wind Turbine torque.

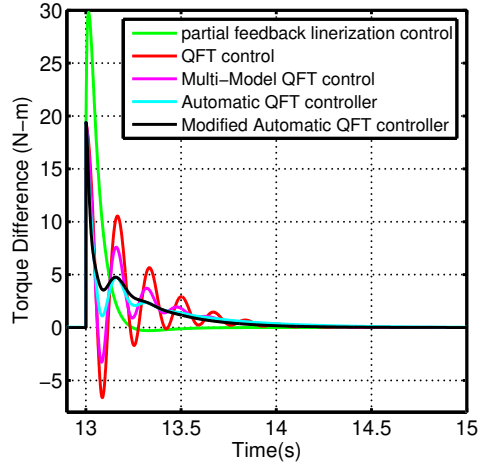


Figure 2.30: Torque difference.

Table 2.6: Proposed controller performance under step variation 9-11 m/s

Parameter	Existing Method	Existing Value	Proposed Method	Proposed Value
Control effort (Load Resistance) Ω Step change in Wind Speed 9-11 m/s	Partial Feedback Linearization Control	41.55+17.83 % Ω Ts=0.8 s	Modified Automated QFT Controller	41.04 Ω Ts=1.3 s
	QFT control	41.55 Ω Ts=1.3 s		
	Multi-Model QFT Controller	41.41 Ω Ts=1.5 s		
	Automated QFT	41.3 Ts=1.3 s		
Maximum Power Extraction (W) $P_{max} = 7840.2W$ Wind Speed 9-11 m/s	Partial Feedback Linearization Control	7763 W $\eta = 99.02\%$	Modified Automated QFT Controller	7780 W $\eta = 99.23 \%$
	QFT control	7763 W $\eta = 99.02\%$		
	Multi-Model QFT Controller	7767.6 W $\eta = 99.07\%$		
	Automated QFT	7772.2 W $\eta = 99.13\%$		
Wind Torque (N-m) Wind Speed 9-11 m/s	Partial Feedback Linearization Control	36- 65.67% N-m Ts= 0.8 s	Modified Automated QFT Controller	36.5+4.11 % N-m Ts= 0.6 s
	QFT control	36+34.03% N-m Ts= 1.2 s		
	Multi-Model QFT Controller	36.1+23.96 % N-m Ts= 0.8 s		
	Automated QFT	36.3+11.57 % N-m Ts= 0.6 s		

2.8 Stochastic wind speed

In order to verify the robustness of the proposed controller, A randomly generated stochastic wind speed is considered shown in Figure 2.31 (a) with rated average speed of wind is 7 m/s. The reference tracking performance analysis of proposed controller is compared with the existing method under different wind conditions shown in Figure 2.31 (b). It is observed that the proposed controller requires the minimum control effort or optimal load resistance while operating as desired. Also, it noteworthy that the proposed controller facilitates in extracting the maximum power corresponding to a given wind velocity in comparison to other well established techniques shown in Figure 2.31 (c). It is highly desired to have a smooth torque variation owing to the associated mechanical structure. Among the other available methods, a smooth torque variation with an improved performance is witnessed with the application of the developed controller shown in Figure 2.31 (d).

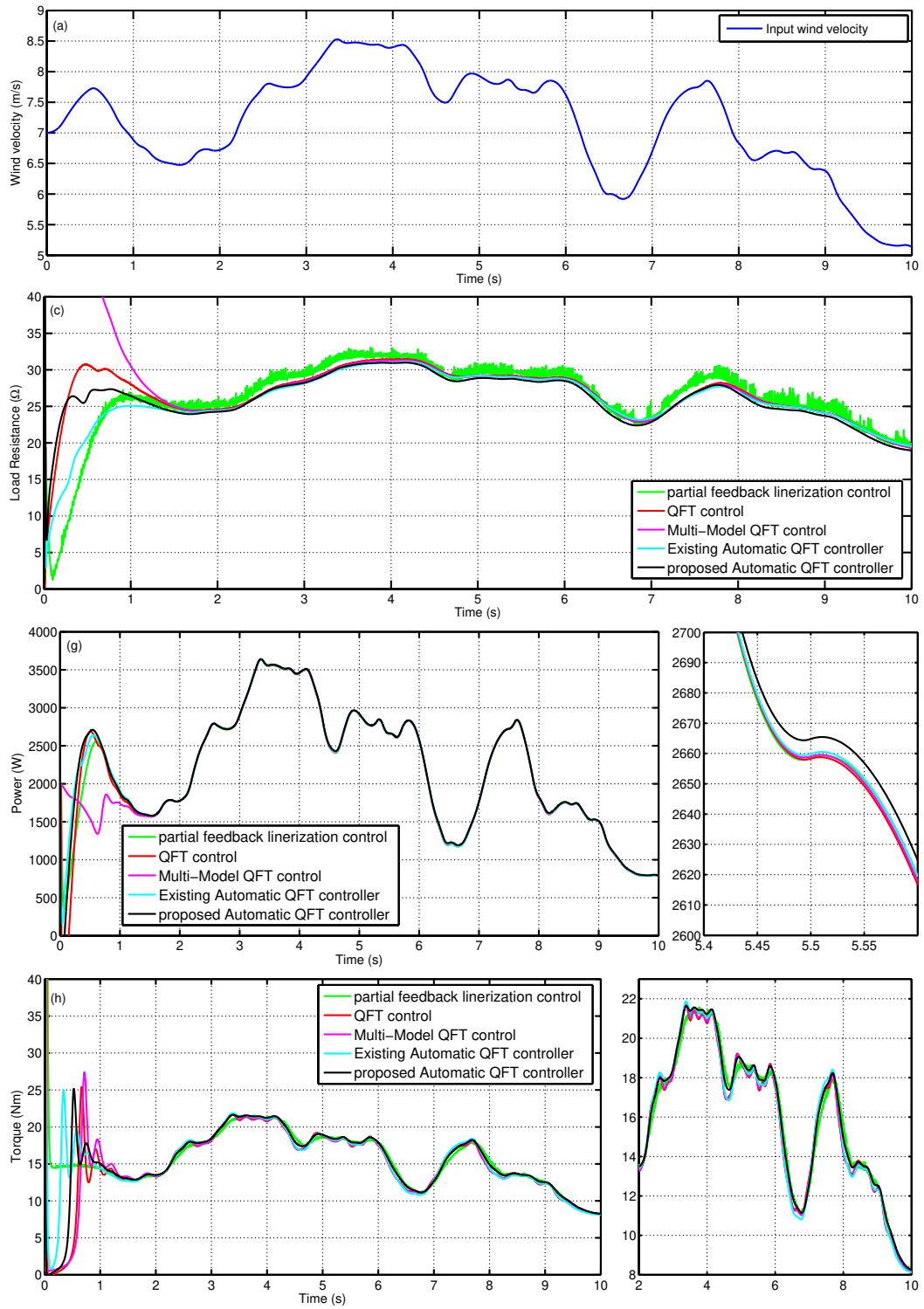


Figure 2.31: Stochastic wind speed (a) Wind Profile (b) Load Resistance (c) output Power (d) Wind Turbine Torque

2.9 Grid connected PMSG based WECS with full-scale Power converters

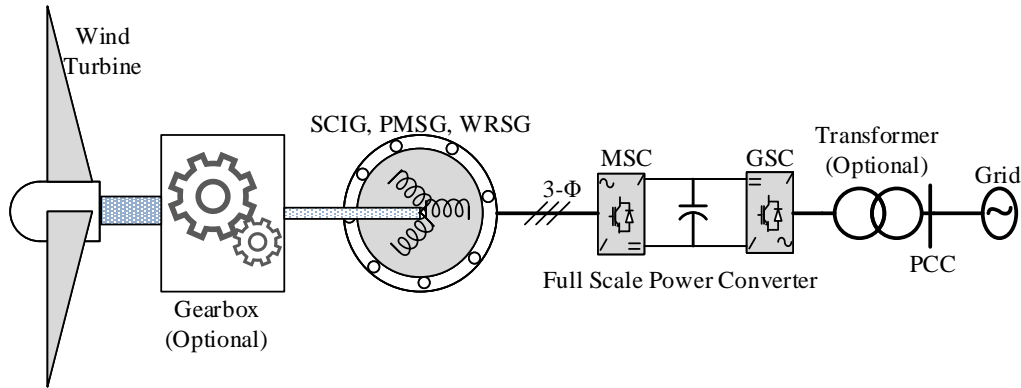


Figure 2.32: Block Diagram of PMSG based WECS with full-scale power converter.

The analysis performed in the previous sections shown the advantage of the proposed controller and proves that, proposed controller shown enhanced performance over existing controllers. In this work, The configuration of PMSG based WECS with a wind generator, and a full-scale power converter composed of machine (generator)-side converter (MSC), DC-link capacitor and GSC is shown in Fig. 2.32.

In order to investigate the effectiveness of the proposed robust QFT controller for maximum power extraction from PMSG based WECS, a complete modelling is done with back to back converters. Wind turbine and PMSG parameters used in this three-phase grid connected simulation is tabulated in Table 2.7. In this simulation, 20 kW at 11 m/s base speed wind turbine and nominal rotating speed of 22 rad/s is considered. surface mounted PMSG has power of 22 KVA with 18 poles and flux linkage of 0.915386 Wb machine is used. Grid voltage is taken as 400 Vrms and the DC-link voltage is selected as 720 V. Wind turbine generator and grid are operating parallel to supply the load of 10 kW. Higher wind speeds the wind turbine feeds the load alone, whereas low wind speeds grid supports the wind generator to supply the desired load.

Table 2.7: PMSG and Wind Turbine parameters

Parameter	Value
Nominal output power	20 kW
Base power for Generator	22 kVA
Grid Voltage V_{rms}	400 V
DC-link Voltage V_{dc}	720 V
Fundamental frequency	50 Hz
Base wind speed	11 m/s
Stator phase Resistance	0.1764 Ω
Armature Inductance	0.00448 H
Flux Linkage	0.915386 Wb
Inertia	1.8 Kg.m ²
pole pairs	18
Filter Inductance	0.01 Ω , 0.0008 H

2.10 Step change in wind profile

Step-change in wind profile is considered to operate grid connected WECS is shown in Figure 2.33.

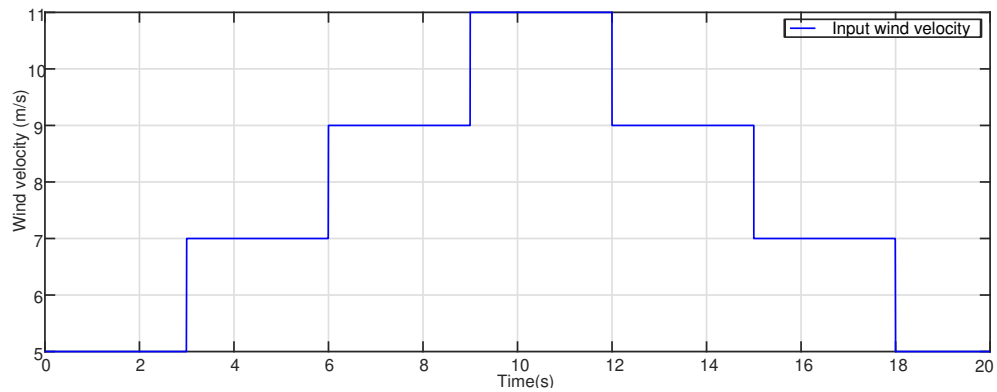


Figure 2.33: wind profile

From Figure 2.34 it is observed that, the proposed controller successfully track the speed reference with least peak and the same is represented as difference of reference

speed to the measured speed for different control methods are presented in Figure 2.35, shown the lowest error measured over the other methods.

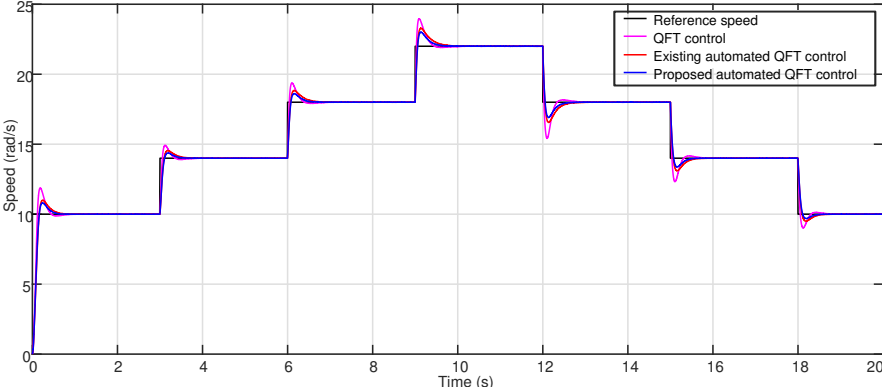


Figure 2.34: Reference tracking

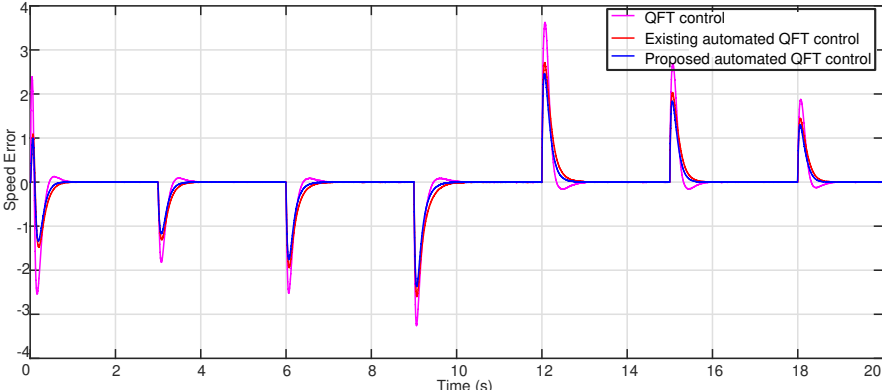


Figure 2.35: Speed error

In order to get smooth operation between DC-to-AC power conversion and injection, DC-link voltage should maintain as desired waveform shown in Figure 2.36. Grid voltage and current plots are showing in Figure 2.38 and Figure 2.37 respectively. In this case, If PMSG generates surplus power, the power inject to grid if it exceeds the load power. It is observed from Figure 2.40, that the proposed controller showing enhanced performance over existing methods to inject real power into grid.

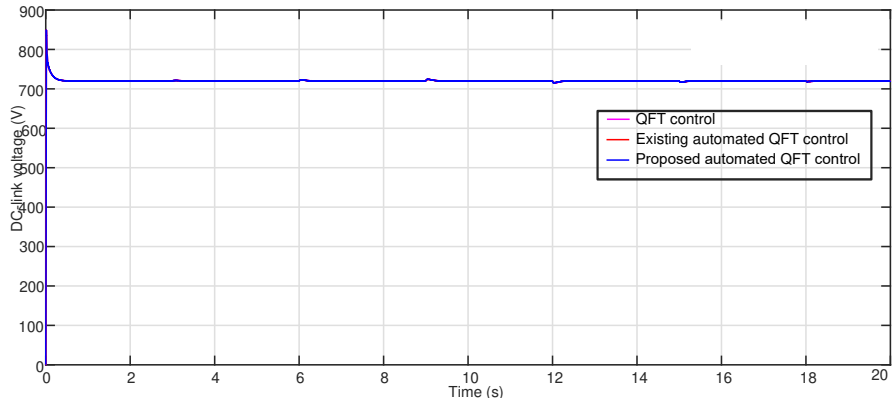


Figure 2.36: DC-link voltage

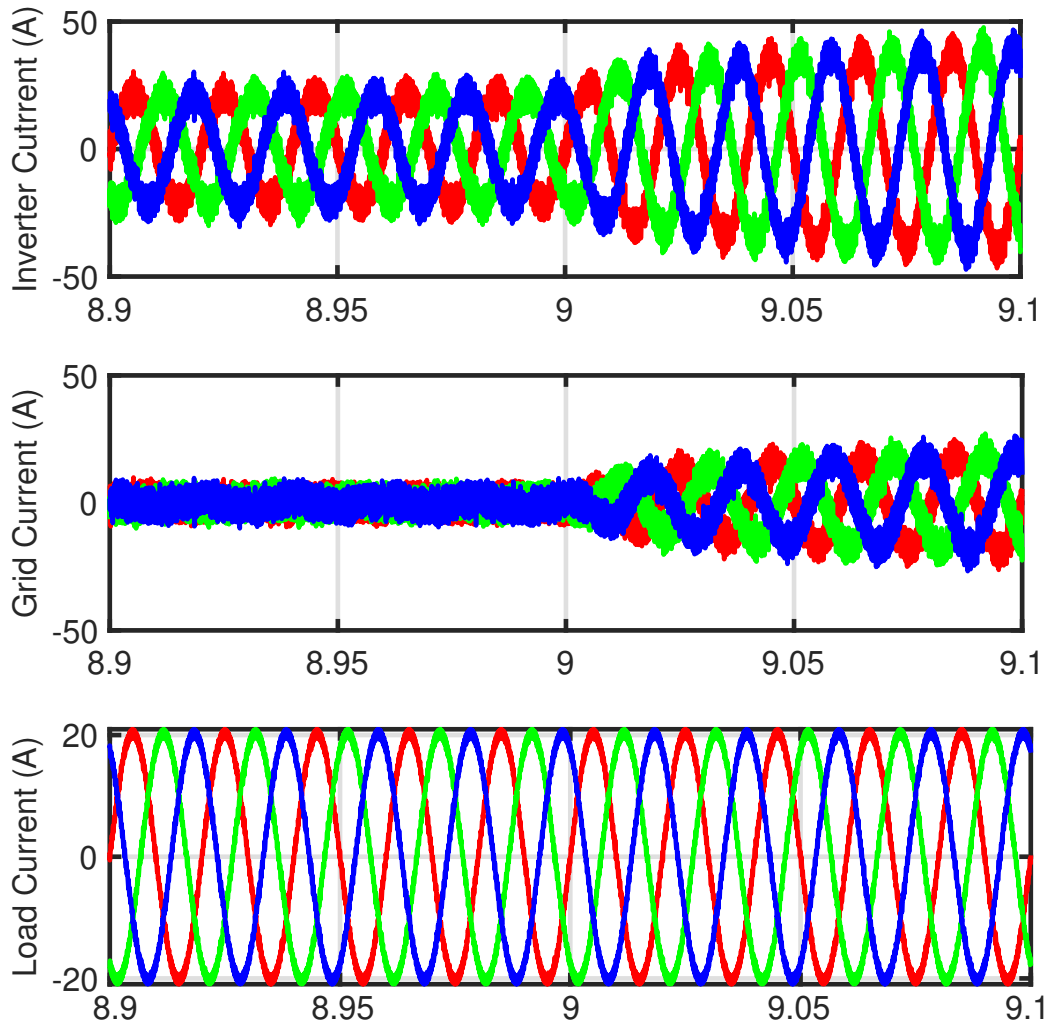


Figure 2.37: Current Injection

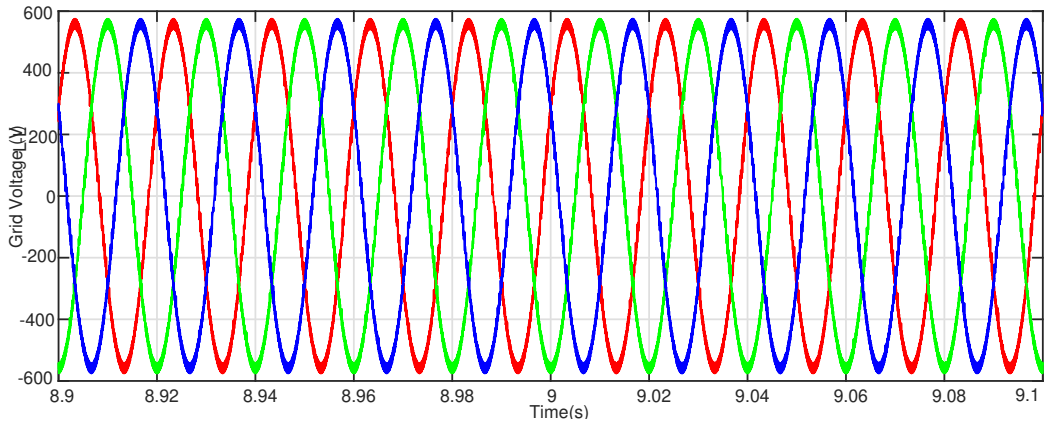


Figure 2.38: Grid Voltage

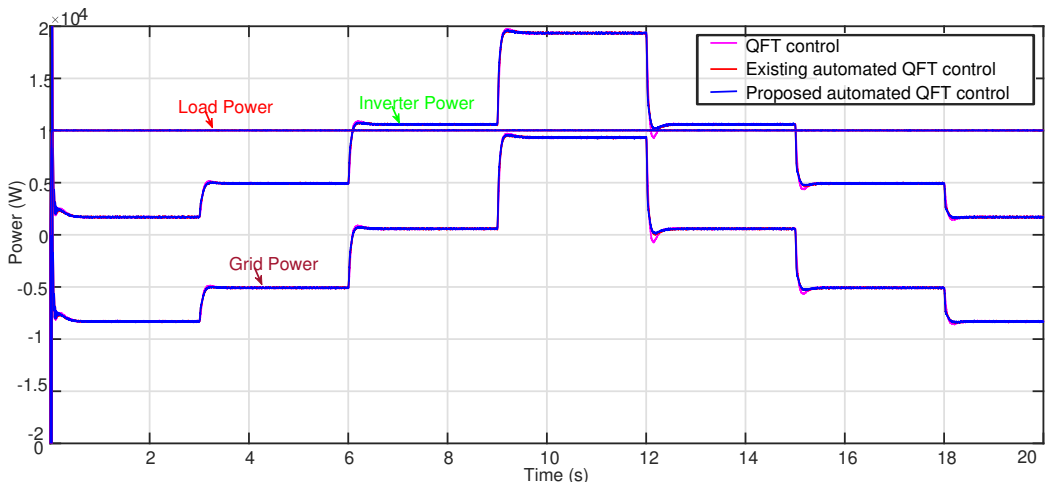


Figure 2.39: Power injection

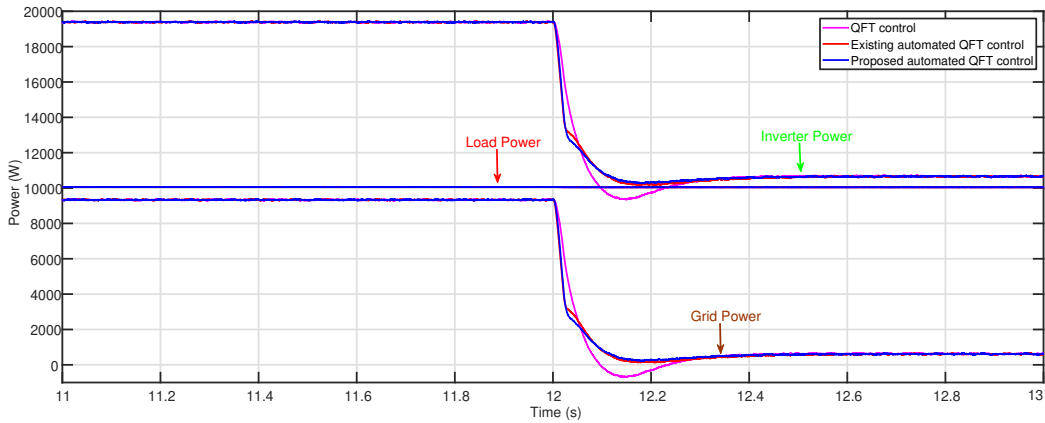


Figure 2.40: Power injection

2.11 Stochastic wind profile

The robustness of the proposed controller is evaluated under stochastic wind speed scenarios shown in Figure 2.41. The maximum power injection capability is achieved with the proposed controller is shown in Figure 2.42. The proposed controller successfully applied to the grid connected wind power system and shown enhanced performance under different wind speed conditions.

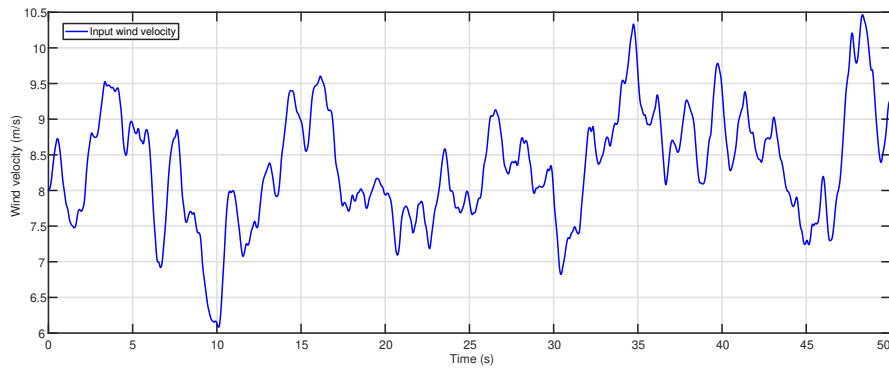


Figure 2.41: wind profile

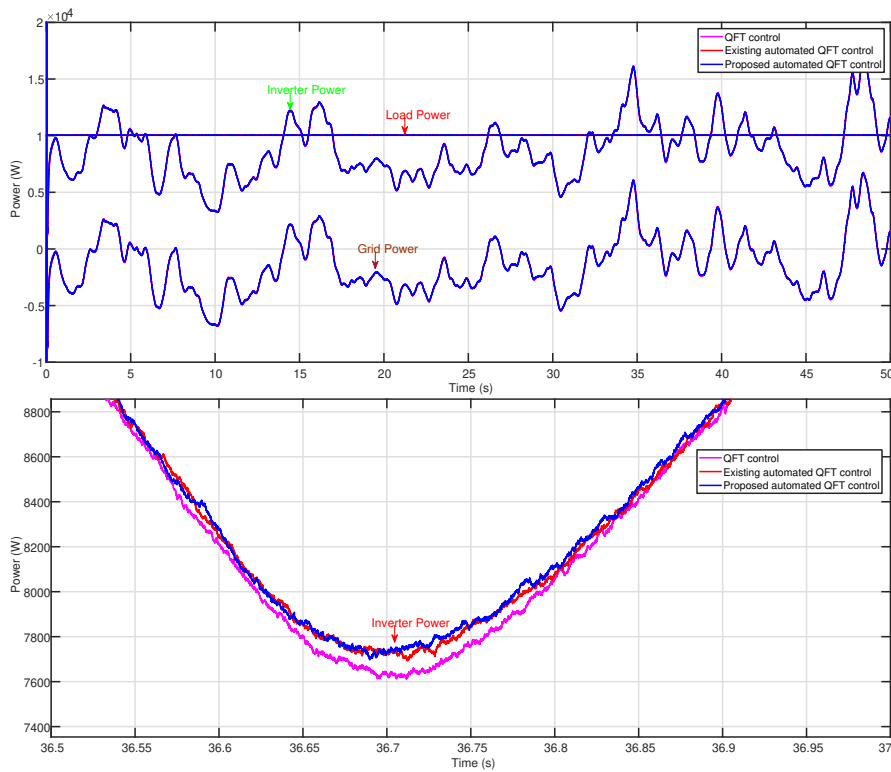


Figure 2.42: Power injection

2.12 Summary

1. In this work, Modified fitness function is introduced to design automatic robust controller to extract maximum power from the PMSG based AWPS in QFT framework.
2. GA based ALS of QFT robust controllers are designed for the original fitness function and modified fitness function. The prominent features of the modified fitness function based proposed controller are as follows.
 - i. It absolutely exhibits the highly desired decreasing modular plot and descending phase response.
 - ii. Addition of a simple arc tangent function helps in shifting the loop-shaping curve closer to the universal bound intern significantly reducing the gain at high frequencies.
 - iii. The usage of GA leads to the effortless acquisition of the controller parameters.
3. It is observed that the proposed controller requires the minimum control input while operating as desired. Also, it noteworthy that the proposed controller facilitates in extracting the maximum power corresponding to a given wind velocity in comparison to other well established techniques.
4. It is highly desired to have a smooth torque variation owing to the associated mechanical structure. Among the other available methods, a smooth torque variation with an improved performance is witnessed with the application of the developed controller.
5. Owing to the inherent variability in the wind power generation, a stochastic wind profile is consider as the test case. The applicability and feasibility of the developed controller is verified through extensive simulations and the results attesting its improved performance against well established methods are presented.
6. The proposed controller shown enhanced performance over existing controllers, for the grid connected PMSG based WECS to extract maximum power with least deviation from nominal values.

Chapter 3

QFT controller for Grid connected Photovoltaic system

3.1 Introduction

Alexandre Edmond Becquerel discovered the photovoltaic effect in 1839. According to Becquerel theory, electricity generation is possible with solar energy with suitable arrangements or experimental setup known as photo-voltaic effect or Becquerel effect. In 1873, willoughby smith discovered the photo conductive nature in selenium. In 1876, williams adams, demonstrated the electricity generation using selenium when it exposes to light. In 1883, Charles fitts designed first solar cell, the efficiency is about 1%. further improvements in the semiconductor material, the efficiency of silicon is increased to 6%-20%. When the solar solar cells are commercially introduced, it is used in space applications due to its high cost and immature technology. Over the past three decades, advancement in technology creates significant growth in photovoltaic (PV) industry in home and commercial applications. PV system generation capacity varies from watts for mobile devices to gigawatts for grid-connected or off-grid applications. In comparison with conventional resources, the reduction of electricity produced from solar PV remains high, technical report published by National Renewable Energy Laboratory ((Mathur, 2009)). PV power generation has advantages which have led to their rapid expansion are given below :

- * Solar energy abundantly available
- * Reliability-long life and static operation-free of noise

* enhanced efficiency and lower prices

* Highly modular and adaptable for different levels of capacity

Two kinds of semiconductors, namely silicon p-type and n-type, form a solar cell. The silicon type p is generated by the addition of atoms, such as boron or gallium, which have an external energy level of one less electron than silicon. Because the boron has one less electron than the electron that is required to connect with the Silicon atoms around it, an electron vacancy or "hole" will be established.

N-type silicon is manufactured with electrons that have one more atom than silicon, like phosphorous and mercury, on their external surface. Phosphorus has five outer-energy electrons. After doping the silicon with phosphorous and boron, a free electron-hole pair available to generate electricity through external circuit. To improve the efficiency of silicon based solar cell, N-type layer with low thickness and high doping and P-layer high thickness with low doping are used to design the PV cell. Theoretical studies, proves that efficiency of solar cell is around 30%, but practically 20% efficiency is achieved. The manufacture of crystalline PV modules uses recent techniques to consume a considerable amount of energy, thus preventing further price reductions. In this work address this issue, by accurate modelling of PV circuit and further, the designed model is simulated for 24-hours using the practical data taken from my institution National Institute of Technology (NITK).

3.2 Photovoltaic-system classification

Grid-tied Photovoltaic (PV) systems are divided into large, intermediate and small-scale systems, based on their power generation capacity (Ramakumar and Bigger, 1993). A small scale PV system generates less than 50 kW. A large scale PV system generates more than 1MW. PV system generating capacity between 50 kW and 1MW are considered as intermediate scale. The flexible design and dispersed design of the PV systems frequently cause uncertain limits between system classifications. The acquired PV system capability can exceed 1MW, which can be considered to be a big scale. Indeed, hundreds of small, medium and high grid-connected structures can be made up, combined or consisting of the assembly. The majority of grid-connected inverters generally have a capacity of less than 1 MW. In some cases, a single large-scale system can not be distinguished exactly from a set of small or medium-sized

systems. In some instances, it is difficult to differentiate a given large-scale scheme from a collection of smaller or medium sized structures. The bulk of grid-connected inverters generally have less than 1 MW ability.

A PV system with a grid can be integrated into the stand-alone or grid-connected mode with the battery storage system for operation. Battery storage can actively transmit to the grid during peak hours by means of substantial energy storage. It also smooths the power generation and reduces the impact of the intermission of solar energy. Therefore, whether they are integrated with battery storage is one classification of the PV systems. However, battery storage is not included in most of the grid-connected PV schemes. The latest categorization concentrates on the voltage level of PCC, where the power generation and distribution network in the interactive system intersects. Generally, low voltage integrated schemes are generally mounted near the energy consumers such as housing or business structures. The maximum power point (MPPT)-algorithm is primarily used to control these devices, in attempt to inject effective energy into the system from PV generators. Generally, PV power systems that connect the grid can be classified into Distributed MPPT (DMPPT) and Centralized MPPT (CMPPT) (Femia et al., 2008) systems. Unlike traditional approaches, DMPPT systems are sub-classified based on the level where MPPT tracking is applied (Xiao et al., 2016), at cell level, sub-module level, module and string, where MPPT is applicable to the function.

3.3 Centralized MPPT Systems

A PV grid consists of several simultaneous strings to attain the required power rating. Every string is created from a number of PV modules in sequence in order to satisfy the grid-connected converter output voltage demands. CMPPT devices monitor the maximum point of authority with a distributed grid tier inverter (Romero-Cadaval et al. (2013b)). Figure 3.1(a) indicates a three-stage conversion process. PV system linked to the PV output terminal by the power converter. The grid connection is the circuit that connects the power electronics converters to the electricity network. Topology is normally complicated due to the multiple steps of transformation. But the system uses a beneficial high frequency transformer because it is compact, fast and inexpensive.

The two-stage interfacing topology as shown in Figure 3.1(b). The DC link in

the DC network is essential because it provides power buffers for the DC / DC and the DC / AC converters. The DC / DC converter is known as the PVSC (PVSC). The DC / AC conversion is known as the GSC (Grid-side Conversion). The PV side converter provides the PV generator-PVSC filtering feature. The DC-link network is typically composed of capacitor banks which reduce harmonics arising from the DC / AC transition and the high-frequency switches (Hu et al., 2015). A one-stage conversion process, including only a DC and grid connection, is shown in figure 3.1(c). The unit turns the PV output into LFAC directly using a grid-connected PV inverter and offers galvanic insulation via a low frequency transformer. The PV relation is the same as the DC connection, so only the latter is stated. Figure 3.2(a) displays an underground grid-connected PV network with a two-stage conversion. Clearly indicated are the PV, DC and grid connections. The PV connection with the DC link in the analogous single phase conversion process, is shown in Figure 3.2 (b). GSC is the most important component, DC is converted into a grid connection, and MPPT feature is introduced. At the DC link, an essential function exists and the high-frequency dynamics are isolated. The PVSC is primarily managed by the MPPT feature in the multi-stage conversion systems to provide the highest level of solar power collections. One of the GSC's main control features is DC Connection Voltage Command. The multi-phase DC-link arrangement not only splits control functions into two different roles but also provides mobility to incorporate flexible DC / DC MPPT systems to improve (El Moursi et al., 2013) energy efficiency. Simplicity and good transfer performance have been shown by the one-stage control system.

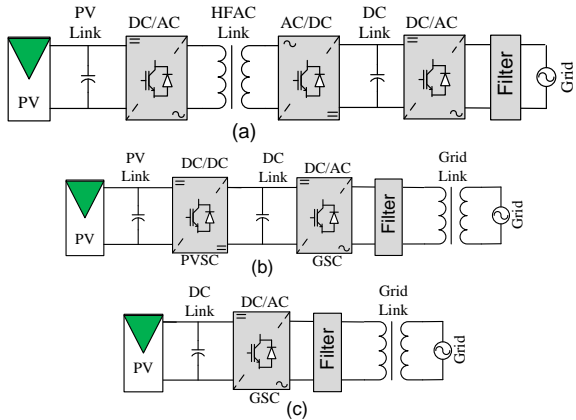


Figure 3.1: Centralised MPPT with galvanic isolation (a) three-stage (b) two-stage (c) single-stage

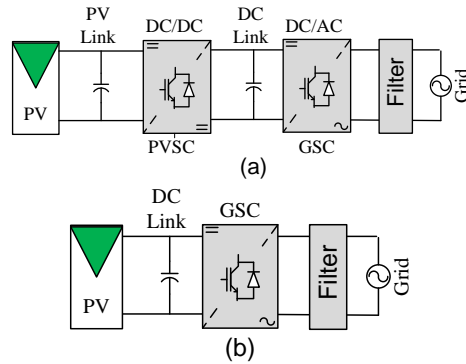


Figure 3.2: Centralised MPPT without galvanic isolation (a) two-stage (b) single-stage

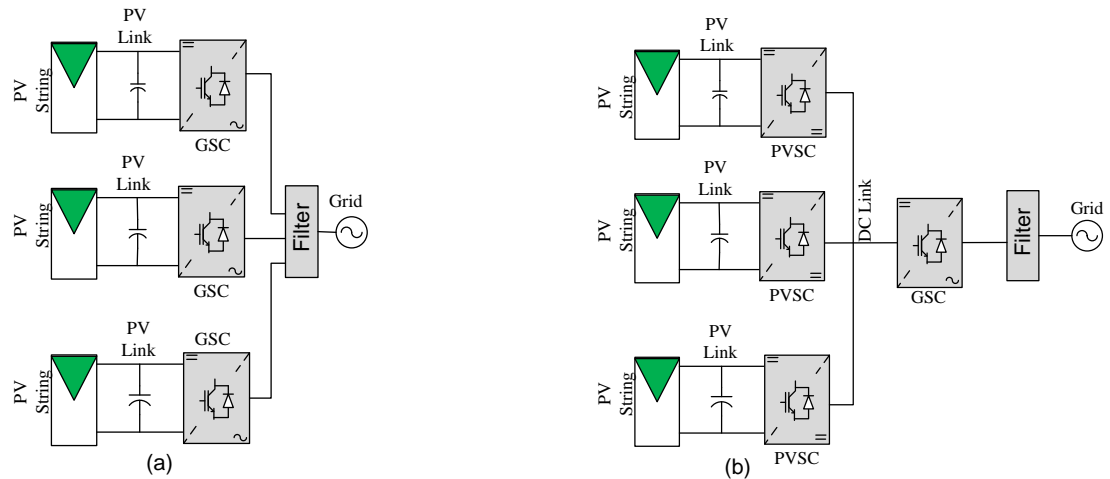


Figure 3.3: Distributed MPPT at PV string level (a) parallel inverter (b) parallel converter operation

3.4 Distributed MPPT Systems

3.4.1 String Level

DMPPT received substantial interest in work to address the problem of PV shortcomings (Femia et al., 2008). In commercial PV inverter products, it has been widely used at string level. For DC microgrid applications, the DMPPT approach has also been implemented. A PV array usually consists of several parallel strings. To prevent inconsistencies between strings, the idea of string inverter was added. Like CMPPT, the DC / AC grid module is graded instead of the whole PV range and it is attached to the individual PV lines. As shown in Figure 3.3(a), which displays multiple PV links, the Solar energy are gathered through string inverters and provided with an

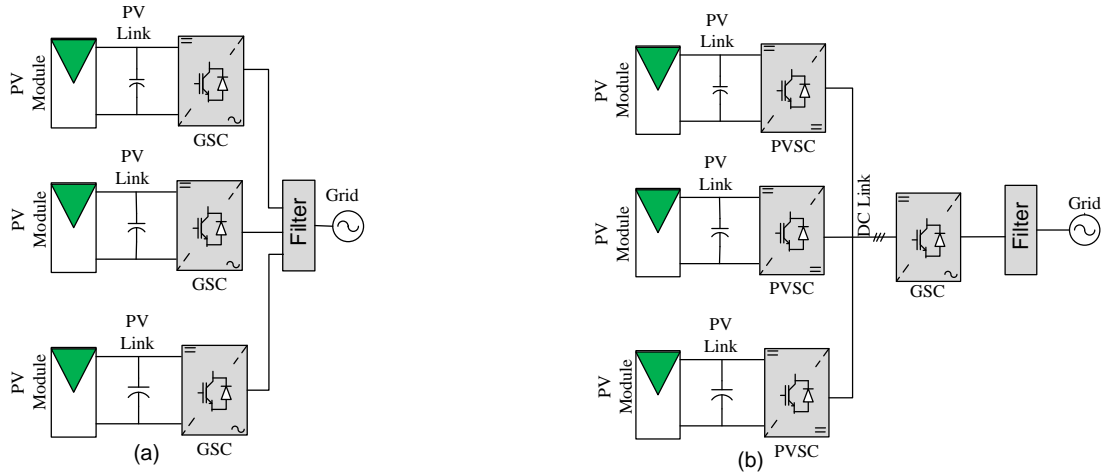


Figure 3.4: Configurations of (a) MIPI (b) MIPC for grid interconnections

AC connection. The grid link consists of a number of AC filters required to ensure the quality of the injection power. Another example of a grid-connected system with three distributed maximum point trackers at string level is figure 3.3 (b). A separate DC / DC converter is used to modulate the output of each string and to control it for MPPT. This way, the power degradation caused by a mismatching effect at string level is reduced to a minimum, since the power of each PV string is individually extracted and processed. The DC / DC and DC / AC converters may be either independent units or integrated into the same box with the DC / AC inverter. The power of each PV string can be extracted and processed. The DC / DC and DC / AC converter is also possible. Some commercial systems inside combine the DC / DC units for independent MPPT (Romero-Cadaval et al., 2013b) string levels.

3.4.2 Module Level

Module-integrated converters offer independent MPPT operations in each PV module that allow local optimization and decrease power losses due to partial shading and mismatches (Xiao et al., 2013).

3.4.2.1 Module-integrated parallel inverters

The module-integrated parallel inverter (MIPI) output terminals are connected to the AC network in parallel. As illustrated in Figure 3.4(a), each PV module is integrated and connected with a single MIPI.

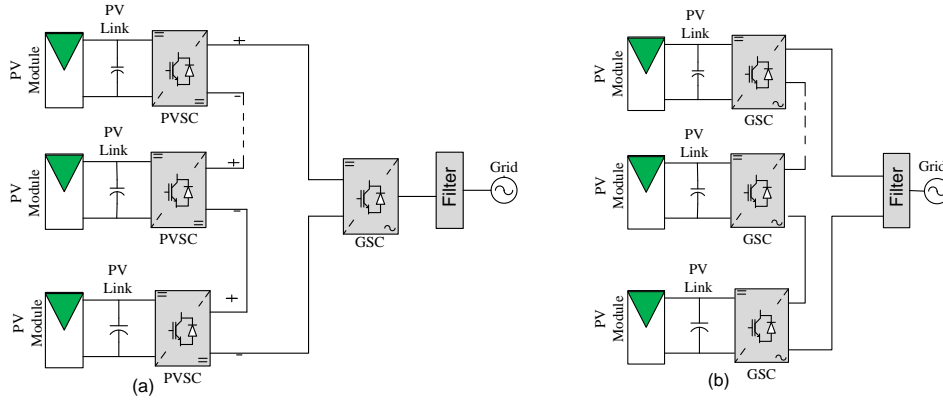


Figure 3.5: Configurations of (a) MISC (b) MISI for grid interconnections

3.4.2.2 Module-integrated Parallel Converters

Unlike MIPIs, MIPCs perform only DC / DC convert and integrate the PV modules into a common DC bus in parallel. PV modules are converted by MIPIs. As shown in figure 3.4(b), a DC bus may be linked to DC or AC grids by hierarchical DC / AC converters.

3.4.2.3 Module-integrated Series Converters

Module-integrated series (MISCs), also known as commercial power optimizers, are combined with MPPT and DC / DC conversion units. Unlike MIPC outputs, as shown in the figure 3.5(a), MISC output is serially connected to a DC string. In order to build a DC link which is used to create a DC micro grid or an AC grid via a centralized DC / AC inverter, the DC string can be connected parallel to other DC strands.

3.4.2.4 Module-integrated Series Inverters

Previously, a new design was introduced utilizing module-integrated inverter sequence (MISIs) (Jafarian et al., 2015). As shown in Figure 3.5 (b) this configuration can also be referred to as cascade AC modules, the output terminals of the MISI are attached to a stacked AC line.

3.4.3 Sub-module Level

PV sub-modules are not separate units, but are laminated panel parts. Laminated PV modules usually consist of 60 or 72 solar cells in 3 to 4 sub-modules. An illustration in which each sub-module consists of 24 serial PV cells with parallel linked bypass diodes is shown in Figure 3.6 (a). DMPPT offers better output than module-level approaches in reducing mismatches on the sub-module level. A sub-module usually has a voltage of less than 15V. The voltage level is compatible with the requirements of laptop and other mass-produced portable devices, and the components used to build sub-modulus converters are widely available.

3.4.3.1 Submodule-integrated Converters

In order to carry out MPPT and DC / DC conversion features as shown in Figure 3.6 (a) submodule-integrated converters (subMICs) are integrated in pv sub-modules. The output terminals of the subMICs are connected as a string in series that provides a grid integration voltage stack. The sub-MIC DC bus can be directly connected to the DC microgrid. SubMIC-based system control in 2 stages for AC network interconnections: transition to the DC / DC and conversion to the DC / AC. The recommended topology utilizes synchronous buck converters due to high performance and its broad conversion ranges to match the output currents between sub-MISCs.

3.4.4 Cell Level

In order to achieve MPPT at the PV cell level, an integrated power management architecture was suggested. The fully integrated circuit was claimed to completely eliminate partial shading difficulties Shawky et al. (2014). Figure 3.6(b) shows the cell-level DMPPT implementation. The synchronous boost converters are used in the system topology. The frequency is set to 500 kHz to reduce the size. The solution seems to be ideal for bringing the MPP operation down to the micro-level but disadvantages are caused by the cost and complexity of the systems, due to a large number of converter units. In addition, a high-efficiency boost converter is difficult to design for high input current and low input voltages of typical PV cells.

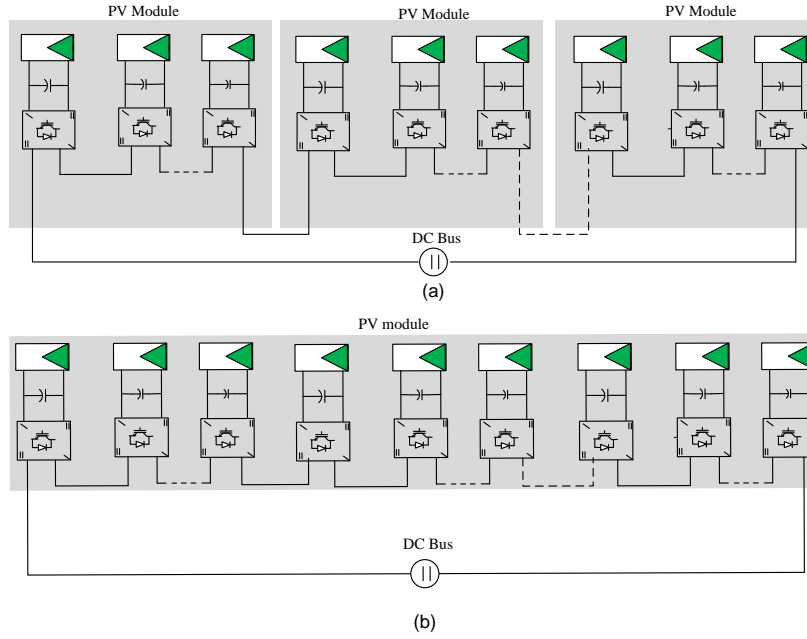


Figure 3.6: Series configurations of (a) submodule-integrated (b) cell-integrated series converters to form a DC link

3.4.5 Ideal and Complete single Diode PV Models

This section establishes various SPV circuit models available in literature and are broadly classified into : (a) Ideal single diode PV model (ISPV). (b) ISPV with shunt resistance (ISPV-1). (c) ISPV with series resistance (ISPV-2). (d) Complete single diode PV model (CSPV).

3.4.6 ISPV Parameterization

By applying Kirchoff's current law (KCL) for the ISPV circuit shown in Fig. 3.7(a), $V - I$ characteristic equation is given by,

$$i_{pv} - i_{ph} + i_s \left(e^{\frac{qv_{pv}}{kT_c A}} - 1 \right) = 0 \quad (3.1)$$

where i_s and A are the two unknown parameters that are computed using the DP

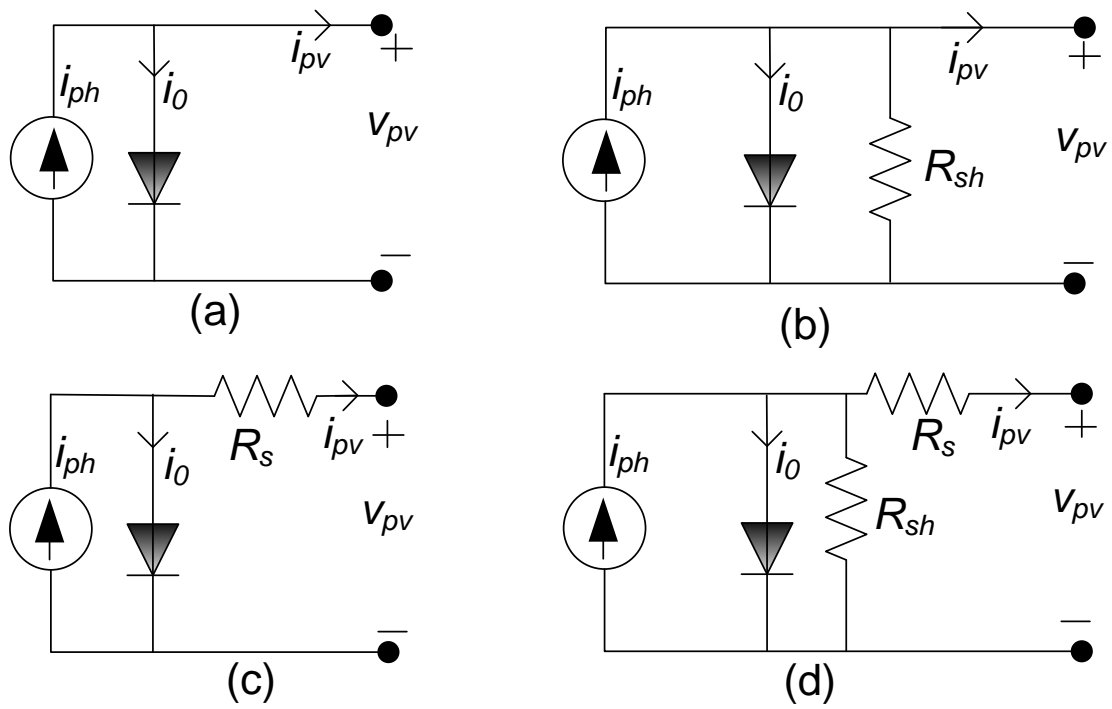


Figure 3.7: Equivalent circuit of PV models (a) ISPV (b) ISPV-1 (c) ISPV-2 (d) CSPV

values. Under short-circuit ($I_{sc}, 0$) and open-circuit condition ($0, V_{oc}$), from Eq. (3.1),

$$\begin{aligned} i_{ph} &= I_{sc} \\ i_{ph} &= i_s \left(e^{\frac{qV_{oc}}{kT_c A}} - 1 \right) \end{aligned} \quad (3.2)$$

The combined equation at extreme points and equation at MPP are given by,

$$I_{sc} - i_s \left(e^{\frac{qV_{oc}}{kT_c A}} - 1 \right) = 0 \quad (3.3)$$

$$I_{sc} - i_s \left(e^{\frac{qV_m}{kT_c A}} - 1 \right) - I_m = 0 \quad (3.4)$$

Diode thermal voltage V_t is given by,

$$V_t = \frac{kT_c}{q} \quad (3.5)$$

From Eq.3.3 and Eq. 3.4, the system matrix is given by,

$$F(x_p) = \begin{bmatrix} I_{sc} - i_s(p) (e^{\psi_{oc}} - 1) \\ I_{sc} - i_s(p) (e^{\psi_m} - 1) - I_m \end{bmatrix} \quad (3.6)$$

The Jacobian matrix $J_F(x_p)$ is derived from Eq. 3.6 is given by,

$$J_F(x_p) = \begin{bmatrix} e^{\psi_{oc}} - 1 & \frac{i_s(p)\psi_{oc}}{A(p)} e^{\psi_{oc}} \\ e^{\psi_m} - 1 & \frac{i_s(p)\psi_m}{A(p)} e^{\psi_m} \end{bmatrix} \quad (3.7)$$

where $F(x_p)$ is the system matrix to be solved, $J_F(x_p)$ is the jacobian matrix, $\psi_{oc} = \frac{V_{oc}}{V_t A(p)}$, $\psi_m = \frac{V_m}{V_t A(p)}$ and $x_p = [i_s(p) \ A(p)]^T$ are the state variables. It can be inferred from Eq. (3.6) that the value of A chosen greatly affects the convergence since it present in exponential term. This entails that a random initial guess may cause the newton method fail to converge necessitating a sufficiently close initial guess. A summery of fast convergent third order Newton type method for n-dimensional problems is discussed in Darvishi and Barati (2007).

$$\begin{aligned} \Delta x_{p+1} &= -J_F(x_p)^{-1}(F(x_p) + F(x_{p+1})) \\ x_{p+1} &= x_p + \Delta x_{p+1} \end{aligned} \quad (3.8)$$

where x_{p+1} and x_p are the solutions after $p + 1$ and p iterations.

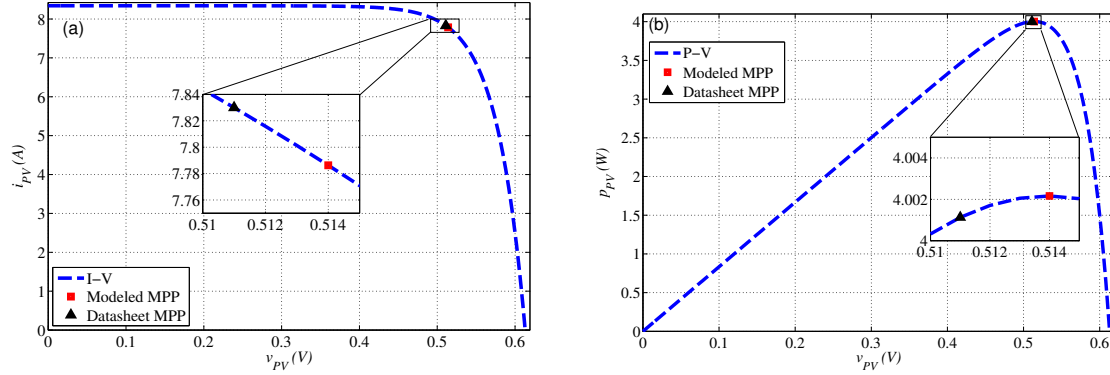


Figure 3.8: (a) $I - V$ curve (b) $P - V$ curve of PV cell under constant irradiation (1000 W/m^2) and standard test conditions (STC) for ISPV

Figure 3.8 depicts the predicted $I - V$ and $P - V$ curves based on ISPV for Q6LPT3-G2 multi-crystalline PV cell ($V_{oc} = 0.613 \text{ V}$; $I_{sc} = 8.34 \text{ A}$; $V_m = 0.511 \text{ V}$; $I_m = 7.83 \text{ A}$). The estimated parameters are: $i_s = 4.2434 \times 10^{-7} \text{ A}$ and $A = 1.42016$. Following the IV curve, as shown in Figure 3.8 (a), the MPP is identified (0.514 V, 7.786 A). The deviation in the MPP between the simulation and DP is highlighted and the same is shown in Figure 3.8. It is obvious that the ISPV exhibits inadequate accuracy due to its inability in satisfying all equations.

3.4.7 ISPV-1 Parameterization

Figure 3.7(b) shows the modified ISPV which includes R_{sh} and is referred as ISPV-1. By applying KCL for the ISPV-1 its $V - I$ equation is given by,

$$i_{pv} - i_{ph} + i_s \left(e^{\frac{v_{pv}}{V_t A}} - 1 \right) + \frac{V_{pv}}{R_{sh}} = 0 \quad (3.9)$$

where i_s , R_{sh} and A are the three unknown parameters. As a result, following equations are formulated :

$$\begin{aligned} i_{ph} &= I_{sc} \\ i_{ph} &= i_s \left(e^{\frac{V_{oc}}{V_t A}} - 1 \right) + \frac{V_{oc}}{R_{sh}} \end{aligned} \quad (3.10)$$

The combined equation at extreme points and MPP are given by,

$$I_{sc} - i_s \left(e^{\frac{V_{oc}}{V_t A}} - 1 \right) - \frac{V_{oc}}{R_{sh}} = 0 \quad (3.11)$$

$$I_{sc} - i_s \left(e^{\frac{V_m}{V_t A}} - 1 \right) - \frac{V_m}{R_{sh}} - I_m = 0 \quad (3.12)$$

Further the zero rate of change of power at MPP is given by,

$$p_{pv} = v_{pv} i_{pv} = v_{pv} i_{sc} - v_{pv} i_s \left(e^{\frac{v_{pv}}{V_t A}} - 1 \right) - \frac{v_{pv}^2}{R_{sh}} \quad (3.13)$$

$$\left. \frac{dp_{pv}}{dv_{pv}} \right|_{(V_m, I_m)} = 0 = I_{sc} - i_s \left[\left(1 + \frac{V_m}{V_t A} \right) e^{\frac{V_m}{V_t A}} - 1 \right] - \frac{2V_m}{R_{sh}}. \quad (3.14)$$

The overall system equations are given by,

$$F(x_p) = \begin{bmatrix} I_{sc} - i_s(p) [e^{\psi_{oc}} - 1] - \frac{V_{oc}}{R_{sh}(p)} \\ I_{sc} - i_s(p) [e^{\psi_m} - 1] - \frac{V_m}{R_{sh}(p)} - I_m \\ I_{sc} - i_s(p) [(1 + \psi_m) e^{\psi_m} - 1] - \frac{2V_m}{R_{sh}(p)} \end{bmatrix}. \quad (3.15)$$

where $x_p = [i_s(p) \ R_{sh}(p) \ A(p)]^T$ are the state variables. Further, the Jacobian matrix derived from system equations with respect to x_p and is given below.

$$J_F(x_p) = \begin{bmatrix} 1 - e^{\psi_{oc}} & \frac{V_{oc}}{R_{sh}^2} & \frac{I_s(p)\psi_{oc}}{A(p)} e^{\psi_{oc}} \\ 1 - e^{\psi_m} & \frac{V_m}{R_{sh}^2} & \frac{I_s(p)\psi_m}{A(p)} e^{\psi_m} \\ 1 - e^{\psi_m}(1 + \psi_m) & \frac{2V_m}{R_{sh}^2} & \frac{I_s(p)\psi_m}{A(p)} e^{\psi_m}(2 + \psi_m) \end{bmatrix} \quad (3.16)$$

Figure. 3.9 shows that the predicted $I - V$ and $P - V$ curves based on ISPV-1 for Q6LPT3-G2 multi-crystalline PV cell. The estimated parameters are: $i_s = 1.0189 \times 10^{-6} A$, $R_{sh} = -5.9337 \Omega$ and $A = 1.49715$. It is explicit that the negative value of R_{sh} indicates an unrealistic physical model. Thereby, proving that ISPV-1 is not appropriate in modeling the Q6LPT3-G2 multi-crystalline PV cell. The deviation in MPP between the simulation and DP is highlighted in Figure 3.9.

3.4.8 ISPV-2 Parameterization

Figure 3.7(c) shows a modified configuration of ISPV with a series resistance R_s and is referred to as ISPV-2. By applying KCL for the ISPV-2, following V-I equation is

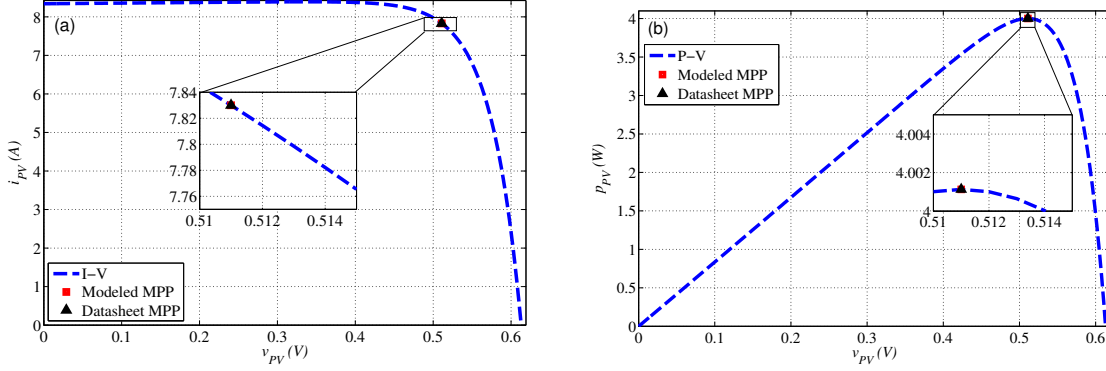


Figure 3.9: (a) $I - V$ curve (b) $P - V$ curve of PV cell under constant irradiation (1000 W/m^2) and STC for ISPV-1

obtained.

$$i_{\text{pv}} - i_{\text{ph}} + i_{\text{s}} \left(e^{\frac{(v_{\text{pv}} + i_{\text{pv}} R_{\text{s}})}{V_{\text{t}} A}} - 1 \right) = 0 \quad (3.17)$$

where i_{s} , i_{ph} , R_{s} and A are the four unknown parameters present in Eq. (3.17). As a result, minimum four equations are required to solve for the unknown parameters under given by,

$$i_{\text{ph}} - i_{\text{s}} \left(e^{\frac{I_{\text{sc}} R_{\text{s}}}{V_{\text{t}} A}} - 1 \right) - I_{\text{sc}} = 0 \quad (3.18)$$

$$i_{\text{ph}} - i_{\text{s}} \left(e^{\frac{V_{\text{oc}}}{V_{\text{t}} A}} - 1 \right) = 0 \quad (3.19)$$

$$i_{\text{ph}} - i_{\text{s}} \left(e^{\frac{(V_{\text{m}} + I_{\text{m}} R_{\text{s}})}{V_{\text{t}} A}} - 1 \right) - I_{\text{m}} = 0 \quad (3.20)$$

Further the rate of change of power with respect to PV voltage is as follows :

$$\begin{aligned} \frac{dp_{\text{pv}}}{dv_{\text{pv}}} &= i_{\text{pv}} + \frac{di_{\text{pv}}}{dv_{\text{pv}}} v_{\text{pv}} \\ di_{\text{pv}} &= df(i_{\text{pv}}, v_{\text{pv}}) = \frac{\delta f}{\delta i_{\text{pv}}} di_{\text{pv}} + \frac{\delta f}{\delta v_{\text{pv}}} dv_{\text{pv}}. \\ \frac{di_{\text{pv}}}{dv_{\text{pv}}} &= \frac{\frac{\delta f}{\delta v_{\text{pv}}}}{1 - \frac{\delta f}{\delta i_{\text{pv}}}} \end{aligned} \quad (3.21)$$

The equation pertaining to zero rate of change of power at MPP condition as derived from Eq. (3.21) is given by,

$$\left. \frac{dp_{\text{pv}}}{dv_{\text{pv}}} \right|_{(V_{\text{m}}, I_{\text{m}})} = 0 = I_{\text{m}} - \frac{I_{\text{s}} (V_{\text{m}} - I_{\text{m}} R_{\text{s}})}{V_{\text{t}} A} e^{\frac{V_{\text{m}} + I_{\text{m}} R_{\text{s}}}{V_{\text{t}} A}} \quad (3.22)$$

The complete set of system equations are as follows:

$$F(x_p) = \begin{bmatrix} i_{ph}(p) - i_s(p) (e^{\psi_{sc}} - 1) - I_{sc} \\ i_{ph}(p) - i_s(p) (e^{\psi_{oc}} - 1) \\ i_{ph}(p) - i_s(p) (e^{\psi_{mpp}} - 1) - I_m \\ I_m - \frac{I_s(V_m - I_m R_s)}{V_t A} e^{\psi_{mpp}} \end{bmatrix} \quad (3.23)$$

where

$$\begin{aligned} \psi_{sc} &= \frac{I_{sc} R_s(p)}{V_t A(p)} \\ \psi_{mpp} &= \frac{(V_m + I_m R_s(p))}{V_t A(p)} \\ \psi_d &= \frac{V_m - I_m R_s(p)}{V_t A(p)} \end{aligned} \quad (3.24)$$

$$J_F(x_p) = \begin{bmatrix} 1 & 1 - e^{\psi_{sc}} & -\frac{I_s(p)\psi_{sc}}{R_s(p)} e^{\psi_{sc}} & \frac{I_s(p)\psi_{sc}}{A(p)} e^{\psi_{sc}} \\ 1 & 1 - e^{\psi_{oc}} & 0 & \frac{I_s(p)\psi_{oc}}{A(p)} e^{\psi_{oc}} \\ 1 & 1 - e^{\psi_{mpp}} & -\frac{I_s(p)I_m}{V_t A(p)} e^{\psi_{mpp}} & \frac{I_s(p)\psi_{mpp}}{A(p)} e^{\psi_{mpp}} \\ 0 & -\psi_d e^{\psi_{mpp}} & J_{43} & J_{44} \end{bmatrix} \quad (3.25)$$

where

$$\begin{aligned} J_{43} &= \frac{I_m i_s(p)}{V_t A(p)} (1 - \psi_d) e^{\psi_{mpp}} \\ J_{44} &= \frac{i_s(p)}{A(p)} \psi_d (1 + \psi_{mpp}) e^{\psi_{mpp}} \end{aligned} \quad (3.26)$$

Fig. 3.10 shows the predicted $I - V$ and $P - V$ curves based on ISPV-2 for Q6LPT3-G2 multi-crystalline PV cell. The estimated parameters are: $i_{ph} \cong 8.34$, $i_s = 5.5806 \times 10^{-8} A$, $R_s = 1.403 \times 10^{-3} \Omega$ and $A = 1.26709$. A deviation in the MPP between the simulation and DP is highlighted in Fig. 3.10. From the result, it is inferred that the ISPV-2 satisfies all the boundary conditions and generates a positive series resistance.

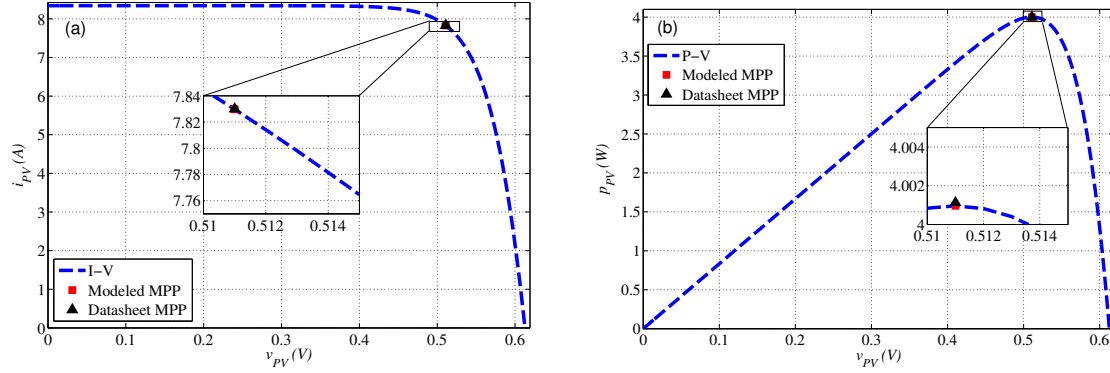


Figure 3.10: (a) $I - V$ curve (b) $P - V$ curve of PV cell under constant irradiation (1000 W/m^2) and STC for ISPV-2

3.4.9 CSPV Parameterization

Figure 3.7 (d) shows ISPV with R_s and R_{sh} and is referred to as CSPV. By applying KCL for the CSPV, its $V - I$ equation is given by,

$$i_{pv} - i_{ph} + i_s \left(e^{\frac{(v_{pv} + i_{pv}R_s)}{V_t A}} - 1 \right) + \frac{(v_{pv} + i_{pv}R_s)}{R_{sh}} = 0 \quad (3.27)$$

where i_s, i_{ph}, R_s, R_{sh} and A are the five unknown parameters. As a result, minimum five equations are required to solve for unknown parameters under the following operating points i.e., open circuit, maximum power point, and short circuit conditions.

$$i_{ph} - i_s \left(e^{\frac{I_{sc}R_s}{V_t A}} - 1 \right) - I_{sc} \left(1 + \frac{R_s}{R_{sh}} \right) = 0 \quad (3.28)$$

$$i_{ph} - i_s \left(e^{\frac{V_{oc}}{V_t A}} - 1 \right) - \frac{V_{oc}}{R_{sh}} = 0 \quad (3.29)$$

$$i_{ph} - i_s \left(e^{\frac{(V_m + I_m R_s)}{V_t A}} - 1 \right) - I_m - \frac{(V_m + I_m R_s)}{R_{sh}} = 0 \quad (3.30)$$

By evaluating Eq. (3.27) using Eq. (3.21) at MPP and short-circuit condition leads to Eq. (3.31) and Eq. (3.32) respectively.

$$\left. \frac{dp_{pv}}{dv_{pv}} \right|_{(V_m, I_m)} = 0 = I_m - \left(\frac{V_m - I_m R_s}{R_{sh}} \right) - \frac{I_s (V_m - I_m R_s)}{V_t A} e^{\frac{V_m + I_m R_s}{V_t A}} \quad (3.31)$$

$$\left. \frac{di_{pv}}{dv_{pv}} \right|_{(0, I_{sc})} = -\frac{1}{R_{sh}} = -\frac{\frac{1}{R_{sh}} + \frac{i_s}{V_t A} e^{\frac{i_{sc} R_s}{V_t A}}}{1 + \frac{R_s}{R_{sh}} + \frac{i_s R_s}{V_t A} e^{\frac{i_{sc} R_s}{V_t A}}} \quad (3.32)$$

Further simplifying Eq. (3.32) yields in,

$$R_s + \frac{i_s R_{sh}}{V_t A} e^{\frac{i_{sc} R_s}{V_t A}} (1 - R_{sh}) = 0 \quad (3.33)$$

The consolidated system equations are,

$$F(x_p) = \begin{bmatrix} i_{ph}(p) - i_s(p) (e^{\psi_{sc}} - 1) - I_{sc} \left(1 + \frac{R_s(p)}{R_{sh}(p)}\right) \\ i_{ph}(p) - i_s(p) (e^{\psi_{oc}} - 1) - \frac{V_{oc}}{R_{sh}(p)} \\ i_{ph}(p) - i_s(p) (e^{\psi_{mpp}} - 1) - I_m - \frac{\psi_p}{R_{sh}(p)} \\ I_m - \left(\frac{\psi_d V_t A}{R_{sh}(p)}\right) - i_s(p) \psi_d e^{\psi_{mpp}} \\ R_s + i_s(p) \psi_{sh} e^{\psi_{sc}} \end{bmatrix} \quad (3.34)$$

where

$$\begin{aligned} \psi_{sh} &= \frac{R_{sh}}{V_t A} (1 - R_{sh}) \\ \psi_p &= V_m + I_m R_s(p) \end{aligned} \quad (3.35)$$

and $x_p = [i_{ph}(p) \ i_s(p) \ R_s(p) \ R_{sh}(p) \ A(p)]^T$ are the state variables.

$$J_F(x_p) = \begin{bmatrix} 1 & 1 - e^{\psi_{sc}} & J_{13} & \frac{I_{sc} R_s}{R_{sh}^2} & \frac{i_s \psi_{sc}}{A} e^{\psi_{sc}} \\ 1 & 1 - e^{\psi_{oc}} & 0 & \frac{V_{oc}}{R_{sh}^2} & \frac{i_s \psi_{oc}}{A} e^{\psi_{oc}} \\ 1 & 1 - e^{\psi_{mpp}} & J_{33} & \frac{\psi_p}{R_{sh}^2} & J_{35} \\ 0 & -\psi_d e^{\psi_{mpp}} & J_{43} & \frac{\psi_d V_t A(p)}{R_{sh}^2} & J_{45} \\ 0 & -\psi_{sh} e^{\psi_{sc}} & J_{53} & J_{54} & J_{55} \end{bmatrix} \quad (3.36)$$

where

$$\begin{aligned} J_{13} &= -\frac{I_{sc}}{R_{sh}} - \frac{i_s(p) \psi_{sc}}{R_s} e^{\psi_{sc}} \\ J_{33} &= -\frac{I_m}{R_{sh}} - \frac{i_s(p) I_m}{V_t A(p)} e^{\psi_{mpp}} \\ J_{35} &= \frac{i_s \psi_{mpp}}{A} e^{\psi_{mpp}} \end{aligned} \quad (3.37)$$

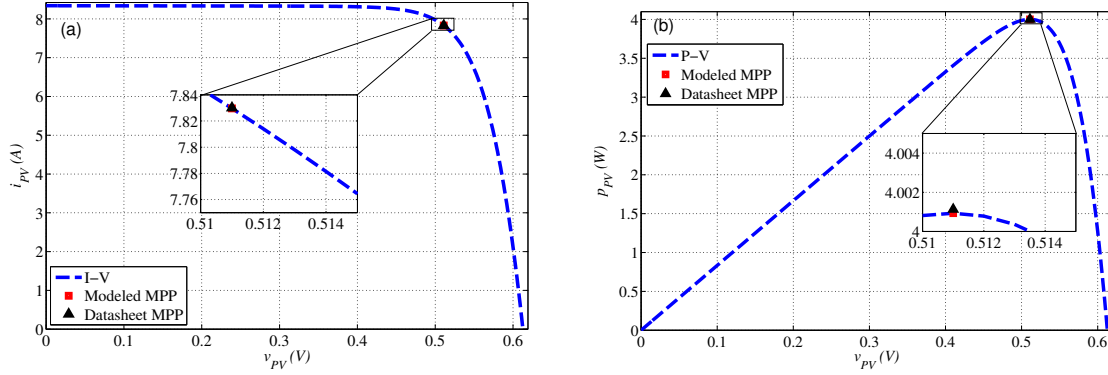


Figure 3.11: (a) $I - V$ curve (b) $P - V$ curve of PV cell under constant irradiation (1000 W/m^2) and STC for CSPV

$$\begin{aligned}
 J_{43} &= \frac{I_m}{R_{sh}} + \frac{i_s(p)I_m}{V_t A(p)} (1 - \psi_d) e^{\psi_{mpp}} \\
 J_{45} &= \frac{i_s(p)\psi_d}{A(p)} (1 + \psi_{mpp}) e^{\psi_{mpp}} \\
 J_{53} &= 1 - \frac{i_s I_{sc} \psi_{sh}}{V_t A(p)} e^{\psi_{sc}} \\
 J_{54} &= \frac{i_s (1 - 2R_{sh})}{V_t A(p)} e^{\psi_{sc}} \\
 J_{55} &= -\frac{i_s \psi_{sh}}{A} e^{\psi_{sc}} (1 + \psi_{sc})
 \end{aligned} \tag{3.38}$$

Figure 3.11 shows that the predicted $I - V$ and $P - V$ curves based on CSPV for Q6LPT3-G2 multi-crystalline PV cell. The estimated parameters are: $i_{ph} \cong 8.34$, $i_s = 3.0177 \times 10^{-8} \text{ A}$, $R_s = 1.6584 \times 10^{-3} \Omega$, $R_{sh} = 33.9402 \Omega$ and $A = 1.22715$. A deviation in the MPP between the simulation and DP is highlighted in Figure 3.11. From the result, it is evident that CSPV satisfies all the boundary conditions with negligible deviation. Thus, CSPV qualifies a suitable circuit model for simulation studies.

3.5 System Performance Evaluation and Necessary Steps

3.5.1 Performance Indices

Following the systematic modelling of PV, it is essential to benchmark by comparing the simulated characteristics with that of DP. This task is accomplished by incorporating a few of the performance indices of two types. The first type helps in attesting the modelled PV performance in the absence of experimental data and are as follows:

$$\begin{aligned}
 D_{IV} &= \sqrt{\left(\frac{\tilde{I}_m - I_m}{I_m}\right)^2 + \left(\frac{\tilde{V}_m - V_m}{V_m}\right)^2} \\
 D_{PV} &= \sqrt{\left(\frac{\tilde{P}_m - P_m}{P_m}\right)^2 + \left(\frac{\tilde{V}_m - V_m}{V_m}\right)^2}
 \end{aligned} \tag{3.39}$$

With the availability of experimental data, a more realistic performance indices are formulated which are referred to as root-mean-square deviation (RMSD) and normalized RMSD (NRMSD). The RMSD is the difference in the experimentally measured $V - I$ and obtained outputs of the developed model as given in (3.40). Further, the NRMSD is obtained by normalizing the RMSD with the data points in DP.

$$\begin{aligned}
 I_{\text{RMSD}} &= \sqrt{\frac{\sum_{p=1}^N (\tilde{I}_{pv} - I_{pv})^2}{N}} \\
 I_{\text{NRMSD}} &= \frac{I_{\text{RMSD}}}{I_{sc}} \\
 P_{\text{RMSD}} &= \sqrt{\frac{\sum_{p=1}^N (\tilde{P}_{pv} - P_{pv})^2}{N}} \\
 P_{\text{NRMSD}} &= \frac{P_{\text{RMSD}}}{P_m}
 \end{aligned} \tag{3.40}$$

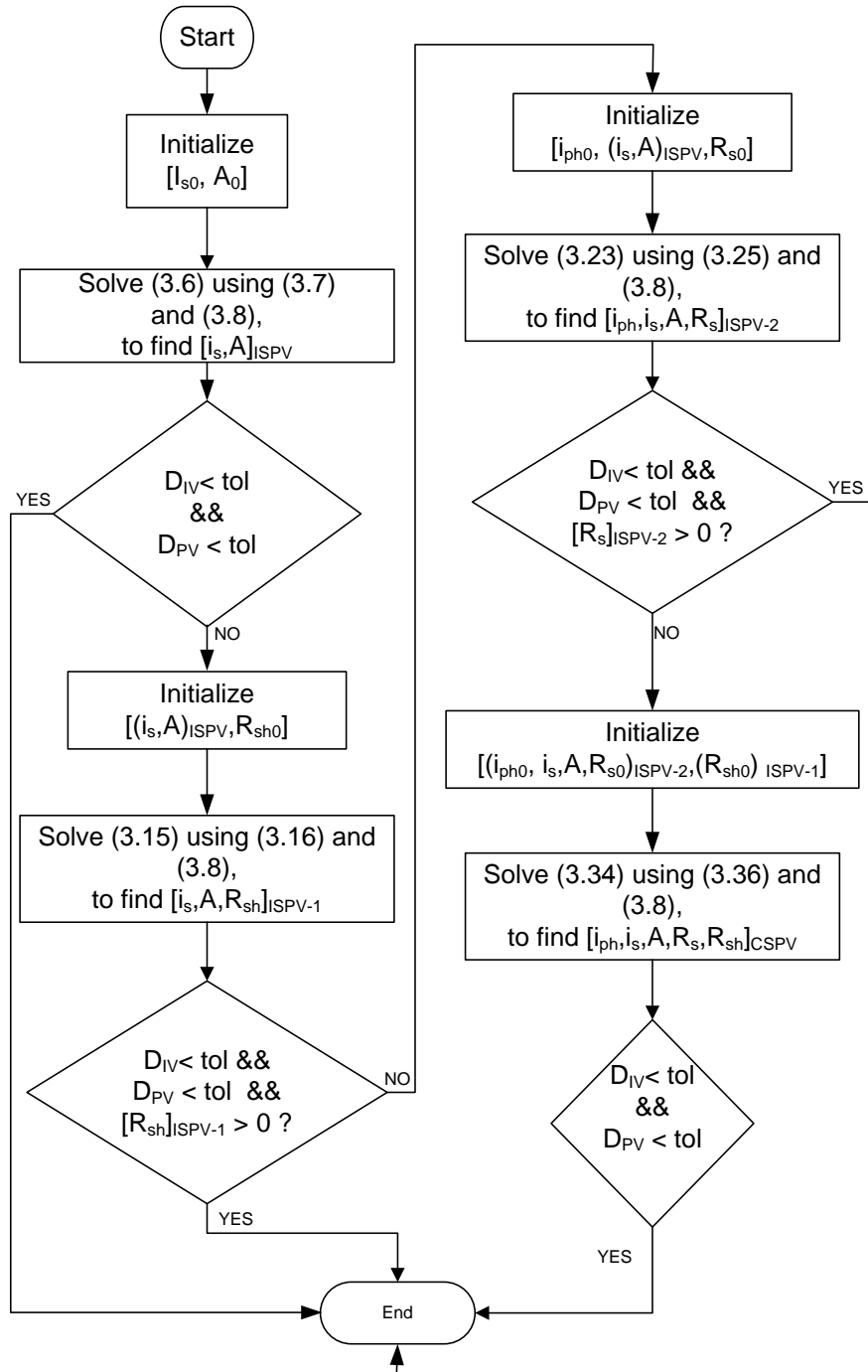


Figure 3.12: Flowchart of PV circuit model identification

Table 3.1: Comparison of Circuit Model Accuracy

PV Cell Model	Circuit Model	i_{ph} (A)	i_s (A)	A	$R_{sh}(\Omega)$	$R_s(\Omega)$	No.of Iterations	D_{IV}	D_{PV}
Q6LPT3-G2 multi-crystalline PV cell	ISPV	8.34	$4.24321e^{-07}$	1.42016	∞	0	5	0.0081	0.0059
	ISPV-1	8.34	$1.01893e^{-06}$	1.49715	-5.9338	0	7	$< 1e^{-16}$	$< 1e^{-16}$
	ISPV-2	$\cong 8.34$	$5.58062e^{-08}$	1.26709	∞	$1.4039e^{-03}$	5	$< 1e^{-5}$	$< 1e^{-5}$
	CSPV	$\cong 8.34$	$3.01771e^{-08}$	1.22715	33.9403	$1.6584e^{-03}$	7	$< 1e^{-6}$	$< 1e^{-6}$
	Newton Method	$\cong 8.34$	$1.94126e^{-08}$	1.2	20.1896	$1.8333e^{-03}$	9	$< 1e^{-5}$	$< 1e^{-5}$

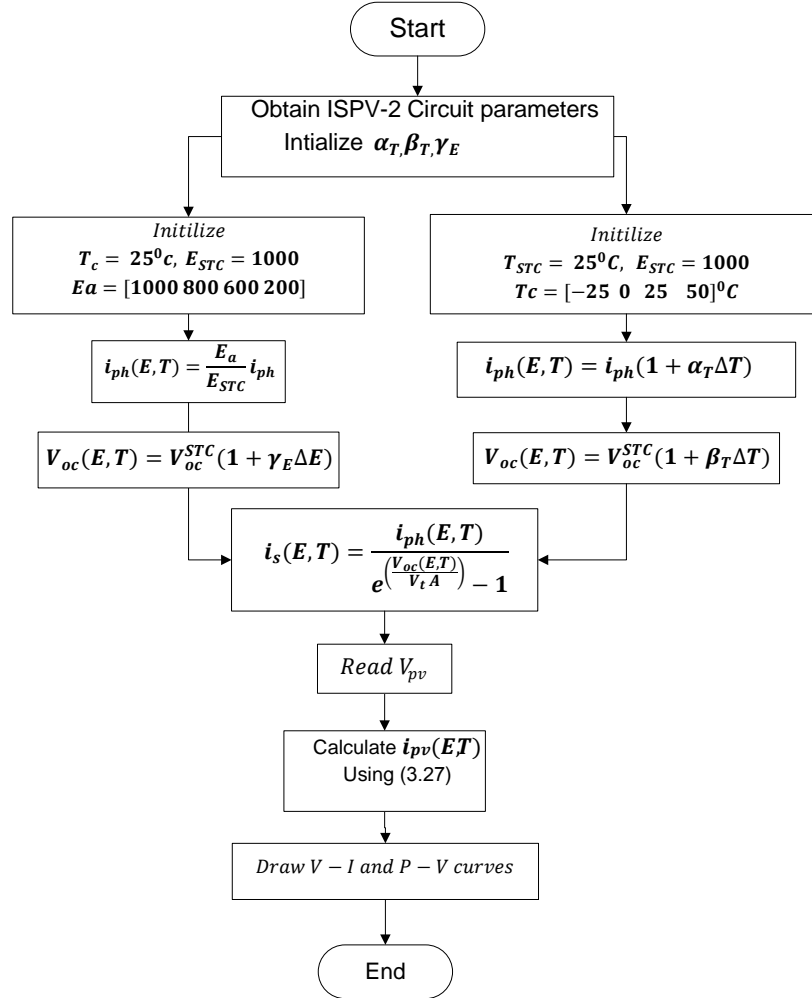


Figure 3.13: Flowchart of $I-V$ and $P-V$ curves plotting under varying environmental condition

3.5.2 Circuit Model Identification

The primary objective of this report was to investigate the accurate circuit model for Q6LPT3-G2 multi-crystalline PV cell. Performance indices aids in determining the accuracy and suitability of the developed model. An algorithm deliberating the essential steps to be followed in determining the best fitting circuit model shown in Figure 3.12. In a nutshell, first, the ISPV model, followed by ISPV-1 and ISPV-2 based modelling of Q6LPT3-G2 multi-crystalline is carried out. Following the observed setbacks like poor performance indices, unrealistic parametric value and computational complexity with the application of above modeling approaches, the CSPV is applied. The so obtained system parameters are tabulated in Table 3.1. It is evident from Table 3.1, that ISPV-2 and CSPV circuits are successful in capturing and exhibiting the simulated Q6LPT3-G2 multi-crystalline PV cell characteristics.

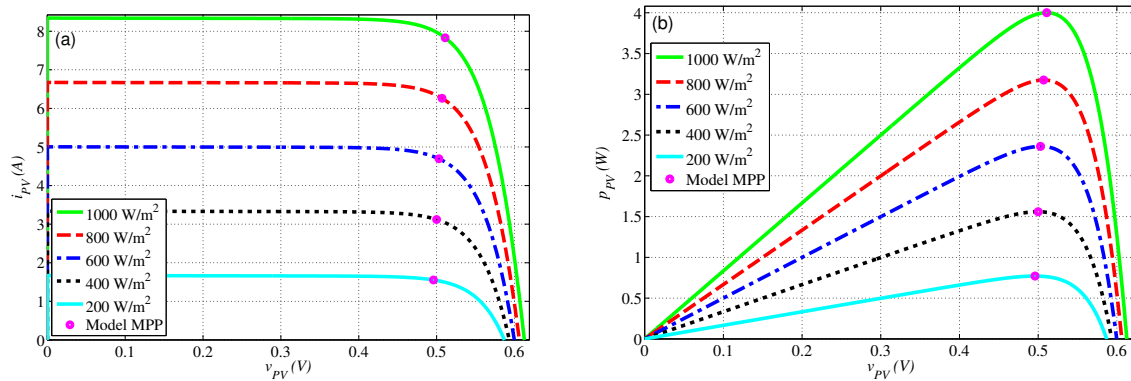


Figure 3.14: (a) $I - V$ curve (b) $P - V$ curve of PV cell under varying irradiance

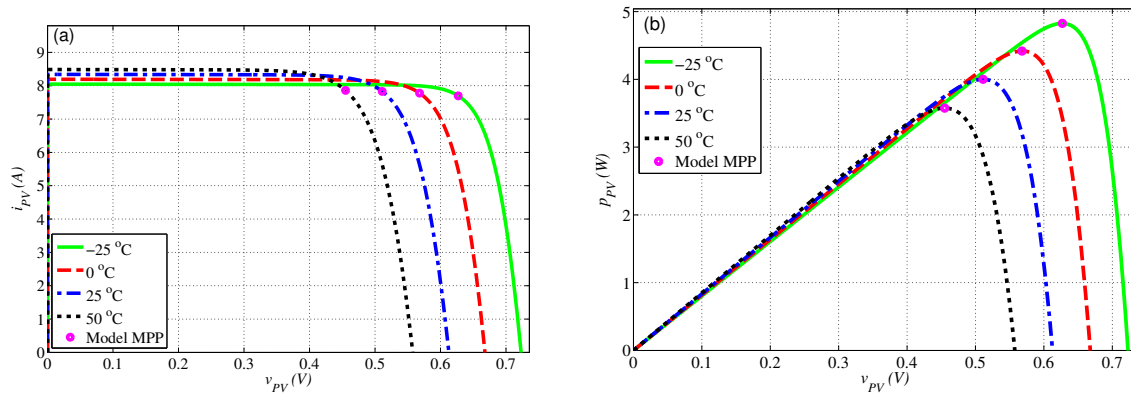


Figure 3.15: (a) $I - V$ curve (b) $P - V$ curve of PV cell under varying temperature

Finally, the $I - V$ and $P - V$ curves of Q6LPT3-G2 multi-crystalline cell under varying irradiation and temperature are depicted in Fig. 3.14 and Fig. 3.15 respectively. The estimated voltage and current at MPP under different environmental conditions are listed in Table 3.2. From the result plots a close agreement between the obtained curves and those in DP is witnessed.

Table 3.2: MPP under varying Environmental Conditions

Temperature ($^{\circ}C$)	Irradiance (kW/m^2)	V_{mpp}	I_{mpp}
25	1000	12.264	7.83
	800	12.168	6.26
	600	12.072	4.69
	400	12.000	3.12
	200	11.904	1.55
-25	1000	15.048	7.70
0		13.632	7.78
25		12.264	7.83
50		10.920	7.86

3.5.3 PV Converter

In this section synchronous buck converter (SBC) shown in Figure 3.16, is used due to its high efficiency for low voltage applications. It is important to design a topology that gives maximum power yield, without increasing the circuit complexity.

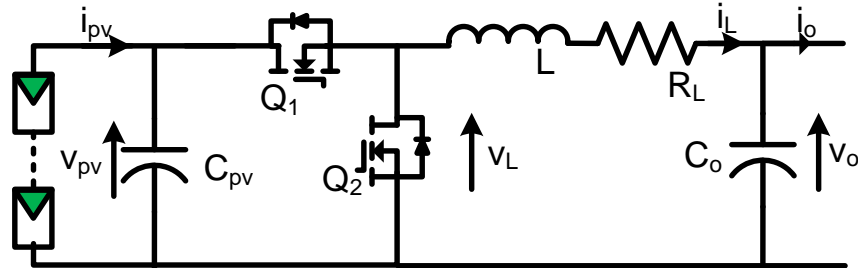


Figure 3.16: Synchronous buck converter (SBC)

When switch Q_1 is on and Q_2 is off the system dynamics can be represented as,

$$\begin{aligned} i_L &= \frac{1}{L} \int (v_{pv} - i_L R_L - V_o) dt \\ v_{pv} &= \frac{1}{C_{pv}} \int (i_{pv} - i_L) dt \\ v_o &= \frac{1}{C_o} \int (i_L - i_o) dt \end{aligned} \quad (3.41)$$

When switch Q_1 is off and Q_2 is on the system dynamics can be represented as,

$$\begin{aligned} i_L &= \frac{1}{L} \int (-i_L R_L - V_o) dt \\ v_{pv} &= \frac{1}{C_{pv}} \int (i_{pv}) dt \\ v_o &= \frac{1}{C_o} \int (i_L - i_o) dt \end{aligned} \quad (3.42)$$

By averaging approach (3.41) and (3.42) can be re written as,

$$\begin{aligned} i_L &= \frac{1}{L} \int (d_s v_{pv} - i_L R_L - V_o) dt \\ v_{pv} &= \frac{1}{C_{pv}} \int (i_{pv} - d_s i_L) dt \\ v_o &= \frac{1}{C_o} \int (i_L - i_o) dt \end{aligned} \quad (3.43)$$

State-space representation of SBC is shown in (3.44).

$$\frac{d}{dt} \begin{bmatrix} i_L \\ v_{pv} \end{bmatrix} = \begin{bmatrix} -\frac{R_L}{L} & \frac{d_s}{L} \\ -\frac{d_s}{C_{pv}} & \frac{1}{r_{pv} C_{pv}} \end{bmatrix} \begin{bmatrix} i_L \\ v_{pv} \end{bmatrix} + \begin{bmatrix} -\frac{1}{L} \\ 0 \end{bmatrix} V_o \quad (3.44)$$

$$\begin{cases} i_L = I_L + \hat{i}_L \\ v_{pv} = V_{pv} + \hat{v}_{pv} \\ i_{pv} = I_{pv} + \hat{i}_{pv} \\ d_s = D_s + \hat{d} \\ \hat{i}_{pv} = \frac{\hat{v}_{pv}}{r_{pv}} \end{cases} \quad (3.45)$$

Using (3.45) in (3.44), a small-signal model of SBC is designed and given in (3.46).

$$\left\{ \begin{array}{l} \frac{d}{dt} \begin{bmatrix} \hat{i}_L \\ \hat{v}_{pv} \end{bmatrix} = \begin{bmatrix} -\frac{R_L}{L} & \frac{D_s}{L} \\ -\frac{D_s}{C_{pv}} & \frac{1}{r_{pv}C_{pv}} \end{bmatrix} \begin{bmatrix} \hat{i}_L \\ \hat{v}_{pv} \end{bmatrix} + \begin{bmatrix} \frac{V_{pv}}{L} \\ -\frac{I_L}{C_{pv}} \end{bmatrix} \hat{d} \\ y = \begin{bmatrix} 0 & 1 \end{bmatrix} \begin{bmatrix} \hat{i}_L \\ \hat{v}_{pv} \end{bmatrix} \end{array} \right. \quad (3.46)$$

Controlling the PV voltage by varying the duty cycle in terms of small perturbations is derived as a transfer function model from state-space model given in (3.46).

$$G_o(s) = \frac{\hat{v}_{pv}(s)}{\hat{d}(s)} = \frac{K_o(b_o s + 1)}{s^2 + 2\zeta_o \omega_o s + \omega_o^2} \quad (3.47)$$

where

$$\left\{ \begin{array}{l} K_o = -\frac{(R_L I_L + V_{pv} D_s)}{L C_{pv}} \\ b_o = \frac{L I_L}{R_L I_L + V_{pv} D_s} \\ \omega_o = \sqrt{\frac{D_s^2}{L C_i} - \frac{R_L}{r_{pv} L C_{pv}}} \\ \zeta_o = \frac{1}{2} \frac{R_L r_{pv} C_{pv} - L}{\sqrt{r_{pv} L C_{pv} (D_s^2 r_{pv} - R_L)}} \end{array} \right. \quad (3.48)$$

3.6 QFT controller design application to PV

3.6.1 Selection of plant with parameter uncertainty

The inverse response transfer function model of PV with synchronous buck converter can be represented as uncertain system, variation of parameters are depends on the operating points (temperature and irradiation).

$$P_o(s) = \frac{\hat{v}_{pv}(s)}{\hat{d}(s)} = \frac{k \left(\frac{s}{z} + 1 \right)}{\left(\frac{s}{\omega_n} \right)^2 + \frac{2\xi}{\omega_n} s + 1} \quad (3.49)$$

Where the uncertainty of plant parameter is given by $-20 \leq k \leq -10$, $1500 \leq z \leq 8000$, $750 \leq \omega_n \leq 1200$, $0.1 \leq \xi \leq 0.5$. Nominal plant parameters $k_o = -17.64$, $z_o = 1705$, $\omega_{no} = 1000$, $\xi_o = 0.4$. The array of frequencies can be selected by inspection of the Bode diagram shown in Figure 3.17. In this case, we select an array of frequencies starting at 1 rad/s, ending at 1,00,000 rad/s, and adding some more frequencies to properly represent the slopes. the frequency vector $\omega = [1 \ 5 \ 10 \ 20 \ 50 \ 100 \ 300 \ 500 \ 1000 \ 2000 \ 5000 \ 10000 \ 20000 \ 30000 \ 50000 \ 70000 \ 100000]$ rad/s.

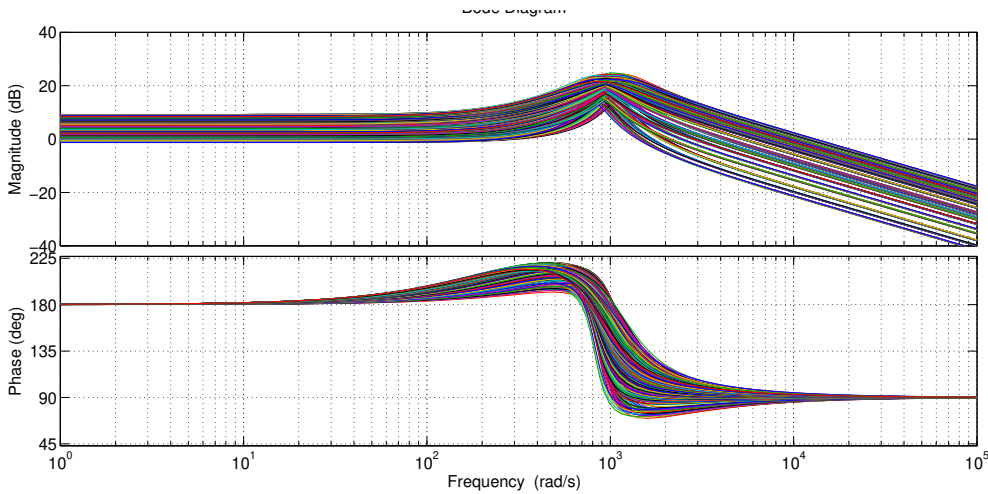


Figure 3.17: Bode diagram of uncertain plant

3.6.2 Template generation

Templates are the pictorial representation of the uncertain plant's magnitude and phase frequency response at fixed frequency. The sketch of the templates for shown in the Nichols chart in Figure 3.18. we can observe that the templates are just vertical

lines at low frequencies, become wider at middle frequencies, and finally collapse again into vertical lines at high frequencies.

3.6.3 Bounds computation

Edge point templates are used here to obtain QFT bounds. Stability margins and performance specifications are transformed to frequency domain to represent the QFT bounds. These QFT bounds are represented in Nichols chart. The computation of QFT bounds is done with quadratic inequalities. Closed loop robust stability margins are expressed as follows

$$\left| \frac{L_g}{1 + L_g} \right| \leq \gamma_1 \quad \forall P \in \{p\} \quad (3.50)$$

Usually $\gamma_1 = 1.8 = 5.1055$ dB then gain margin = 3.83771 and phase margin = 32.2552. The gain margin indicates the amount of gain can be increased and the phase margin indicates the requirement of phase lag to reach the stability limit. Stability specification should satisfy at each and every frequency point. transfer function of disturbance rejection at plant output is given by,

$$T_2(s) = \frac{0.001s}{0.001s + 1} \quad (3.51)$$

$\omega_d = [1 \ 5 \ 10 \ 20 \ 50 \ 100 \ 300 \ 500 \ 1000]$ rad/s. The upper and lower reference tracking bounds for the considered PV system are defined by

$$\begin{aligned} \gamma_{7U}(s) &= \frac{0.0005s + 1}{1.2967 \times 10^{-7}s^2 + 0.000648s + 1} \\ \gamma_{7L}(s) &= \frac{1}{1.1111 \times 10^{-5}s^2 + 0.0067s + 1} \end{aligned} \quad (3.52)$$

$\omega_{ref} = [1 \ 5 \ 10 \ 20 \ 50 \ 100 \ 300 \ 500 \ 1000 \ 2000]$ rad/s. By grouping all the stability and tracking bounds to calculate the worst case possibilities shown in Figure 3.23.

3.6.4 Loop shaping

Loop shaping is nothing but adding gain, zeros, and poles to the open loop system manually or automatically to satisfy the worst case specifications. Accordingly, we can design a controller in the frequency domain. Manual loop shaping is difficult for the beginners. So automatic controller design algorithms are interesting in real

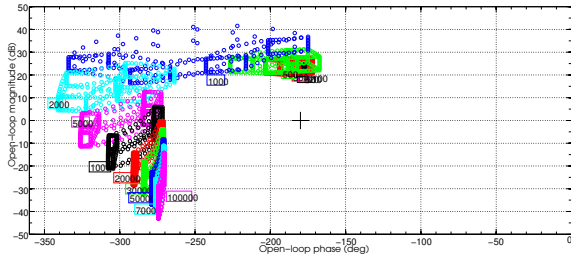


Figure 3.18: Uncertain plant templates

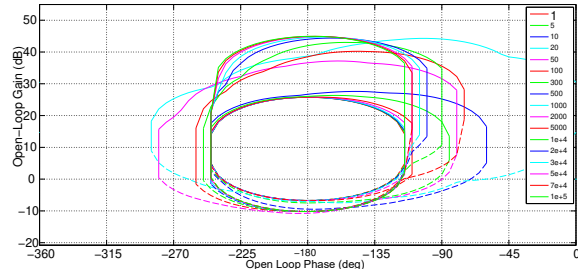


Figure 3.19: Robust stability bound

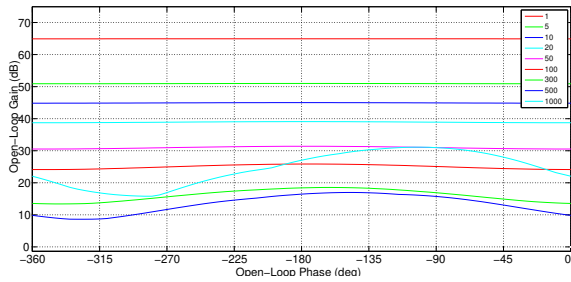


Figure 3.20: performance bound of disturbance rejection at plant output

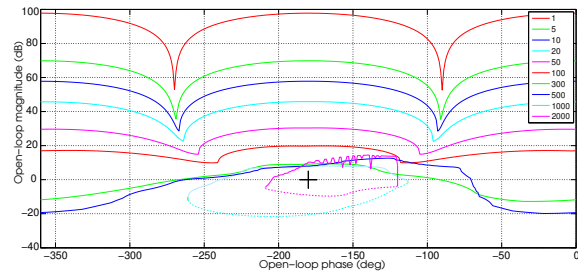


Figure 3.21: Reference tracking bounds

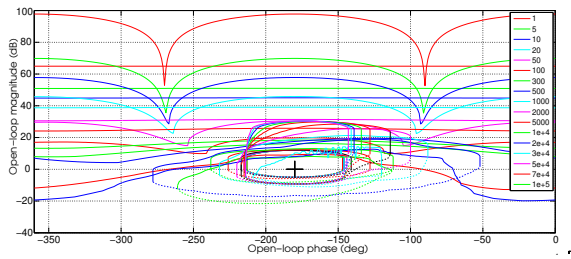


Figure 3.22: Superposition of bounds

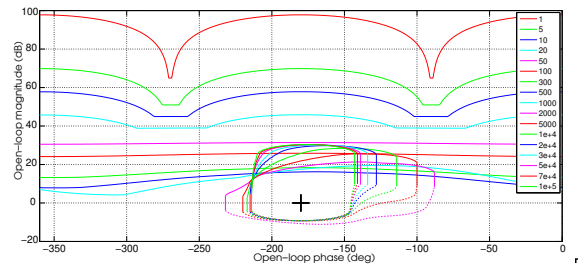


Figure 3.23: Intersection of bounds

world problems. The intersection of bounds or worst case bounds is significant for the design QFT robust controller. ALS methodology used to design GA based QFT robust controllers.

$$G(s) = \frac{-0.0004s^2 - 0.44s - 120}{0.0004348s^2 + s} \quad (3.53)$$

Locus of the closed loop transmission as nearer to the Universal bound is desired. From Figure 3.24 we can say that the open loop phase of $L_0(s)$ to the universal bound is closer at every frequency.

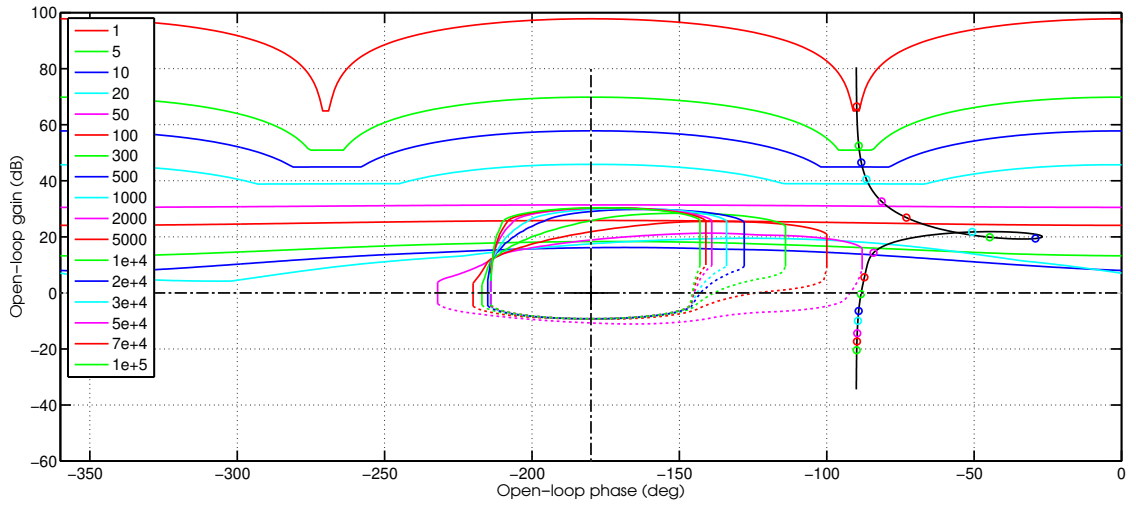


Figure 3.24: Automated loop-shaping

3.6.5 Pre-filter Design

Once the controller is designed the final task is to design pre-filter in two degrees of freedom control structure. Pre-filter designing or pre-filter shaping is same as loop shaping. The importance of pre-filter design is to track the desired output from the input. The plant with the designed pre-filter response may satisfy all the performance specifications and need not lie between the extreme limits of the frequency domain responses.

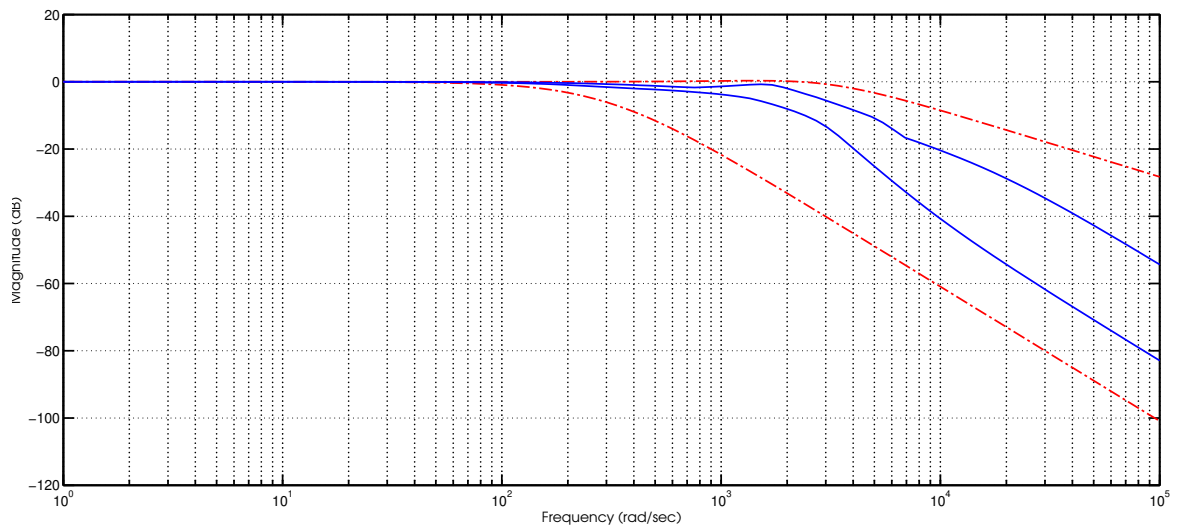


Figure 3.25: Reference tracking in frequency domain

Pre-filter designed for the above controllers is shown in (3.54).

$$F(s) = \frac{1}{0.0009091s + 1} \quad (3.54)$$

dashed red lines are the upper and lower reference tracking bounds defined in Equation (3.52). the solid blue lines are with in the bounds at every frequency response shown in Figure 3.25.

3.6.6 Validation

Once the design of the controller and pre-filter is finished, it will be convenient to analyze the performance of the complete control system under different scenarios. This includes frequency-domain analysis of each specification and for all the significant plants within the model uncertainty.

The analysis of the closed-loop stability in the frequency domain is shown in Figure 3.26. The dashed red line is the stability specification γ_1 , and the solid blue line represents the worst case of the function $PG/(1 + PG)$ at each frequency due to the model uncertainty. The control system meets the stability specification, as the solid line is below the dashed line γ_1 in all cases.

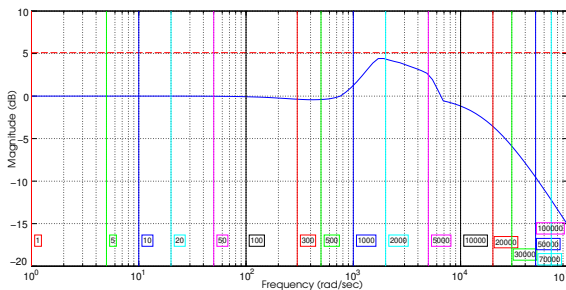


Figure 3.26: Stability margins

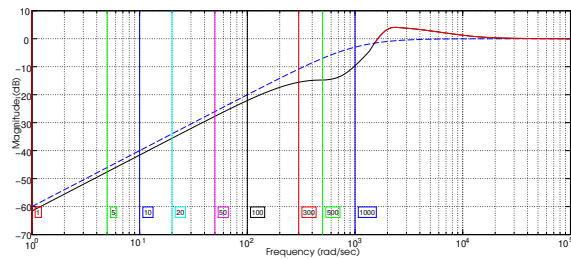


Figure 3.27: Disturbance rejection

The frequency-domain analysis of the disturbance rejection at the output of the plant specification, is shown in Figure 3.27. The dashed line is the sensitivity specification and the solid black line represents the worst case of the function $1/(1 + PG)$ at each frequency due to the model uncertainty. The control system meets the sensitivity specification in all cases, as the solid black line is below the dashed blue line from 0 to 1000 rad/s.

3.7 Simulation Results

The grid-tied PV systems configuration is shown in Figure3.28. In order to evaluate the effect of partial shadings, to explain new control policies, automate process setup and evaluation of system complexity, etc., subMIC-based systems modeling and simulation is required. In contrast, device outputs can also be tested with QFT dependent MPPT controllers by using MATLAB Simulation in the same conditions for shading, partial shading and non-shading.

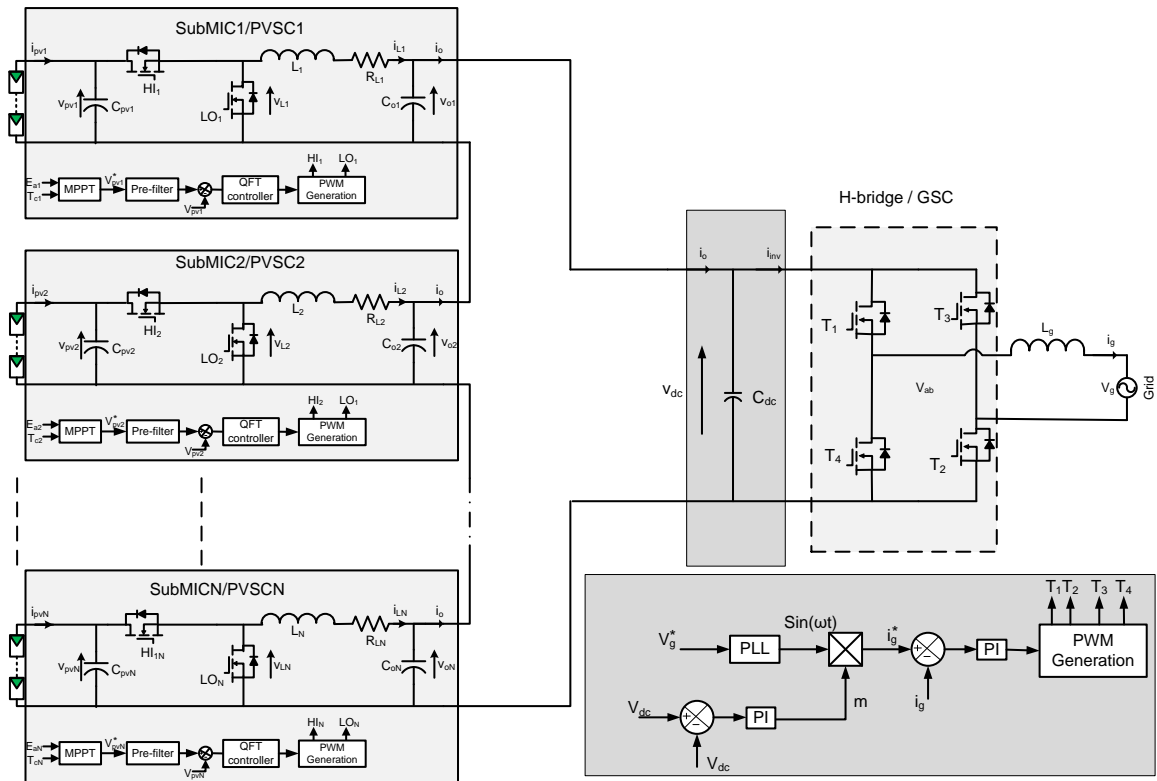


Figure 3.28: Block diagram of Submodule integrated grid connected PV system

3.7.1 Comparison of existing and proposed MPPT controllers simulation

The objective of this simulation is to show the advantage of the proposed controller over existing controller in terms of performance enhancement for grid connected PV system shown in Figure 3.30- 3.33. The Typical design simulates a down-scaled PV device with twelve subMIC’s. The simulation patterns of partial shading sequence, as

shown in Figure 3.29. Partially shaded sub-modules are 1, 2, and 3, while the other obtain standard radiation of $1 \text{ kW} / \text{m}^2$. The irradiation of sub-module 1 first reduces from 1 to $0.6 \text{ kW} / \text{m}^2$, which is then raised to $0.8 \text{ kW} / \text{m}^2$, $t= 0.3 \text{ s}$ and $t= 0.4 \text{ s}$ respectively as shown in Figure 3.29. The radiance falls from 0.8 to $0.6 \text{ kW} / \text{m}^2$ in sub-module 2 and then to $1 \text{ kW} / \text{m}^2$. The irradiance falls from $0.8 \text{ kW} / \text{m}^2$ to $0.6 \text{ kW} / \text{m}^2$ for sub-module 3.

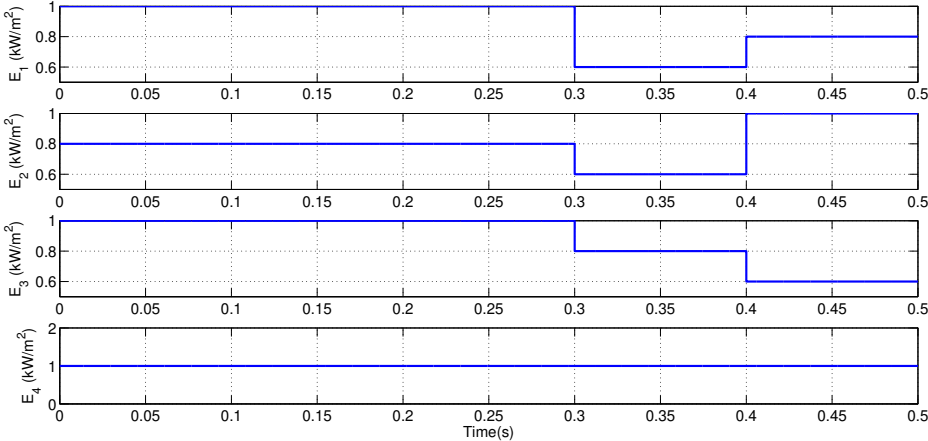


Figure 3.29: Simulated partial shading pattern

In Figures 3.30 and 3.31, they demonstrate the variations of the PV voltages and PV currents at PV sub-module level. EC and AQFT is the existing Q-parametrization controller and automated proposed QFT controller.

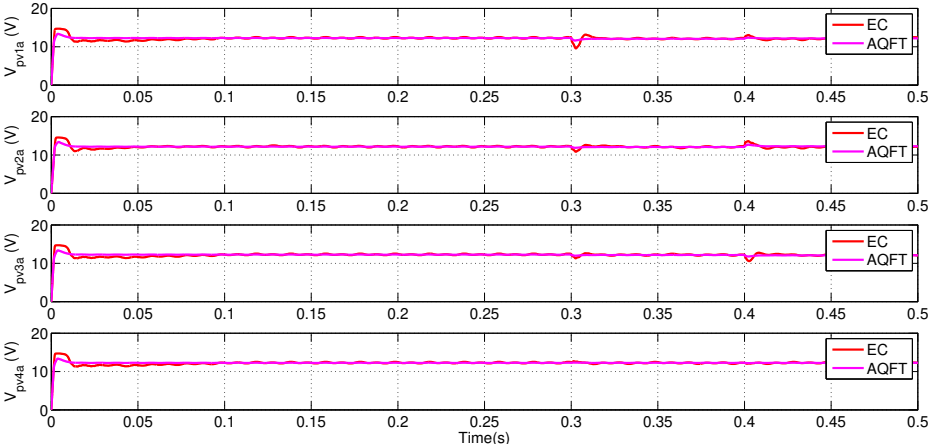


Figure 3.30: PV output voltage

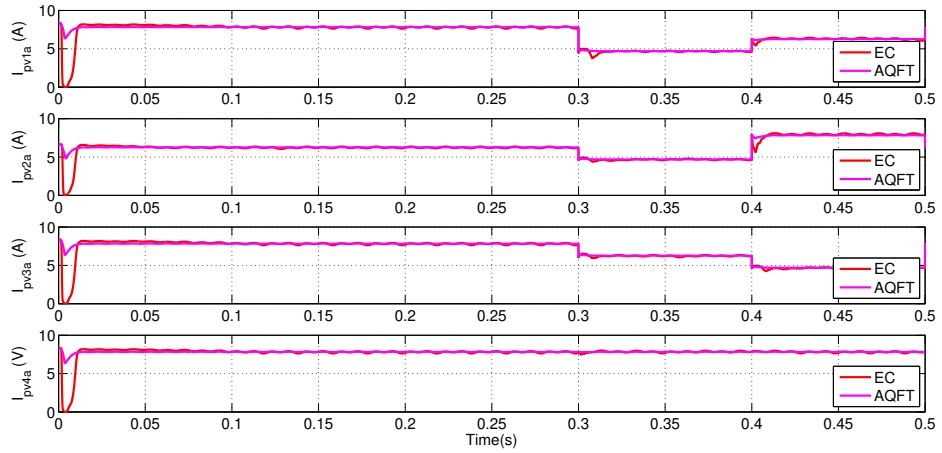


Figure 3.31: PV output current

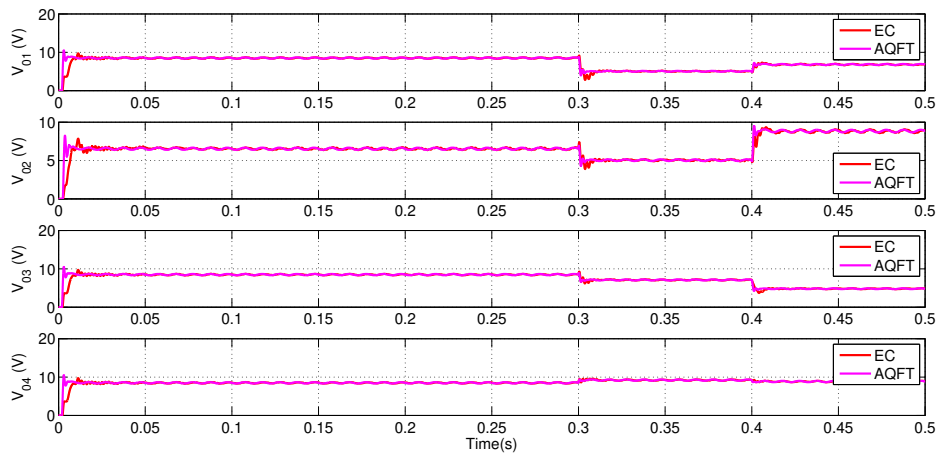


Figure 3.32: Output voltage of subMICs

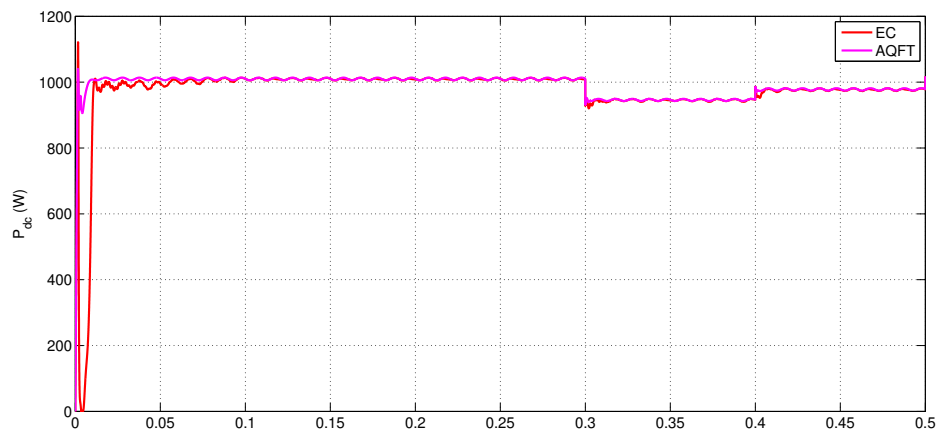


Figure 3.33: Total output power

Observations

The following drawbacks are observed in the existing controller.

1. ideal single diode model is considered, which is not efficient and accurate model.
2. Transient behaviour is observed in SMICs voltage and power during the partial shading conditions.
3. The steady state behaviour shows a decay at initial stage of the PV voltage.

Figure 3.34 displays the grid voltage waveforms V_g , grid current I_g , V_{dc} , and I_o , for the existing q-parametrization partial shading method.

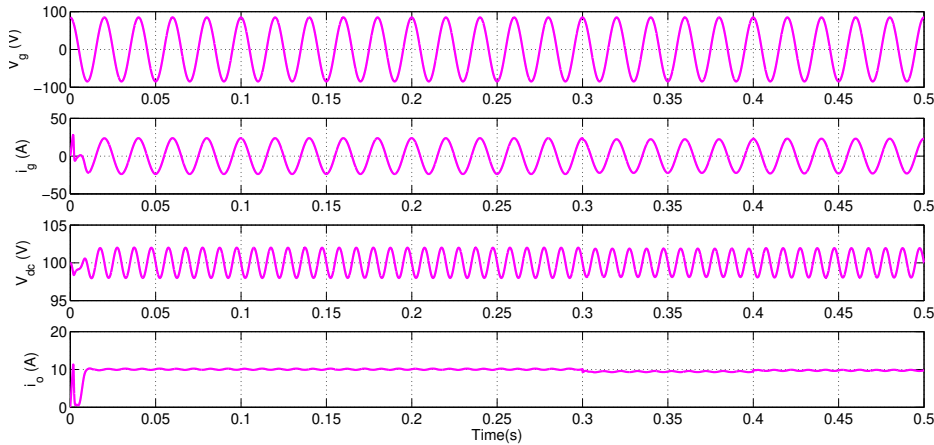


Figure 3.34: grid voltage V_g , grid current i_g , dc-link voltage V_{dc} , and output current of the string i_o

Accurate tracking of PV voltage under uniform or partial shading conditions and the above mentioned drawbacks can overcome with the proposed controller.

3.7.2 Comparison of switching and average model simulation with Proposed MPPT controller

Complete single diode circuit parameters are used to design PV system, the QFT based automated MPPT controller is used to extract maximum power under above mentioned partial shading pattern and obtained the results as shown in Figure 3.35-3.41.

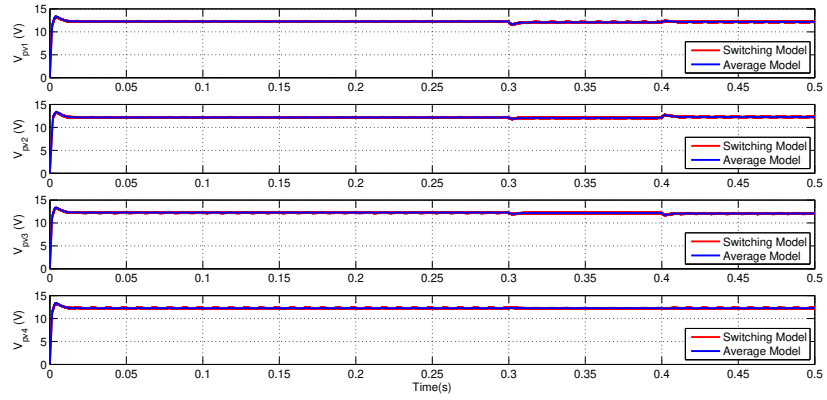


Figure 3.35: PV output voltage

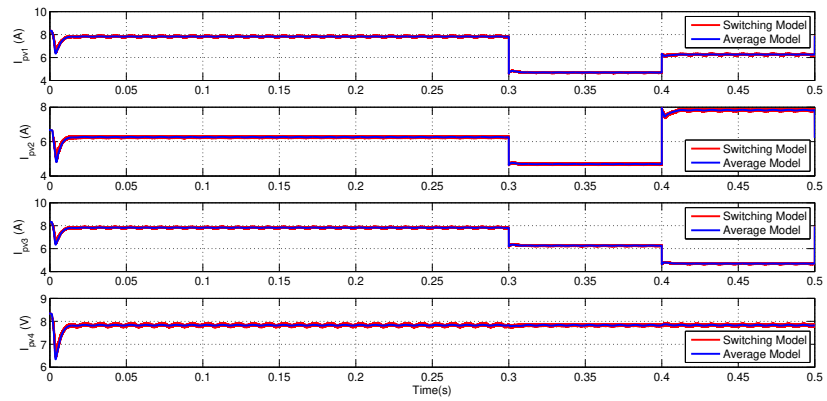


Figure 3.36: PV output current

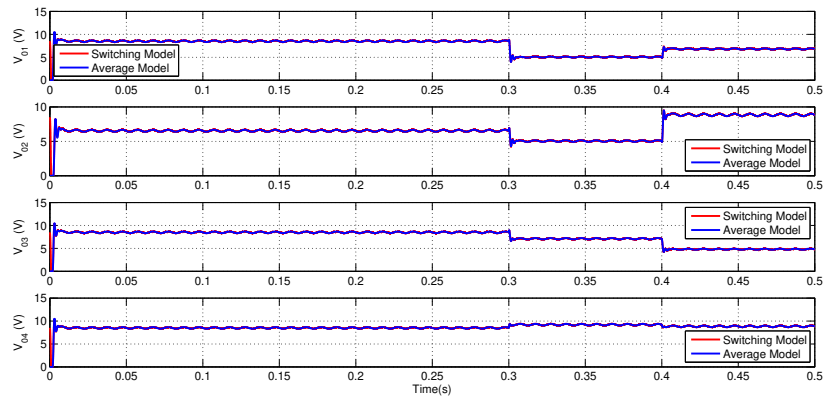


Figure 3.37: Output voltage of subMICs

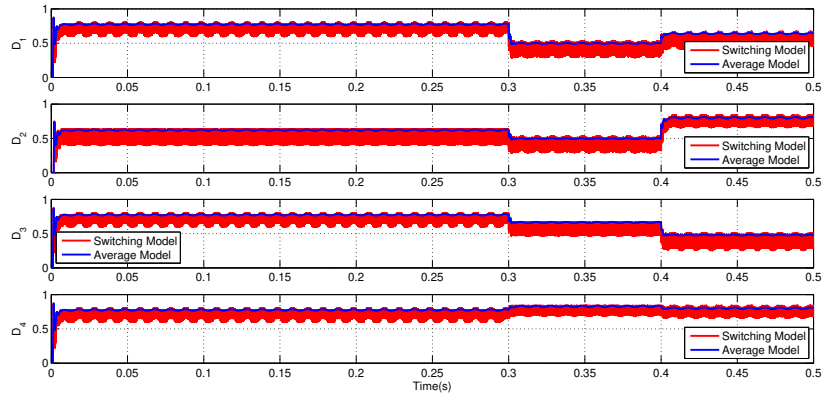


Figure 3.38: Duty cycle of subMIC

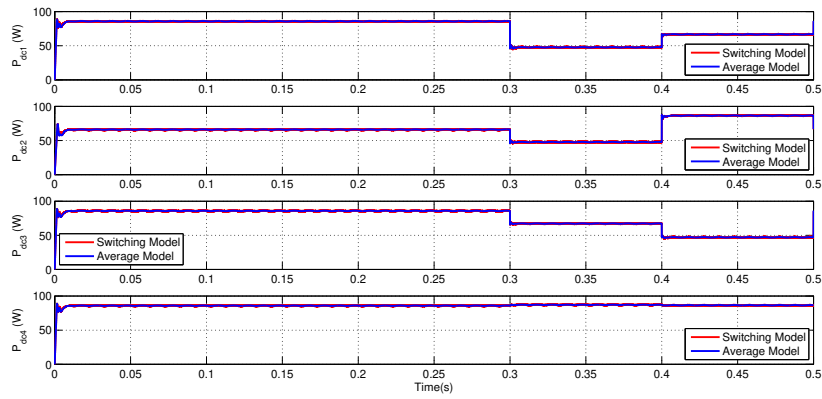


Figure 3.39: SubMICs output power

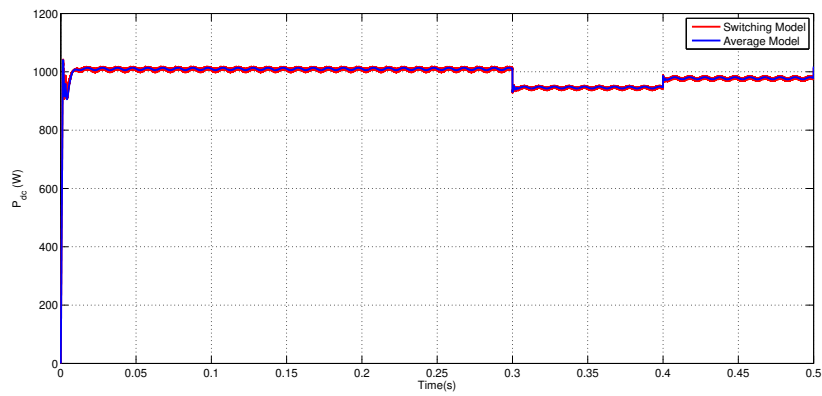


Figure 3.40: Total output power

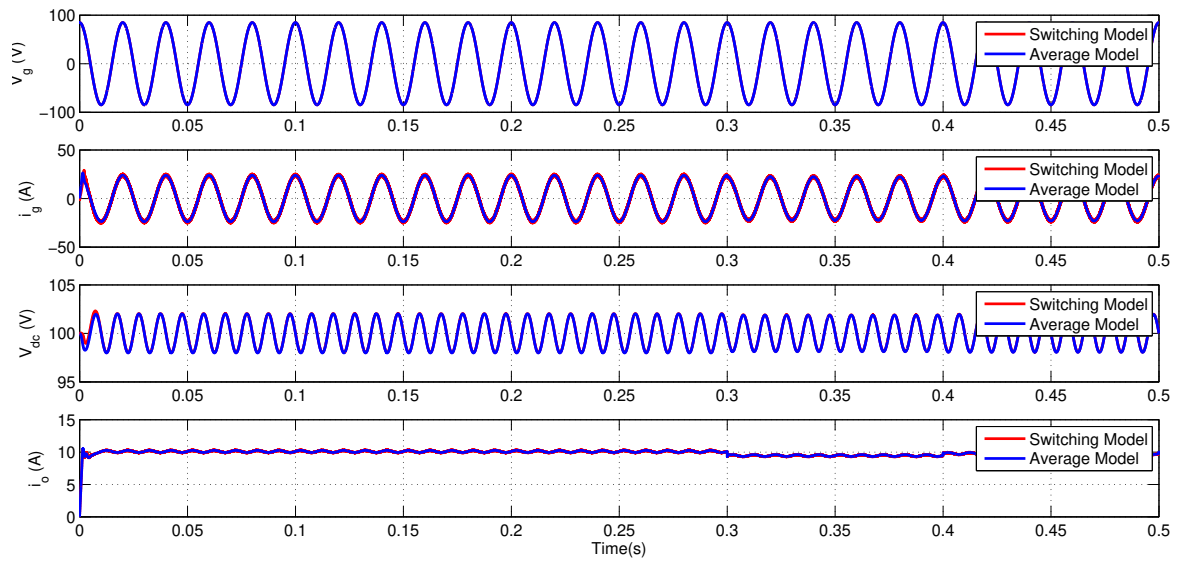


Figure 3.41: grid voltage V_g , grid current i_g , dc-link voltage V_{dc} , and output current of the string i_o

3.7.3 Real time environmental data (24-Hrs.)

Long-term simulations are significant to understand the real time operation of grid tied renewable energy system configurations. Large PV power system is considered to perform long term simulations, 45 SMICs for 45 PV sub-modules and grid connected inverter.

SMICs are connected in series to maintain the required DC-link voltage V_{dc} of 380 V and we can extract from each SMIC output power 85 W, so the total output power injecting in to the grid is 3.8 kW. 24-hour long term simulation is performed with the proposed QFT controller based MPPT model takes 24-hrs.for simulation which shows real time operation.

Real world irradiation and temperature data collected from National Renewable Energy Laboratory (NREL), location at Mangalore, Karnataka, India is shown in Figure 3.42 and Figure 3.43 respectively. In the present work the capability of the proposed CSPV model along with the QFT controller performance is verified. The simulation results are shown in Figure 3.44 to Figure 3.50. PV voltage is not accurately tracking by the existing controller (Khan and Xiao, 2016), but proposed controller can successfully tracked the reference PV voltage.

The efficacy of the proposed controller is evaluated by comparing with the existing Q-parametrization method based MPPT controller. The observed values are tabulated in Table 3.3, 10 W power difference in sub-module level and 480 W in the total output power is observed, which shown the effectiveness of the proposed method in terms of maximum power extraction under real time conditions.

$$\Delta P_{dcs} = P_{dcs,QFT} - P_{dcs,Q-parameterization} \quad (3.55)$$

$$\Delta P_{dc} = P_{dc,QFT} - P_{dc,Q-parameterization} \quad (3.56)$$

where P_{dcs} represents sub-module level output power and P_{dc} represents total output power. $P_{dcs,QFT}$ and $P_{dcs,Q-parameterization}$ represents the sub-module level power extracted from PV through proposed QFT controller and Q-parametrization controller respectively.

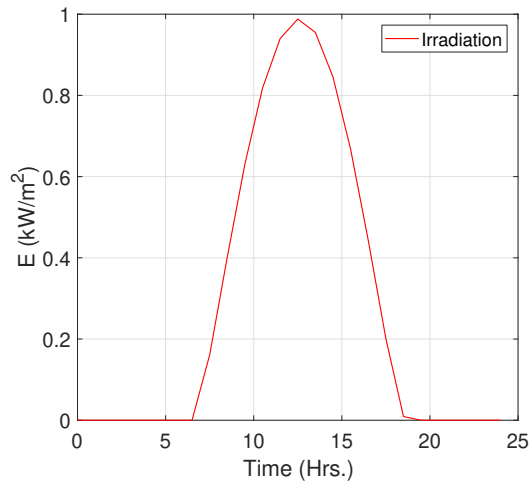


Figure 3.42: Irradiation

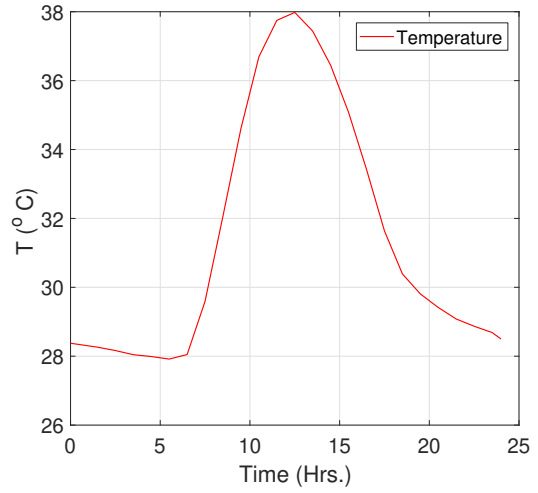


Figure 3.43: Temperature

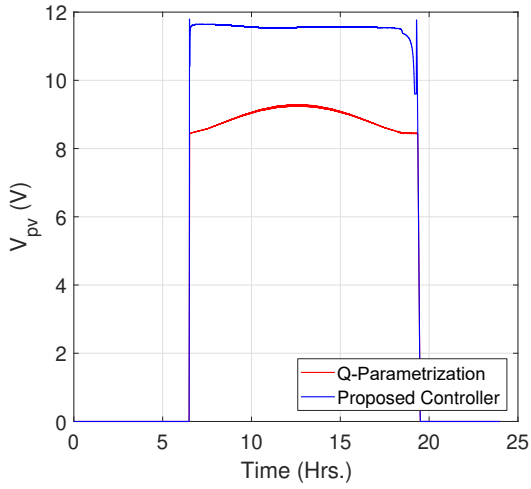


Figure 3.44: PV voltage

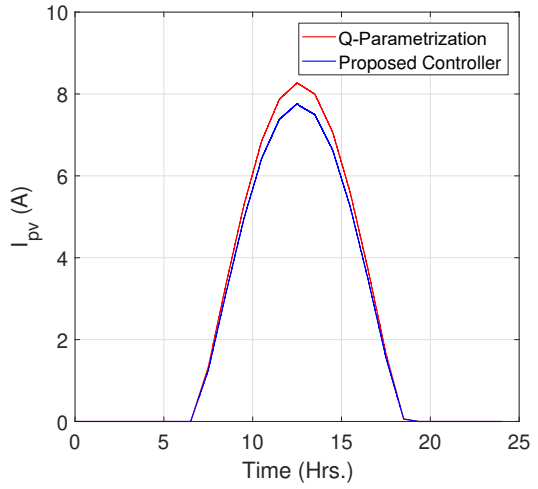


Figure 3.45: PV current

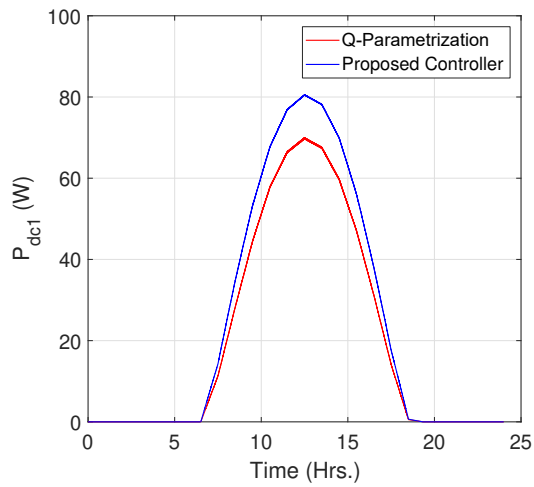


Figure 3.46: SMICs power

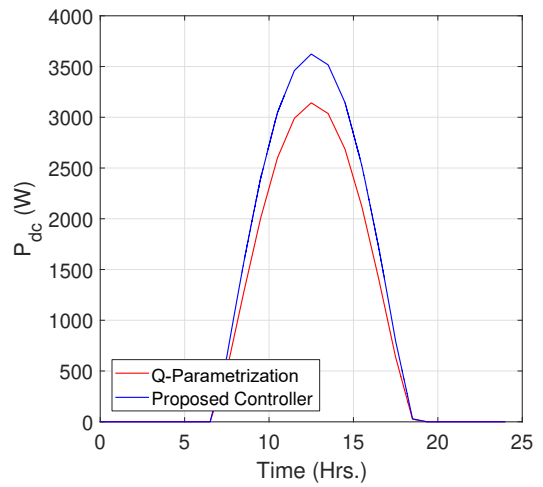


Figure 3.47: Total power

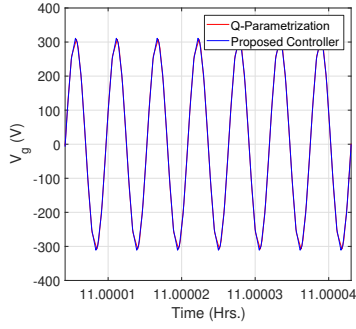


Figure 3.48: Grid voltage

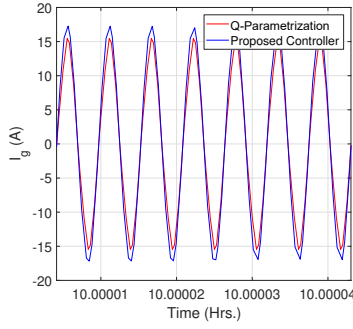


Figure 3.49: Grid current

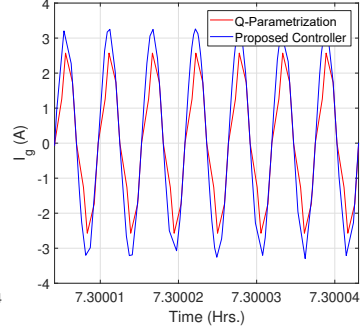


Figure 3.50: Grid current

Table 3.3: Comparison of existing and proposed controller based Power extraction

Date : 29-03-2014, Location ID : 25819, Country: India, Latitude: 12.95, Lonitude: 74.85

Time (HH:MM)	E (W/m ²)	Temperature (°C)	PV sub-module output power (W)			Total Output Power (W)		
			Q-parametrization (Khan and Xiao, 2016)	Proposed QFT Controller	ΔP_{des}	Q-parametrization (Khan and Xiao, 2016)	Proposed QFT Controller	ΔP_{dc}
05:30	0	27.91685729	0	0	0	0	0	0
06:30	0	28.04862815	0	0	0	0	0	0
07:30	161	29.5969175	11.27	14.25	2.98	507.2	641.5	134.3
08:30	402	32.07496668	28.3	34.8	6.5	1273.8	1566.4	292.6
09:30	631	34.61026331	44.5	53.29	8.79	2003.7	2397.6	393.9
10:30	818	36.69159425	57.8	67.7	9.9	2599.4	3046.2	446.8
11:30	940	37.74944418	66.4	76.9	10.5	2989.7	3459.8	470.1
12:30	988	37.97959691	69.9	80.5	10.6	3142.5	3622.9	480.4
13:30	955	37.43649917	67.5	78.15	10.65	3036.97	3516.5	479.53
14:30	845	36.44463484	59.7	69.9	10.2	2686.18	3144.7	458.52
15:30	667	35.07642794	47.1	56.07	8.97	2118.907	2523.8	404.893
16:30	443	33.42125606	31.25	38.05	6.8	1405.194	1712.1	306.906
17:30	201	31.63689792	14.11	17.63	3.52	634.96	793.4	158.44
18:30	9	30.38816041	0.548	0.654	0.106	24.655	29.4	4.745
19:30	0	29.80810416	0	0	0	0	0	0

3.7.4 Real time environmental data (24-Hrs.) with partial shading condition

Partial shading pattern is applied to the six sub-modules, which utilises 60% of the total irradiation and the remaining 39 sub-modules are healthy. A comparative study is performed between proposed and existing controller under partial shading conditions.

Partial shading pattern is applied in the morning at 09:30 Hrs. to 11:30 Hrs. shown in Figure 3.51- Figure 3.61 and the observed values are tabulated in Table 3.4, which shown the proposed controller performance to extract maximum power under partial shading conditions. Partial shading pattern is applied in the evening at 14:30 Hrs. to 16:30 Hrs. shown in Figure 3.62- Figure 3.71, the observed values are tabulated in Table 3.5. Under partial shading conditions the PV current undergoes a short circuit value of PV current with the existing controller but proposed controller outperforms under partial shading conditions.

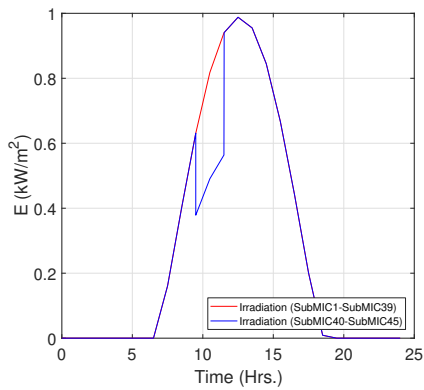


Figure 3.51: Irradiation

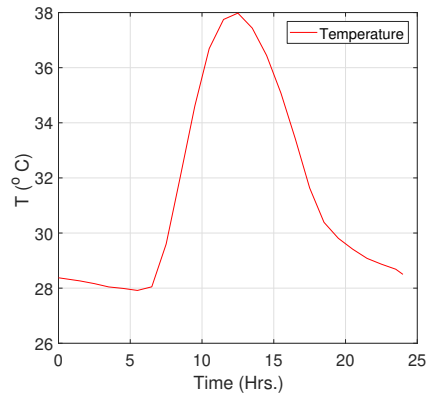


Figure 3.52: Temperature

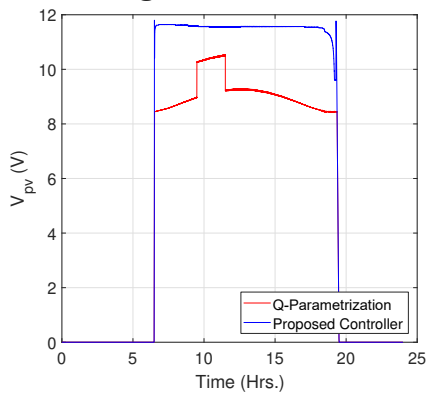


Figure 3.53: PVSV₁₋₃₉

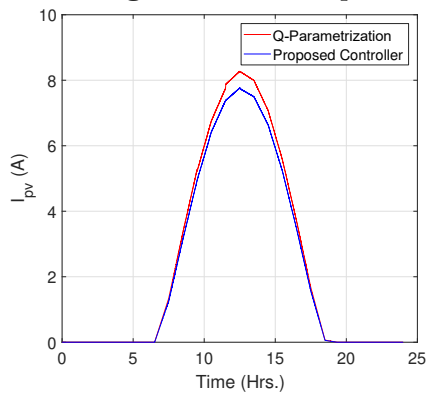


Figure 3.54: PVSC₁₋₃₉

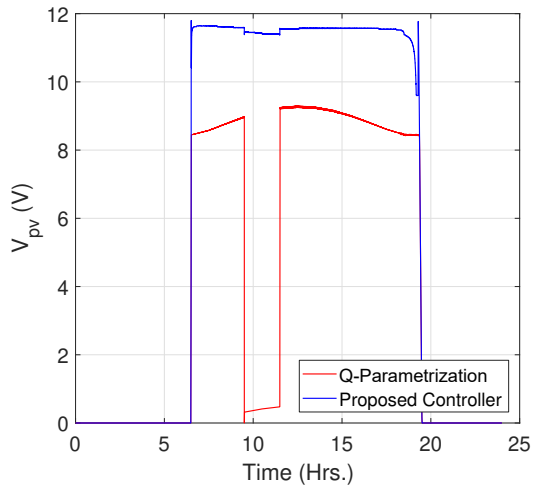


Figure 3.55: PVSv₄₀₋₄₅

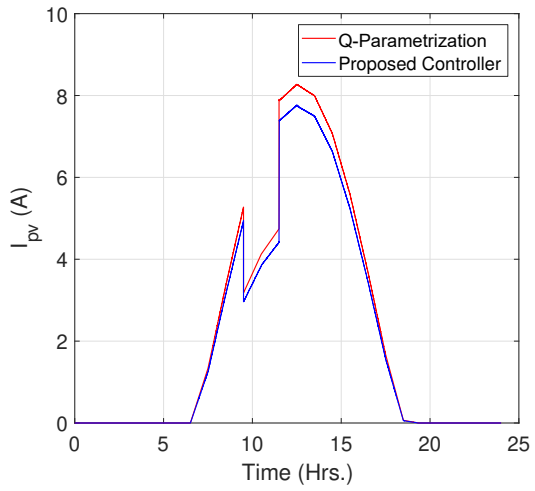


Figure 3.56: PVSC₄₀₋₄₅

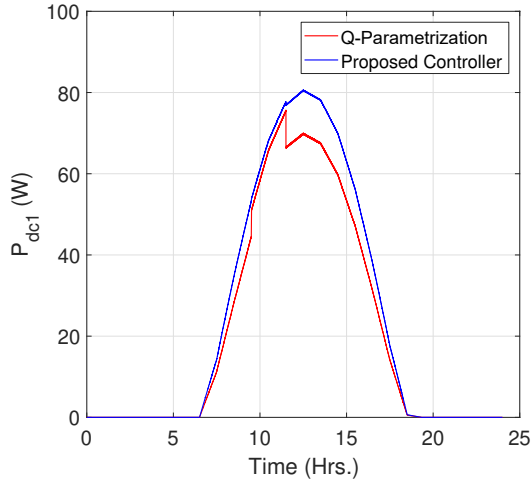


Figure 3.57: PVSP₁₋₃₉

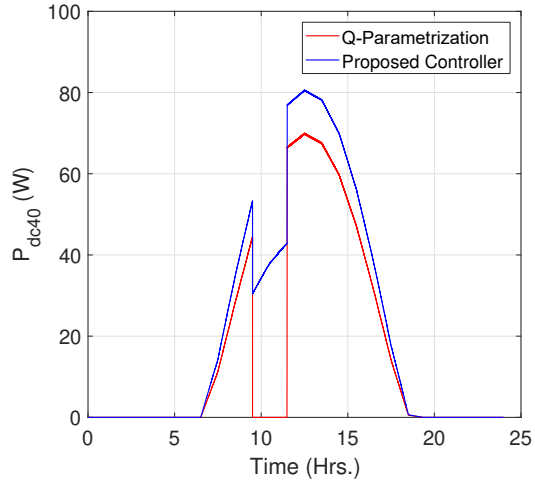


Figure 3.58: PVSP₄₀₋₄₅

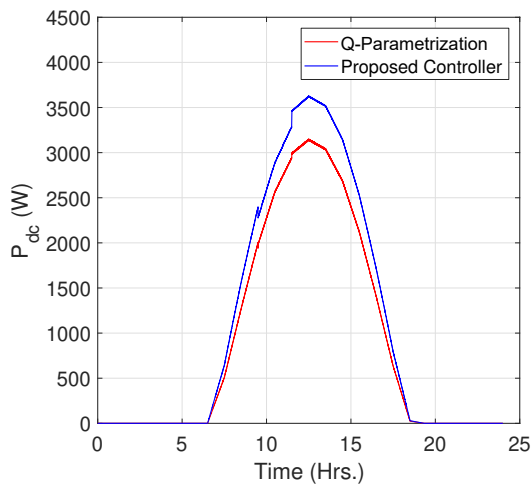


Figure 3.59: PV output power

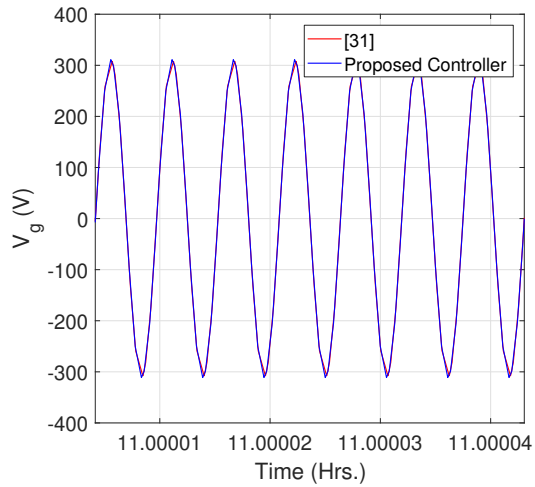


Figure 3.60: Grid voltage

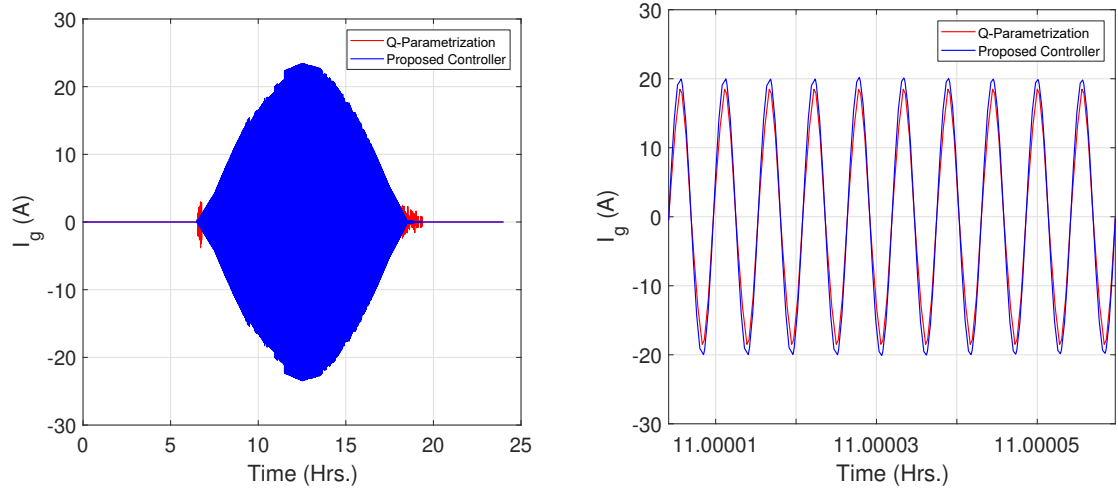


Figure 3.61: Grid current

Table 3.4: Comparison of existing and proposed controller under partial shading (09:30 Hrs.-11:30 Hrs.)

Date : 29-03-2014, Location ID : 25819, Country: India, Latitude: 12.95, Lonitude: 74.85								
Time (HH:MM)	E (W/m ²)	Temperature (°C)	PV sub-module output power (W)		ΔP_{dcs}	Total Output Power (W)		
			Q-parametrization (Khan and Xiao, 2016)	Proposed QFT Controller		Q-parametrization (Khan and Xiao, 2016)	Proposed QFT Controller	ΔP_{dc}
05:30	0	27.91685729	0	0	0	0	0	0
06:30	0	28.04862815	0	0	0	0	0	0
07:30	161	29.5969175	11.27	14.25	2.98	507.2	641.5	134.3
08:30	402	32.07496668	28.3	34.8	6.5	1273.8	1566.4	292.6
09:30	631	34.61026331	50.82	53.5	8.79	1988	2275.6	287.6
	378.6	34.61026331	0	30.5	30.5			
10:30	818	36.69159425	65.73	68.25	9.9	2566	2889.5	323.5
	490.8	36.69159425	0	38.06	38.06			
11:30	940	37.74944418	66.4	76.9	10.5	2989.7	3459.8	470.1
12:30	988	37.97959691	69.9	80.5	10.6	3142.5	3622.9	480.4
13:30	955	37.43649917	67.5	78.15	10.65	3036.97	3516.5	479.53
14:30	845	36.44463484	59.7	69.9	10.2	2686.18	3144.7	458.52
15:30	667	35.07642794	47.1	56.07	8.97	2118.907	2523.8	404.893
16:30	443	33.42125606	31.25	38.05	6.8	1405.194	1712.1	306.906
17:30	201	31.63689792	14.11	17.63	3.52	634.96	793.4	158.44
18:30	9	30.38816041	0.548	0.654	0.106	24.655	29.4	4.745
19:30	0	29.80810416	0	0	0	0	0	0

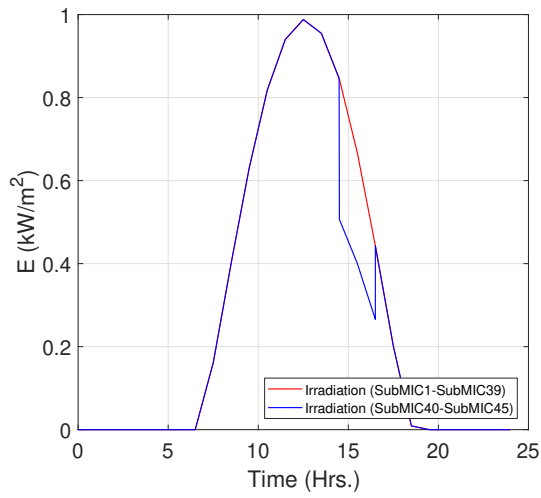


Figure 3.62: Irradiation

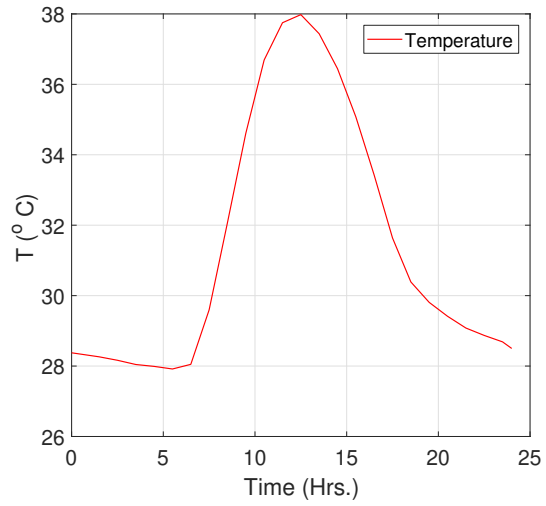


Figure 3.63: Temperature

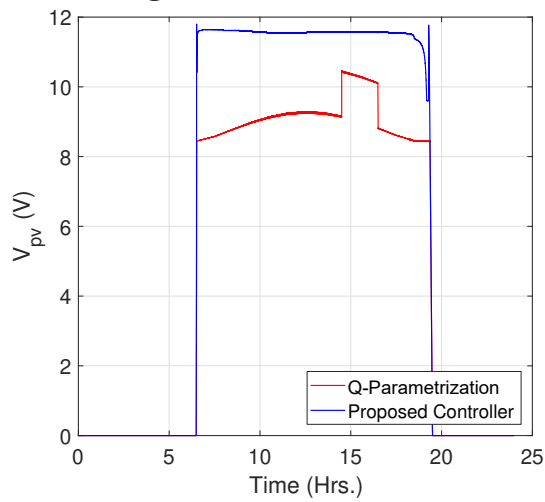


Figure 3.64: PVS V_{1-39}

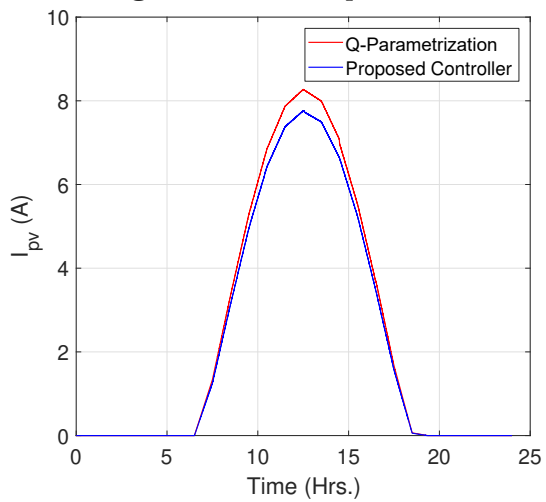


Figure 3.65: PVS I_{1-39}

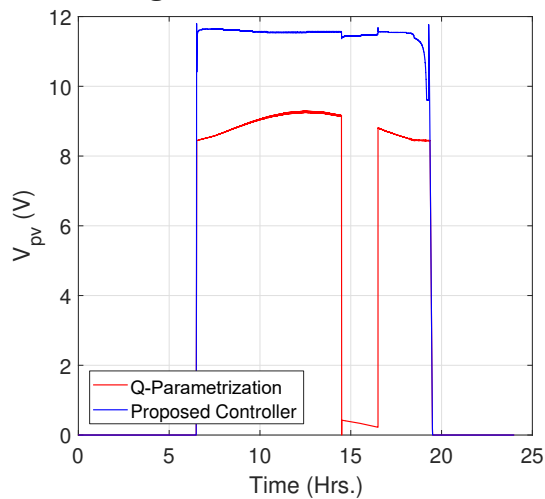


Figure 3.66: PVS V_{40-45}

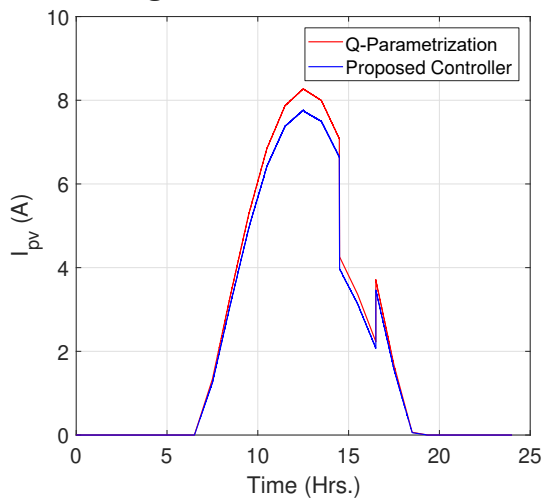


Figure 3.67: PVS I_{40-45}

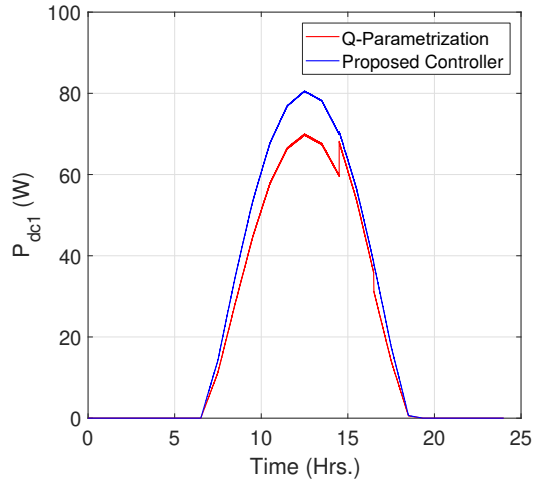


Figure 3.68: PVSP_{1–39}

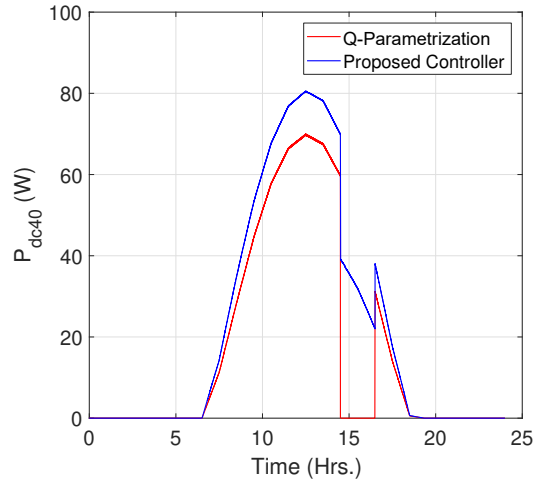


Figure 3.69: PVSP_{40–45}

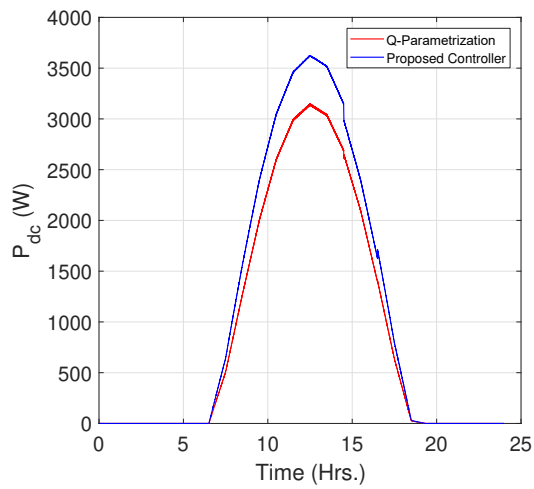


Figure 3.70: PV output power

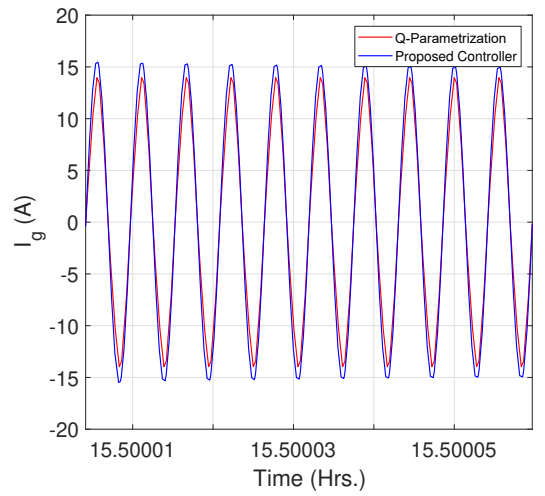


Figure 3.71: Grid current

Table 3.5: Comparison of existing and proposed controller under partial shading (14:30 Hrs.-16:30 Hrs.)

Date : 29-03-2014, Location ID : 25819, Country: India, Latitude: 12.95, Longitude: 74.85								
Time (HH:MM)	E (W/m ²)	Temperature (°C)	PV sub-module output power (W)			Total Output Power (W)		
			Q-parametrization (Khan and Xiao, 2016)	QFT Controller	ΔP_{dcs}	Q-parametrization (Khan and Xiao, 2016)	QFT Controller	ΔP_{dc}
05:30	0	27.91685729	0	0	0	0	0	0
06:30	0	28.04862815	0	0	0	0	0	0
07:30	161	29.5969175	11.27	14.25	2.98	507.2	641.5	134.3
08:30	402	32.07496668	28.3	34.8	6.5	1273.8	1566.4	292.6
09:30	631	34.61026331	44.5	53.29	8.79	2003.7	2397.6	393.9
10:30	818	36.69159425	57.8	67.7	9.9	2599.4	3046.2	446.8
11:30	940	37.74944418	66.4	76.9	10.5	2989.7	3459.8	470.1
12:30	988	37.97959691	69.9	80.5	10.6	3142.5	3622.9	480.4
13:30	955	37.43649917	67.5	78.15	10.65	3036.97	3516.5	479.53
14:30	845	36.44463484	68	70.6	2.6	2652	2986.5	334.5
	507	36.44463484	0	39.24	39.24			
15:30	667	35.07642794	53.76	56.5	2.74	2096	2395.5	299.5
	400.2	35.07642794	0	31.88	31.88			
16:30	443	33.42125606	31.25	38.05	6.8	1405.194	1712.1	306.906
17:30	201	31.63689792	14.11	17.63	3.52	634.96	793.4	158.44
18:30	9	30.38816041	0.548	0.654	0.106	24.655	29.4	4.745
19:30	0	29.80810416	0	0	0	0	0	0

3.7.5 Real time environmental data (24-Hrs.) with wide range of temperature

In future the temperature may vary drastically so it is important to study the PV performance at wide range. The following study clarifies the advantage of proposed controller performance under wide range of temperature shown in Figure 3.72- Figure 3.80, the observed values are tabulated in Table 3.6, which gives the information of the maximum power extraction over wide range of temperature.

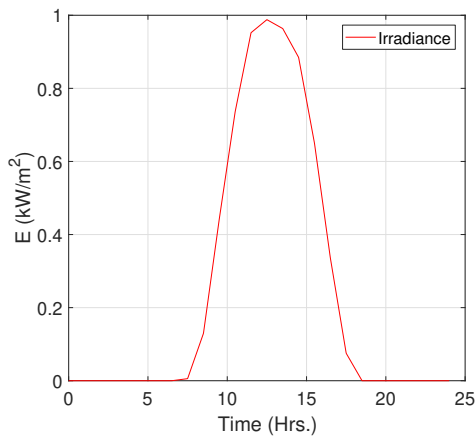


Figure 3.72: Irradiation

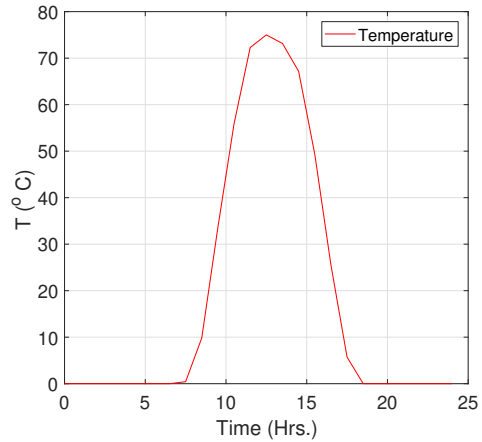


Figure 3.73: Temperature

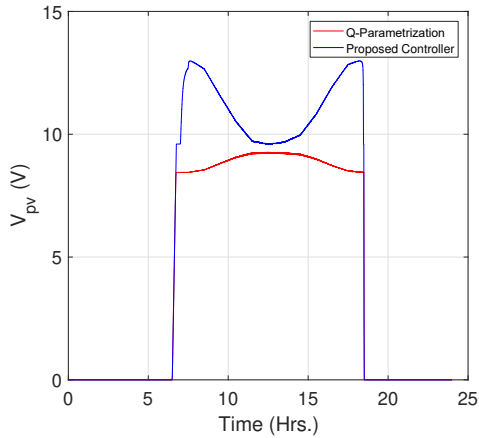


Figure 3.74: PV voltage

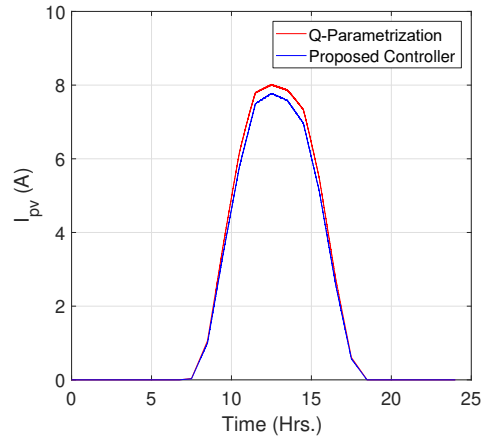


Figure 3.75: PV current

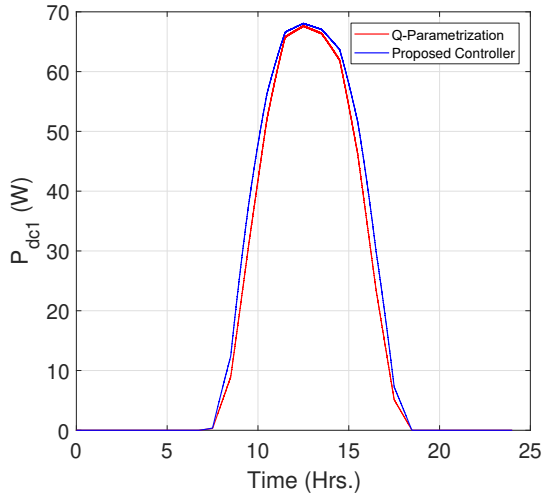


Figure 3.76: SMICs power

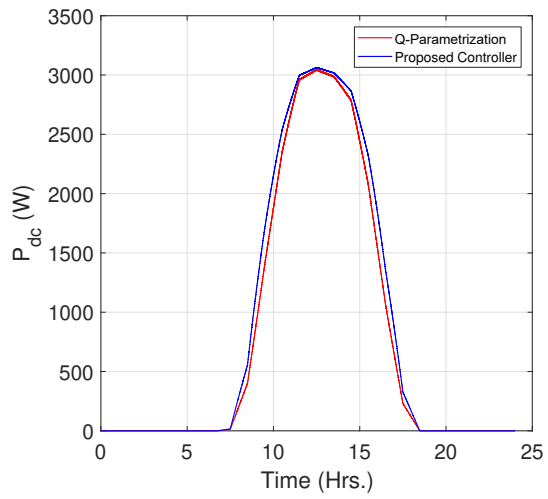


Figure 3.77: Total power

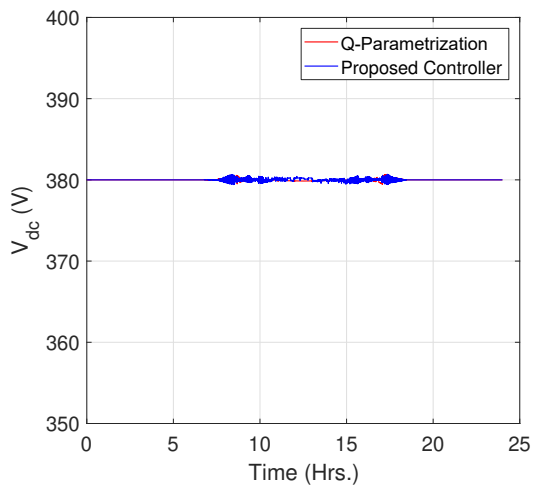


Figure 3.78: DC-link voltage

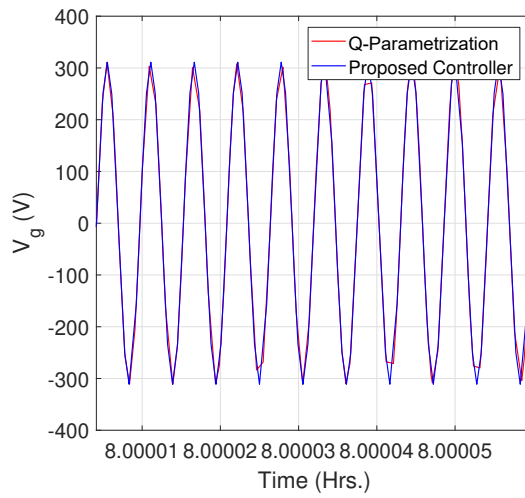


Figure 3.79: Grid voltage

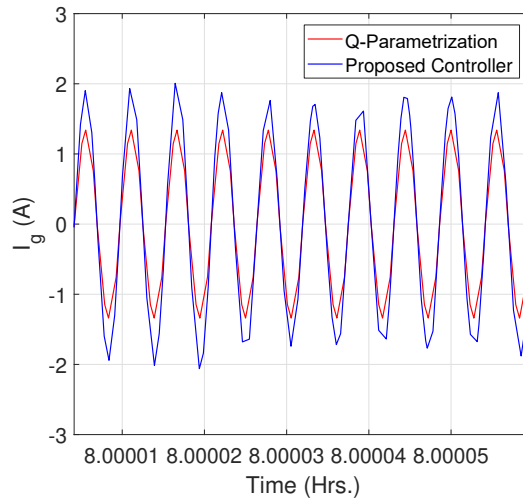


Figure 3.80: Grid current

Table 3.6: Comparison of existing and proposed controller under wide range of temperature

Date : 29-03-2014, Location ID : 25819, Country: India, Latitude: 12.95, Lonitude: 74.85									
Time (HH:MM)	E (W/m ²)	Temperature (°C)	PV sub-module output power (W)			Total Output Power (W)			
			Q-Parametrization (Khan and Xiao, 2016)	Proposed QFT Controller	ΔP_{des}	Q-Parametrization (Khan and Xiao, 2016)	Proposed QFT Controller	ΔP_{dc}	
09:00	286.4	21.74	20.02	26.042	6.022	900.85	1171.9	271.05	
09:30	443.285	33.65	31.25	38.034	6.784	1406.25	1711.5	305.25	
10:00	589.8	44.77	41.79	47.835	6.045	1880.5	2152.6	272.1	
10:30	736.3	55.89	52.15	56.34	4.19	2346.5	2535.2	188.7	
11:00	844.3	64.09	59.38	61.8	2.42	2671	2781.5	110.5	
11:30	952.3	72.29	65.78	66.6	0.82	2960	2997.5	37.5	
12:00	970.15	73.64	66.73	67.34	0.61	3002	3030.5	28.5	
12:30	988	75	67.62	68.05	0.43	3043	3062.5	19.5	
13:00	975.79	74.073	67	67.57	0.57	3015	3041	26	
13:30	963.5	73.14	66.37	67.07	0.7	2987	3018.1	31.1	
14:00	924.14	70.15	64.22	65.41	1.19	2891	2943.7	52.7	
14:30	884.69	67.1575	61.9	63.67	1.77	2785	2865.7	80.7	
15:00	767.3	58.245	54.27	57.97	3.7	2442	2608.8	166.8	
15:30	649.9	49.33	46.08	51.48	5.4	2074	2316.2	242.2	
16:00	493.05	37.43	34.83	41.51	6.68	1567.5	1868.1	300.6	
16:30	336.22	25.52	23.57	30.022	6.452	1060.7	1350.98	290.28	

Partial shading pattern is applied to all 45 sub-modules in the afternoon at 11:00 Hrs. to 13:00 Hrs. shown in Figure 3.81 - Figure 3.89, the observed values are tabulated in Table 3.7, which shown the effectiveness of the proposed method in terms of maximum power extraction over wide range of temperature along with the partial shading pattern.

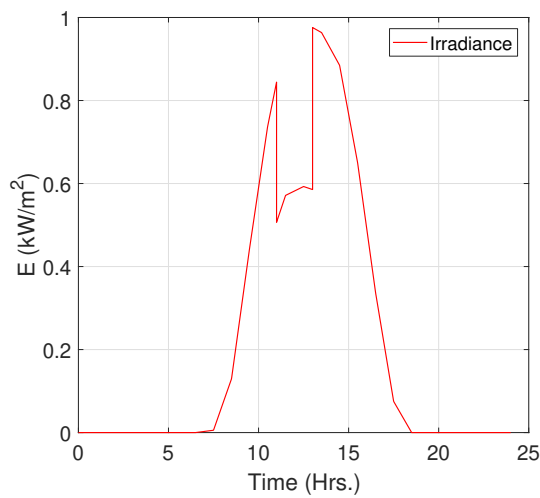


Figure 3.81: Irradiation

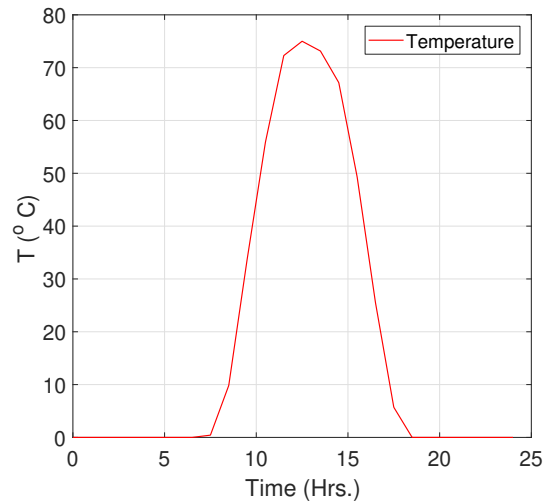


Figure 3.82: Temperature

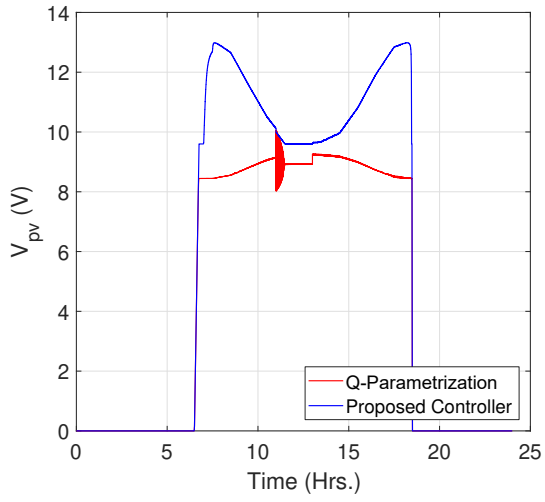


Figure 3.83: PV voltage

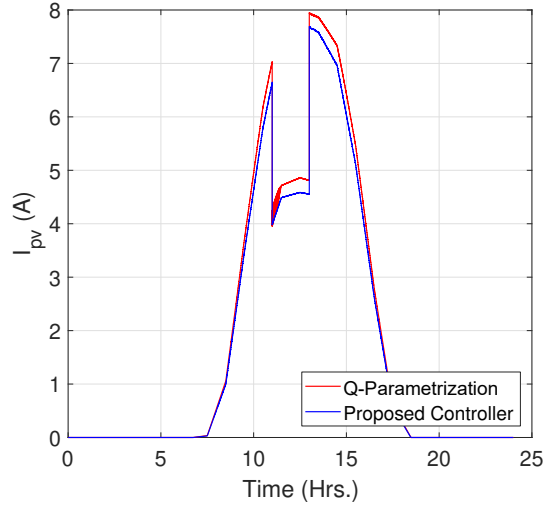


Figure 3.84: PV current

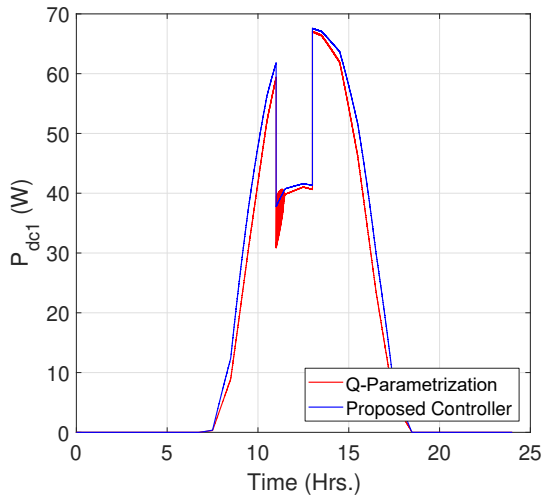


Figure 3.85: SMICs power

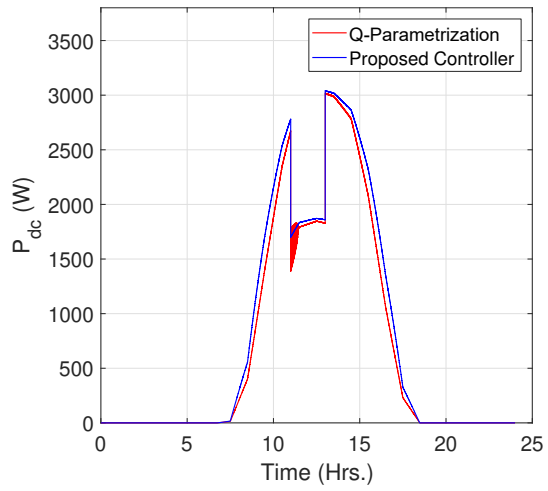


Figure 3.86: Total power

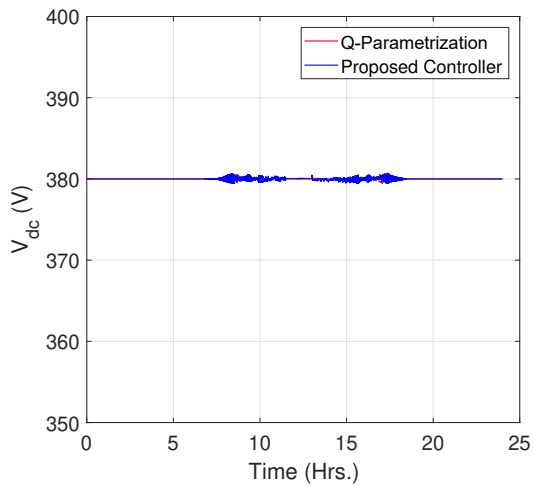


Figure 3.87: DC-link voltage

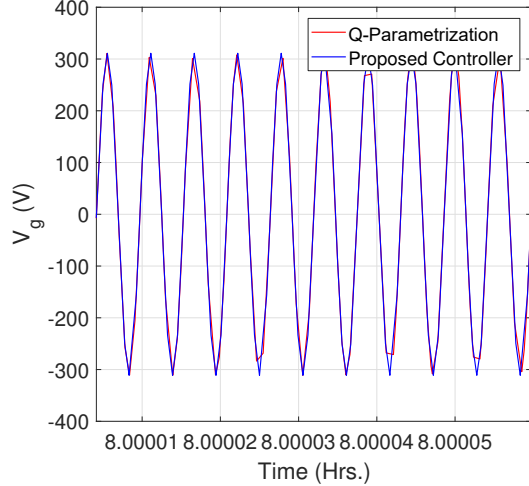


Figure 3.88: Grid voltage

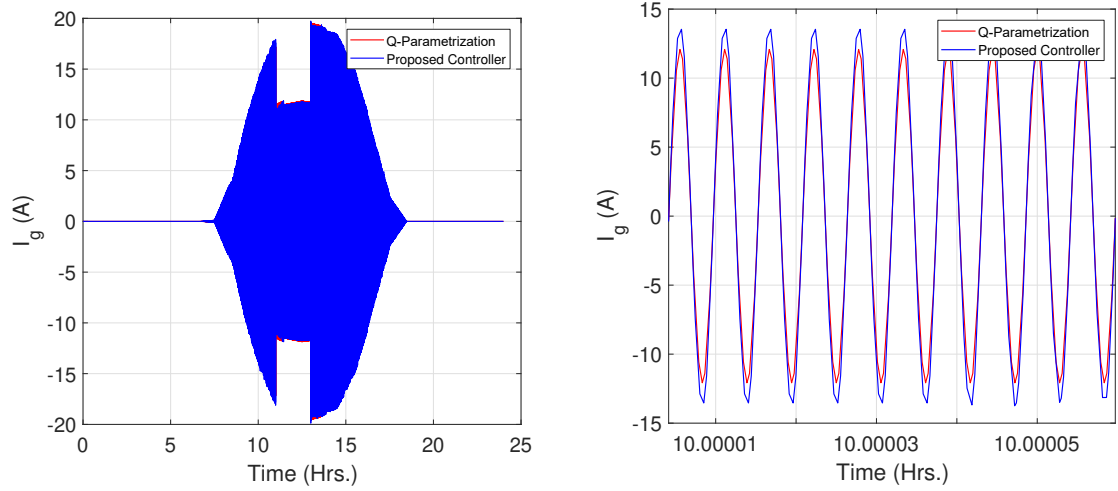


Figure 3.89: Grid current

Table 3.7: Comparison of existing and proposed controller under wide range of temperature with partial shading pattern

Date : 29-03-2014, Location ID : 25819, Country: India, Latitude: 12.95, Lonitude: 74.85									
Time (HH:MM)	E (W/m ²)	Temperature (°C)	PV sub-module output power (W)			ΔP_{dcs}	Total Output Power (W)		
			Q-Parametrization (Khan and Xiao, 2016)	Proposed QFT Controller			Q-Parametrization (Khan and Xiao, 2016)	Proposed QFT Controller	ΔP_{dc}
09:00	286.4	21.74	20.02	26.042	6.022	900.85	1171.9	271.05	
09:30	443.285	33.65	31.25	38.034	6.784	1406.25	1711.5	305.25	
10:00	589.8	44.77	41.79	47.835	6.045	1880.5	2152.6	272.1	
10:30	736.3	55.89	52.15	56.34	4.19	2346.5	2535.2	188.7	
11:00	506	64.09	35	37.775	2.775	1600	1699.8	99.8	
11:30	571.385	72.29	39.84	40.756	0.916	1793	1834.1	41.1	
12:00	582.09	73.64	40.46	41.195	0.735	1820.5	1853.75	33.25	
12:30	592.8	75	41.05	41.595	0.545	1847.5	1871.75	24.25	
13:00	975.79	74.073	67	67.57	0.57	3015	3041	26	
13:30	963.5	73.14	66.37	67.07	0.7	2987	3018.1	31.1	
14:00	924.14	70.15	64.22	65.41	1.19	2891	2943.7	52.7	
14:30	884.69	67.1575	61.9	63.67	1.77	2785	2865.7	80.7	
15:00	767.3	58.245	54.27	57.97	3.7	2442	2608.8	166.8	
15:30	649.9	49.33	46.08	51.48	5.4	2074	2316.2	242.2	
16:00	493.05	37.43	34.83	41.51	6.68	1567.5	1868.1	300.6	
16:30	336.22	25.52	23.57	30.022	6.452	1060.7	1350.98	290.28	

3.8 Summary

- In this chapter, A simple circuit model identification algorithm with a fast convergent Newton-type iterative method is developed to identify the PV circuit parameters, thereby enhancing the simulation accuracy. The simplicity of the algorithm is that gives flexibility to select best fit circuit model for each PV cell.
- Automatic loop-shaping based robust controller is designed for the linearised CSPV transfer function model by using genetic algorithm in QFT framework for maximum power extraction.
- A simple simulation technique for simulating single phase grid-tied PV systems is presented and verified the proposed average model with switching model to reduce the simulation time.
- The proposed automated QFT controller is useful to analyze the system behaviour under uncertain conditions due to variation of irradiance and temperature. The effectiveness of the proposed controller is simulated and analysed under various real time temperature and irradiation conditions at National Institute of Technology Karnataka.
- The proposed controller performance in SMIC based single phase grid connected PV system is validated with the existing Q-parameterization controller in terms of maximum power extraction under different environmental conditions. Simulation results confirms that the effectiveness of the proposed controller over existing controller.

Chapter 4

QFT controller design for grid connected PEM fuel cell

4.1 Introduction

The world's largest economy has been compelled to seek new energy sources which could ensure the sustainability of natural resources in the future due to fossil fuel scarcity and increased emissions of carbon dioxide, global warming and climate change. As a consequence, over the past few decades, the use of renewable energy sources such as wind, solar, energy, biomass, waves and tidal energy has grown rapidly (Erdinc and Uzunoglu, 2012). Unpredictability and the dependence on whether conditions are the pervasive drawbacks to all of the above described alternative energy systems, such characteristics bring to the importance of power storage. At present, hydrogen is currently one of the most promising storage technology. The device which transforms hydrogen into electricity is called a fuel cell (FC). On the basis of the reaction between hydrogen and oxygen, FC converts chemical energy saved in hydrogen into electric energy. In recent years, numerous types of FCs were developed, proton-exchange membrane FC (PEMFC) is the most used commonly at the user level due to their high-performance at low temperature with fast startup, high-power density and low oxidation rate in comparison to other types of FCs (Dicks and Rand, 2018) .

In the present scenario of high energy crisis and environmental pollution motivated towards green energy power generation. In this work, PEMFC is modelled based on the electrical circuit model by considering thermal effect. Power flow control and peak point tracking are significant in grid-tied renewable energy systems to improve

power factor and efficient energy extraction. In this thesis, the design of robust controllers for the power electronic converters of the grid-connected PEM fuel cell with thermal modeling is deliberated. Further, the transfer function model of the power electronic converters is derived by considering uncertainty in system parameters. A low complexity algorithm is used to design the converter parameters from the uncertainty range. The proposed robust automated power flow controller is designed to minimize the objective function using a genetic algorithm in the quantitative feedback theory framework. The robustness and disturbance rejection with enhanced transient response of the proposed controller is evaluated under heavy and light loading conditions, DC-link voltage and grid voltage distortion uncertainty conditions are investigated. Finally, comprehensive simulations are performed to validate the proposed controller performance with the existing controller under the above-mentioned uncertainty conditions. This chapter is organised as follows, first section describes the PEMFC modelling, next section describes the DC-DC converter modelling and controller design. next section deliberate that LCL-filter and H-bridge inverter modelling and active and reactive power flow controller design steps are discussed. Final section presents the analysis of simulation study of proposed controller performance with different power injecting/absorbing conditions. In addition to that the controller performance evaluated under uncertainty conditions.

4.2 Dynamic Electric circuit Model of PEMFC

In this section, mathematical equations are presented to design the circuit model for simulation of PEMFC is shown Figure 4.1. Mathematical model consists output voltage and losses pertaining to activation, operational (ohmic) and concentration of charge carriers. charging effect of double layer due to electrodes are also considered. The output voltage of PEMFC is given by,

The total PEM fuel cell reaction can be described as,



The fuel cell stack output voltage can then be calculated as

$$\begin{aligned} V_{out} &= n_s V_{fc,cell} = E - V_{act} - V_{ohmic} - V_{conc} \\ V_{fc,cell} &= E_{cell} - V_{act,cell} - V_{ohmic,cell} - V_{conc,cell} \end{aligned} \quad (4.2)$$

where E , V_{out} is the fuel cell stack internal and output voltage (V), n_s the number of cells in the stack (V). The total voltage drop due to activation, ohmic, concentration of charge carriers are represented as V_{act} , V_{ohm} , V_{conc} . Where V_{fc} , $V_{ohm,cell}$, $V_{act,cell}$ and $V_{conc,cell}$ are the cell output voltage, activation, ohmic, and concentration voltage drop at cell level, respectively.

Under normal operating conditions, the FC stack output voltage is less than E_{cell} due to FC losses. Therefore,

$$E = E_0^0 + \frac{RT}{2F} \ln [p_{H_2}(p_{O_2}^{0.5})] - k_E(T - 298.15) - \lambda_e I(s) \frac{\tau_e s}{\tau_e s + 1} \quad (4.3)$$

The last term in the above equation referred to the effect of oxidant delays.

4.2.1 PEMFC Voltage Drops

The activation voltage drop is depends on the PEMFC temperature and current, is given below

$$V_{act} = V_{act1} + V_{act2} \quad (4.4)$$

$$V_{act1} = (T - 298).a + \eta_0 \quad (4.5)$$

$$R_{act} = \frac{V_{act2}}{I} = \frac{T.b.ln(I)}{I} \quad (4.6)$$

where η_0 , a , b are empirical constants, is the voltage drop is independent of current but depends on the temperature. V_{act2} is depends on the both temperature and current.

4.2.2 Ohmic Voltage Drop

A PEMFC's ohmic resistance comprises the polymer membrane resistance, conducting resistance between membrane and electrode, as well as electrode resistances. The total

voltage drop can be expressed as

$$V_{ohm} = IR_{ohm} = V_{ohm,membrane}V_{ohm,a} + V_{ohm,c} \quad (4.7)$$

R_{ohm} is a function of temperature and current can be expressed by,

$$R_{ohm} = R_{ohm,0} + k_{RI}I - K_{RT}T \quad (4.8)$$

where R_{ohm0} is the constant term. k_{RI} the constant for calculating $R_{ohm}(\Omega/A)$, k_{RT} the constant for calculating $R_{ohm}(\Omega/K)$

4.2.3 Concentration Voltage drop

Concentration gradients can be formed by mass diffusion from the gas channels to the reaction sites (to the catalyst surfaces) during the reaction process. The main reason for this concentration voltage drop is slow reactant transport (products) at high current densities to (from) reaction sites (Cownden et al., 2001). any water film covering anode and cathodic catalyst surfaces may also contribute to this decrease in voltage. (Larminie et al., 2003). The equivalent resistance due to the concentration loss is given by,

$$R_{Conc} = \frac{V_{Conc}}{I} = -\frac{RT}{zFI} \ln \left(1 - \frac{I}{I_{limit}} \right) \quad (4.9)$$

4.2.4 Double-Layer Charge effect

In PEMFC, the electrodes in the figure 4.1 are segregated through a solid membrane which only permits the passage of hydrogen protons but prevents the movement of the electron.. The electrons are pulled from the anode by the outer load and deposited on the cathode layer attracted by the hydrogen protons. Therefore, over the boundary between the porous cathode and the membrane (Corrêa et al., 2004), two charged layers of opposite polarity are created. The layers, also known as double electrochemicals, can store power and act as a super-capacitor.

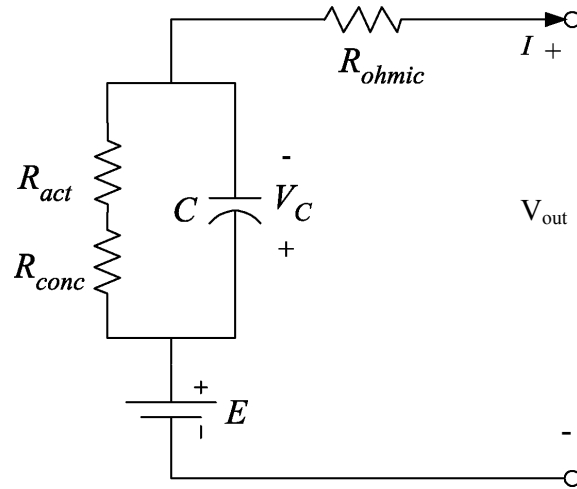


Figure 4.1: Electrical circuit model of PEMFC

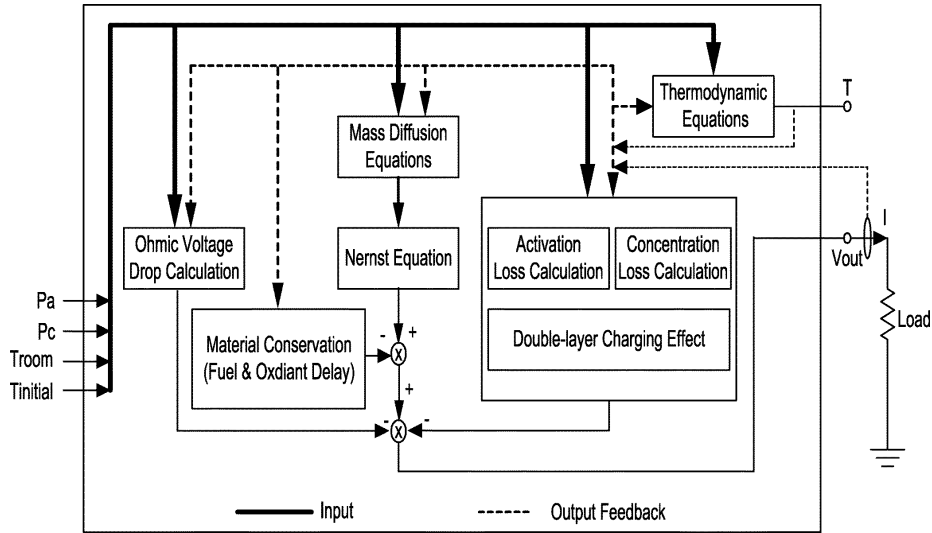


Figure 4.2: Dynamic model of PEMFC with thermal effect

The voltage across C in Figure 4.1 can be written as:

$$V_C = \left(I - C \frac{dV_C}{dt} \right) (R_{act} + R_{conc}) \quad (4.10)$$

The double-layer charge effect is integrated into the modeling, by using V_c for calcu-

lating V_{out} . From Figure 4.16, the fuel cell output voltage can be written as follows:

$$V_{out} = n_s V_{fc,cell} = E - V_{act} - V_{ohmic} - V_C$$

4.3 Thermal Model of PEMFC

The net heat rate due to the chemical reaction in the fuel cell shown in Figure 4.2, which leads to variation in temperature, can be described as:

$$\dot{q}_{net} = \dot{q}_{chem} - \dot{q}_{loss} - \dot{q}_{sens+latent} - \dot{q}_{elec} \quad (4.11)$$

where \dot{q}_{net} , \dot{q}_{chem} , \dot{q}_{elec} is heat, chemical and electrical energy (J) respectively. \dot{q}_{loss} the heat loss (J) and $\dot{q}_{sens+latent}$ the sensible and latent heat (J).

The energy released due to the change in the enthalpy of the chemical reaction inside the fuel cell (ΔH) can be written as,

$$\dot{q}_{chem} = \dot{n}_{H_2,consumed} \cdot \Delta G \quad (4.12)$$

where ΔG is the temperature dependent Gibbs free energy equation is as follows,

$$\Delta G = \Delta G_0 - RT \ln \left[p_{H_2}^* \cdot (p_{O_2}^*)^{0.5} \right] \quad (4.13)$$

The electrical power output is calculated as

$$\dot{q}_{elec} = V_{out} \cdot I \quad (4.14)$$

Sensible heat is the heat energy that is transferred by a body that has a temperature higher than its surroundings. Sensible heat transportation rate is the product of the species mol flow rate, its specific heat capacity, and its temperature and the room temperature. Heat of vaporization is used to indicate the amount of energy required when a substance changes its state into gas. Assuming the inlet temperate is the same

as the room temperature, the heat absorbed during the process is given by,

$$\begin{aligned}
 \dot{q}_{\text{sens+latent}} = & (\dot{n}_{\text{H}_2,\text{out}} \cdot T - \dot{n}_{\text{H}_2,\text{in}} \cdot T_{\text{room}}) \cdot C_{\text{H}_2} \\
 & + (\dot{n}_{\text{O}_2,\text{out}} \cdot T - \dot{n}_{\text{O}_2,\text{in}} \cdot T_{\text{room}}) \cdot C_{\text{O}_2} \\
 & + \dot{n}_{\text{H}_2\text{O,generated}} \cdot (T - T_{\text{room}}) \cdot C_{\text{H}_2\text{O},l} \\
 & + \dot{n}_{\text{H}_2\text{O,generated}} \cdot H_V
 \end{aligned} \tag{4.15}$$

By the following formula the energy loss that is primarily transmitted by air convection can be determined,

$$\dot{q}_{\text{loss}} = h_{\text{cell}}(T - T_{\text{room}})N_{\text{cell}}A_{\text{cell}} \tag{4.16}$$

During transitions, the temperature of the fuel cell is calculated as follows,

$$M_{\text{FC}}C_{\text{FC}} \frac{dT}{dt} = \dot{q}_{\text{net}} \tag{4.17}$$

where C_{FC} and M_{FC} are the overall specific heat capacity and mass of fuel cell stack.

4.4 DC-DC Converter Modelling

The output voltage of fuel cell is to be increased to maintain DC-link voltage, so that boost converter is required. Boost converter circuit is shown in Fig. . Inductor

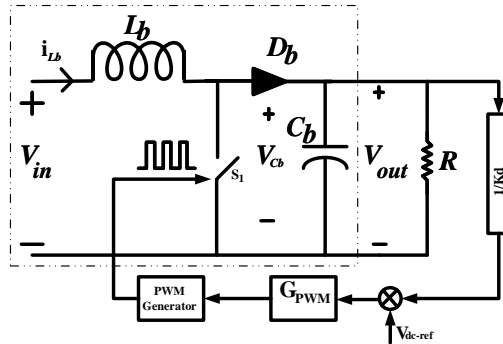


Figure 4.3: Block diagram of boost converter with voltage feedback control

current and capacitor voltage considered as state variables and modelling of continuous

conduction mode of circuit equations are given as, when s_1 is ON,

$$\begin{aligned}\frac{di_{Lb}}{dt} &= \frac{1}{L_b}v_{in} \\ \frac{dv_{cb}}{dt} &= \frac{-1}{RC_b}v_{cb}\end{aligned}\quad (4.18)$$

when s_1 is OFF,

$$\begin{aligned}\frac{di_{Lb}}{dt} &= \frac{-1}{L_b}v_{cb} + \frac{1}{L_b}v_{in} \\ \frac{dv_{cb}}{dt} &= \frac{1}{C_b}i_{Lb} - \frac{1}{RC_b}v_{cb}\end{aligned}\quad (4.19)$$

state-space equations at the operating points is given by,

$$\begin{aligned}\frac{di_{Lb}}{dt} &= \frac{-(1-d)}{L_b}v_{cb} + \frac{1}{L_b}v_{in} \\ \frac{dv_{cb}}{dt} &= \frac{1-d}{C_b}i_{Lb} - \frac{1}{RC_b}v_{cb}\end{aligned}\quad (4.20)$$

Small perturbation applied to circuit variables,

$$\begin{aligned}i_{Lb} &= I_{Lb} + \hat{i}_{lb} \\ v_{Cb} &= V_{Cb} + \hat{v}_{cb} \\ v_{in} &= V_{in} + \hat{v}_{in} \\ v_{out} &= V_{out} + \hat{v}_{out} \\ d &= D + \hat{d}\end{aligned}\quad (4.21)$$

Therefore, small signal model of boost converter equations can be described as,

$$\begin{aligned}\frac{d\hat{i}_{lb}}{dt} &= \frac{-(1-D)}{L_b}v_{cb} + \frac{V_{Cb}}{L_b} + \frac{1}{L_b}v_{in} \\ \frac{d\hat{v}_{cb}}{dt} &= \frac{1-D}{C_b}i_{Lb} - \frac{1}{RC_b}v_{cb} - \frac{I_{Lb}}{C_b}\end{aligned}\quad (4.22)$$

Transfer function model of boost converter is derived from the Equation 4.22, is obtained as

$$\frac{\hat{v}_{out}}{\hat{d}} = \frac{\frac{-I_{Lb}}{C_b} + \frac{(1-D)V_{Cb}}{L_b C_b}}{s^2 + \frac{1}{RC_b}s + \frac{(1-D)^2}{L_b C_b}} \quad (4.23)$$

Where I_{Lb} and V_{Cb} are the steady state values of inductor current and capacitor voltage respectively.

4.5 PEMFC Boost Converter Circuit Design

In this section, 500-W PEM fuel cell model is considered, with output voltage of 29.62 V and output current of 16.88 A shown in Figure 4.5 and Figure 4.4. 8 kW fuel cell stack consists 4 cells in series and 4 cells are connected in parallel, so that the fuel cell output stack voltage and current is 118.48 V and 67.52 A shown in Figure 4.7 and Figure 4.8.

Peak, rated and tolerable ripples in voltage and current are to be considered to design the boost converter circuit parameters. The input voltage of DC-DC converter is equal to the output of fuel cell of 118 V, and the DC-link voltage or the boost converter output voltage is set to 400 V. The switching is selected as 5 kHz. For single phase applications, DC-link voltage is chosen as 400 V. Then the approximate input voltage for DC-DC boost converter can be obtained as $(1 - 0.73) \times 400 = 108$. Therefore, the number of PEMFC stacks to be connected in series to get the voltage of 108 V is,

$$N_s = \frac{V_{FCarray}}{V_{PEMFC}} = \frac{118.48}{29.62} = 4 \quad (4.24)$$

The required number of parallel connected PEMFC stacks is calculated as,

$$N_P = \frac{8000}{4 \times 500} = 4 \quad (4.25)$$

Therefore, 8 kW PEMFC array is composed of $4 \times 4 = 16$, 500-W stacks. The design circuit parameters are shown below,

1. In the first step, equivalent resistance calculation to maintain the constant DC-

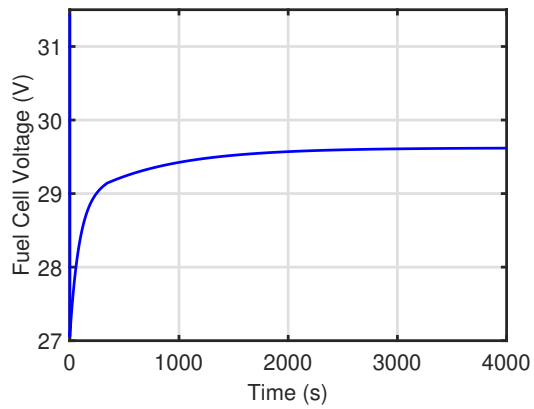


Figure 4.4: fuel cell output voltage

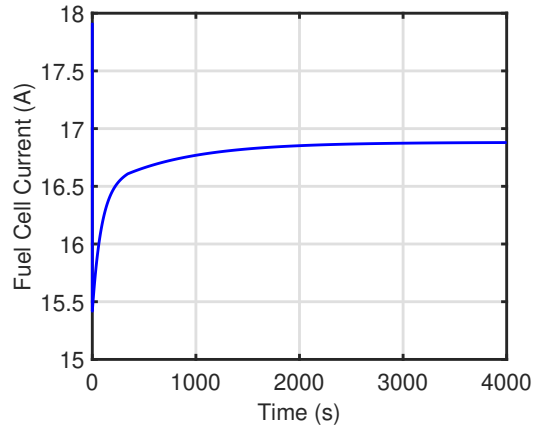


Figure 4.5: fuel cell output current

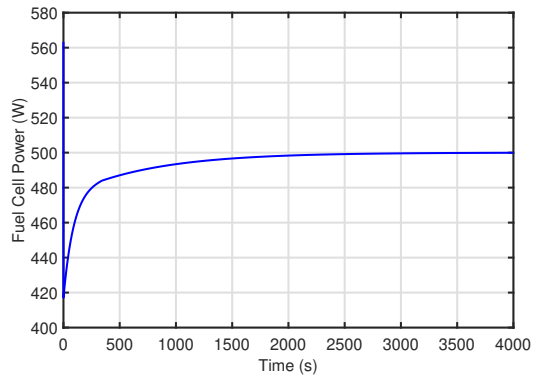


Figure 4.6: fuel cell output Power

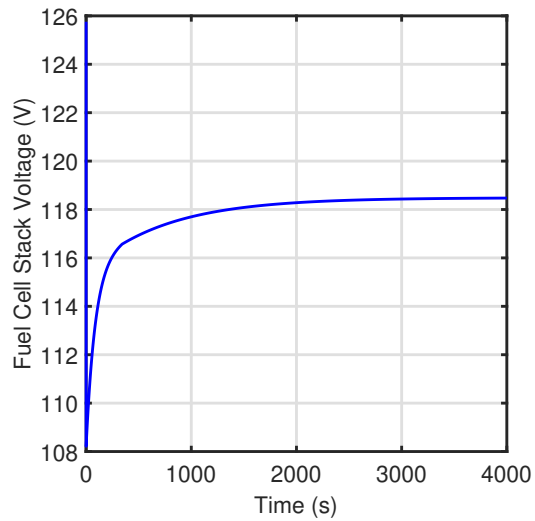


Figure 4.7: fuel cell stack output Voltage

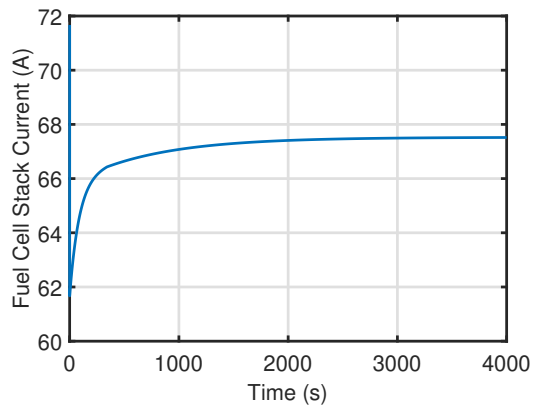


Figure 4.8: fuel cell stack output Current.

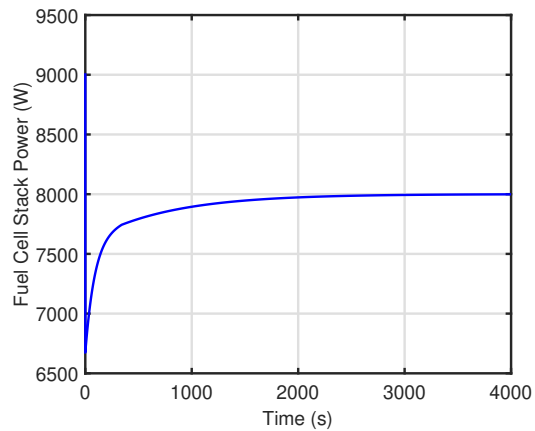


Figure 4.9: fuel cell stack output Power

link voltage at the output of boost converter, is calculated as,

$$R = \frac{V_{out}}{P_{rated}} = \frac{400^2}{8000} = 20\Omega \quad (4.26)$$

2. Duty Ratio is calculated as,

$$D = 1 - \frac{V_{in}}{V_{out}} = 1 - \frac{108}{400} = 0.73 \quad (4.27)$$

3. The maximum current passing through the inductor is calculated as,

$$I_{lb,max} = \frac{V_{in}}{(1-D)^2 R} = 74.07A \quad (4.28)$$

4. Inductance of boost converter value calculated by limiting the input current ripple less than 20%

$$L_b > \frac{5D(1-D)^2 R}{f_s} > \frac{5 \times 0.73 \times 0.27^2 \times 20}{5000} > 0.001H \quad (4.29)$$

So, The inductance should greater than 0.01 H. The uncertainty range is considered as, $1 \text{ mH} < L_b < 10 \text{ mH}$.

5. Capacitance is calculated by limiting the output voltage ripple less than 5%.

$$C_b > \frac{D}{0.05 f_s R} > \frac{0.73}{0.05 \times 20 \times 5000} > 150\mu F \quad (4.30)$$

So, The capacitance should greater than $150\mu F$, The uncertainty range is considered as, $150 \mu F < C_b < 1000 \mu F$.

4.6 Controller Design for Boost converter

Transfer function of PEM fuel cell model is given by,

$$\frac{\hat{v}_{out}}{\hat{d}} = \frac{\frac{-I_{Lb}}{C_b} s + \frac{(1-D)V_{Cb}}{L_b C_b}}{s^2 + \frac{1}{RC_b} s + \frac{(1-D)^2}{L_b C_b}} \quad (4.31)$$

Transfer function model of boost converter is rewritten as,

$$P_{fc} = \frac{K \left(\frac{s}{z} + 1 \right)}{\left(\frac{s}{\omega_n} \right)^2 + 2\xi\omega_n s + 1} \quad (4.32)$$

$$K = \frac{X_2}{(1-D)}, \quad \omega_n = \frac{1-D}{\sqrt{L_b C_b}},$$

$$z = \frac{-(1-D)X_2}{X_1 L_b}, \quad \xi = \frac{1}{2R(1-D)} \sqrt{\frac{L_b}{C_b}} \quad (4.33)$$

where $X_2 = 400$ V, $X_1 = 75$ A, 1 mH $< L_b < 10$ mH, 150 μ F $< C_b < 1000$ μ F, The uncertainty range of parameters in the equation 4.32 is given by, $72 \leq \omega_n \leq 594$, $-1440 \leq z \leq -144$, $0.0926 \leq \xi \leq 0.7561$, $K = 1481.5$.

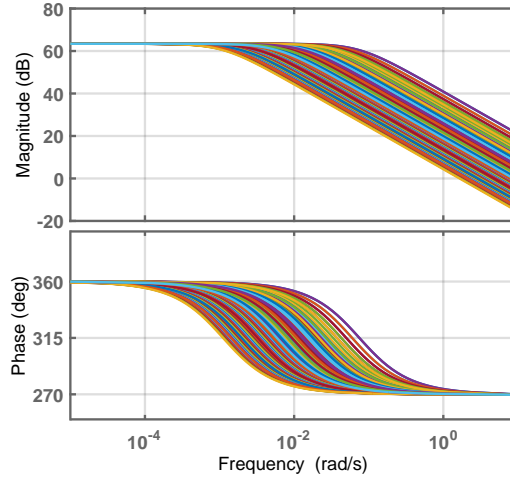


Figure 4.10: Bode response of uncertain DC-DC converter

In this work, the nominal values of inductor current and capacitor voltage is given as, $L_b = 10$ mH, $C_b = 1000$ μ F. The nominal values $K_o = 1481.5$, $\omega_o = 72$, $z_o = -144$, $\xi_o = 0.2928$. The bode plot response of the PEM fuel cell with the uncertain parameters, is shown in Figure. 4.10.

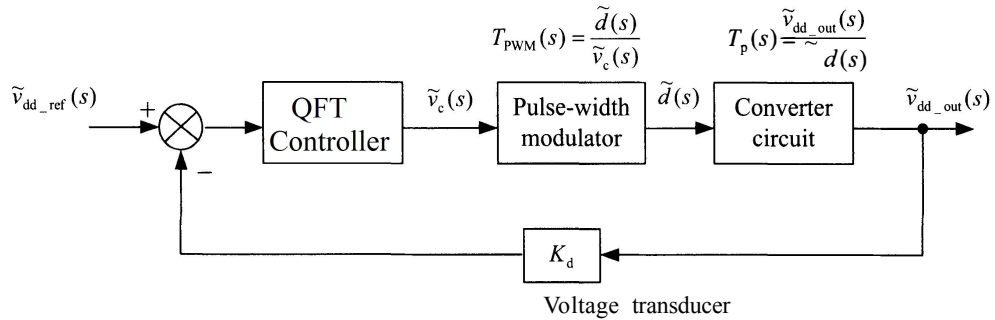


Figure 4.11: Block diagram of QFT controller for the PEM fuel cell

The parameter variations are observed at low-frequency range of about 0.0001 to 1 rad/s shown in Figure 4.10, QFT controller design procedure discussed in section 3.6.1 used to design the controller for this plant, is given by,

$$G_{dc} = \frac{0.02s + 1}{s} \quad (4.34)$$

4.7 LCL Filter Design

The H-bridge inverter is connected to grid through the LCL-filter to achieve fundamental frequency signal. Basically AC filters are three types L-, LC- and LCL- filter. L filter has attenuation band of -20 dB/dec since it is first order system. If the size of the inductor increases to reduce the harmonics, voltage drop increases and cost also increases. L-filter is suitable for low voltage and power applications. LC-filter is second order system, which has attenuation of -40 dB/dec. large capacitance will reduce the cost of the filter but the reactive power flow will increase and high inrush currents are present. The filter resonant frequency depends on the grid impedance. LC filters are suitable for autonomous systems. LCL filter is chosen for this work, due to high attenuation, and better decoupling capability with grid impedance. In this work, 8 kW Inverter is considered with single phase voltage of 230 V, 50 Hz. switching frequency is 10 kHz. DC-link voltage of 400 V. The LCL filter design steps are given as,

1. The size of the inverter side inductor design is made to minimize the current

ripples produced by the H-bridge inverter due to switching operation.

$$\begin{aligned} L_{1min} &= \frac{V_{dc}}{8\lambda_{cL1}I_1f_{sw}} \\ L_{1max} &= \frac{\lambda_{vL1}V_g}{2\pi fI_1} \end{aligned} \quad (4.35)$$

where $I_1 = P_o/V_g$ λ_{vL1} the ratio of RMS values of voltage of the inductor to the capacitor voltage (normally 5%). λ_{cL1} is chosen as 30%.

2. Filter capacitor play major role in handling the reactive power injection between inverter and grid.

$$C = \delta_C \frac{P_o}{\omega_o V_g^2} \quad (4.36)$$

δ_C the ratio of the reactive power to the rated output active power, is chosen as 2%.

3. The grid side inductor size obtained from the grid current ripple limit. The grid side inverter is calculated based on the inverter side inductor. The ratio between grid side inductance to inverter side inductance will vary from 0.5 to 1. In this work chosen 0.6.
4. The calculated values of LCL filter are $L_{1min} = 0.5mH$, $L_{1max} = 1.1mH$, $C_{max} = 14\mu F$, $L_{2min} = 0.6 \times L_{1min}$ and $L_{2max} = 0.6 \times L_{1max}$
5. Filter resonance frequency,

$$\begin{aligned} \omega_{res} &= \sqrt{\frac{L_1 + L_2}{L_1 L_2 C_d}} \\ f_{res} &= \frac{\omega_{res}}{2\pi} \\ 0.5f_{sw} &\leq f_{res} \leq 10f_{sw} \end{aligned}$$

6. Active damping method, resistor is connected in series with the capacitor, is used to damp out the frequency response at the resonance frequency.

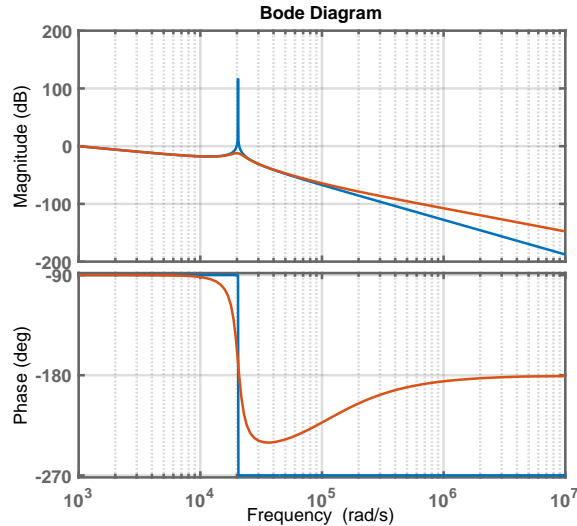
$$r_d = \frac{1}{3 \times \omega_{res} \times C_d} \quad (4.37)$$

Table 4.1: Single phase LCL filter parameters

Parameter	Value
Inverter power	8 KVA
Rated Real Power P_o	8 kW
Grid Voltage V_g	230 V
DC-link Voltage V_{dc}	400 V
Fundamental frequency	50 Hz
Switching frequency	10 kHz
Inverter side Inductor (L_1)	0.6 mH
Grid side Inverter (L_2)	0.4 mH
Filter Capacitor (C_d)	10 μ F
Damping Resistor (r_d)	1 Ω

7. The uncertainty range of filter parameters are given by, $0.5mH \leq L_1 \leq 1.1mH$, $0.3mH \leq L_2 \leq 0.66mH$, $8\mu F \leq C_d \leq 14\mu F$, $0.9\Omega \leq r_d \leq 1.8\Omega$, and the nominal values are tabulated in Table 4.1.

4.8 Voltage and current loop controllers design

**Figure 4.12:** LCL-Filter response

The frequency response of LCL-filter is analysed by formulating the transfer function model with and without damping is shown in Figure 4.12, blue line represents the

undamped LCL-filter response and red line represents the damped filter response is given by,

$$P_{LCL,undamped} = \frac{1}{L_1 \times L_2 \times C_d s^2 + (L_1 + L_2)s}$$

$$P_{LCL,damped} = \frac{r_d \times C_d s + 1}{L_1 \times L_2 \times C_d s^3 + (L_1 + L_2) \times C_d \times r_d s^2 + (L_1 + L_2)s} \quad (4.38)$$

Transfer function model of damped LCL-filter given in Eq. 4.38 can be expressed as uncertainty model by considering the inverter, grid side inductor and filter capacitor parameter variations. Transfer function of uncertainty plant model is given by, rewriting the Eq. 4.38,

$$P_{LCL} = \frac{\frac{1}{L_1+L_2} \left(\frac{s}{C_d r_d} + 1 \right)}{s \left(\left(\frac{s}{\sqrt{\frac{L_1+L_2}{L_1 L_2 C_d}}} \right)^2 + \frac{s}{C_d r_d} + 1 \right)} \quad (4.39)$$

The equivalent transfer function model is as follows

$$P_{LCL}(s) = \frac{k \left(\frac{s}{z} + 1 \right)}{s \left(\left(\frac{s}{\omega_n} \right)^2 + \frac{2\xi}{\omega_n} s + 1 \right)} \quad (4.40)$$

Where the uncertainty of plant parameter is given by, $500 \leq k \leq 1250$, $40 \times 10^3 \leq z \leq 140 \times 10^3$, $10 \times 10^3 \leq \omega_n \leq 25 \times 10^3$, $0.05 \leq \xi \leq 0.3$ and the nominal parameters are $k = 1000$, $z = 100 \times 10^3$, $\omega_n = 20 \times 10^3$, $\xi = 0.1$.

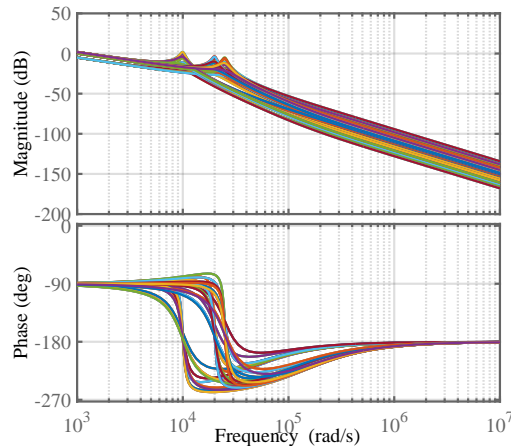


Figure 4.13: Bode response of uncertain LCL filter

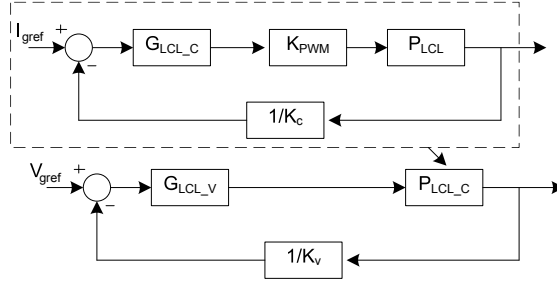


Figure 4.14: Current and Voltage control loops for PEMFC

The designed controller based on the PI method and the proposed controller is given below for the system shown in Figure 4.14,

$$G_{LCLC} = K_p + \frac{2\pi k_r s}{s^2 + 2\pi s + \omega_o^2} \quad (4.41)$$

$$G_{LCLV} = \frac{K_{p1}s + 1}{K_{I1}} \quad (4.42)$$

$$G_{PIC} = \frac{K_{p2}s + 1}{K_{I2}} \quad (4.43)$$

where $K_p = 5$, $K_r = 450$, $K_{p1} = 32.25$, $K_{I1} = 280$, $K_{p2} = 10$, $K_{I2} = 5000$

4.9 Simulation Results

The significance of power factor and power factor correction is becoming ever more significant, both from the point of view of the grid and the consumer, as the penetration of renewable energy sources in the Grid-Connected continues to increase. The power factor is a measurement of the phase difference in a AC power system between voltage and current. The current is in phase with the voltage and the power factor is unitary in purely resistive loads. Capacitive and inductive loads lead to voltage leading or lagging, leading to non-unitary power. A non-unity factor means that both active and reactive power is consumed by the load. The useful component of the AC power is the active power (available in real or true power) that contributes to the work done on a system. Reactive energy oscillates and operates in the process between the generation source and the load. However, reactive capacity is necessary to maintain the system's voltage, deliver magnetizing power to motors and facilitate the transfer of active power via the AC circuit.

The reactive power supply for an AC power grid is very critical. The reactive

power generated by generators should closely correspond to the energy consumed. The voltage is increased by a major power factor (due to the capacitive loads), and by a lagging power factor (due to inductive loads) the voltage is lowered. The increase in reagent power increases the visible power but has no impact on active power. This means the DG's in the system must deliver more visible power, although the system does not do any additional work. Therefore, power factor maintenance and improvement plays a significant role in grid connected renewable energy power system.

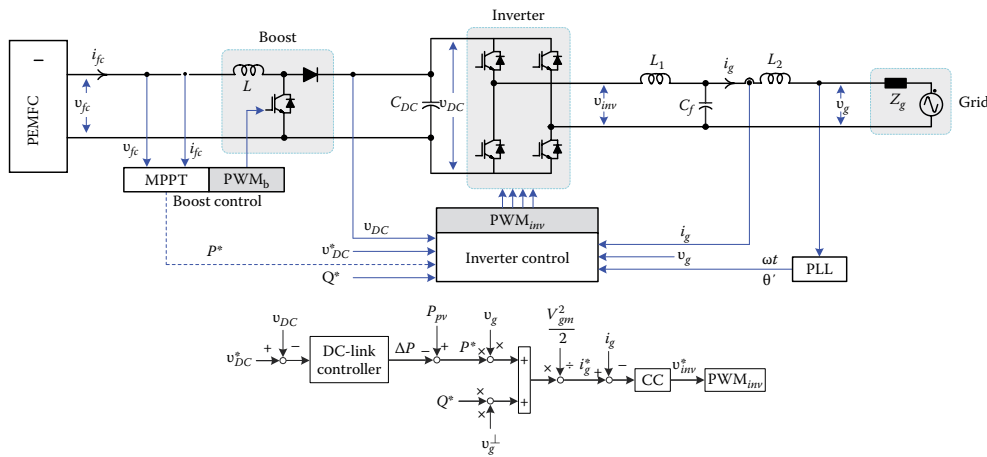


Figure 4.15: Block Diagram of Single-phased grid connected Fuel cell

4.9.1 Case 1: Unity power factor operation

The objective of this simulation is to find the suitable robust controller for desired real power injection into grid. In this case proton exchange membrane fuel cell (PEMFC) supplies only real power to the grid, so that the performance of PI and proposed controller is investigated.

PEMFC power system, consists 8 kW fuel cell is modelled and connected to 8 KVA DC/AC inverter through DC-DC boost converter, which is connected to single phase grid 230 V_{rms} . DC/AC inverter connects dc-link to the grid, dc-link voltage is selected as 400 V. In this simulation, active power requirement of 7.2 kW and reactive power component made zero as reference. The rated active power is decreased to 3.6 kW at $t=2$ s to $t=4$ s. Fuel cell output voltage, current and power with variation of active power requirement is shown in Figs. 4.16. The DC-link voltage is maintained

constant as shown in Fig. 4.17. The variation of grid voltage and current is shown in Fig. 4.18. The measured active and reactive power is shown in Fig. 4.19. The phase difference and power factor variations is shown in Fig. 4.20, It is observed from the result PI controller is not suitable for unit power factor operation, it supplying excessive reactive power which is not desired.

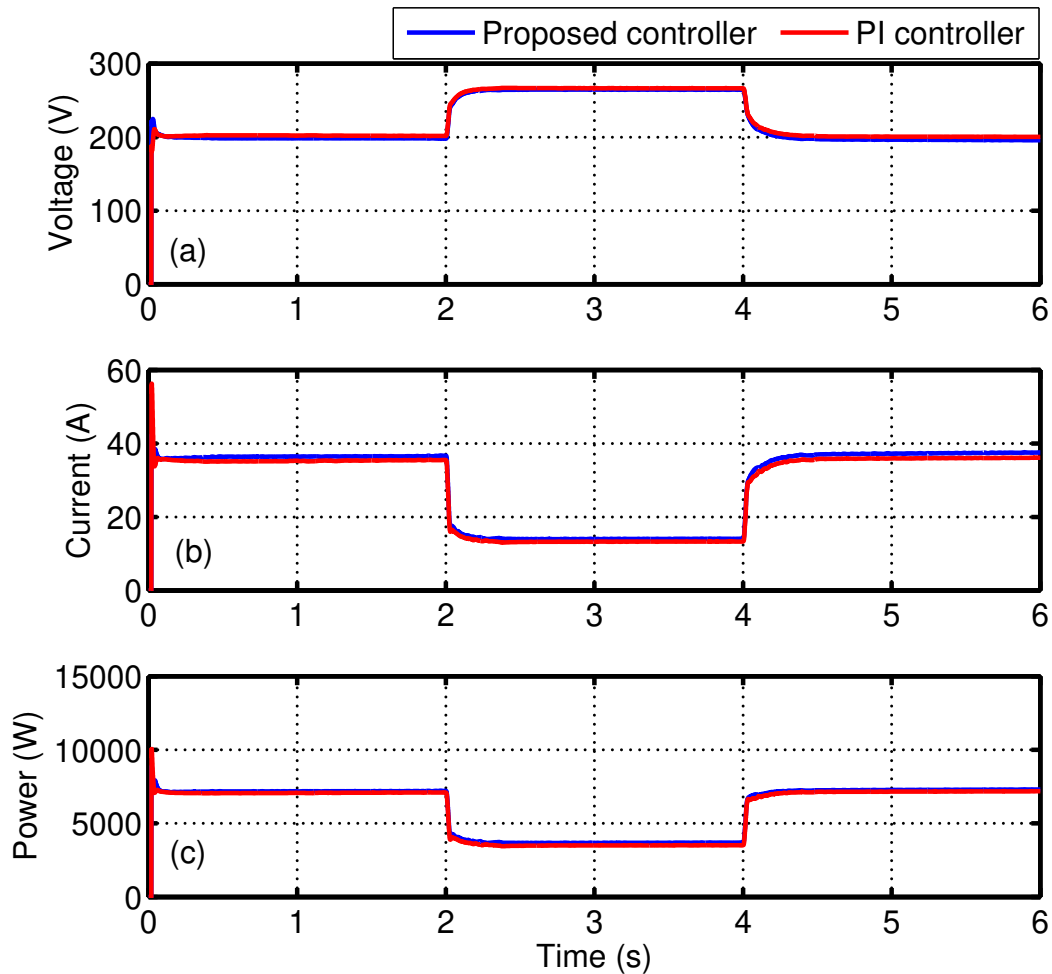


Figure 4.16: fuel cell output (a) voltage (b) current (c) Power

The PI controller is operating at non-unity power factor, but the proposed controller operates at unity power factor as desired. When reactive energy is supplied, the voltage on the network can increase or fall to a point when the generators need to switch off to protect themselves and reduce the generation thereby causing additional problems. The proposed controller shown enhanced performance with unity power factor operation. In the next sections The robustness of the proposed controller is

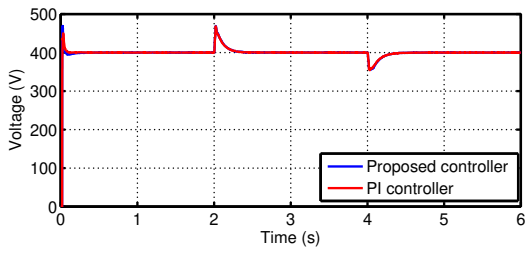


Figure 4.17: DC-link Voltage

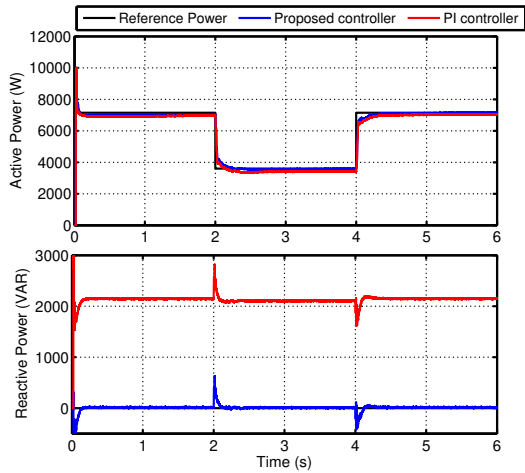


Figure 4.19: Active and Reactive power injection into grid

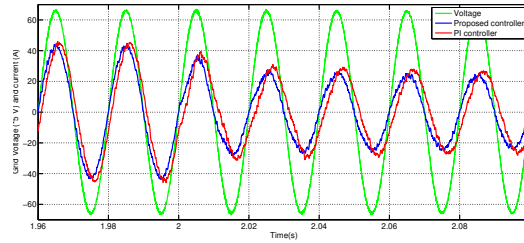


Figure 4.18: Grid voltage and current

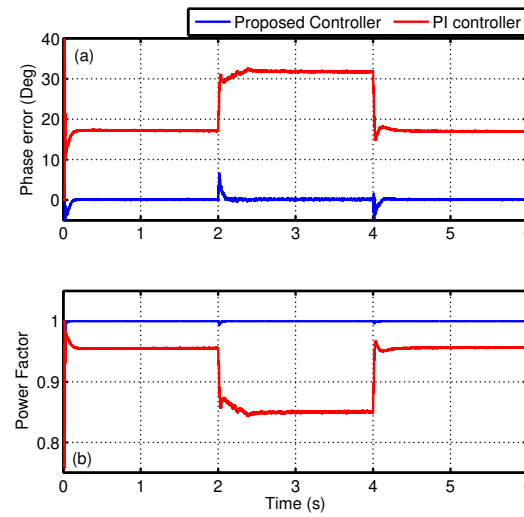


Figure 4.20: (a) Phase difference between grid voltage and current (b) Power factor

evaluated under different uncertain conditions.

With the application of proposed robust controller, Unity power factor and zero phase error is achieved corresponding values are tabulated in Table 4.2.

4.9.2 Case 2: Desired Active power $P=7.2$ kW and $Q= 1$ kVar injected to grid

The advantage and necessity of the proposed controller is discussed in the previous section. When the electric power demand on grid is high, the PEMFC should deliver more real power to grid. The inverter based on fuel cells may also need to control the grid reactively to raise system voltage. The reference values of P and Q are set to 7.2 kW and 1 kVar. In this simulation, The performance of the controller is

Table 4.2: Real Power Injection to Grid (UPF operation)

Parameter	Existing Method	Existing Value	Proposed Method	Proposed Value
Case 1: Full Loading (P=7200 W and Q=0)				
Power Factor	PI	0.9562	Automated QFT Controller	1
Phase Difference (Deg)		17.04		0.1637
Case 1.1: Half-Full Loading (P=3600 W and Q=0)				
Power Factor	PI	0.8506	Automated QFT Controller	1
Phase Difference		31.93		0.2379

investigating with active and reactive power control under heavy loading and light loading conditions. The fuel cell based DG operates heavy loading condition from $t=0$ s to $t=2$ s and light loading condition from $t = 2$ s to $t=4$ s the active power reduced to 3.6 kW, which is normally low. Satisfactory performance is achieved with the proposed QFT robust controller shown in Figs. 4.21-Fig. 4.25.

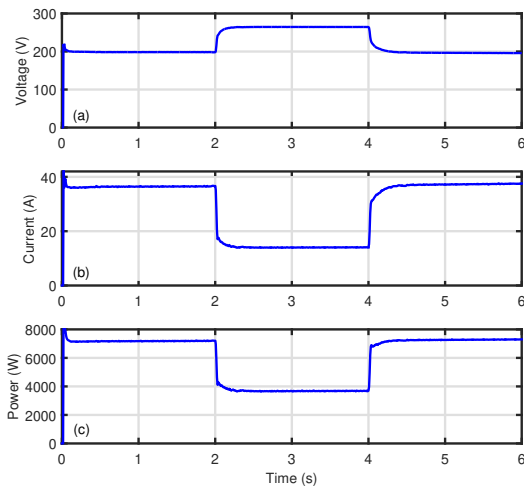


Figure 4.21: fuel cell output (a) voltage (b) current (c) Power

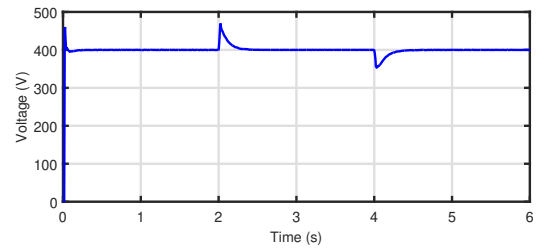


Figure 4.22: DC-link Voltage

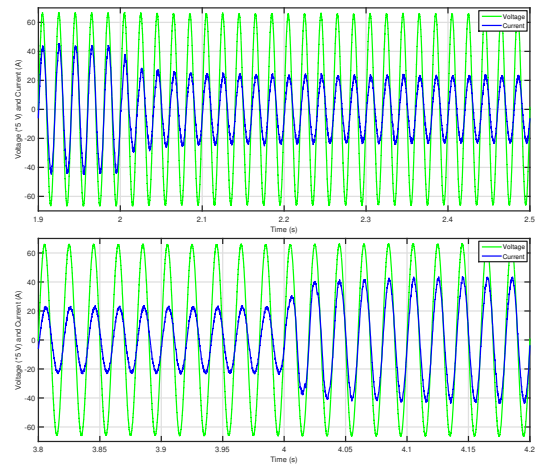


Figure 4.23: Grid voltage and current

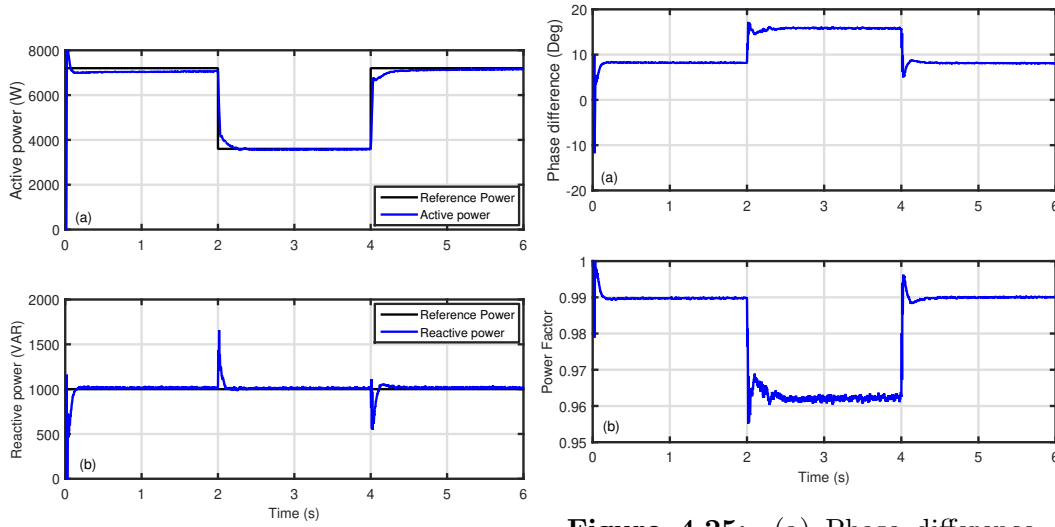


Figure 4.24: Active and Reactive power injection into grid

Figure 4.25: (a) Phase difference between grid voltage and current (b) Power factor

Table 4.3: Real and reactive power Injection

Parameter	Existing Method	Existing Value	Proposed Method	Proposed Value
Case 2: Full Loading (P=7200 W and Q=1000)				
Power Factor	Theoretical	0.9905	Automated QFT	0.9905
Phase Difference (Deg)	Calculation	7.9039	Controller	7.9039
Case 2.1: Half-Full Loading (P=3600 W and Q=1000)				
Power Factor	Theoretical	0.9635	Automated QFT	0.9635
Phase Difference	Calculation	15.52	Controller	15.52

With the application of the proposed robust controller, the system will perform under heavy and light loading conditions under active power injection and reactive power consumption, corresponding values are tabulated in Table 4.4.

4.9.3 Case 3: Desired Active power P=7.2 kW injected to grid and Q= - 1 kW Consumed from grid

When the electric power demand on grid is high, the PEMFC should deliver more real power to grid. The system may also need to supply the inverter with reactive energy to raise grid voltage. The reference values of P and Q are set to 7.2 kW and

-1 kVar (Consumed from grid). In this simulation, The performance of the controller is investigating with active and reactive power control under heavy loading and light loading conditions. The fuel cell based DG operates heavy loading condition from $t=0$ s to $t=2$ s and light loading condition from $t = 2$ s to $t=4$ s the active power reduced to 3.6 kW, which is normally low. Satisfactory performance is achieved with the proposed QFT robust controller shown in Figs. 4.26-Fig. 4.28.

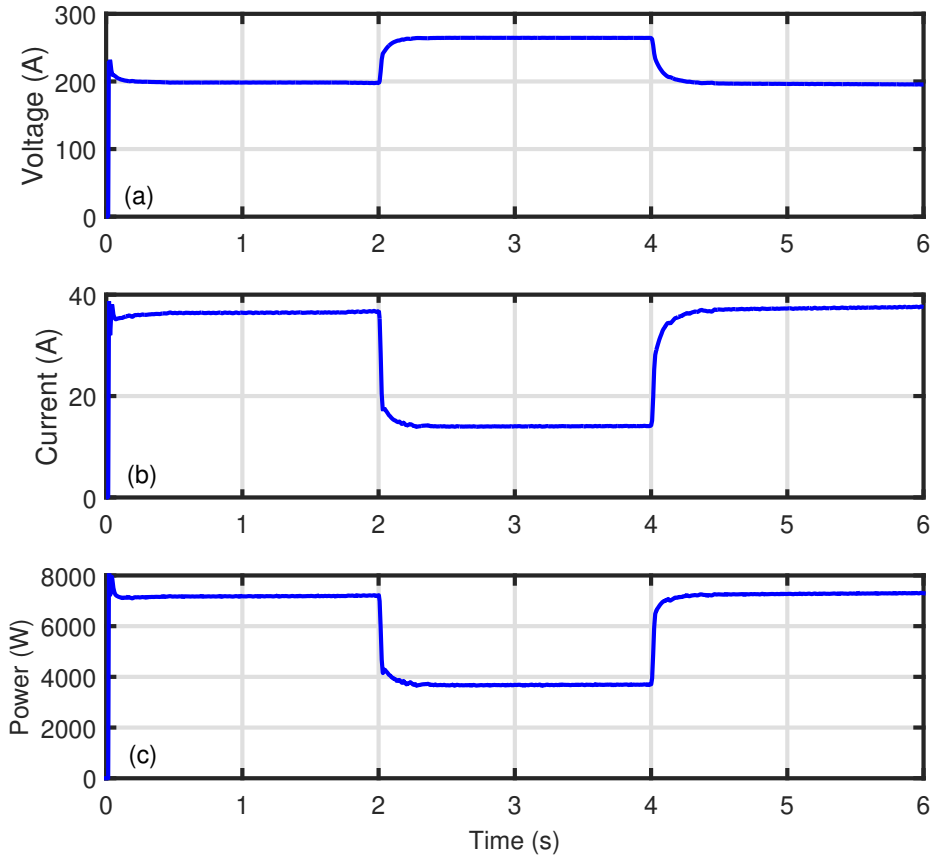


Figure 4.26: fuel cell output (a) voltage (b) current (c) Power

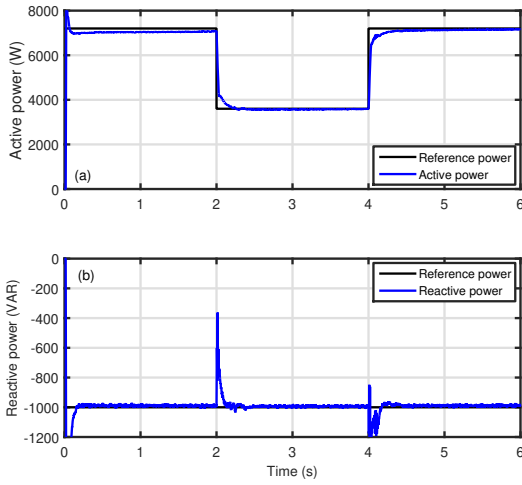


Figure 4.27: Active and Reactive power injection into grid

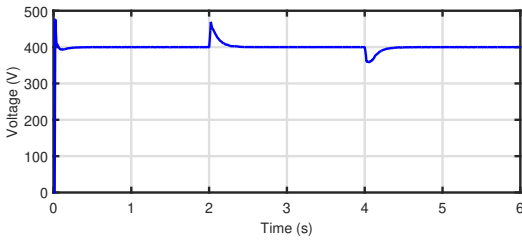


Figure 4.29: DC-link Voltage

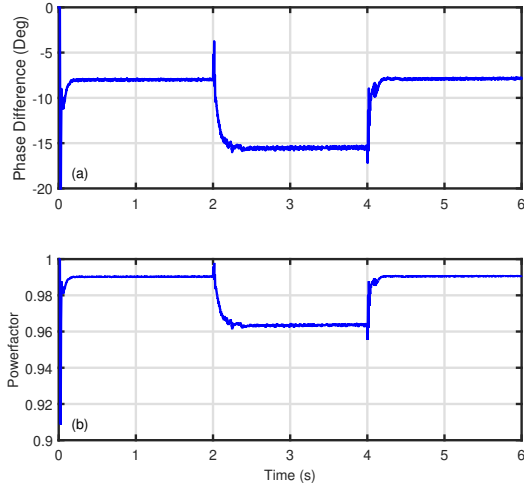


Figure 4.28: (a) Phase difference between grid voltage and current (b) Power factor

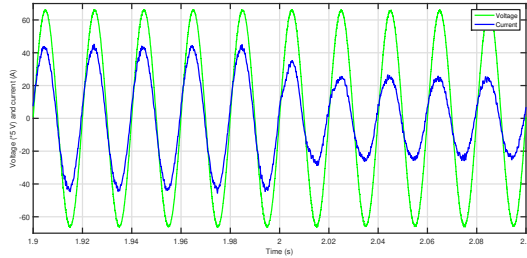


Figure 4.30: Grid voltage and current

Table 4.4: Real power Injection and reactive power consumption

Parameter	Existing Method	Existing Value	Proposed Method	Proposed Value
Case 2: Full Loading (P=7200 W and Q=-1000)				
Power Factor	Theoretical Calculation	0.9905	Automated QFT Controller	0.9905
Phase Difference (Deg)		-7.9039		-7.9039
Case 2.1: Half-Full Loading (P=3600 W and Q=-1000)				
Power Factor	Theoretical Calculation	0.9635	Automated QFT Controller	0.9635
Phase Difference (Deg)		-15.52		-15.52

4.9.4 Case 4: DC-link Voltage uncertainty

As the output current of the FCs approaches a certain amount, the output voltage of the FCs may drop sharply due to large ohms and voltage falls, which may ultimately lead in the voltage converter to weak voltage regulation and input DC voltages instability. A 15% decrease in the boost converter reference voltage from $t = 2$ s to $t = 4$ s is considered to determine the impact of input voltage uncertainty. Fig. 4.31 demonstrates the output power of the fuel cell voltage, current and power for the proposed QFT controller. In the event of fluctuations in input DC voltage, the result shows the satisfactory output of the proposed method for controlling active and reactive power. Output voltage and current of fuel cell are also shown in Fig. 4.31.

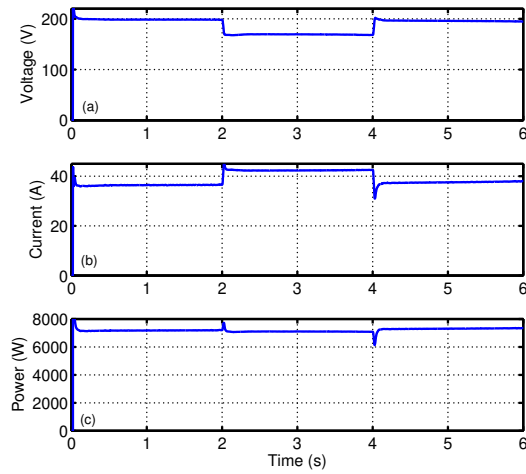


Figure 4.31: fuel cell output (a) voltage (b) current (c) Power

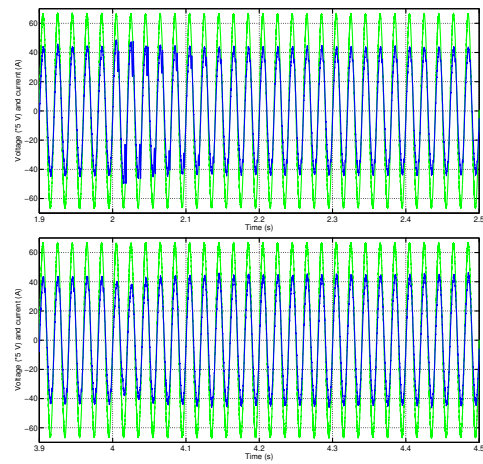


Figure 4.32: Grid voltage and current

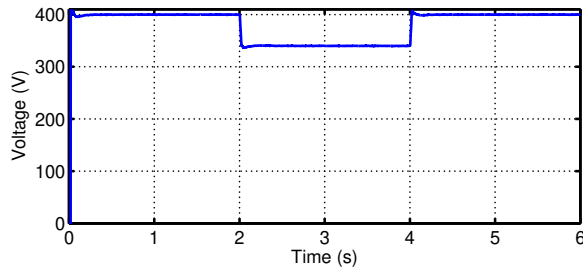


Figure 4.33: DC-link Voltage

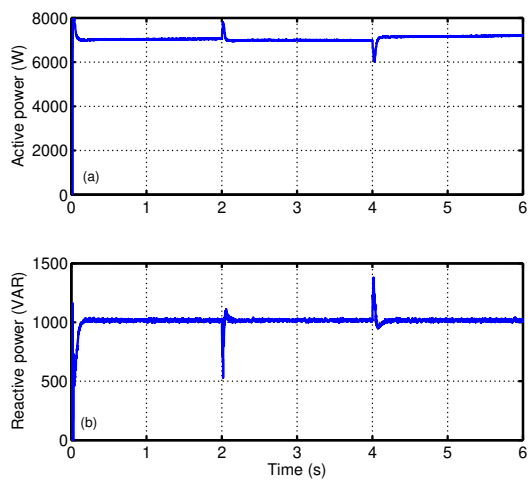


Figure 4.34: Active and Reactive power injection into grid

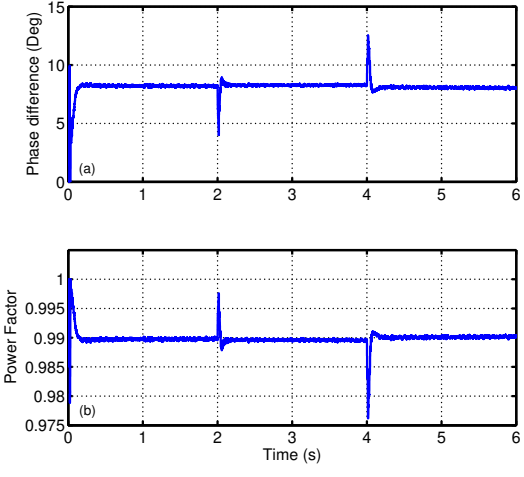


Figure 4.35: (a) Phase difference between grid voltage and current (b) Power factor

4.9.5 Case 5: Grid Voltage uncertainty

To evaluate the robustness of proposed QFT controller with respect to the grid-side voltage variations. Grid voltage increased by 15% from $t = 1$ s to $t = 3$ s and decreased by 15% from $t=3$ s to $t=5$ s.

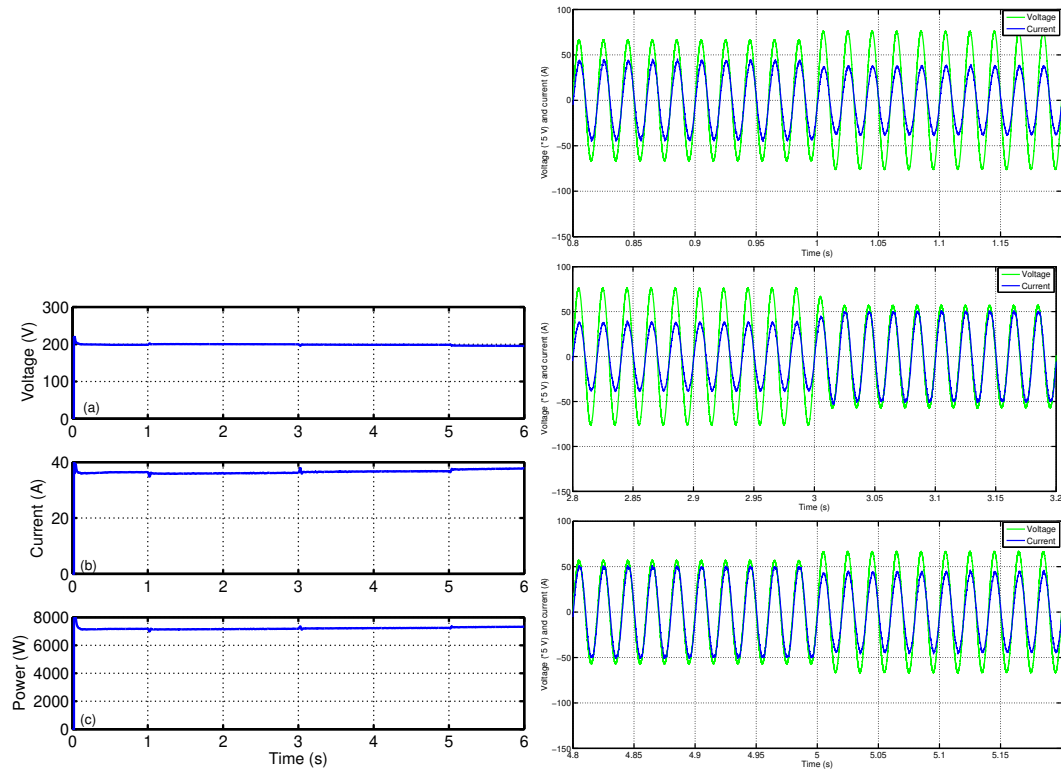


Figure 4.36: fuel cell output (a) voltage (b) current (c) Power

Figure 4.37: Grid voltage and current

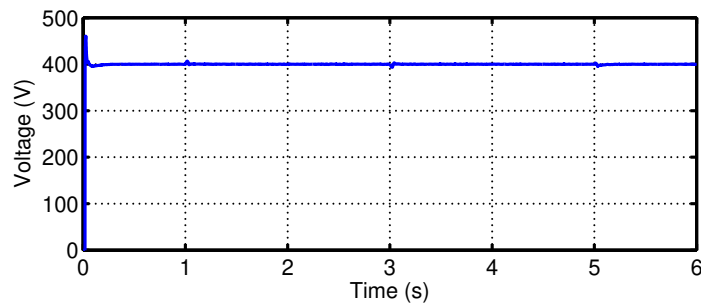


Figure 4.38: DC-link Voltage

The Figure 4.39 shows that, despite the distortion of grid voltage, the proposed

controller can successfully control the output of the system and improve grid disruption.

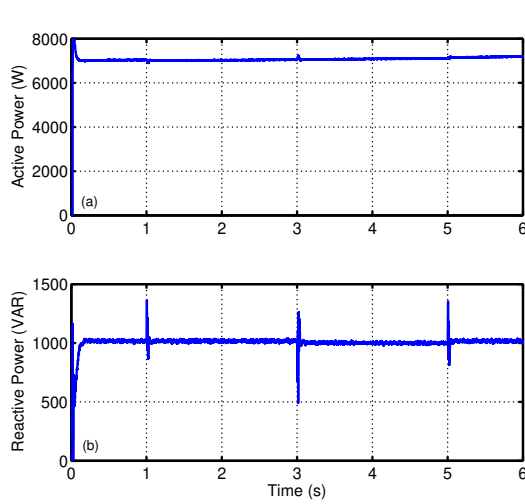


Figure 4.39: Active and Reactive power injection into grid

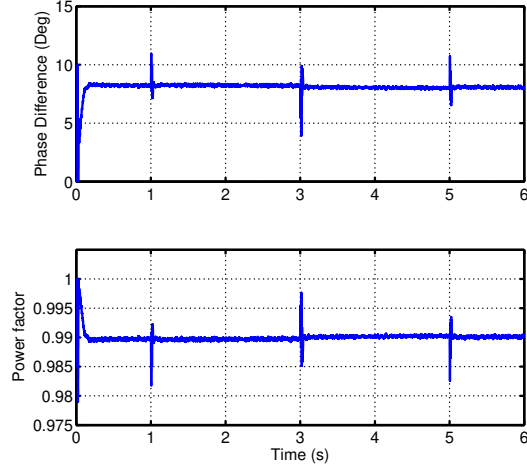


Figure 4.40: (a) Phase difference between grid voltage and current (b) Power factor

4.10 Summary

1. Active and reactive power controller design for grid connected PEMFC system were investigated.
2. Genetic algorithm based automated QFT controller is designed for DC-DC boost converter and Inverter to regulate DC-link voltage and power flow control respectively.
3. Two loop (voltage and current) control scheme used to control the active and reactive power flow of the inverter.
4. The PI controller is not suitable to control the active and reactive power, but the proposed controller shown enhanced performance with unity power factor while feeding the resistive load.
5. The robustness of the proposed controller is successfully evaluated by careful assessment of QFT controller under different uneven conditions like heavy and light loading conditions. Further, uncertain conditions like, DC-link voltage and grid voltage distortion conditions also investigated.

Chapter 5

QFT controller for Hybrid green renewable energy power system

The constantly growing energy usage, the rising cost, and exhaustion of coal and oil and the growing global environmental concerns have created a lot of attention in sustainable energy distributed sources, such as green sources of renewable energy, fuel cell-based generation systems. Power generation from wind and solar photovoltaic systems is one of the most promising technological generation of renewable energy, with growth exceeding most optimistic expectations. Power generation from fuel cell is a clean and efficient. Their numerous merits, including high efficiency, null and low emissions of polluting gases and flexible modular structures have great potential for being a crucial power production technology of the future. Wind and solar energy are highly climate dependent. Multi-source hybrid renewable energy systems offer greater power reliability than systems that consist of one resource. Hybrid renewable energy systems have therefore attracted global attention in research. In this chapter, the PMSG based WECS,PV and PEMFC model developed in previous chapters is used to design a grid connected hybrid wind-PV-FC system.

5.1 Unit Sizing

The size of each generation unit play vital role in hybrid systems. The unit sizing procedure elaborated based on the electrical energy consumption of residential buildings in IIT Bombay campus with the system structure consists hybrid green renewable energy with wind-PV-FC system. The load data is collected by IIT Bombay campus

(Mammen et al., 2018). The dataset consists of electricity consumption data from 60 (3 BHK) apartments located inside the campus. The data recorded at each building using smart-meter at sampling time of 5s. The data is down sampled at 1-hour granularity.

For this work, 33 apartments load data on 27-05-2018 (Sunday) is used to find the unit sizing of hybrid system. The total load demand of 33 3BHK apartments are calculated as 17.6 kW. The average wind speed varies 5 m/s to 7 m/s in western coastal region. On an average 15% of installed capacity can utilize effectively. In order to utilize the maximum power generation from wind, The maximum capacity of wind turbine is chosen as 80 kW. 80 kW wind turbine consist of 4 parallel operation of 20 kW wind turbines. The solar irradiation continuously varies from morning to evening, the utilization factor of PV can be selected as 10% over a period of one year. PV rating calculated as,

$$P_{pv,rating} = \frac{P_{Dem} - P_{Wind,rated} \times windutilizationfactor}{PVutilizationfactor} \quad (5.1)$$

The calculated PV array size is calculated 56 kW. To leave safe margin, an 57.7 kW of PV array is used. The configuration of PV array is modelled as 84 series and 8 parallel sub-module converters, each PV sub-module (24 cells) generates $v_{pv} = 12.26V$, $i_{pv} = 7.83A$ and $p_{pv} = 96W$.

A synchronous buck converter is used to maintain stable power from PV with $v_{o1} = 8.6V$, $i_{o1} = 10A$ and $P_{o1} = 86W$ (Khan and Xiao, 2016). When there is no wind and solar energy, a fuel cell must supply the highest demand. Therefore, from the above Fig. 5.2 the peak load demand 28.8 kW. To leave safe margin, the fuel cell is modelled with 32 kW consists of 8 series and 8 parallel connected fuel cell stacks are used.

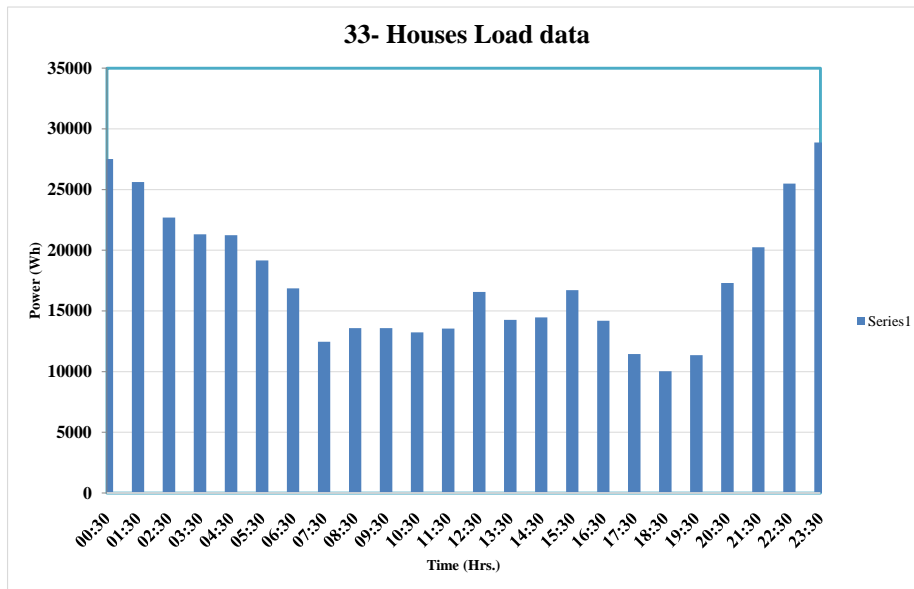


Figure 5.1: 24-Hrs Load data (Mammen et al., 2018).

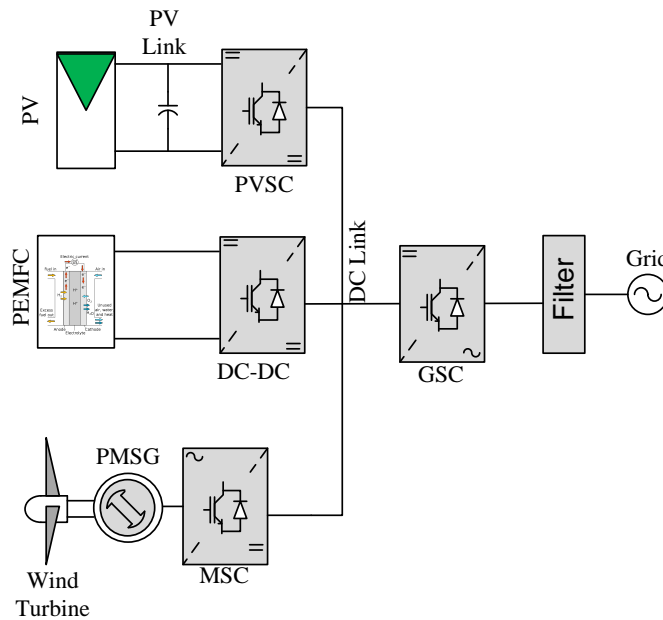


Figure 5.2: Grid Connected Hybrid Renewable energy system

5.2 80 kW PMSG based WECS Performance

In this section, wind farm configuration, and the simulation results are presented. Based on the unit sizing procedure discussed in the previous section 5.1, 80 kW permanent magnet synchronous generator (PMSG) based wind energy conversion system has to be designed. IIT Bombay campus is residential area, so that small rating with parallel operated wind systems are preferable for easy operation.

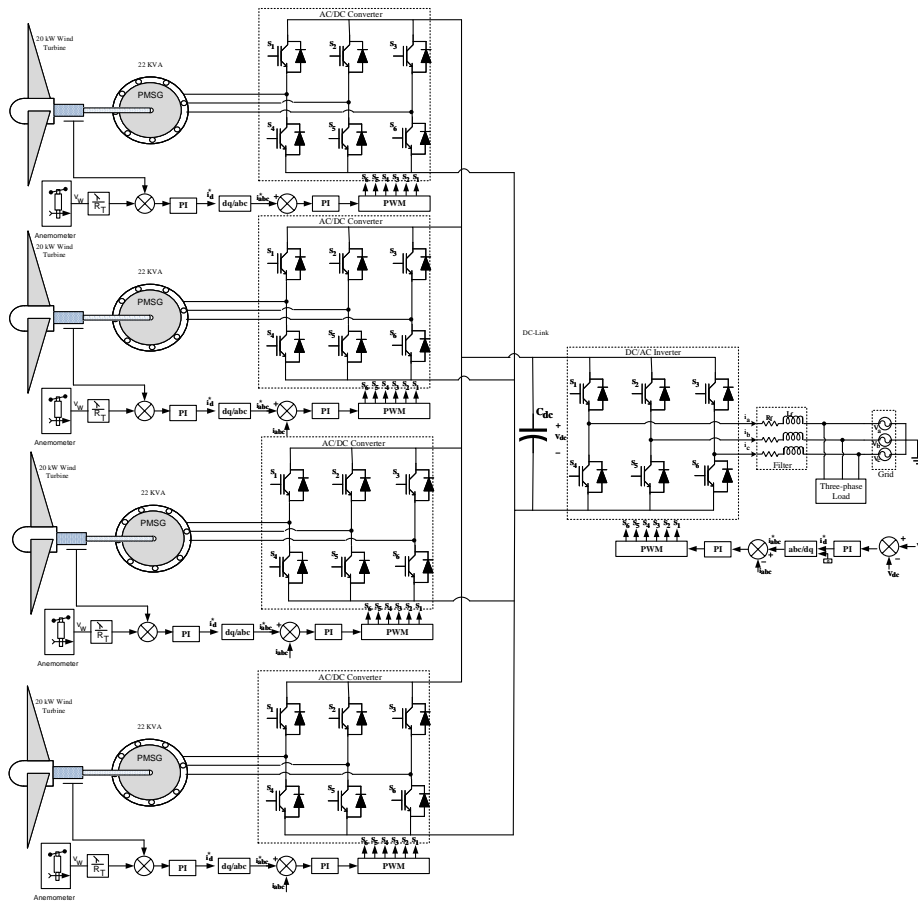


Figure 5.3: Schematic diagram of grid connected wind power system

The block diagram of grid connected 80 kW PMSG wind turbine is shown in Figure 5.3, 20 kW at 11 m/s base speed wind turbine and nominal rotating speed of 22 rad/s is considered. surface mounted PMSG has power of 22 KVA with 18 poles and flux linkage of 0.915386 Wb machine is used. Grid voltage is taken as $400 V_{rms}$ and the DC-link voltage is selected as 720 V.

In this work, 4 wind turbines are connected in parallel, each 20 kW wind turbines

connected to 22 KVA PMSG machines are chosen. In the coastal region, the average wind speed is selected as 6 m/s. Three phase grid connected 20 kW PMSG based WECS under step variation in wind speed is analysed in the second chapter. In this chapter, the robustness of the proposed controller under stochastic variation of wind speed is evaluated and the wind speed is shown in Fig. 5.4.

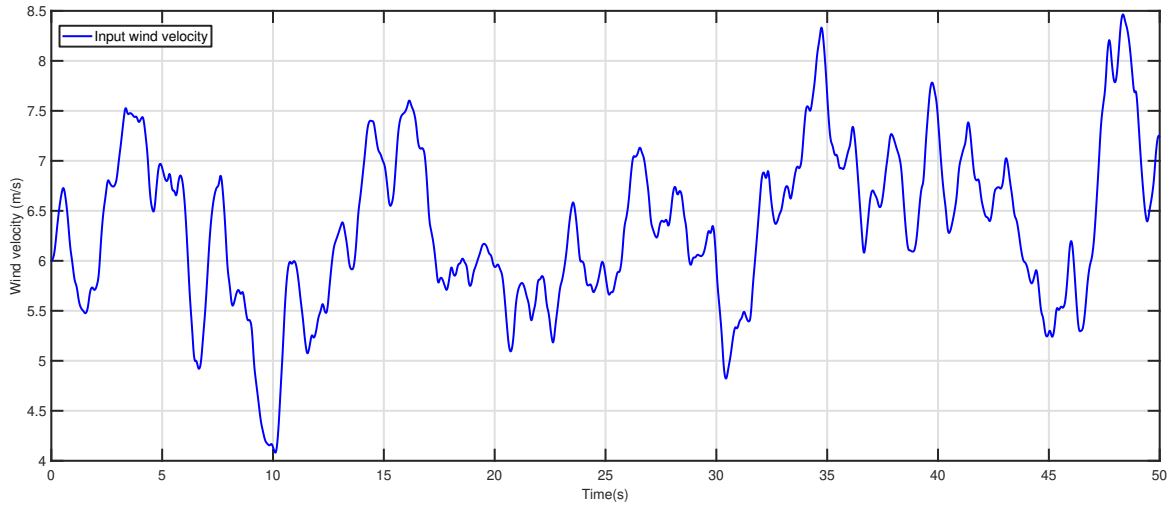


Figure 5.4: wind profile

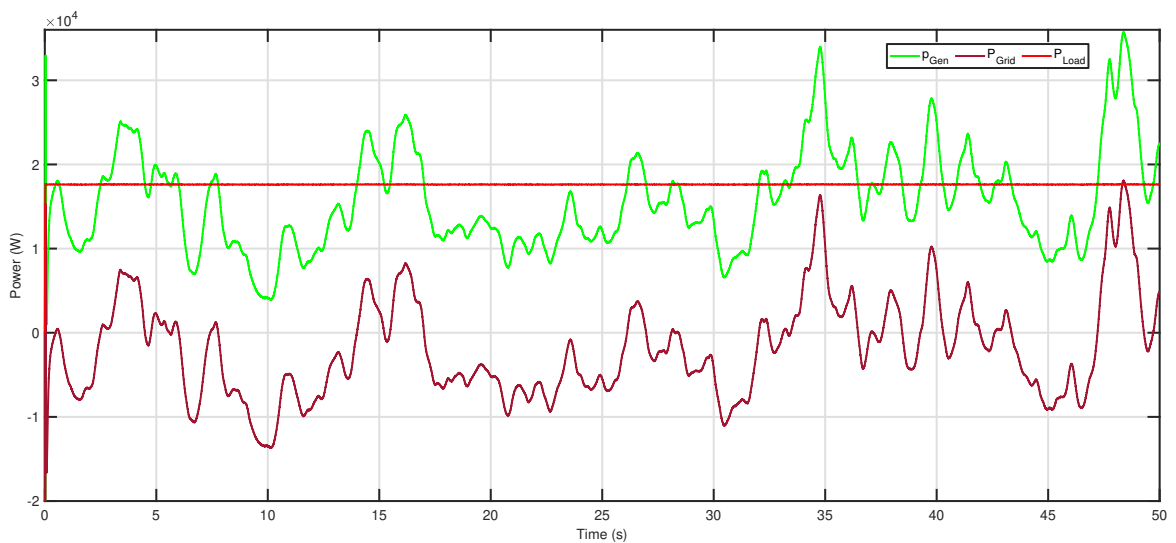


Figure 5.5: Power injection

In Figure 5.5, the average load is considered as 18 kW is highlighted with red colour, the total generated power from PMSG based WECS for the given wind speed

is highlighted with green colour, and the grid power shown in Orange colour. The wind speed is less than 6.5 m/s from 20 s to 25 s shown in Figure 5.4, The power injection from the inverter is less than the load demand shown in Figure 5.5. In this case grid supplies the power to maintain the fixed load to operate continuously. The wind speed is more than 6.5 m/s from 33- 36 s shown in Figure 5.4, The power injection from inverter is higher than the load demand, so the generated inverter power injected to grid shown in Figure 5.5. It is observed from Figure 5.5 that whenever wind turbine unable to supply the load power, grid supplies and for higher wind speeds, the grid receives the surplus power.

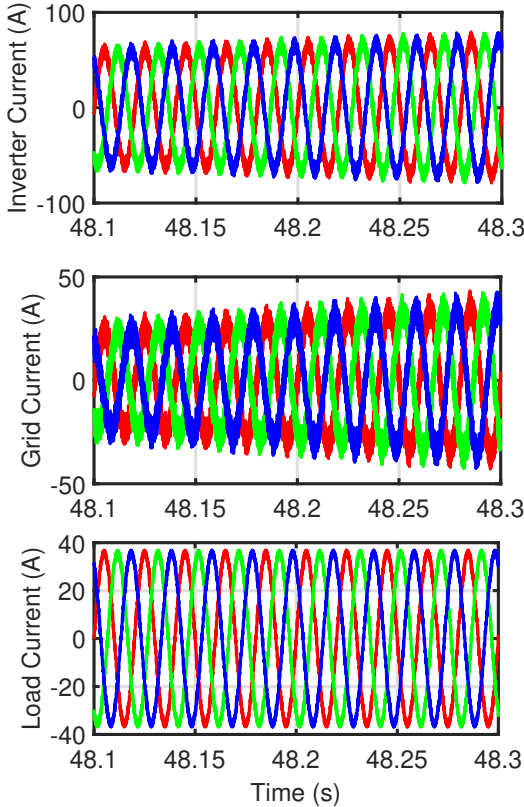


Figure 5.6: Current Injection

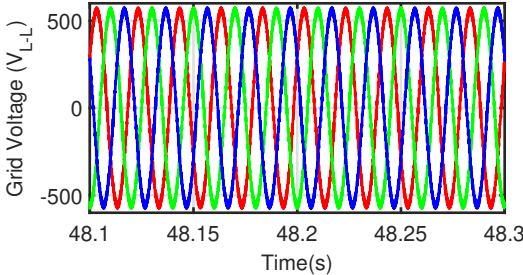


Figure 5.7: Grid Voltage

The inverter, grid and load currents are shown in Figure 5.6, The inverter current higher than the load current so the surplus power injected to the grid. Grid voltage response at power injection from inverter to grid is shown in Figure 5.7.

5.3 57.7 kW Grid connected PV

Photovoltaic systems are gaining popularity among the renewable energy sources, with high demand in the energy sector and reducing the environmental pollution from the excess of non-renewable energy sources. One of the key decisions to consider before installation is to choose a suitable size and location for installing a large photovoltaic system. Based on the unit sizing procedure elaborated in the previous section 5.1, 57.7 kW PV is selected and the block diagram is shown in Figure 5.8.

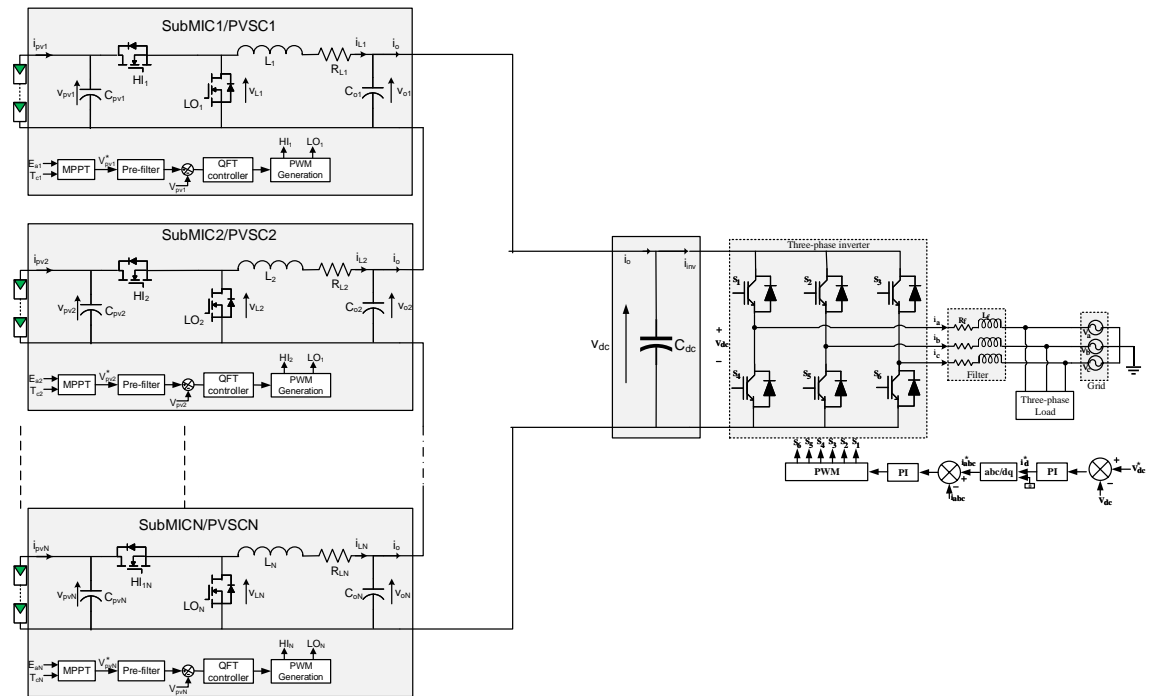


Figure 5.8: Schematic diagram three-phase grid tied PV system

In this work, maximum power point tracking controller is implemented for PV at sub-module level. Each sub-module consists 24 cells in series, the output voltage and current of sub-module is 12.26 V and 7.83 A respectively. The output power of PV sub-module is 96 W. A buck converter is implemented for each sub-module, the output voltage and current values are 8.6 V and 10 A respectively. The total output power from sub-module integrated converter (SMIC) is calculated as 86 W. As per the requirement 84 series and 8 parallel configuration of SMIC's are required.

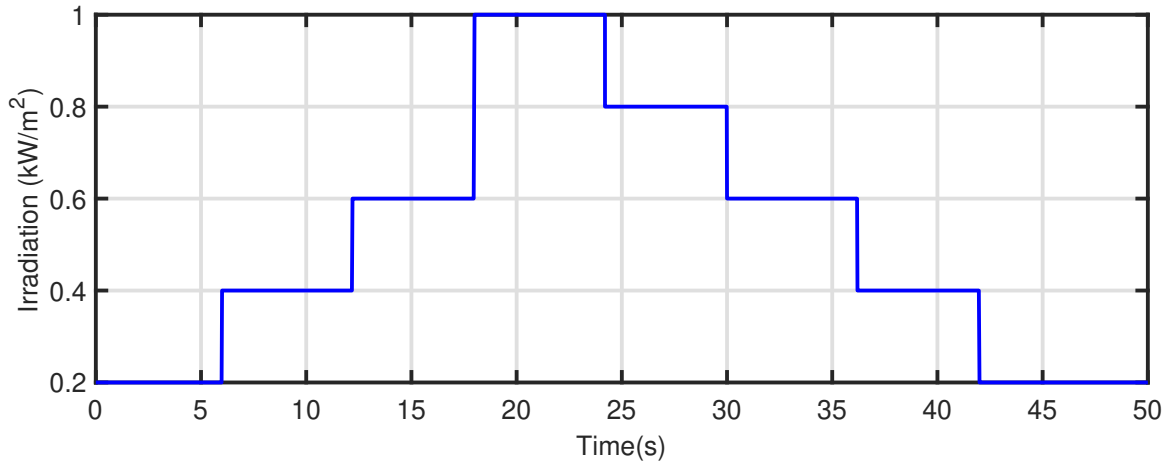


Figure 5.9: Irradiation

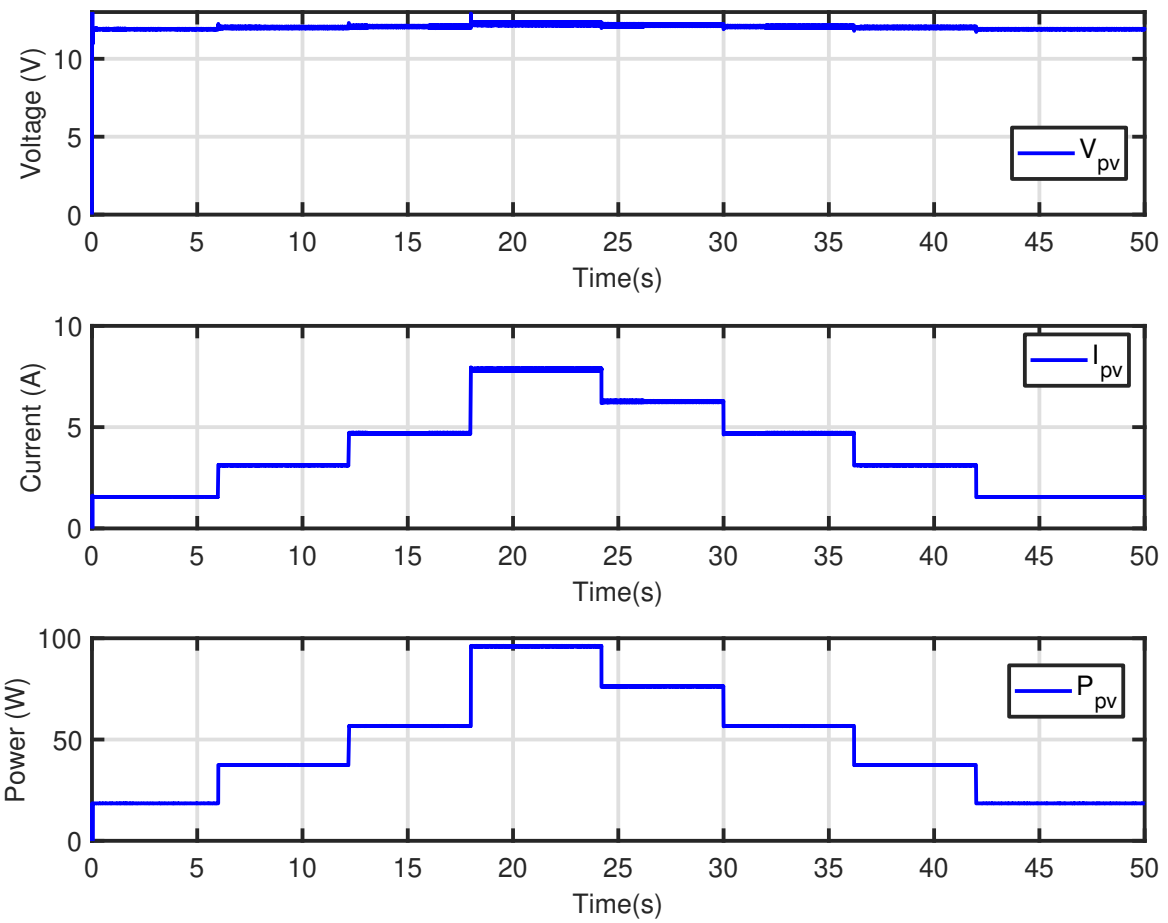


Figure 5.10: PV voltage current and power

Step variation of irradiation is considered to evaluate the performance of the robust

controller for grid connected PV system is shown in Figure 5.9. The PV voltage, current and power variations under constant temperature of 25 °C, step variation in irradiance is shown in Figure 5.10. The PV voltage, current and power values are tabulated in Table 5.1.

Table 5.1: PV voltage and current under step variation of irradiation

Temperature (°C)	Irradiation (kW/m ²)	$V_{mpp}(V)$	$I_{mpp}(A)$	$P_{mpp}(W)$
25	1000	12.264	7.83	96.027
	800	12.168	6.26	76.172
	600	12.072	4.69	56.617
	400	12.000	3.12	37.440
	200	11.904	1.55	18.451

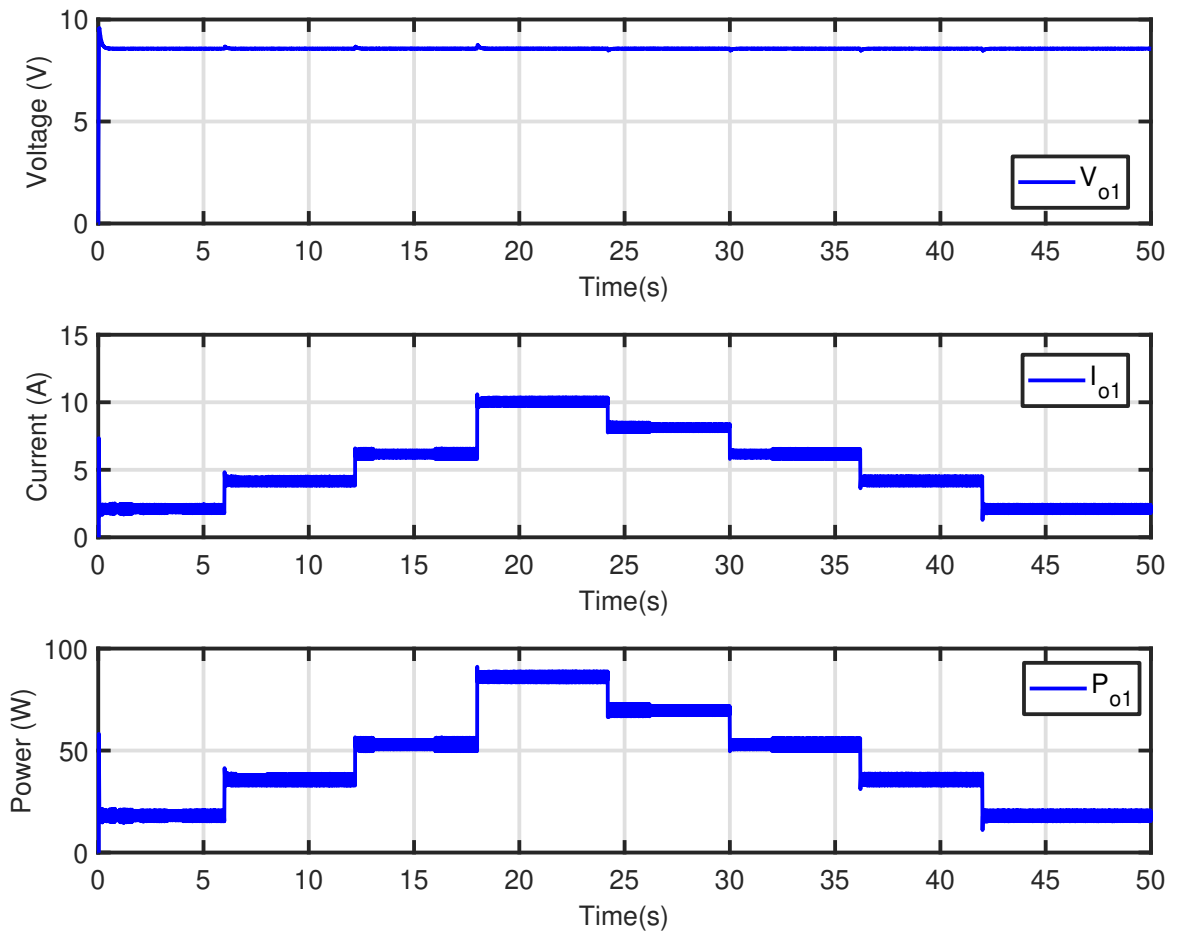


Figure 5.11: SMIC voltage current and power

SMIC output voltage current and power variations are described in Figure 5.11 and the corresponding values are tabulated in Table 5.2.

Table 5.2: PV-SMIC voltage, current and power under step variation of irradiation

Temperature ($^{\circ}C$)	Irradiation (kW/m^2)	$V_{mpp}(V)$	$I_{mpp}(A)$	$P_{mpp}(W)$
25	1000	8.6	10	86
	800	8.532	8	68.256
	600	8.465	6	50.79
	400	8.415	4	33.66
	200	8.347	2	16.694

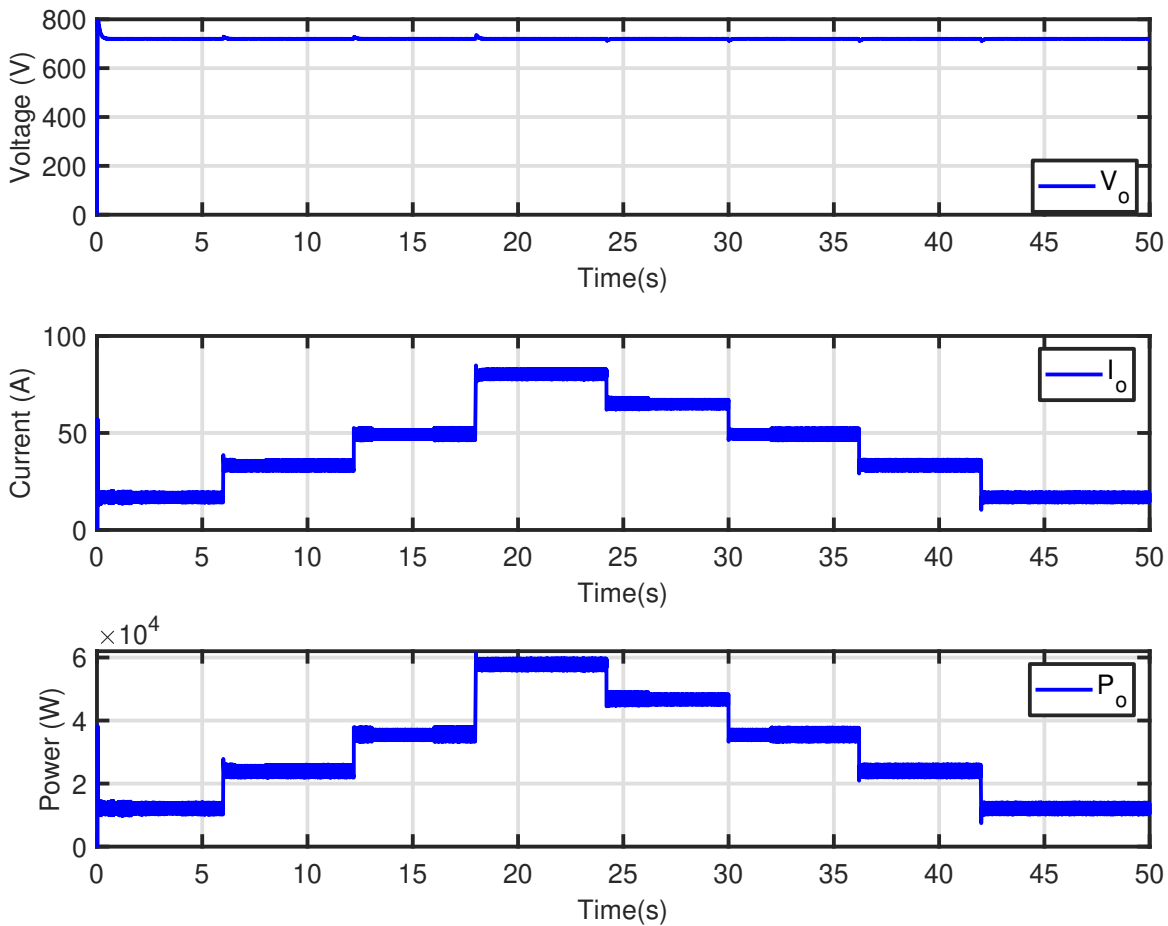


Figure 5.12: Total output voltage current and power

To design 57.7 kW PV system, 84 series and 8 parallel SMIC are required, the

output power is shown in Figure 5.12 and the corresponding values are tabulated under different irradiance conditions in Table 5.3.

Table 5.3: Total SMIC voltage, current and power under step variation of irradiation

Temperature ($^{\circ}C$)	Irradiance (kW/m ²)	$V_{mpp}(V)$	$I_{mpp}(A)$	$P_{mpp}(kW)$
25	1000	722.4	80	57.792
	800	716.688	64	45.868
	600	711.06	48	34.130
	400	706.86	32	22.619
	200	701.148	16	11.218

The power electronic converter helps to maintain the constant DC-link voltage shown in Figure 5.13. The grid voltage is considered as $400 V_{rms}$, as shown in Figure 5.14. This simulation work intends to show the inverter operation under three cases. It is observed from Figure 5.15, at $t = 0$ to 12 s and $t = 36$ s to 50 s, both the inverter and grid supplies power to feed the load. At $t = 12$ to 18 s and $t = 30$ s to 36 s, the inverter alone supplies the power to load. At $t = 18$ s to 30 s, the inverter feeds the load and also the grid receives the surplus power from inverter. Primarily, the inverter controller is designed to feed the load, later the surplus amount of power injected in to grid. The power injection is shown in Figure 5.15. The current injection to grid and load is shown in Figure 5.16 - 5.18.

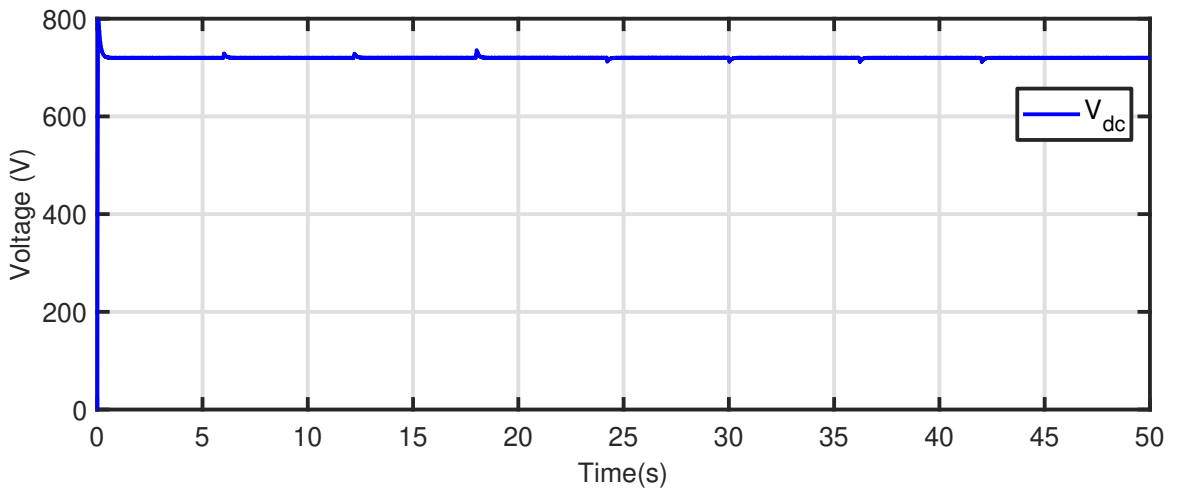


Figure 5.13: DC-link voltage

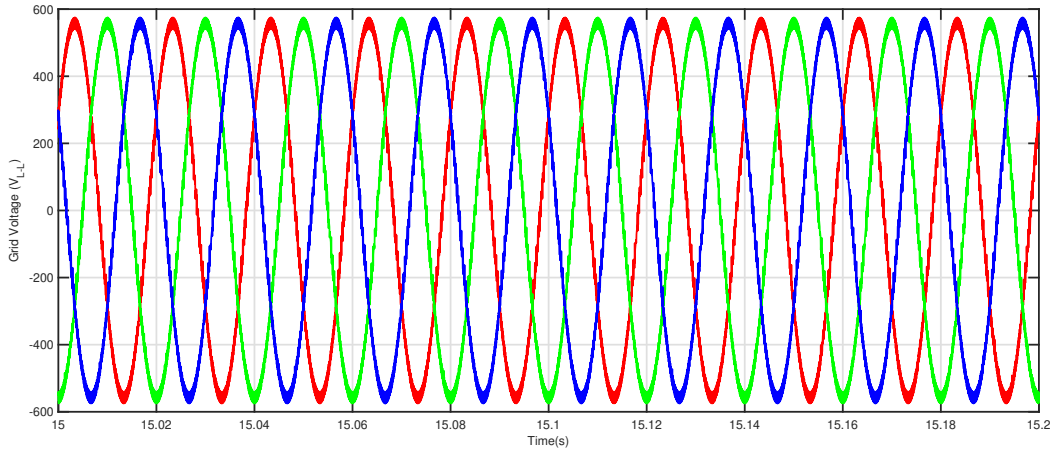


Figure 5.14: Grid Voltage

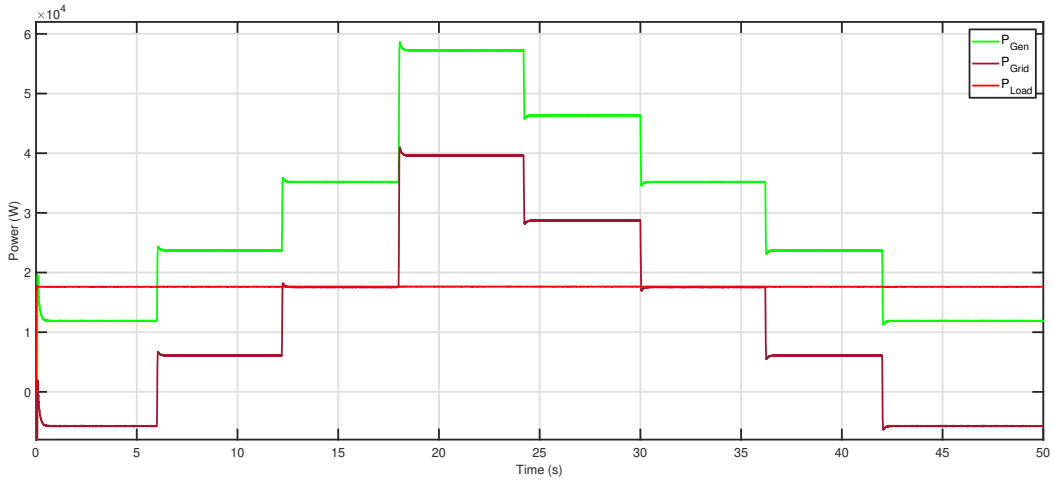


Figure 5.15: Inverter grid and load power

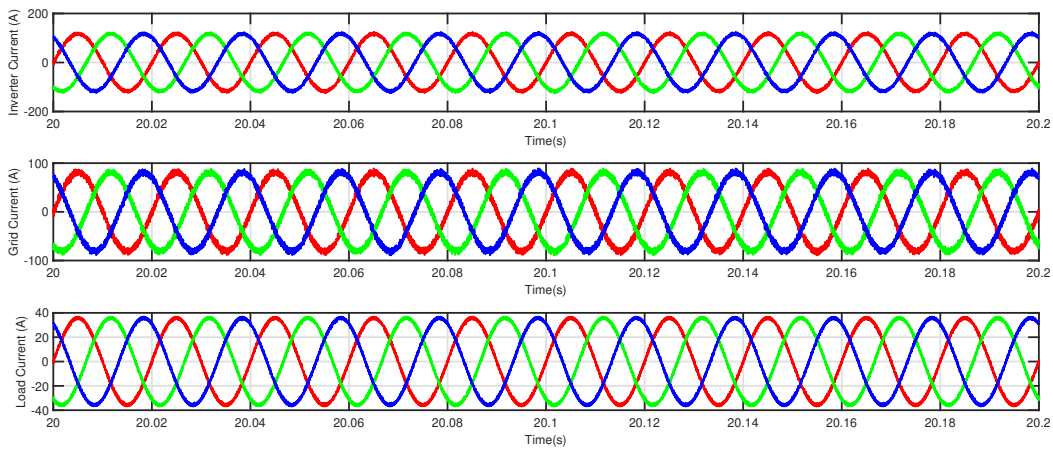


Figure 5.16: Inverter grid and load current

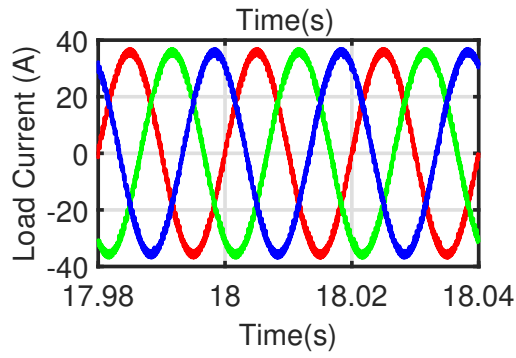
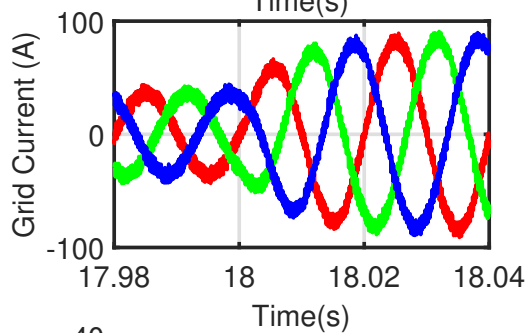
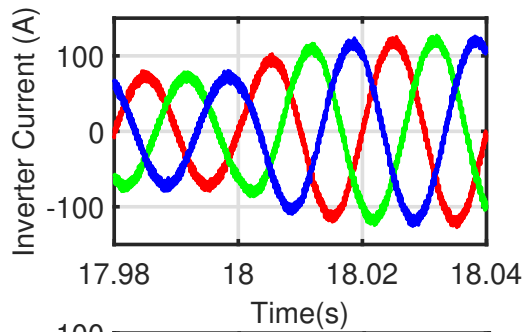


Figure 5.17: Current Injection

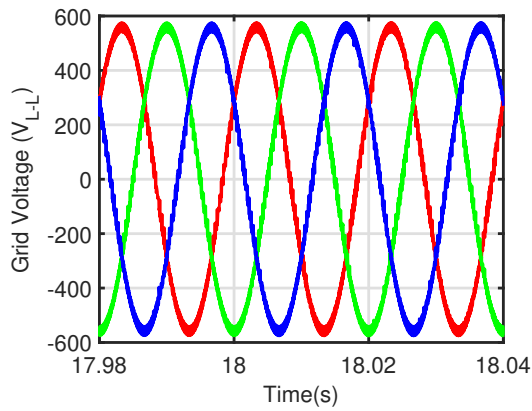


Figure 5.19: Grid Voltage

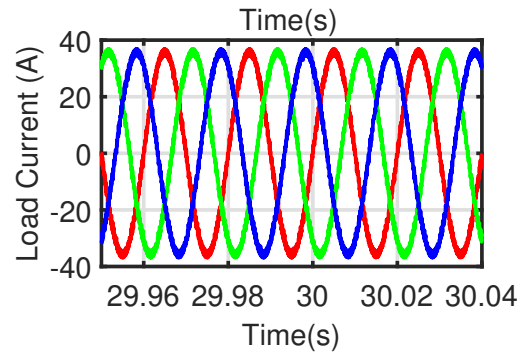
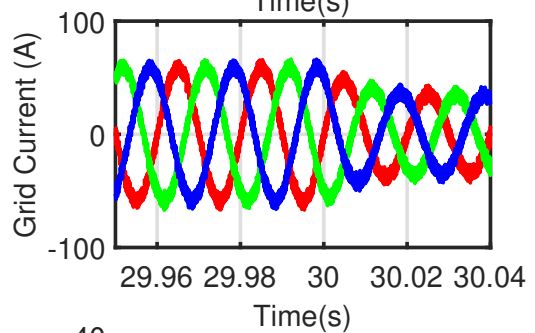
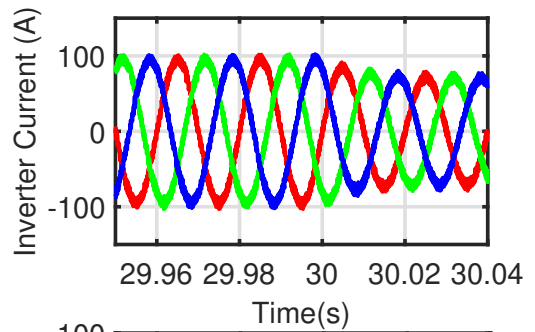


Figure 5.18: Current Injection

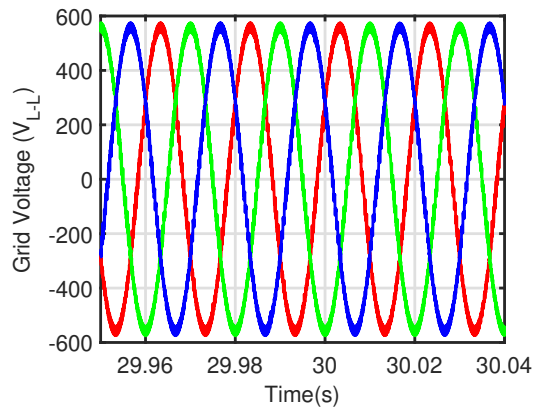


Figure 5.20: Grid Voltage

5.4 80 kW PMSG based WECS and 57.7 kW Grid connected PV

The renewable energy sources are intermittent in nature due to their dependency on environmental conditions. In the previous sections, the individual sources like wind and PV with grid intervention is used to feed the load.

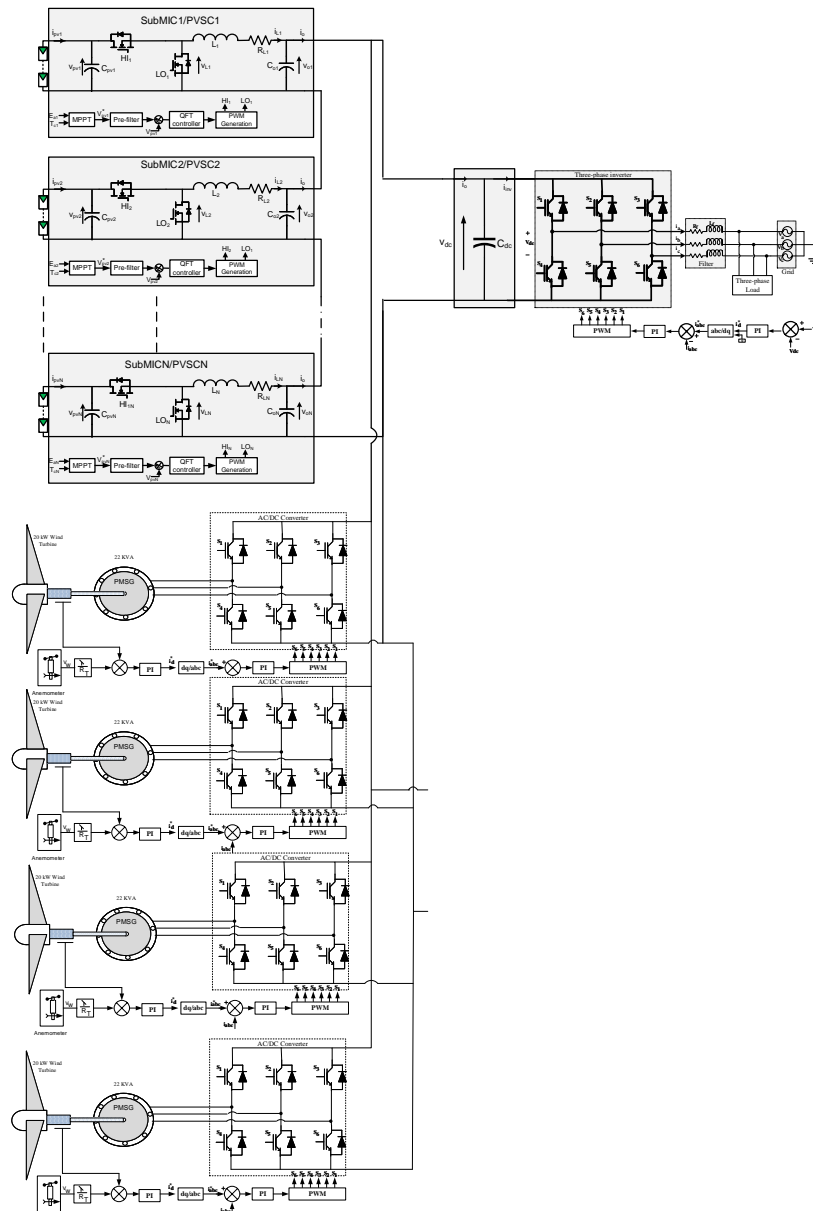


Figure 5.21: Schematic diagram of grid connected PV and wind power system

In this section, hybrid renewable energy configuration with PV and wind energy system is considered to feed the load, which is independent of grid is shown in Figure 5.21. So, the power generated from renewable energy sources is used to feed the load and the surplus power injected into grid. In this case, hybrid system is designed with the pre-designed renewable energy sources of 57.7 kW PV and 80 kW PMSG based wind system, the rating is considered as per the unit sizing procedure discussed in section 5.1.

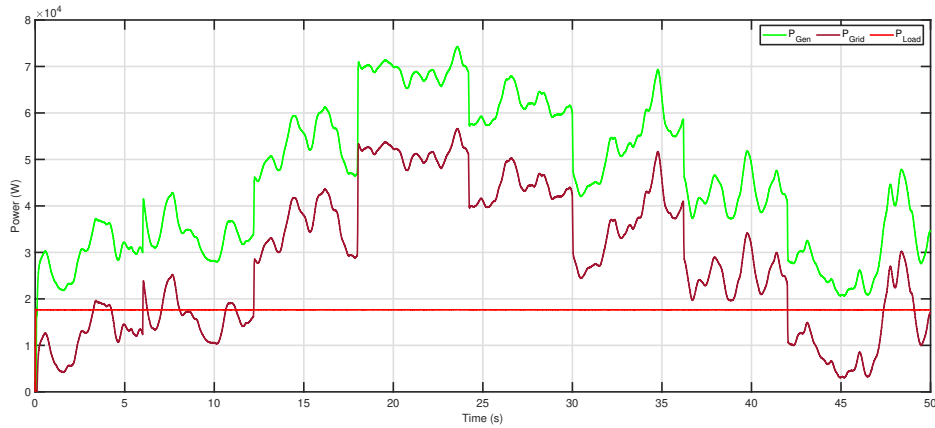


Figure 5.22: Inverter grid and load power

The proposed hybrid system is simulated for $t = 50$ s. The grid power (maroon colour) is positive, means it will absorb the power from inverter. The inverter power is positive (green colour solid line), which is higher than the load power (red colour solid line) so that the surplus plus can inject to grid as shown in Figure 5.22. In this hybrid system, the inverter, grid and load current injection waveforms are plotted shown in Figure 5.23.

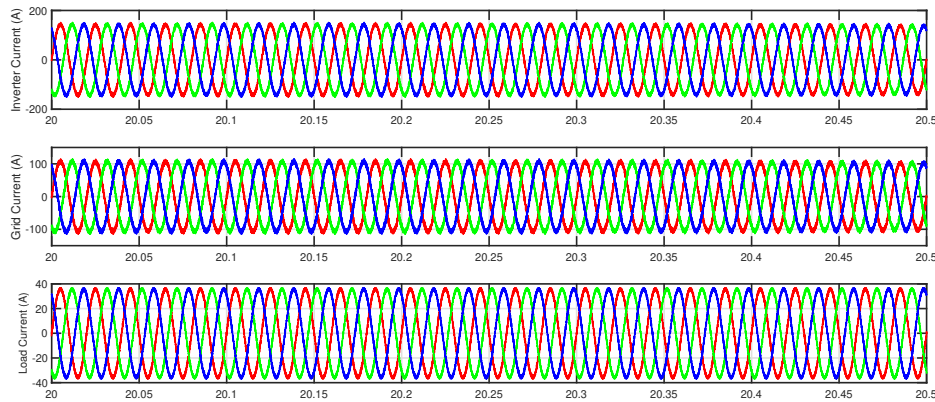


Figure 5.23: Inverter grid and load current

5.5 32 kW PEMFC Grid connected operation

In this case, 32 kW PEMFC grid connected is designed based on the unit sizing procedure proposed in the previous section 5.1 is shown in Figure 5.24. 500 W fuel cell is considered, each fuel cell delivers 29.62 V, 16.88 A and 500 W voltage, current and power are discussed in chapter 4.5. Fuel cell stack is designed based on the boost converter input voltage and PEMFC output power. 32 kW fuel cell stack consists of 8 cells in series and 8 cells are connected in parallel, so that the fuel cell output stack voltage and current is 236.96 V, 135.04 A and 32 kW power shown in Figure 5.25, Figure 5.26 Figure 5.27 respectively. PEMFC fuel cell is a constant power source, to support renewable energy generation due to their intermittent nature. PEMFC will take long time to reach its steady state value that is discussed in chapter 4.5. In this work, the system is simulated for 1200 s to prove that the system operated under normal condition for a long duration.

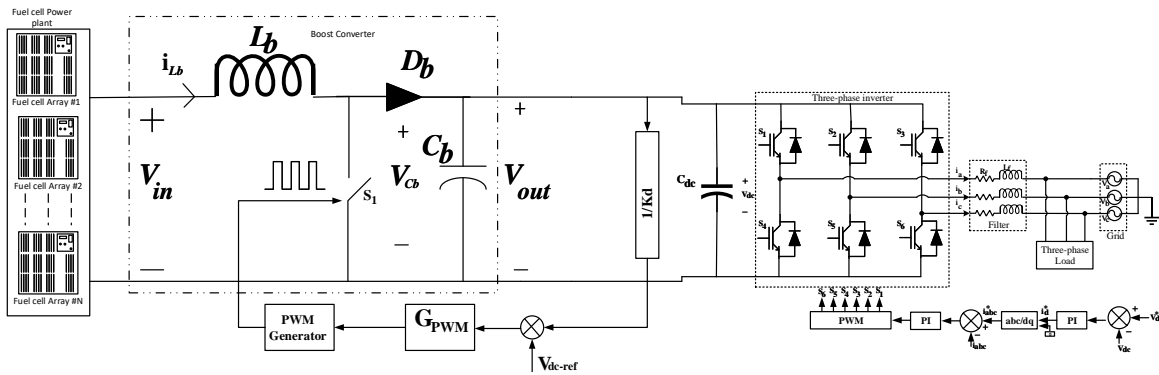


Figure 5.24: Schematic diagram three-phase grid tied FC power plant

5.5.1 Boost Converter Circuit Design

Peak, rated and tolerable ripples in voltage and current are to be considered to design the boost converter circuit parameters. The input voltage of DC-DC converter is equal to the output of fuel cell of 237 V, and the DC-link voltage or the boost converter output voltage is set to 720 V. The switching is selected as 5 kHz. For three phase applications, DC-link voltage is chosen as 720 V. Then the approximate input voltage of boost converter is calculated as $(1 - 0.67) \times 720 = 237$ V. Therefore, the number

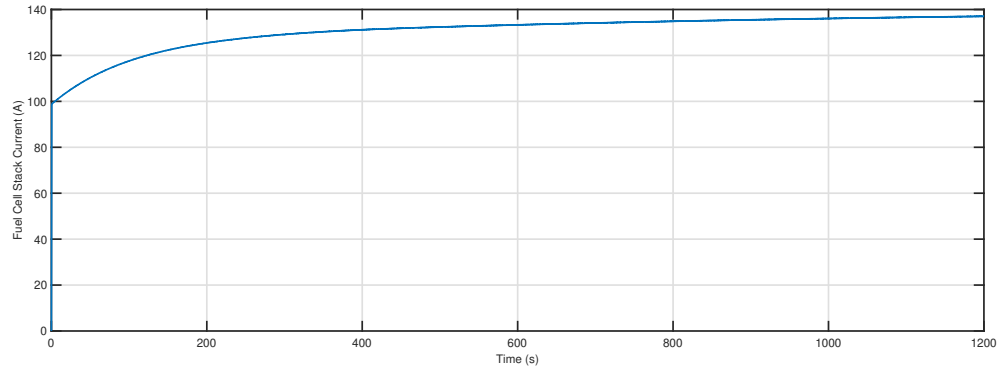


Figure 5.25: FC stack current

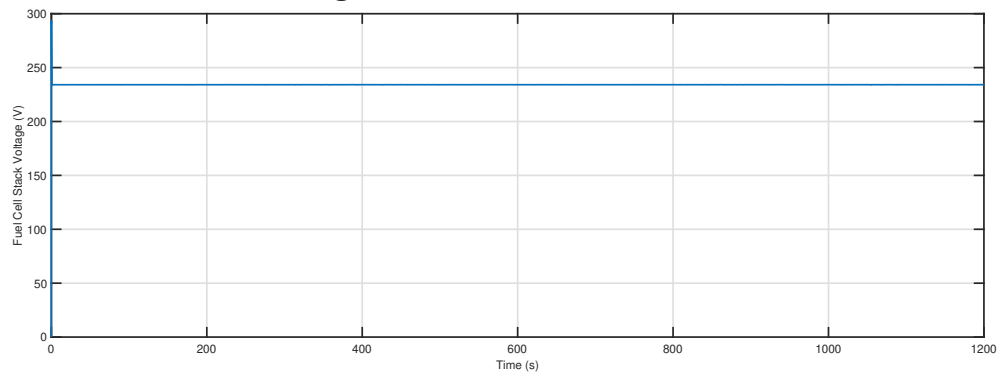


Figure 5.26: FC stack Voltage

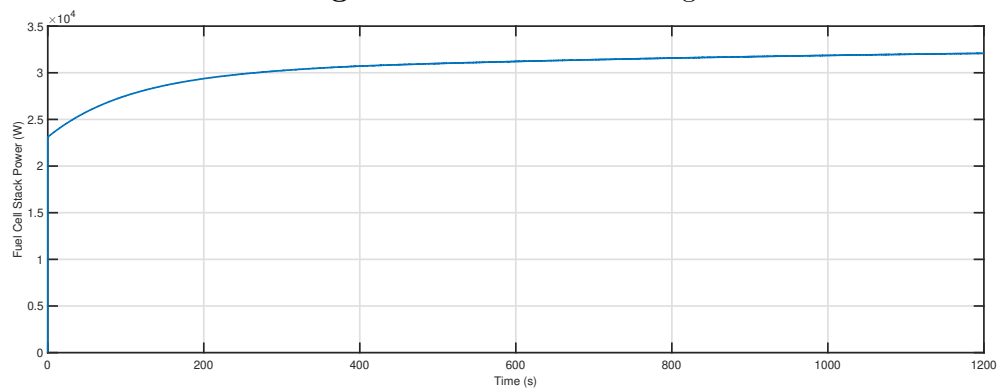


Figure 5.27: FC stack power

of series PEMFC stacks calculated as follows,

$$N_s = \frac{V_{FCarray}}{V_{PEMFC}} = \frac{237}{29.62} = 8 \quad (5.2)$$

The required number of parallel connected PEMFC stacks is calculated as,

$$N_P = \frac{32000}{8 \times 500} = 8 \quad (5.3)$$

Therefore, 32 kW PEMFC array is composed of $8 \times 8 = 64, 500 - W$ stacks. The design circuit parameters are shown below,

1. In the first step, equivalent resistance calculation to maintain the constant DC-link voltage at the output of boost converter, is calculated as,

$$R = \frac{V_{out}^2}{P_{rated}} = \frac{720^2}{32000} = 16.2\Omega \quad (5.4)$$

2. Duty Ratio is calculated as,

$$D = 1 - \frac{V_{in}}{V_{out}} = 1 - \frac{237}{720} = 0.6708 \quad (5.5)$$

3. The maximum current passing through the inductor is calculated as,

$$I_{lb,max} = \frac{V_{in}}{(1 - D)^2 R} = 135A \quad (5.6)$$

4. Inductance of boost converter value calculated by limiting the input current ripple less than 20%

$$L_b > \frac{5D(1 - D)^2 R}{f_s} > \frac{5 \times 0.6708 \times 0.3291^2 \times 16.2}{5000} > 0.0011H \quad (5.7)$$

So, The inductance should greater than 0.001 H. The uncertainty range is considered as, $1 \text{ mH} < L_b < 10 \text{ mH}$.

5. Capacitance is calculated by limiting the output voltage ripple less than 5%.

$$C_b > \frac{D}{0.05 f_s R} > \frac{0.6708}{0.05 \times 16.2 \times 5000} > 165\mu F \quad (5.8)$$

Table 5.4: Boost converter parameters

Parameter	Value
Inverter power	33 KVA
Rated Real Power P_o	32 kW
Grid Voltage V_{rms}	400 V
DC-link Voltage V_{dc}	720 V
Fundamental frequency	50 Hz
Switching frequency	5 kHz
Inductor	6 mH
Capacitor	800 μ F

So, The capacitance should be greater than $150\mu\text{F}$, The uncertainty range is considered as, $150 \mu\text{F} < C_b < 1000 \mu\text{F}$.

. The power output of PEMFC, Grid is shown in Figure 5.28. The generated power from PEMFC is injected to the load, the remaining power injected to grid.

32 kW PEMFC is designed for the three phase grid connected inverter system with residential load demand. The output power of the PEMFC fuel cell is represented as a green solid line, load demand is shown in a red line and the blue line represents the grid output power shown in Figure 5.28. It is observed from Figure 5.28 that, from $t = 0$ s to $t = 200$ s the PEMFC generates power less than the load demand so that the grid power is negative and it generates the power to feed the load. From $t = 200$ s to $t = 1200$ s the PEMFC is capable of generating more than the load power. So the grid power is positive, meaning it absorbs the surplus power.

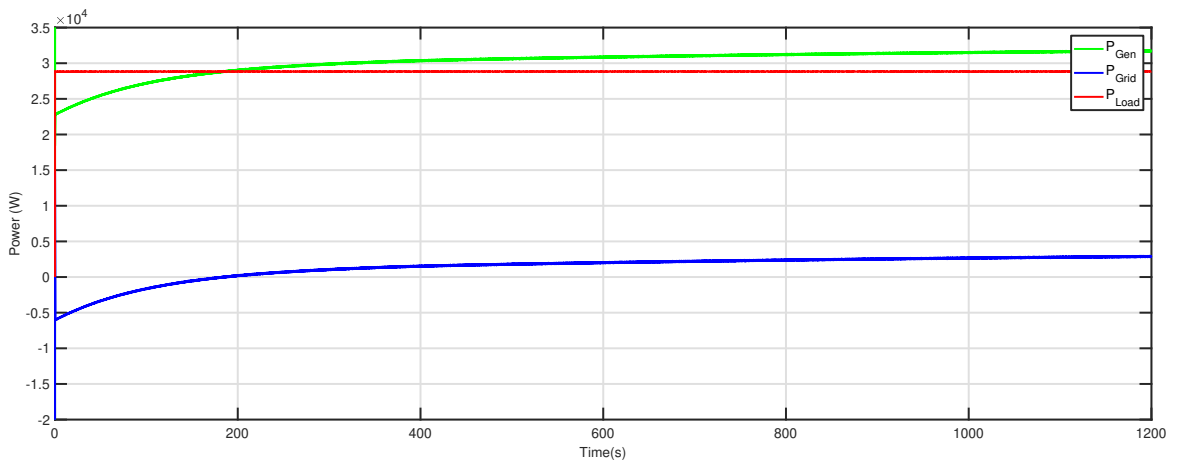


Figure 5.28: Inverter, grid and load power

5.6 80 kW WT, 57.7 kW PV and 32 kW PEMFC Grid connected operation

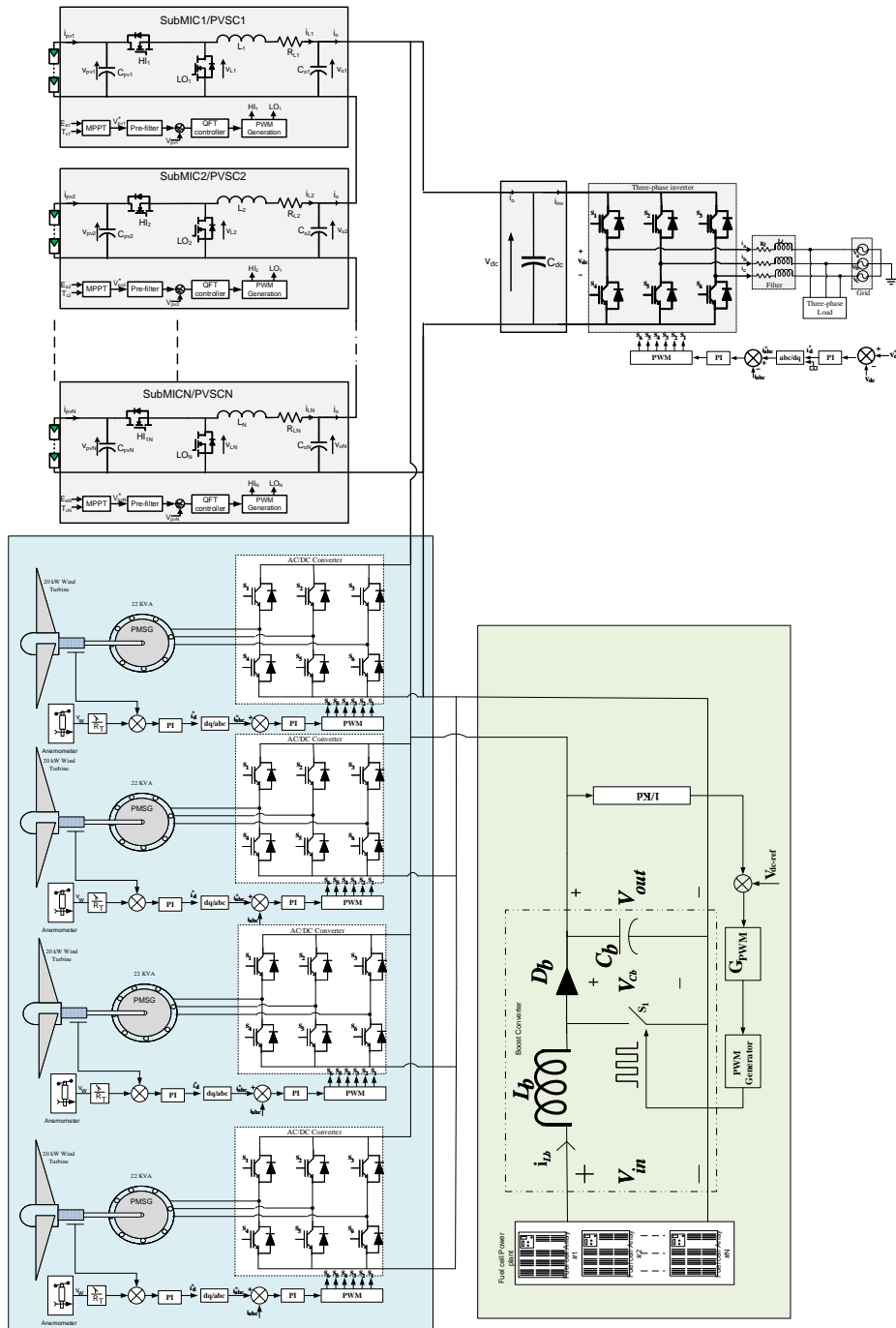


Figure 5.29: Schematic diagram of grid connected hybrid renewable power system

In this simulation, PMSG based WECS, PV and PEMFC are designed as per the unit sizing procedure discussed in section 5.1, to feed the residential load considered in IIT Bombay campus. The output power from all the sources is shown in Figure 5.30. The Inverter power (green line) from $t = 0$ s to $t = 50$ s is higher than the load power (red line), and the grid power (maroon line) is positive so that grid absorbs power from inverter. So the hybrid system provides the surplus power to grid and load demand.

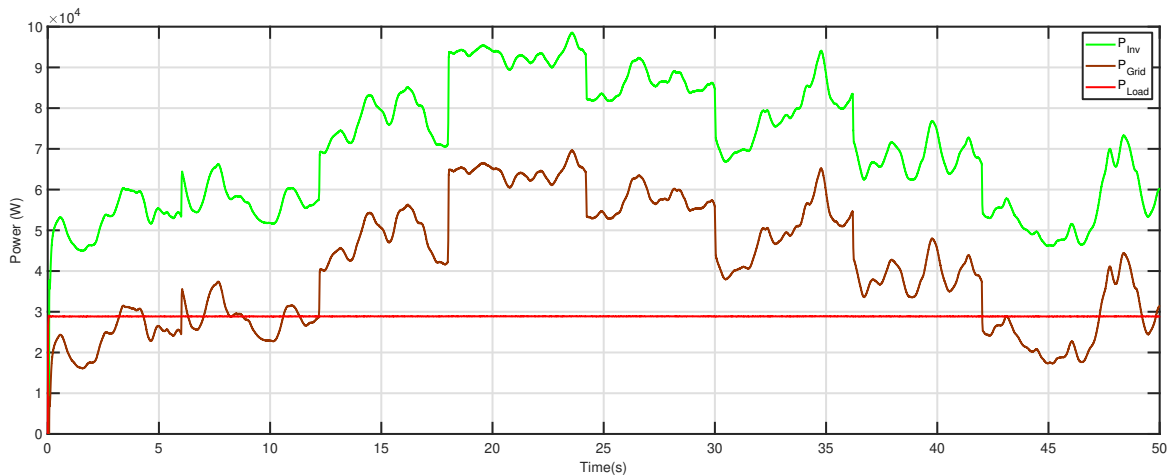


Figure 5.30: Power

5.7 Summery

Unit sizing procedure applied to the renewable energy sources to generate desired power as per the load. A General overview on DC-coupled hybrid system configuration and system integration is discussed. The controller performance is evaluated by operating all the renewable energy sources at their maximum power point. The operation of individual and hybrid configuration is evaluated under stochastic environmental conditions to show the robustness of the proposed controller.

Chapter 6

Conclusion

The research work described in this dissertation draws the following conclusions,

1. In this work, Modified fitness function is introduced to design automatic robust controller to extract maximum power from the Permanent magnet synchronous generator based automated wind power system in quantitative feedback theory (QFT) framework. Genetic algorithms (GA) are preferable for their direct search nature in solution space and high-quality solutions in optimization. GA based automated loop-shaping (ALS) of QFT robust controllers are designed for the existing fitness function and modified fitness function. Both controllers are satisfying all the performance specifications in the time domain and frequency domain. With the application of proposed controller, the high frequency gain is reduced to a value of 63.65% as compared to the application of existing method described in the literature. Thus, the sensitivity of proposed controller to high frequency noise is minimum and requires reduced control effort. The coefficients of fitness function play a major role in designing the optimal controller. Shaft electromagnetic oscillations are reduced and the optimal controller input can be achieved so the maximum power extraction is possible with the proposed strategy.
2. In addition with the robust QFT controller design, accurate parametrization methodology is proposed. Pertinent PV circuit model is identified based on accuracy using proposed methodology. The PV system with buck converter is modelled as uncertain system. The proposed robust QFT controller is designed for the uncertain system to inject maximum power into grid under different envi-

ronmental conditions at sub-module level. Performance comparison of proposed controller with Q-parametrization controller is performed. The data is collected from my institute, National Institute of Technology, Karnataka. Long term (24-hour) simulations are performed and achieved enhanced performance over the existing method.

3. Further, active and reactive power controller is designed based on proposed methodology. Performance comparison of proposed controller with PI controller to inject desired active and reactive power into grid is analysed. The proposed controller shown enhanced performance over the existing controller under different uncertain conditions.
4. Finally, hybrid system is designed based on the unit sizing procedure for the power consumption of IIT Bombay campus. Maximum power extraction for the hybrid renewable energy system is achieved with the proposed automated robust QFT controller under different environmental conditions.

6.1 Scope for Future Work

Future scope of the current work based on the work carried out in this dissertation, to show the path for the future researchers which includes,

- The proposed automated quantitative feedback theory (QFT) based robust controller design methodology using genetic algorithm can be used to design the fractional order controller to improve the controller optimal performance .
- The sub-module level configuration of PV system shown a great performance. So hardware implementation for the hybrid renewable energy system at sub-module level grid connected or autonomous PV system will improve the power system stability and reliability.

Bibliography

- Adamo, F., Attivissimo, F., Di Nisio, A., and Spadavecchia, M. (2011). Characterization and testing of a tool for photovoltaic panel modeling. *IEEE Transactions on Instrumentation and Measurement*, 60(5):1613–1622.
- Ali, H. I., Noor, S. B. B. M., Bashi, S., and Marhaban, M. H. (2012). Quantitative feedback theory control design using particle swarm optimization method. *Transactions of the Institute of Measurement and Control*, 34(4):463–476.
- Ballance, D. and Gawthrop, P. (1991). Control systems design via a quantitative feedback theory approach. In *Control 1991. Control'91., International Conference on*, pages 476–480. IET.
- Benavides, N. D. and Chapman, P. L. (2008). Modeling the effect of voltage ripple on the power output of photovoltaic modules. *IEEE Transactions on Industrial Electronics*, 55(7):2638–2643.
- Blaabjerg, F., Chen, Z., and Kjaer, S. B. (2004). Power electronics as efficient interface in dispersed power generation systems. *IEEE transactions on power electronics*, 19(5):1184–1194.
- Blaabjerg, F., Liserre, M., and Ma, K. (2011). Power electronics converters for wind turbine systems. *IEEE Transactions on industry applications*, 48(2):708–719.
- Blunier, B. and Miraoui, A. (2007). Air management in pem fuel cells: State-of-the-art and prospectives. In *2007 International Aegean Conference on Electrical Machines and Power Electronics*, pages 245–254. IEEE.
- Borghesani, C., Chait, Y., and Yaniv, O. (2003). The *QFT* frequency domain control design toolbox. *Terasoft, Inc., San Diego, CA*. <http://www.terasoft.com/qft/QFTManual.pdf>.

- Bryant, G. and Halikias, G. (1995). Optimal loop-shaping for systems with large parameter uncertainty via linear programming. *International Journal of Control*, 62(3):557–568.
- Cannizzaro, S., Di Piazza, M., Luna, M., and Vitale, G. (2014a). Generalized classification of pv modules by simplified single-diode models. In *Industrial Electronics (ISIE), 2014 IEEE 23rd International Symposium on*, pages 2266–2273. IEEE.
- Cannizzaro, S., Di Piazza, M., Luna, M., and Vitale, G. (2014b). *PVID*: An interactive *MATLAB* application for parameter identification of complete and simplified single-diode pv models. In *Control and Modeling for Power Electronics (COMPEL), 2014 IEEE 15th Workshop on*, pages 1–7. IEEE.
- Cárdenas, R., Peña, R., Alepuz, S., and Asher, G. (2013). Overview of control systems for the operation of dfigs in wind energy applications. *IEEE Transactions on Industrial Electronics*, 60(7):2776–2798.
- Carrillo, C., Montaño, A. O., Cidrás, J., and Díaz-Dorado, E. (2013). Review of power curve modelling for wind turbines. *Renewable and Sustainable Energy Reviews*, 21:572–581.
- Celik, A. N. and Acikgoz, N. (2007). Modelling and experimental verification of the operating current of mono-crystalline photovoltaic modules using four-and five-parameter models. *Applied energy*, 84(1):1–15.
- Chait, Y. and Yaniv, O. (1993). Multi-input/single-output computer-aided control design using the quantitative feedback theory. *International Journal of Robust and Nonlinear Control*, 3(1):47–54.
- Chatterjee, A., Keyhani, A., and Kapoor, D. (2011). Identification of photovoltaic source models. *IEEE Transactions on Energy conversion*, 26(3):883–889.
- Chen, Q. and Hollot, C. (1999). Automatic loop-shaping of *QFT* controllers via linear programming. *ASME J. Dyn. Syst. Meas. Control*, 121:351357.
- Chen, Z., Guerrero, J. M., and Blaabjerg, F. (2009). A review of the state of the art of power electronics for wind turbines. *IEEE Transactions on power electronics*, 24(8):1859–1875.

- Cheng, Z., Ren, P., Xu, Y. L., and Zhang, H. N. (2017). Model and control of fuel supply systems of hydrogen/oxygen fuel cell. *The Journal of Engineering*, 2017(13):773–777.
- Conroy, J. F. and Watson, R. (2008). Frequency response capability of full converter wind turbine generators in comparison to conventional generation. *IEEE transactions on power systems*, 23(2):649–656.
- Corrêa, J. M., Farret, F. A., Canha, L. N., and Simoes, M. G. (2004). An electrochemical-based fuel-cell model suitable for electrical engineering automation approach. *IEEE Transactions on industrial electronics*, 51(5):1103–1112.
- Cownden, R., Nahon, M., and Rosen, M. (2001). Modelling and analysis of a solid polymer fuel cell system for transportation applications. *International Journal of Hydrogen Energy*, 26(6):615–623.
- Cutululis, N. A., Ceanga, E., Hansen, A. D., and Sørensen, P. (2006a). Robust multi-model control of an autonomous wind power system. *Wind Energy: An International Journal for Progress and Applications in Wind Power Conversion Technology*, 9(5):399–419.
- Cutululis, N. A., Ceanga, E., Hansen, A. D., and Sørensen, P. (2006b). Robust multi-model control of an autonomous wind power system. *Wind Energy*, 9(5):399–419.
- Darvishi, M. and Barati, A. (2007). A third-order newton-type method to solve systems of nonlinear equations. *Applied Mathematics and Computation*, 187(2):630–635.
- Dicks, A. and Rand, D. A. J. (2018). *Fuel cell systems explained*. Wiley Online Library.
- Dwari, S. and Parsa, L. (2010). An efficient high-step-up interleaved *DC-DC* converter with a common active clamp. *IEEE Transactions on Power Electronics*, 26(1):66–78.
- Ekanayake, J. and Jenkins, N. (2004). Comparison of the response of doubly fed and fixed-speed induction generator wind turbines to changes in network frequency. *IEEE Transactions on Energy conversion*, 19(4):800–802.

- El Moursi, M. S., Xiao, W., and Kirtley Jr, J. L. (2013). Fault ride through capability for grid interfacing large scale pv power plants. *IET Generation, Transmission & Distribution*, 7(9):1027–1036.
- Erdinc, O. and Uzunoglu, M. (2012). Optimum design of hybrid renewable energy systems: Overview of different approaches. *Renewable and Sustainable Energy Reviews*, 16(3):1412–1425.
- Errami, Y., Maaroufi, M., and Ouassaid, M. (2013). Maximum power point tracking of a wind power system based on the *PMSG* using sliding mode direct torque control. In *2013 International Renewable and Sustainable Energy Conference (IRSEC)*, pages 218–223. IEEE.
- Femia, N., Lisi, G., Petrone, G., Spagnuolo, G., and Vitelli, M. (2008). Distributed maximum power point tracking of photovoltaic arrays: Novel approach and system analysis. *IEEE Transactions on Industrial Electronics*, 55(7):2610–2621.
- Garcia-Sanz, M. (2017). *Robust control engineering: practical QFT solutions*. CRC press.
- Garcia-Sanz, M., Eguinoa, I., Barreras, M., and Bennani, S. (2008). Nondiagonal *MIMO QFT* controller design for darwin-type spacecraft with large flimsy appendages. *Journal of Dynamic Systems, Measurement, and Control*, 130(1):011006.
- Garcia-Sanz, M. and Guillen, J. (2000). Automatic loop-shaping of *QFT* robust controllers via genetic algorithms. *IFAC Proceedings Volumes*, 33(14):603–608.
- Garcia-Sanz, M. and Houppis, C. H. (2012). *Wind energy systems: control engineering design*. CRC press.
- Garcia-Sanz, M., Mauch, A., and Philippe, C. (2009). *QFT* control toolbox: an interactive object-oriented *MATLAB CAD* tool for quantitative feedback theory. In *6th IFAC Symposium on Robust Control Design, ROCOND*, volume 9.
- Garcia-Sanz, M. and Molins, C. (2008). *QFT* robust control of a vega-type space launcher. In *Control and Automation, 2008 16th Mediterranean Conference on*, pages 35–40. IEEE.

- Garcia-Sanz, M. and Molins, C. (2010). Automatic loop shaping of *QFT* robust controllers with multi-objective specifications via nonlinear quadratic inequalities. In *Aerospace and Electronics Conference (NAECON), Proceedings of the IEEE 2010 National*, pages 348–353. IEEE.
- Garcia-Sanz, M. and Oses, J. (2004). Evolutionary algorithms for automatic tuning of *QFT* controllers. *Modelling, Identification, and Control*.
- Gera, A. and Horowitz, I. (1980). Optimization of the loop transfer function. *International Journal of Control*, 31(2):389–398.
- Goldberg, D. E. and Holland, J. H. (1988). Genetic algorithms and machine learning. *Machine learning*, 3(2):95–99.
- Gutman, P. (1996). Qsyn-the toolbox for robust control systems design for use with *MATLAB*, users guide. *El-Op Electro-Optics Industries Ltd, Rehovot, Israel*.
- Hamelin, J., Agbossou, K., Laperriere, A., Laurencelle, F., and Bose, T. (2001). Dynamic behavior of a pem fuel cell stack for stationary applications. *International Journal of Hydrogen Energy*, 26(6):625–629.
- Heydari, M. and Smedley, K. (2015). Comparison of maximum power point tracking methods for medium to high power wind energy systems. In *2015 20th Conference on Electrical Power Distribution Networks Conference (EPDC)*, pages 184–189. IEEE.
- Horowitz, I. (2001). Survey of quantitative feedback theory (*QFT*). *International journal of robust and nonlinear control*, 11(10):887–921.
- Horowitz, I. M. (1963). *Synthesis of feedback systems*. New York: Academic Press.
- Houpis, C. and Sating, R. (1997). *MIMO QFT* cad package (version 3). *International Journal of robust and nonlinear control*, 7(6):533–549.
- Houpis, C. H. and Garcia-Sanz, M. (2012). *Wind energy systems: control engineering design*. CRC press.
- Houpis, C. H., Rasmussen, S. J., and Garcia-Sanz, M. (2005). *Quantitative feedback theory: fundamentals and applications*. CRC press.

- Hu, Y., Du, Y., Xiao, W., Finney, S., and Cao, W. (2015). DC-link voltage control strategy for reducing capacitance and total harmonic distortion in single-phase grid-connected photovoltaic inverters. *IET Power Electronics*, 8(8):1386–1393.
- Huang, P.-H., Xiao, W., Peng, J. C.-H., and Kirtley, J. L. (2016). Comprehensive parameterization of solar cell: Improved accuracy with simulation efficiency. *IEEE Transactions on Industrial Electronics*, 63(3):1549–1560.
- Hyvarinen, J. and Karila, J. (2003). New analysis method for crystalline silicon cells. In *Photovoltaic Energy Conversion, 2003. Proceedings of 3rd World Conference on*, volume 2, pages 1521–1524. IEEE.
- Ishaque, K. and Salam, Z. (2011). An improved modeling method to determine the model parameters of photovoltaic (pv) modules using differential evolution (de). *Solar Energy*, 85(9):2349–2359.
- Jafarian, H., Mazhari, I., Parkhideh, B., Trivedi, S., Somayajula, D., Cox, R., and Bhowmik, S. (2015). Design and implementation of distributed control architecture of an ac-stacked pv inverter. In *Energy Conversion Congress and Exposition (ECCE), 2015 IEEE*, pages 1130–1135. IEEE.
- Jang, M., Ciobotaru, M., and Agelidis, V. G. (2012). A single-phase grid-connected fuel cell system based on a boost-inverter. *IEEE transactions on power electronics*, 28(1):279–288.
- Jeyasenthil, R., Purohit, H., and Nataraj, P. (2014). Automatic loop shaping in *MIMO QFT* using interval consistency based optimization technique. In *Industrial Electronics (ISIE), 2014 IEEE 23rd International Symposium on*, pages 75–80. IEEE.
- Kadri, R., Gaubert, J.-P., and Champenois, G. (2011). An improved maximum power point tracking for photovoltaic grid-connected inverter based on voltage-oriented control. *IEEE transactions on industrial electronics*, 58(1):66–75.
- Kaldellis, J. K. (2010). *Stand-alone and hybrid wind energy systems: technology, energy storage and applications*. Elsevier.
- Katal, N. and Narayan, S. (2016a). Optimal *QFT* controller and pre-filter for buck converter using flower pollination algorithm. In *Power Electronics, Intelligent*

Control and Energy Systems (ICPEICES), IEEE International Conference on, pages 1–6. IEEE.

- Katal, N. and Narayan, S. (2016b). *QFT* based robust positioning control of the pmsm using automatic loop shaping with teaching learning optimization. *Modelling and Simulation in Engineering*, 2016.
- Khan, O. and Xiao, W. (2016). An efficient modeling technique to simulate and control submodule-integrated pv system for single-phase grid connection. *IEEE Transactions on Sustainable Energy*, 7(1):96–107.
- Khanh, L. N., Seo, J.-J., Kim, Y.-S., and Won, D.-J. (2010). Power-management strategies for a grid-connected *PV-FC* hybrid system. *IEEE transactions on power delivery*, 25(3):1874–1882.
- Koutroulis, E. and Kalaitzakis, K. (2006). Design of a maximum power tracking system for wind-energy-conversion applications. *IEEE transactions on industrial electronics*, 53(2):486–494.
- Larminie, J., Dicks, A., and McDonald, M. S. (2003). *Fuel cell systems explained*, volume 2. J. Wiley Chichester, UK.
- Li, H. and Chen, Z. (2008). Overview of different wind generator systems and their comparisons. *IET Renewable Power Generation*, 2(2):123–138.
- Lim, L. H. I., Ye, Z., Ye, J., Yang, D., and Du, H. (2015). A linear identification of diode models from single *i-v* characteristics of pv panels. *IEEE Transactions on Industrial Electronics*, 62(7):4181–4193.
- Lingyun, X., Lefei, S., Wei, H., and Cong, J. (2011). Solar cells parameter extraction using a hybrid genetic algorithm. In *Measuring Technology and Mechatronics Automation (ICMTMA), 2011 Third International Conference on*, volume 3, pages 306–309. IEEE.
- Liserre, M., Sauter, T., and Hung, J. Y. (2010). Future energy systems: Integrating renewable energy sources into the smart power grid through industrial electronics. *IEEE industrial electronics magazine*, 4(1):18–37.

- Maggio, G., Recupero, V., and Pino, L. (2001). Modeling polymer electrolyte fuel cells: an innovative approach. *Journal of power sources*, 101(2):275–286.
- Mammen, P. M., Kumar, H., Ramamritham, K., and Rashid, H. (2018). Want to reduce energy consumption, whom should we call? In *Proceedings of the Ninth International Conference on Future Energy Systems*, page 1220. ACM.
- Mathur, J. (2009). *Introduction to wind energy systems: basics, technology and operation*. Springer.
- Molins, C. and Garcia-Sanz, M. (2009). Automatic loop-shaping of *QFT* robust controllers. In *Aerospace & Electronics Conference (NAECON), Proceedings of the IEEE 2009 National*, pages 103–110. IEEE.
- Muller, S., Deicke, M., and De Doncker, R. W. (2002). Doubly fed induction generator systems for wind turbines. *IEEE Industry applications magazine*, 8(3):26–33.
- Nehrir, M. H. and Wang, C. (2009). *Modeling and control of fuel cells: distributed generation applications*, volume 41. John Wiley & Sons.
- Nejabatkhah, F. and Li, Y. W. (2014). Overview of power management strategies of hybrid *AC/DC* microgrid. *IEEE Transactions on Power Electronics*, 30(12):7072–7089.
- Ortiz-Conde, A., Lugo-Munoz, D., and García-Sánchez, F. J. (2012). An explicit multiexponential model as an alternative to traditional solar cell models with series and shunt resistances. *IEEE Journal of Photovoltaics*, 2(3):261–268.
- Pena, R., Clare, J., and Asher, G. (1996). Doubly fed induction generator using back-to-back pwm converters and its application to variable-speed wind-energy generation. *IEE Proceedings-Electric Power Applications*, 143(3):231–241.
- Qin, H. and Kimball, J. W. (2011). Parameter determination of photovoltaic cells from field testing data using particle swarm optimization. In *Power and Energy Conference at Illinois (PECI), 2011 IEEE*, pages 1–4. IEEE.
- Ramakumar, R. and Bigger, J. (1993). Photovoltaic systems. *Proceedings of the IEEE*, 81(3):365–377.

- Romero-Cadaval, E., Spagnuolo, G., Franquelo, L. G., Ramos-Paja, C. A., Suntio, T., and Xiao, W. M. (2013a). Grid-connected photovoltaic generation plants: Components and operation. *IEEE Industrial Electronics Magazine*, 7(3):6–20.
- Romero-Cadaval, E., Spagnuolo, G., Franquelo, L. G., Ramos-Paja, C. A., Suntio, T., and Xiao, W. M. (2013b). Grid-connected photovoltaic generation plants: Components and operation. *IEEE Industrial Electronics Magazine*, 7(3):6–20.
- Ropp, M. E. and Gonzalez, S. (2009). Development of a *MATLAB*/simulink model of a single-phase grid-connected photovoltaic system. *IEEE transactions on Energy conversion*, 24(1):195–202.
- Sating, R., Horowitz, I., and Houppis, C. (1993). Development of a *MIMO QFT* cad package (ver. 2), air force institute of technology, wright-patterson afb, oh 45433, usa. In *American Control Conference*.
- Shawky, A., Helmy, F., Orabi, M., Qahouq, J. A., and Dang, Z. (2014). On-chip integrated cell-level power management architecture with *MPPT* for *PV* solar system. In *Applied Power Electronics Conference and Exposition (APEC), 2014 Twenty-Ninth Annual IEEE*, pages 572–579. IEEE.
- Siwakoti, Y. P. and Blaabjerg, F. (2016). Single switch nonisolated ultra-step-up *DC-DC* converter with an integrated coupled inductor for high boost applications. *IEEE Transactions on Power Electronics*, 32(11):8544–8558.
- Soon, J. J. and Low, K.-S. (2012). Photovoltaic model identification using particle swarm optimization with inverse barrier constraint. *IEEE Transactions on Power Electronics*, 27(9):3975–3983.
- Stark, C., Pless, J., Logan, J., Zhou, E., and Arent, D. J. (2015a). Renewable electricity: Insights for the coming decade. Technical report, National Renewable Energy Lab.(NREL), Golden, CO (United States).
- Stark, C., Pless, J., Logan, J., Zhou, E., and Arent, D. J. (2015b). Renewable electricity: Insights for the coming decade. Technical report, National Renewable Energy Lab.(NREL), Golden, CO (United States).
- Thompson, D. and Nwokah, O. (1989). Stability and optimal design in quantitative feedback theory. In *ASME Winter Annual Meeting*.

- Thongam, J., Bouchard, P., Beguenane, R., and Fofana, I. (2010). Neural network based wind speed sensorless *MPPT* controller for variable speed wind energy conversion systems. In *2010 IEEE Electrical Power & Energy Conference*, pages 1–6. IEEE.
- Veerachary, M. and Khas, H. (2006). Psim circuit-oriented simulator model for the nonlinear photovoltaic sources. *IEEE Transactions on Aerospace Electronic Systems*, 42:735–740.
- Villa, L. F. L., Ho, T.-P., Crebier, J.-C., and Raison, B. (2013). A power electronics equalizer application for partially shaded photovoltaic modules. *IEEE Transactions on Industrial Electronics*, 60(3):1179–1190.
- Villalva, M. G., Gazoli, J. R., and Ruppert Filho, E. (2009). Comprehensive approach to modeling and simulation of photovoltaic arrays. *IEEE Transactions on power electronics*, 24(5):1198–1208.
- Wang, F., Wu, X., Lee, F. C., Wang, Z., Kong, P., and Zhuo, F. (2013). Analysis of unified output *MPPT* control in subpanel pv converter system. *IEEE Transactions on power Electronics*, 29(3):1275–1284.
- Wang, M. and Nehrir, M. (2001). Fuel cell modeling and fuzzy logic-based voltage control. *International Journal of Renewable Energy Engineering*, 3(2):320–325.
- Wang, W., Wu, D., Wang, Y., and Ji, Z. (2010a). H_∞ gain scheduling control of *PMSG*-based wind power conversion system. In *2010 5th IEEE Conference on Industrial Electronics and Applications*, pages 712–717. IEEE.
- Wang, X., Yuvarajan, S., and Fan, L. (2010b). *MPPT* control for a *PMSG*-based grid-tied wind generation system. In *North American Power Symposium 2010*, pages 1–7. IEEE.
- Wei, C., Zhang, Z., Qiao, W., and Qu, L. (2016). An adaptive network-based reinforcement learning method for *MPPT* control of *PMSG* wind energy conversion systems. *IEEE Transactions on Power Electronics*, 31(11):7837–7848.
- William, S. and Li, Z. (2017). *Electricity generation using wind power*. World scientific.

- Wu, B., Lang, Y., Zargari, N., and Kouro, S. (2011). *Power conversion and control of wind energy systems*, volume 76. John Wiley & Sons.
- Xiao, W., Dunford, W. G., and Capel, A. (2004). A novel modeling method for photovoltaic cells. In *Power Electronics Specialists Conference, 2004. PESC 04. 2004 IEEE 35th Annual*, volume 3, pages 1950–1956. IEEE.
- Xiao, W., Dunford, W. G., Palmer, P. R., and Capel, A. (2007). Regulation of photovoltaic voltage. *IEEE Transactions on Industrial Electronics*, 54(3):1365–1374.
- Xiao, W., Edwin, F. F., Spagnuolo, G., and Jatskevich, J. (2013). Efficient approaches for modeling and simulating photovoltaic power systems. *IEEE journal of photovoltaics*, 3(1):500–508.
- Xiao, W., El Moursi, M. S., Khan, O., and Infield, D. (2016). Review of grid-tied converter topologies used in photovoltaic systems. *IET Renewable Power Generation*, 10(10):1543–1551.
- Yang, S., Zhang, X., Zhang, C., Xie, Z., and Li, F. (2010). Sensorless control for *PMSG* in direct-drive wind turbines. In *The 2nd International Symposium on Power Electronics for Distributed Generation Systems*, pages 81–84. IEEE.
- Yaramasu, V. and Wu, B. (2016). *Model predictive control of wind energy conversion systems*. John Wiley & Sons.
- Yaramasu, V., Wu, B., Sen, P. C., Kouro, S., and Narimani, M. (2015). High-power wind energy conversion systems: State-of-the-art and emerging technologies. *Proceedings of the IEEE*, 103(5):740–788.
- Yazdani, A., Di Fazio, A. R., Ghoddami, H., Russo, M., Kazerani, M., Jatskevich, J., Strunz, K., Leva, S., and Martinez, J. A. (2011). Modeling guidelines and a benchmark for power system simulation studies of three-phase single-stage photovoltaic systems. *IEEE transactions on power delivery*, 26(2):1247–1264.
- Yong, Y. and Huiqing, W. (2019). Adaptive perturb and observe maximum power point tracking with current predictive and decoupled power control for grid-connected photovoltaic inverters. *Journal of Modern Power Systems and Clean Energy*, pages 1–11.

Yuehua, H., Huanhuan, L., Guangxu, L., and Chunguo, Y. (2014). The largest wind energy capture based on feedback linearization control. In *Unifying Electrical Engineering and Electronics Engineering*, pages 1011–1018. Springer.

Publications Based on Thesis

Conference

1. Hemachandra Gudimindla and Manjunatha Sharma K, "Performance Analysis of Automated Quantitative Feedback Theory Based Robust Controller for Photovoltaic Converter," , in 2017 IEEE International Conference on Emerging Trends and Innovations In Engineering And Technological Research (ICETI-ETR), Ernakulam, 2018, pp. 1-7.
2. Hemachandra Gudimindla and Manjunatha Sharma K, "Performance analysis of robust and nonlinear MPPT controllers for autonomous wind power system," 9th in 2016 IEEE 7th Power India International Conference (PIICON), Bikaner, 2016, pp. 1-6.

Journal

1. Hemachandra Gudimindla and Manjunatha Sharma K, Accurate parametrization and methodology for selection of pertinent single diode photovoltaic model with improved simulation efficiency," , Elsevier, Solar Energy, vol. 174, pp. 582-592, 2018 (SCI Indexed).
2. Hemachandra Gudimindla and Manjunatha Sharma K, "Design and performance analysis of quantitative feedback theory based automated robust controller: An application to uncertain autonomous wind power system", AIMS Energy, vol. 6, no. 4, pp. 576-592, 2018 (ESCI Indexed).
3. Hemachandra Gudimindla and Manjunatha Sharma K, "Performance analysis of automated genetic quantitative feedback theory based robust controller for long-term grid tied PV system simulations", Journal of Modern Power Systems and Clean Energy, Springer, 2019. (SCI Indexed) (Under Review).

Curriculum Vitae

Hemachandra Gudimindla

Research Scholar, Dept. of Electrical and Electronics Engineering
National Institute of Technology Karnataka, Surathkal

E-Mail: sandhyahemachandra@gmail.com

Date of Birth: 02-06-1988

Ph.No: +91- 8618899095

LinkedIn : www.linkedin.com/in/hemachandrag/

Google-site : <https://sites.google.com/view/hemachandra/home>



Education

Jawaharlal Nehru Technological University, Anantapur, Andhra Pradesh, India

Master of Technology in Control Systems, Electrical and Electronics Engineering

2010-2013

73.67%

Sree Vidyanikethan Engineering College, Tirupathi, Andhra Pradesh, India

Bachelor of Technology, Electrical and Electronics Engineering

2005-2009

56.34%

Sri Venkateswara Junior College, Chittoor, Andhra Pradesh, India

Class XII , Intermediate Board of Education

May 2005

80.10%

AP Residential School, Gyarampalli, Andhra Pradesh, India

Class X, SSC

March 2003

90.14%

Work Experience

Assistant Professor, Dept. of Electrical Electronics Engineering., Srinivasa
Ramanujan Institute of Technology, Anantapur, June 2012-July 2014